Investigation of Large-Area Spray Deposited Donor (Sb, Ba, Nb, Ta) Doped SnO_2 Thin Films for Transparent Conducting Electrode Applications

THESIS

Submitted in partial fulfilment of the requirements for the award of the degree of

Doctor of Philosophy

IN
PHYSICS

BY

R. RAMARAJAN

(Roll No: 715083)

Under the supervision of

Dr. K. Thangaraju

DEPARTMENT OF PHYSICS
NATIONAL INSTITUTE OF TECHNOLOGY
WARANGAL-506004, (T. S.), INDIA

September 2020

DECLARATION

This is to declare that the work presented in the thesis entitled ***"Investigation of Large-Area Spray Deposited Donor (Sb, Ba, Nb, Ta) Doped SnO_2 Thin Films for Transparent Conducting Electrode Applications***" is a bonafide work done by me under the supervision of Dr. K. Thangaraju, Associate Professor, Department of Physics, and was not submitted elsewhere for the award of any degree.

I declare that this written submission represents my ideas in my own words and where other's ideas or words have been included, I have adequately cited and referenced the original sources. I also declare that I have adhered to all principles of academic honesty and integrity and have not misrepresented or fabricated or falsified any idea/data/fact/ source in my submission. I understand that any violation of the above will be a cause for disciplinary action by the Institute and can also evoke penal action from the sources which have thus not been properly cited or from whom proper permission has not been taken when needed.

Date: 13. 05. 2020 **R. RAMARAJAN**

Place: NIT Warangal **(Roll No: 715083)**

NATIONAL INSTITUTE OF TECHNOLOGY, WARANGAL

CERTIFICATE

This is to certify that the work presented in the thesis entitled ***"Investigation of Large-Area Spray Deposited Donor (Sb, Ba, Nb, Ta) Doped SnO_2 Thin Films for Transparent Conducting Electrode Applications***" is a bonafide work carried out by Mr. **R. RAMARAJAN** under my supervision and was not submitted elsewhere for the award of any degree.

Date: 13. 05. 2020

Place: NIT Warangal

Dr. K. THANGARAJU

Associate Professor

Research supervisor

Acknowledgements

I would like to express my sincere heartfelt gratitude to my research supervisor, Dr. K. Thangaraju, *Associate Professor,* Department of Physics, NIT Warangal for his constructive guidance, relentless encouragement, and his love of research motivated me throughout my research life. I very much appreciate the freedom to pursue my research interests that he has given for completion of this research work. Moreover, he inspired to ensure the completion of this work. His expertise, availability to discuss ideas and willingness to share his knowledge were instrumental. For this, I will be eternally grateful.

I must also extend my gratitude to my research mentor Dr. D. Paul Joseph, Assistant Professor, Department of Physics, NIT Warangal, for his great patience, efficient guidance and lots of help. He taught fundamental research ideas on material science and thin-film technology, which certainly form a concrete basis of my material science knowledge, that can help me forever. Thanks a lot, Dr. D. Paul Joseph for everything you have done for me. I'm sure, the knowledge that I gained with you will help to fulfill my research dreams.

I express my sincere thanks to the Director, National Institute of Technology, Warangal, for having given me the opportunity to carry out the work and allowing me to submit the work in the form of thesis. I express my sincere thanks to MHRD, New Delhi for the financial support in the form of fellowship.

I express my thanks NIT-Warangal TEQIP – II program for research seed grant (2014) towards procuring the custom-made spray pyrolysis unit. I express my thanks SERB, Govt. of India for research grant under the file No.: YSS/2014/000191.

I express my sincere thanks to Prof. D. Dinakar, Head, Department of Physics, NITW, for his valuable suggestions and support. I express my sincere thanks to Former Heads of Department of Physics, NITW, for their valuable help and support.

I sincerely thank the members of the Doctorial scrutiny committee (DSC) Prof. Prof. R. L. N. Sai Prasad, Department of Physics, NITW, Dr. D. Paul Joseph, Department of Physics, NITW, Dr. B. Srinivas, Department of Chemistry, NITW, for their valuable suggestions at every stage of my research.

I am very much thankful to Dr. M. Kovendhan, Department of Environmental Engineering, Inha University, Incheon, South Korea and Dr. V. Ganapathy (ARCI), Hyderabad, India for their help in experimental measurements. I am extremely thankful to Dr. R. Ramesh Babu, School of Physics, Bharathidasan University, Tamil Nadu, India for his valuable support. I also thank Dr. P Saravanan, Defence Metallurgical Research Laboratory (DMRL), Hyderabad for his help in experimental measurements, Prof. A. Subrahmanyam, department of Physics, IIT Madras for his help in conducting Kelvin probe study in his laboratory.

I am thankful to senior faculty members of our department, Prof. S.V.S. Ramana Reddy, Prof. Sai Sankar, Prof. L. Ramgopal Reddy, Prof. R. L. N. Sai Prasad, Prof. K. Venugopal Reddy, for their encouragement and support.

I take this opportunity to express my gratitude to Dr. B. Sobha, Dr. T. Venkatappa Rao, Dr. P. Abdul Azeem, Dr. P. Syam Prasad, Dr. Sourabh Roy, Dr. D. Haranath, Dr. Kusum Kumari, Dr. V. Jayalakshmi, Dr. R. Rakesh Kumar, Dr. K Udaykumar, Dr. Vijay Kumar, Dr. Surya K. Ghosh, Dr. Hitesh Borkar, Dr. Aalu Boda, Department of Physics, National Institute of Technology, Warangal for their valuable advice, encouragement and moral support in my career.

I express my thanks to Dr. M Raja Vishwanathan, Assistant Professor, Humanities & Social Science Department, NIT Warangal for his help during my thesis work.

I would also like to extend my sincere thanks to Prof. M. K. Mohan and B. Srinivasa Rao for providing CAM facilities for experimental measurements. I would also like to thank Mr. Srinivas and Mrs. Ramya, Technicians, NIT warangal for their help to record XRD characterization and SEM-EDX characterization of my samples.

I indeed thank Prof. V. Ravichandran, Former Head, Department of Nuclear Physics, University of Madras Chennai, Dr. K. Ravichandran, Department of Nuclear Physics, University of Madras Chennai, Prof. P.R. Umarani, Department of Physics, Presidency College, Chennai, Dr. V. Murugan, former HOD, Physics Department, Vivekananda College, Chennai, for their care on my personal life, and for the way they explained the subject, the freedom to learn Physics throughout the under and post graduate degrees.

With all happiness I acknowledge the cheerful assistance rendered by all my senior research colleagues Dr. S. Rajkumar, Dr. V. Himamaheswara Rao, Dr. P.V.N. Kishore, Mr. M. Mohan babu, Mr. D. Gnyaneshwar, Dr. Hari Krishna for their encouragement thoughout the period of my research.

I thank all the research colleagues Dr. Ashish kumar, Ms. P. M. Pratheeksha, Dr. K. Uma Devi, Mr. T. Ramesh, Mr. Lal Singh, Ms. Sravanthi, Mr. Nagaraju, Mr. Srinath, Mr. VDR Pavan, Ms. Manjula, Mr. N. Purusotham Reddy, Mr. Buchaiah, Mr. Ramesh, Mr. C. Ravikanth Reddy, Mr. K. Venkata Ashish Srivatsav, Ms. Meenu mariya solly, Mr. Mahantesh Reddy, and other co-research scholars for their munificent support.

I am happy to express my heartfelt thanks to my dear friends Mr. S. Shankar (MLA), Mr. Ranjith kumar (IISc Bangalore), Mr. Jayachandran, Mr. Kulanchiyappan, Mr. Dhayal, Mr. Prasanth, Mr. Ramamoorthi, Mr. K. Muruganatham (Brother) for their support and encouragement during the entire course of my personal life. I am very much thankful to all the faculty members Department of Physics Presidency college Chennai, Faculty members Department of Nuclear Physics University of Madras Chennai, and my school teachers, Govt HSS, Kandachipuram, Villupuram, Tamilnadu, for their motivation and encouragement.

It would not have been possible for me to enter my research journey without their motivation, cooperation and encouragement. heart goes to my beloved Family Members who with all their patience, prayers and faith in the Almighty, waited all these long years to see me reaching this stage. Their blessings and care always gave me new fervor and gusto to do something more with perfection. I always remember and cherish the encouragement and inspiration provided by my mother and father during the course of my research work.

Date: 01. 09. 2020

R. RAMARAJAN

Place: NIT Warangal.

"If a country is to be corruption free and become a nation of beautiful minds, I strongly feel there are three key societal members who can make a difference. They are the father, the mother and the teacher".

Dr. A. P. J. Abdul Kalam

DEDICATED TO

MY PARENTS

Ambika Ramanathan

and

Bhanumathi

Preface

In recent years, transparent conducting oxide (TCO) materials have attracted considerable attention for potential applications in optoelectronic devices due to their unique electrical and optical properties. More importantly, drastically increasing display device's usage cause more demand for indium tin oxide (ITO) and fluorine doped tin oxide (FTO) electrodes usage. The scarcity of indium and optimization difficulty of FTO lead to development of alternative material in this research area. Therefore, the development of highly efficient and cost-effective TCEs are today's demand. There are several alternative materials that are well explored for TCE application such as, metal nanowires, carbon nanotubes, graphene, multi-oxide systems, and conducting organic polymer materials. But the problem is, even though the metallic nanowires show good electrical properties, it possesses a low figure of merit values due to low optical property, and also stability and lifetime are very less compared to metal oxide TCO materials. The carbon based TCE materials show low electrical transport properties, and organic TCE materials are expensive and time-consuming process than metal oxide system deposition. More interestingly, the binary metal oxide optimization is easier than ternary metal oxide system, because of easy to control the phase formation. These aspects inspired us to explore the binary TCO material by doping with various elements using the cost-effective deposition technique. The AO_2 binary rutile structure offers high flexibility to incorporate dopants at the 'A' site yielding doped rutile structure. In AO_2 rutile structure, altering the stoichiometry or doping with different donor elements of a different valence state help in tuning the optical and electrical properties appreciably.

Among the AO_2 systems, SnO_2 system is one of the best host materials for transparent conducting oxide application. This research work mainly focuses to explore SnO_2 by doping with various elements. The systems explored are Sb-doped SnO_2 (ATO), Ba and Sb co-doped SnO_2 (BATO), Nb-doped SnO_2 (NTO), and Ta-doped SnO_2 (TTO). Finally, various optimized

TCO films are deposited on large area (10×10 cm^2) and selected TCO films were tested as TCE in dye-sensitized solar cell (DSSC) devices.

The research work presented in this thesis is divided into seven chapters and the outline of each chapter is briefly given below,

Chapter 1: - Gives a general introduction, literature review, application of the TCO materials, alternative TCO materials, fundamental properties of TCO materials. This chapter also deals with the several transparent conducting electrode materials (TCE) classification based on the oxide and non-oxide forms. This chapter highlights the scope and objectives of the research work.

Chapter 2: - This chapter discuss the experimental methods and basics of various analytical instruments, which are used in this research work. Beginning of this chapter deals with introduction to thin films, thin-film growth methods, thin-film formation, and spray pyrolysis deposition technique. This chapter also gives overview of various characterization instrument's basics principle, description, and specifications.

Chapter 3: - This chapter describes the details of transparent conducting Sb-doped tin oxide (ATO) thin films deposited on the glass substrates as a function of substrate temperature by cost-effective spray pyrolysis technique. The deposited ATO thin films were investigated by various characterization techniques such as X-ray diffraction, XPS, SEM-EDS, AFM, UV-visible, Hall Effect, Raman analysis, and temperature-dependent resistivity study by four probe methods. Finally, the best optimized concentration was chosen for a large area (10×10 cm^2) coating. The variation of the sheet resistance of a large area deposited film was estimated across every 1×1 cm^2 surface area. The temperature-dependent electrical study was carried out to find the resistance stability of the film. The surface work function was also estimated by kelvin probe method.

Chapter 4: - This chapter deals with the details of Ba and Sb co-doped SnO_2 (BATO) thin films deposited by cost-effective spray pyrolysis method. The ATO film generally has a grey

tinge upon on doping with Sb, this may affect the optical transmittance of the film. To overcome this issue without sacrificing the TCO properties, the ATO film is explored by co-doping with barium (Ba) in SnO_2 system. The structural, optical and temperature-dependent electrical properties of the BATO thin films were studied as a function of varying Ba concentration. Finally, a large area (10×10 cm^2) optimal 2 wt% of Ba and 5 wt% of Sb doped SnO_2 (BATO2) film was deposited and investigated by various analytical techniques. The BATO2 film has been successfully used as electrode in DSSC device. Interestingly, the optimized results of BATO thin film is found to be better alternative TCE material compared to ATO film.

Chapter-5: - This chapter presents the deposition and characterization of niobium-doped tin oxide (NTO) film using spray pyrolysis technique. The structural properties such as crystallinity, average crystallite size, and texture coefficient of the NTO films were analyzed as a function of Nb concentration. Finally, the optimized 1.5 wt% of Nb doped SnO_2 (NTO3) film was chosen for large area (10×10 cm^2) coating. The variation of the sheet resistance of a large area deposited film was estimated across every 1×1 cm^2 surface area. The results evidenced from NTO films are promising as an indium free alternative TCE material for optoelectronic device applications.

Chapter 6: - This chapter deals with the optimization of sprayed Ta doped SnO_2 thin films (TTO) onto glass substrates for TCO application. Finally, the optimized 4 wt% of Ta doped SnO_2 (TTO4) thin film was selected for large area coating. Part of the large area deposited TTO4 film has been successfully used as electrode in DSSC device. The TTO4 thin film is found to be a promising alternative TCO electrode.

Chapter-7: - The final chapter presents the summary and conclusions drawn from the investigations carried out on best optimized properties of the donor (Sb, Ba-Sb, Nb, Ta)-doped SnO_2 thin films. This chapter compares the results of optimized TCO materials with better optoelectronic properties to serve as an alternative TCO material to replace/supplement the commercial ITO and FTO electrodes.

List of Symbols

Symbol	Description
L	Average crystallite size
β	Full Width at Half Maximum (FWHM)
θ	Diffraction angle
d	Inter-planar spacing
'a', 'b', and 'c'	Lattice constants
TC_{hkl}	Texture coefficient
T_r	Transmittance
T_{av}	Average transmittance
R_{gh}	Roughness
t	Film thickness
I_{0hkl}	Standard peak intensity
I_{hkl}	Observed peak intensity
α	Absorption coefficient
h	Planck's constant
ν	Frequency
E_g	Band gap
E_{optg}	Total optical band gap
ΔEg	Band gap shifting
m*	Reduced mass
m_e	Effective mass of electron
m_h	Effective mass of hole
Eu	Urbach energy
Γ	Raman vibration mode
E_F	Fermi Energy

ϕ	Surface work function
I_0	Incident light intensity
ρ	Resistivity
n_c	Carrier concentration
e	Charge of the electron
μ	Mobility
R_S	Sheet Resistance
V	Measured Voltage
I	Applied Current
$\Omega/\square$	Ohm per Square
σ	Conductivity
E_a	Activation energy
K_B	Boltzmann constant
N	Defects density
V_{oc}	Open-circuit voltage
J_{sc}	Short-circuit current density
FF	Fill factor
P_{in}	Incident light power
η	Power conversion efficiency

List of Abbreviations

Abbreviation	Description
TCO	Transparent Conducting Oxide
TCE	Transparent Conducting Electrode
ITO	Indium Tin Oxide
FTO	Fluorine doped Tin oxide
ATO	Antimony doped Tin oxide
BATO	Barium and Antimony co-doped Tin Oxide
NTO	Niobium doped Tin Oxide
TTO	Tantalum doped Tin Oxide
RMS	Root Mean Square
BM-Shift	Moss–Burstein shift
V_{BM}	Valence Band Maximum
C_{BM}	Conduction Band Minima
FoM	Figure of Merit
XRD	X-ray Diffraction
JCPDS	Joint Committee on Powder Diffraction Standards
SEM	Scanning Electron Microscope
EDS	Energy Dispersive X-ray Spectroscopy
UV-vis-NIR	Ultraviolet-visible-Near infrared Spectroscopy
PL	Photoluminescence
AFM	Atomic Force Microscopy
KP	Kelvin Probe
OLED	Organic Light Emitting Diode
DSSC	Dye-Sensitized Solar Cell
EIS	Electrochemical Impedance Spectroscopy

List of Figures

List of Tables

Contents

CHAPTER: 1

Introduction

Innovations in display and energy harvesting materials and/or devices are the heart of modern technology which are enabled by unique properties of a certain class of materials. The transparent conducting electrode (TCE) materials are inevitable component in the modern technology for energy harvesting and low power consuming optoelectronic devices. The modern technology is aimed at minimizing environmental pollution especially those created by non-renewable energy sources so as to reduce global warming [1,2]. Newer and clean energy production with low cost and low power consuming devices are of more demand in the renewable energy sector in which the TCE materials play a vital role [3,4]. More importantly, the TCEs have significant applicability in the modern optoelectronic devices due to their unique coexisting contradicting (optical and electrical) properties without which many of the technological advantages in the renewable energy sector may not be possible.

1.1. Basics of transparent conducting electrodes

Metals are highly conducting due to overlap of the conduction band and valence band and it contains enormous number of free electrons. Transparent materials are generally insulators and semiconductors which possess completely filled valence band and empty conduction band. Materials that exhibit excellent combination of electrical transport properties and good optical transparency (>85%) in the visible region are called '***Transparent Conducting Electrodes***' [5–7]. The TCE materials should have high optical transparency in the visible region and enormous free charge carriers to conduct electricity like a metal. In this group of materials, one property is strongly correlated with the second property. Achieving high optical transparency and good electrical conductivity within the same host material is challenging. To achieve these properties, it is necessary to understand the basics of these materials such as structural, surface, optical and electrical properties [8,9]. To some extent the computational and theoretical approaches have helped us to understand the physical/chemical aspects lying behind these transparent conducting materials [10,11]. Such a unique class of materials are very useful in a variety of optoelectronic devices, particularly in the renewable energy sector to harvest energy from sunlight [12–14], and also in storage devices [15,16]. The low energy consumption devices such as LEDs/LCDs, touch screens, display units, smart-phones, smart windows, sensors, etc.,[17–20] use a variety of TCEs. The TCE materials are widely used in optoelectronic

gadgets due to their compactness, relatively low-cost production, reliability, low power consumption, etc. [21].

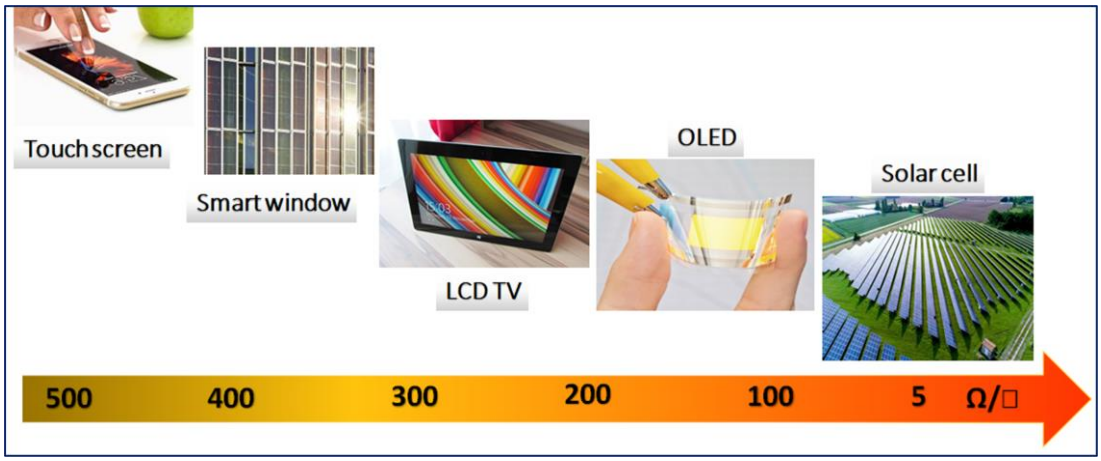

Fig. 1.1. Sheet resistance range of TCEs for application in various optoelectronic devices.

1.2. TCE materials

The transparent conducting electrode materials generally possess wide band gap (> 3.1 eV) offering higher transmittance in the visible region, and enhanced free carrier concentration (> 10^{20} cm^{-3}) providing a metallic-like conductivity [8]. We make use of a variety of TCE materials in our day to day life in the form of thin film electrodes in several modern devices [22]. Figure 1.1 indicates various TCEs incorporated low power consuming devices and their requirements based on sheet resistance values [23]. All these devices need specific TCE materials with appropriate dopants to attribute the required optical and electrical properties.

1.2.1. Historical outlook of TCE materials

The discovery of first TCE material was reported by the German Physicist, Karl Badeker, in 1907. He demonstrated an n-type cadmium oxide (CdO) film and showed high conductivity by simply oxidizing 'Cd' metal film by post-annealing in air [24]. The oxygen vacancies led to enhanced free carrier concentration to promote metallic-like conductivity in CdO. While CdO is not extensively used in the commercial devices due to its toxic nature, but its high electron mobility makes it interesting for theoretical considerations. Badeker et al also reported other TCE materials such as Cu_2O and PbO by sputtering technique and subsequent oxidation in air [24]. Rapid development in TCE materials has resulted with the help of quantum mechanics which has enabled the basic understanding of the physical and chemical behavior of such materials [25,26]. Later, in 1947, American inventor Harold McMaster patented 'Tin

oxide' (SnO_2) thin film as a TCE deposited by chemical spray pyrolysis method [27]. The SnO_2 based transparent heater film was used in aircraft windshields during the second world war [28], however this material was not possessing electrical properties like CdO. The important technological developments on thin film TCE materials are presented chronologically as follows. The most important TCE material used for the last three decades to till date is the indium-tin oxide alloys (In_2O_3: Sn) also called as indium-tin-oxide (ITO). Corning laboratories invented the first ITO as a TCE material, during tests on metal oxide insulator fabrication in 1930's [29] which was later patented in 1947 [30]. The best ITO films with a resistivity of 1.77×10^{-4} Ω cm and visible transmittance around 85 % was reported by Fraser and Cook [31]. The modern TCE materials were firstly commercialized by Rupperecht in 1954 [32]. Presently, all kinds of flat panel display devices are made up of ITO electrodes, and this application signifies good profit for the ITO manufacturing sector. Review articles on TCEs have been repeatedly reported from time to time. Holland et al completely reviewed the early work of TCO film in 1953 [33]. In the middle of 1970's, comprehensive reviews on TCE materials were reported by Haacke [34]. Jarzebsk et al., published important review articles up to 1982 [35]. The deposition methods, characterization techniques, material properties, and applications of TCEs were clearly reviewed by Roy G. Gordon et al [36]. Theoretical model and some critical issues about TCE materials were also addressed computationally [37]. The ITO thin film electrode has some crucial drawbacks such as the rarity of indium source material and high-cost of production leading to the necessity of developing newer alternative TCE materials.

1.2.2. Alternative TCE materials for replacing ITO electrode

The increasing demand on renewable, conservative, sustainable energy after the global warming issue in 1970, has led to development of TCE materials with required properties [38]. Indium-tin oxide is a commercially available and dominantly used TCE material in the optoelectronic industry due to its excellent transmittance (95%) and sheet resistance ≅ 5 Ω/□ [39]. The availability and end use of indium for various applications based on market analysis reported in 2011 is illustrated in Fig. 1.2 [40]. However, the enormous usage of ITO leads to the huge demand of indium source element, and it has been identified as 'critical raw element' as reported by 'Mineral Commodity Summaries' in 2015 [41]. The European commission reported the global production of refined indium at 1,345 tons per annum as investigated by Moss et al. in 2011 [42]. A technical monitoring report indicated the future demand for indium supply to have a significant deficit by 2020 as shown in Fig. 1.3 [40] . However, indium scarcity

and huge demand for high-performance TCOs have motivated a number of researchers to develop newer transparent and conducting materials. Market forecasts have reported use of several TCE materials in mobile phones, tablets, notebooks, monitors, TVs, OLED lighting, organic photovoltaics, solar cells, and electroluminescence display devices [43]. Currently, there are over 200 companies and many institutes worldwide working on alternative TCE materials to replace ITO [44]. Recently, comparison of ITO replacements from the cost vs conductivity point of view covering the market in detail since 2006 is reported by Jennifer Colegrove founder of 'Touch Display Research' (Figure 1.4) [44].

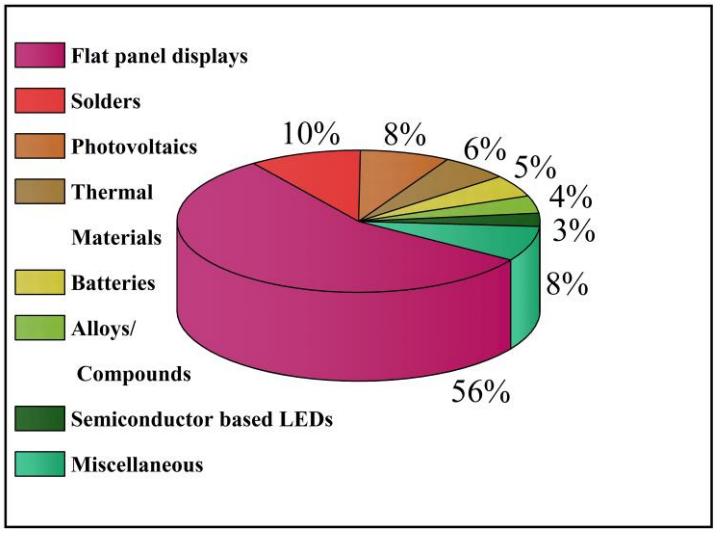

Fig. 1.2. End use of indium for various applications. Adapted from Lokanc et al [40].

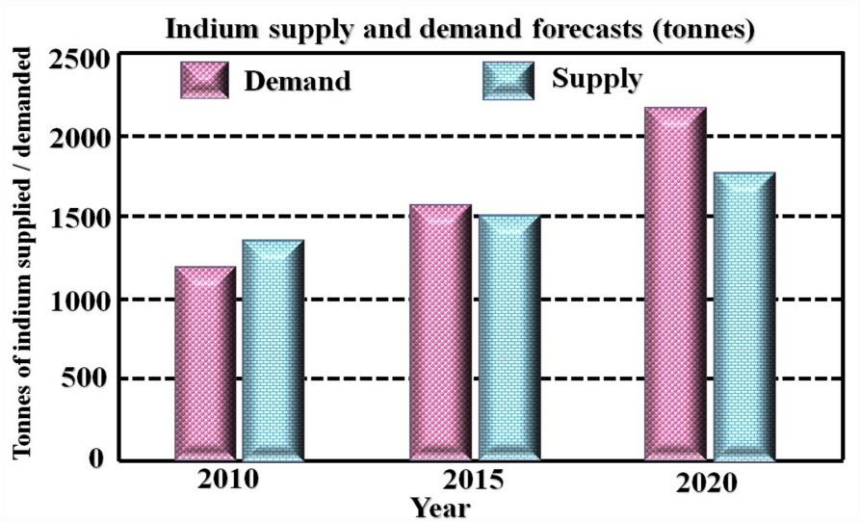

Fig. 1.3. Indium supply and demand forecast report. Adapted from Lokanc et al [40].

There are different types of alternative TCE materials available to replace/supplement ITO such as fluorine doped tin oxide (FTO), Sb-doped SnO_2 (ATO), doped zinc oxide (ZnO), carbon nanotubes (CNTs), graphene oxide (GO), ultra-thin metal nanowires (Ag, Au, Cu, Ni), metallic multilayer system SnO_2/Ag/SnO_2, ZnO/Ag/ZnO, and organic TCE materials (PEDOT:PSS) [45–48]. Each material system has its own advantages and limitations. However, doped tin oxide (SnO_2) is one of the best alternative candidates, particularly fluorine-doped tin oxide film (FTO) was the second largest commercialized TCO which has resistivity comparable to ITO. More importantly, its source materials are inexpensive and non-toxic, in addition, easy to tune the electrical and optical properties [49].

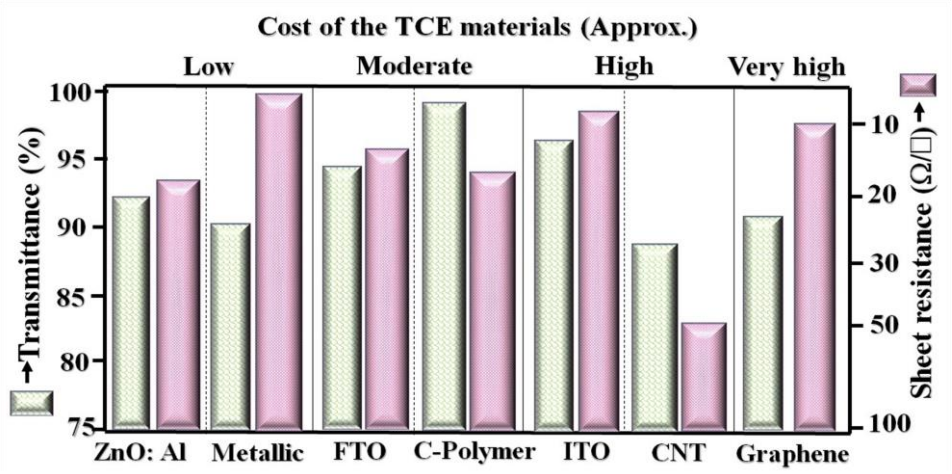

Fig. 1.4. Comparison of cost of ITO replacement materials (Image drawn with input from 'Touch Display Research, ITO-replacement: non-ITO technologies [44].

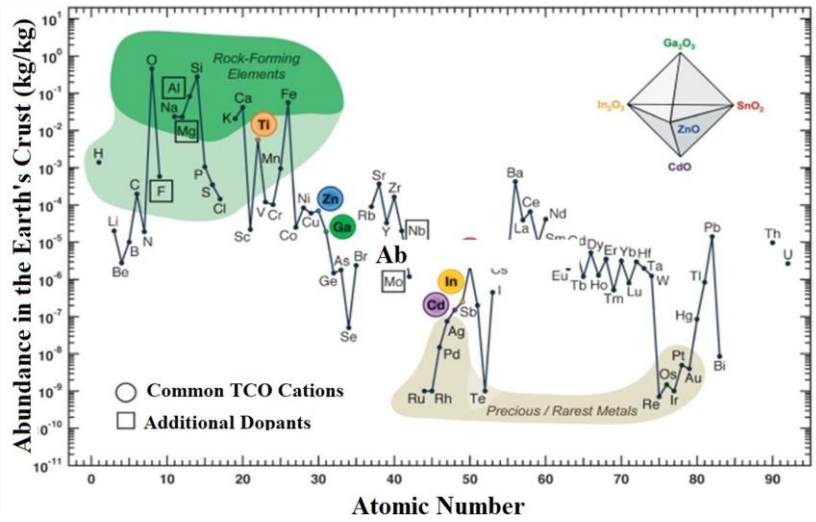

Fig. 1.5. Abundance of host (colored circles) and dopant (squares) elements for plausible TCE applications. Adopted from Pasquarelli et al [51].

1.3. Classification of TCE materials

To achieve the desired "*contradicting properties*" in the host TCE materials, several parameters need to be considered, particularly, dopant element (donor or acceptor), oxidation state, work function, crystalline structure, surface morphology, optical transparency, and electrical transport properties of the materials [50]. The abundance of host and dopant elements available to form efficient alternative TCE materials are illustrated in Fig. 1.5 [51]. The TCE materials can be categorized into two main types, one is oxide based TCE materials and the other is non-oxide based TCE materials. This classification of different types of TCE materials are presented in Fig. 1.6. The TCE materials are chosen for various potential applications based on the specific requirement of combination of electrical and optical properties. For example, n-type TCE materials are important for renewable energy harvesting applications [52], whereas p-type TCE materials are very much useful for LED applications and a hybrid of n-type and p-type materials provide unique properties for applicability in invisible electronics [53].

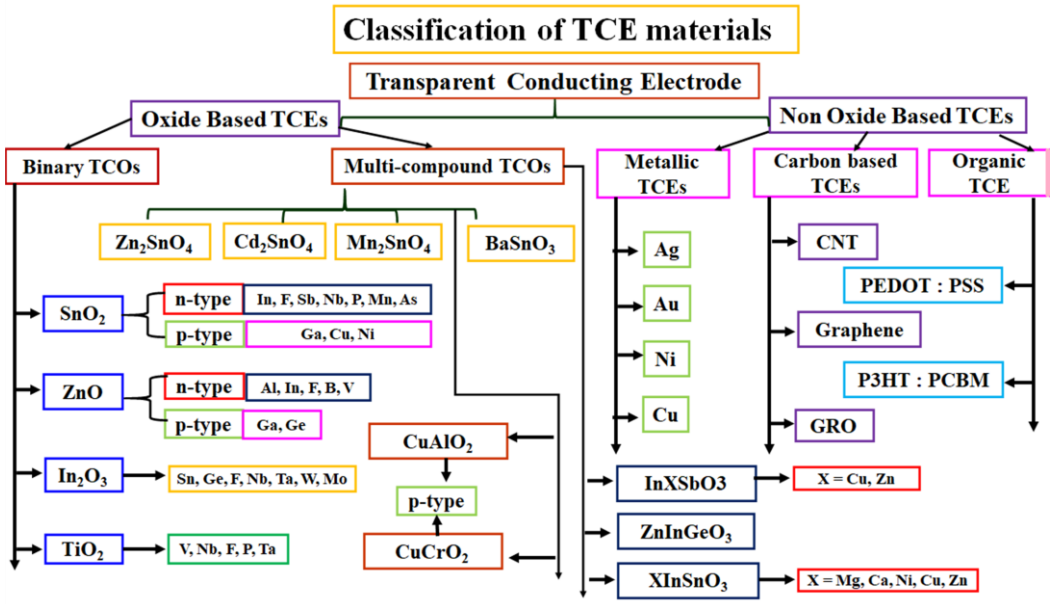

Fig. 1.6. Classification of oxide and non-oxide based TCE materials.

1.3.1. Oxide based TCE electrodes

Some of the oxide-based ceramic materials that exhibit excellent electrical conductivity and optical transparency upon appropriate doping are termed as "Transparent Conducting Oxide" (TCO) [25]. The TCO materials show good optoelectronic properties due to the existence of wide band gap > 3.1 eV and enhanced free carrier concentration $>10^{19}$ cm^{-3} [54].

The TCO materials are thermally and chemically stable compared to the existing metallic and organic TCE materials. The drawbacks of TCO materials are its brittleness, surface roughness, relatively lower electrical conductivity (compared to metallic TCE's) and lower optical transparency (compared to organic materials) [55]. The TCO materials are further classified into two more categories as binary and multinary compound oxide system.

Table 1.1. Relevant parameters of the host and dopant materials for designing effective TCOs.

Group	Element	Oxidational State	Ionic radius (Å)	Coordination Number
Host	O	-2	1.35/ 1.36/1.38/1.4/1.42	2/3/4/6/8
	Sn	+4	0.69/0.76/0.83/0.89/0.95	4/5/6/7/8
	Zn	+2	0.6/0.68/0.74/0.9	4/5/6/8
		+2	0.86	4
	Ti	+3	0.67	4
		+4	0.42/0.51/0.61/0.74	4/5/6/8
Donors/ Acceptors	*F*	-1	1.285/1.3/1.31	2/3/4
	Al	+3	0.39/0.48/0.54	4/5/6
		+3	0.72	6
	Ta	+4	0.68	6
		+5	0.64/0.69/0.74	6/7/8
		+3	0.72	6
	Nb	+4	0.68/0.79	6/8
		+5	0.48/0.64/0.69/0.74	4/6/7/8
	In	+3	0.62/0.8/0.92	4/6/8
	Sb	+3	0.76/0.8/0.76	4/5/6
		+5	0.6	6
	Ga	+3	0.47/0.55/0.62	4/5/6
	P	+3	0.44	6
		+5	0.17/0.29/0.38	4/5/6
	As	+3	0.58	6
		+5	0.34/0.46	4/5
		+4	0.66	6
	W	+5	0.62	6
		+6	0.42/0.51/0.6	4/5/6

1.3.1.1. Binary TCO materials

The binary oxide TCO materials have attracted more attention in optoelectronic applications due to easy tuning of electrical and optical properties. Raw host materials availability and the usage of facile and cost-effective deposition methods are some of the important factors for selecting binary TCO materials [56]. The binary oxide system's chemical composition during film deposition is easily controllable than the ternary and multi-component

oxide system. Most of the binary oxide TCO materials are synthesized using p-block elements that show excellent TCO properties [56]. The phase and band gap formation of the metal oxides are shown in Figs. 1.7(a) and 1.7(b) respectively [57,58]. The SnO_2, In_2O_3, ZnO, and TiO_2 are the frequently used host materials for making efficient TCO electrodes [59]. Undoped host material does not possess the required TCO properties in general, and the desired properties are attributed by way of impurity doping with pentavalent (n-type) and trivalent (p-type) elements [60]. The selection of dopant is made by the valence, ionic radii, effective mass, charge state and finally affordability and natural abundance of the dopant elements [8]. Table 1.1 indicates some of the parameters of the hosts and dopants for designing TCO materials with desirable properties [8].

1.3.1.2. Multi-component TCO materials

In an attempt to find alternatives to replace ITO, researchers have also explored several multi-component oxide systems. There are several materials that fit under this category of TCO, all possessing different combinations of electrical and optical properties specific for a particular application. Multi-component systems such as ternary (Zn_2SnO_4, Cd_2SnO_4, Mn_2SnO_4, $BaSnO_3$) and quaternary oxide system (In_2XSbO_3 where X= Zn, Cu; $XInSnO_3$ where X= Mg, Ca, Cu, Ni, Zn; $ZnInGeO_3$) also possesses significant TCO properties comparable to doped binary oxides system due to higher mobility and carrier concentration [61,62]. The electrical conductivity of the multi-component TCO materials strongly depend on mobility than the free carrier concentration.

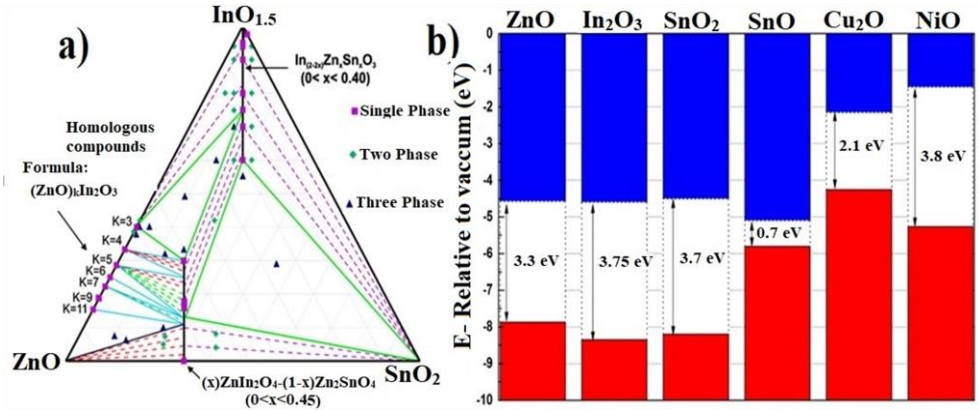

Fig. 1.7. Phase formation (a) and band gap variation (b) of TCO systems. Figure (a) and (b) are adopted from Lide et al [57] and Hoel et al [58] respectively.

The mobility of charge carriers may be affected by the localized states such as native oxygen vacancies and other point defects. The key factor here to improve the mobility is by enhancing the orbital overlap between the conduction and valence band [63]. These multi-component metal oxide systems possess narrow band gap, hence charge carriers move freely in the crystal lattice which has been well proved experimentally and computationally. Several interesting n-type and p-type multi-component hybrid TCOs are explored for advanced device applications [64]. Though the advantages of these multi-component TCOs are attractive, at the same time stabilizing the phase and stoichiometry are cumbersome.

1.3.2. Non-oxide based TCE materials

Advanced developments in optoelectronic devices such as flexible display, flexible solar cells, and flexible storage devices require not only high conductivity and good transparency of TCE materials, but it should also possess specific properties like flexibility, elasticity, tensile strength, elongation, and hardness [65]. For non-oxide TCE materials, crystallinity, nano-structure (nanowires, nanorod, nanosheet), work function, surface morphology (roughness, pores, smooth surface), resistance and chemical stability are more considerable parameters during applicability in advanced devices.

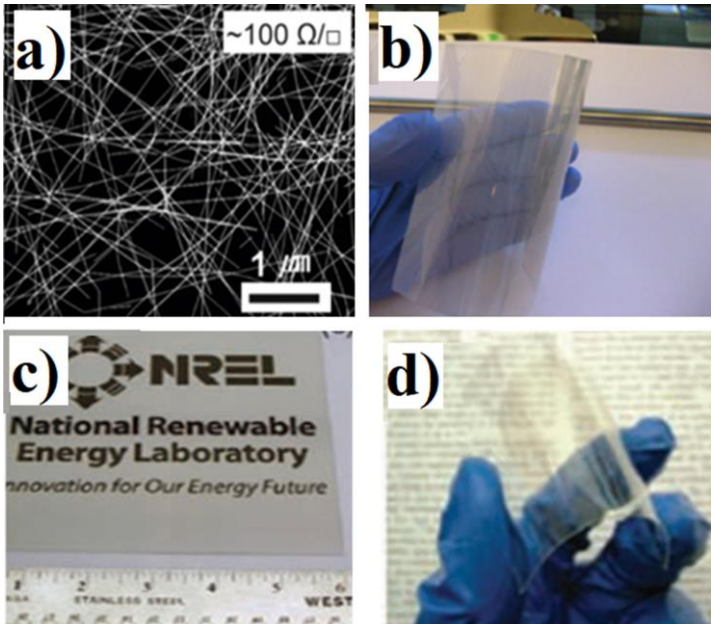

Fig. 1.8. SEM micrographs of Ag nanowires (a) [44], Ag nanowires on PET substrate (b) [66]. The photographs of spray coated CNT film on plastic substrate (c) [45], and grapheme oxide films on plastic substrate (d) (Adopted from Akter and Kim [48]).

The existing oxide based TCO material's usage are limited for certain applications in view of the brittle nature and low electrical conductivity (compared to metallic TCE materials). Another important hurdle is requirement of expensive deposition methods and high post annealing temperature. Optical transparency is forbidden in bulk metallic system, but it is considerable in the ultra-thin metallic films (thickness should be below the skin depth). Interesting optical and electrical properties also exist in carbon-based materials to serve as an TCE. Recently more research work have been carried out in this direction to achieve efficient non-oxide based TCE materials (Fig. 1.8), for example, CNT's [44], Graphene oxide [66], metallic nanowires [45] and organic PEDOT: PSS [48]. These materials are classified under the category of non-oxide based TCEs (Fig. 1.6), and disadvantages of these materials are low optical transparency (metallic nanowires), low resistance stability (organic materials), and low electrical properties (CNT) [67–69]. However, most of these materials have the advantage of large-scale production mostly by facile chemical methods for application in specialized requirements.

1.4. General requirements for TCO materials

It is vital to understand the basics of TCOs so as to further explore them for tuning their properties as per the necessity. The electrical transport properties (mobility, free carrier concentration) and optical properties (transparency, band gap) are dependent on respective material's electronic band structure [70]**.** The hybridization between O 2p state and the metallic 3d state plays an important role to understand the electronic band structure of metal oxide system [25]. The 'contradicting' properties of TCO materials arise due to different electronic band structure of the undoped and 'Sb' doped SnO_2 system as shown in Figs. 1.9(a) and 1.9(b) [71,72]. The electronic band structure is separated by the energy band gap. For direct band gap materials, the minimum of the conduction band and maximum of the valence band lies at the same position whereas it lies at different k-space in indirect band gap materials [72]. Fig. 1.9(b) clearly indicate the probability of the electron density of state (DOS) near the conduction band to be higher for Sb-doped system compared to undoped SnO_2 system. There are several plausible reasons proposed for this higher DOS near the bottom of the conduction band and top of the valence band. The donor and acceptor dopants improve the charge carrier concentration; hence the Fermi level may shift towards the conduction band for the n-type system which otherwise will shift towards the valence band for p-type system. The charge transport properties also play a very vital role in the metal oxide system. In metal oxides, charge transfer occurs

only between the O 2p state and metal 3d state. In the case of doped metal oxide systems, charge transfer occurs not only between the O 2p state and the metal 3d state, but also an intermetallic charge transfer is also taking place. For the SnO_2 system, Sn is covalently bonded with oxygen (O-Sn-O) and exhibit poor electrical properties due to its charge neutralization condition. The total charge of oxygen is -4 and cation Sn is +4, hence SnO_2 system is in the neutralized state. In the case of Sb-doped SnO_2 system, Sb has 5 valence electrons, out of which four electrons are covalently bonded with 'Sn', and the remaining one electron free to move in the SnO_2 lattice improves the electrical conductivity.

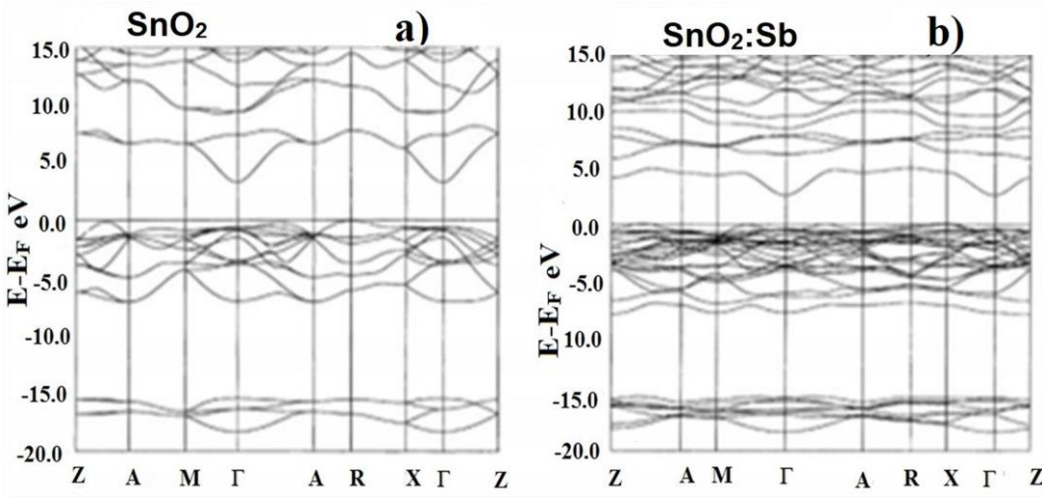

Fig. 1.9. Band structure calculations for (a) SnO_2, (b) Sb doped SnO_2. Adopted from Peng-Fei et al. [71,72].

1.4.1. Optical properties of TCO materials

The light incident on TCO material undergo several interactions such as transmittance, reflection, refraction, and absorption. If light is not absorbed by the material it can be transmitted through or reflected off the surface. The light can also be scattered due to surface roughness and structural defects in the material. All these properties are dependent on the nature of the material. The TCO materials should possess higher transmittance and low absorbance in the visible region [61]. Fig. 1.10 indicates transmittance and absorbance spectra of some of the TCO materials from literature [61]. The transmittance is influenced by the band gap of the material and also affected by the presence of various scattering centers. The fundamental requirement for the TCE material is the optical band gap defined by the energy level difference between the valence band maximum (VBM) and conduction band minimum (CBM). The band

gap of various TCO materials are shown in Fig. 1.11 [73]. In metallic oxide system, transparent conducting properties not only depend on the band gap but also on the dopant contribution, oxygen vacancies, and defect structure to a greater extent.

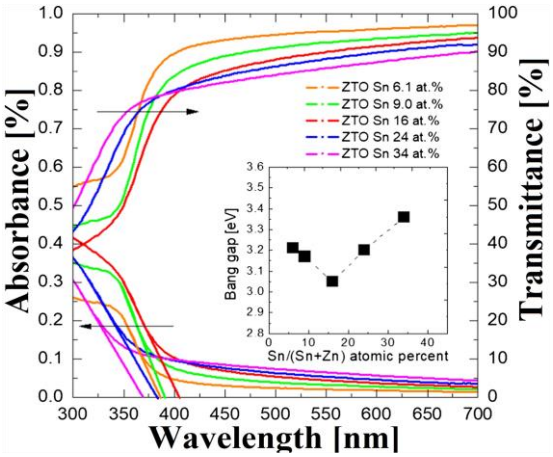

Fig. 1.10. Transmittance and absorbance spectra of TCO materials. Adopted from Mathur et al [61].

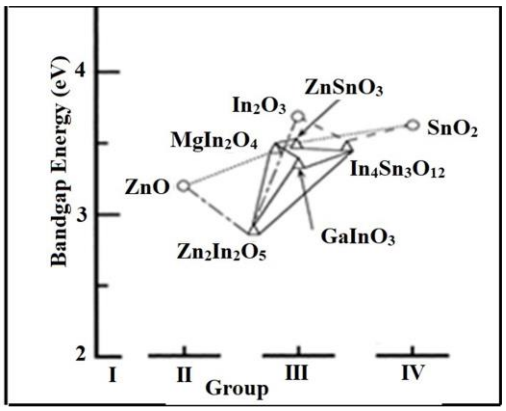

Fig. 1.11. Energy band gap of various TCO materials. Adopted from Batzill and Diebold [72].

The optical band gap is directly related to transparency of the system; i,e, transparency increases with increasing band gap [74]. The substitutional dopant and defects create excess of electrons close to the conduction band. This effect will shift the Fermi level above the conduction band (Fig. 1.12) leading to modification of the band gap of the material, familiarly known as the Moss–Burstein shift [8].

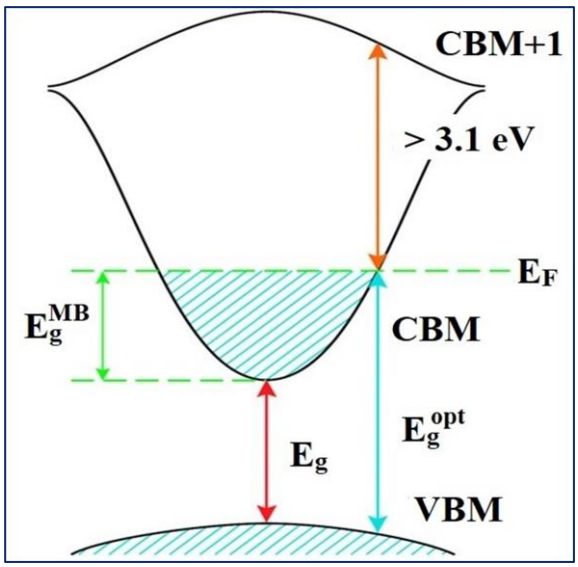

Fig. 1.12. Illustration of the Moss–Burstein shift of the energy band diagram of a doped semiconductor. Adopted from Dixon et al [8].

The Moss–Burstein shift is expressed as follows,

$$E_g = E_{CBM} - E_{VBM} \quad (1.1)$$

$$E^{g}_{Opt} = E^{MB}_{g} + E_g = E_F - E_{VBM} \quad (1.2)$$

where E_g is the gap between VBM and CBM, E_g^{opt} is the optical band gap corresponding to the smallest allowed optical transition from the VB to the CB, E^{MB}_g is the energy of Moss–Burstein shift and E_F is the Fermi energy [8]. This Fermi level shift upon doping leads to degeneracy in a semiconductor.

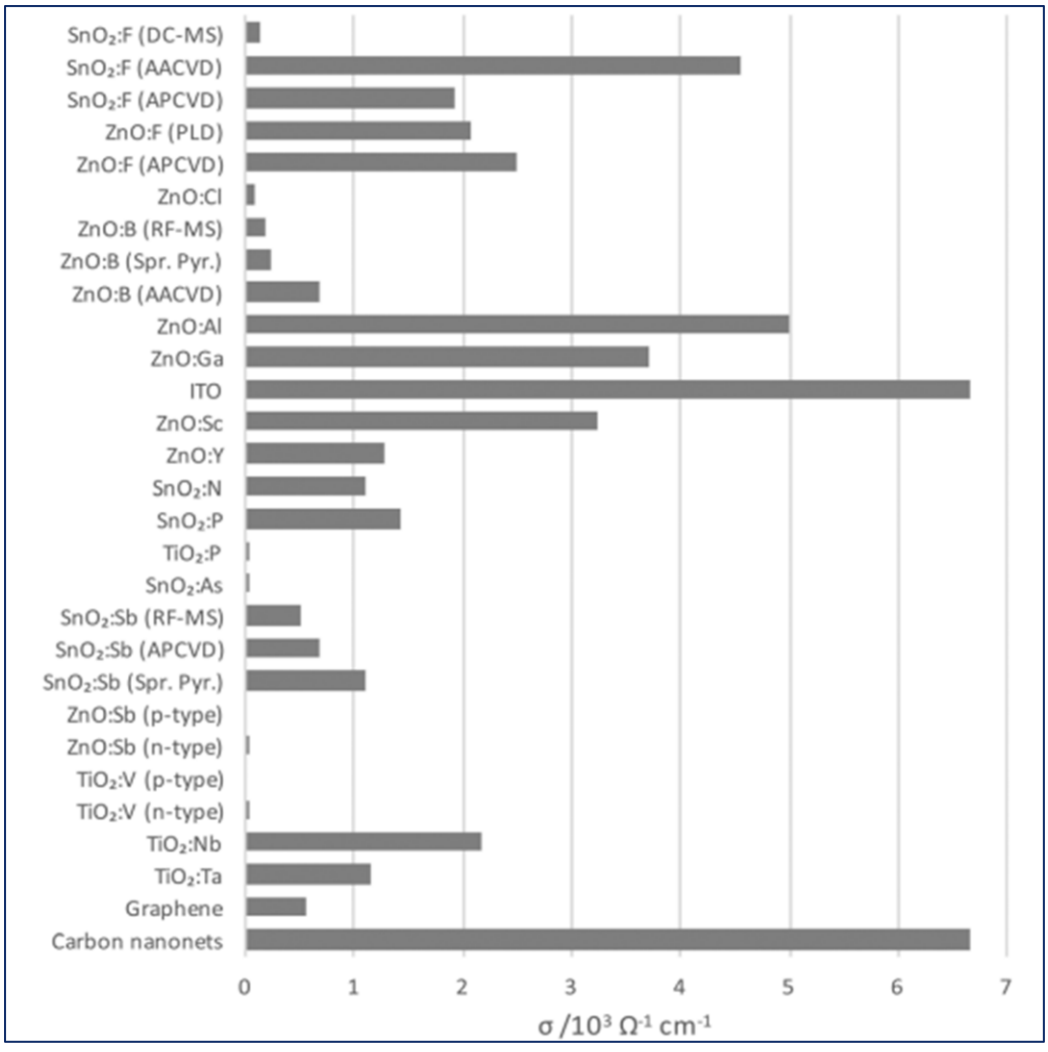

Fig. 1.13. Conductivity of various TCE materials. Adopted from Dixon et al [8].

1.4.2. Electrical properties of TCO materials

Electrical conductivity arises in pure semiconductor due to free carriers introduced by native oxygen vacancies. In the case of doped semiconducting system, conductivity depends on free carrier concentration (n_c) and mobility (μ) of the free carriers. The electrical conductivity (σ) of the semiconductor is expressed as follows [75],

$$\sigma = qn_e\mu_n + qn_p\mu_p \qquad (1.3)$$

Where q is the charge of the respective carrier, n_e and n_p are the concentration of the electrons and holes respectively, and μ_n and μ_p are the mobility of electrons and holes respectively in the semiconducting material. Substitutional doping of donor elements is extensively used to achieve n-type TCO materials with excellent conductivity. The free carrier mobility may be possible due to their small effective mass of the carrier [76]**.** The conductivity of various TCE materials are shown in Fig. 1.13 [8]. Oxygen vacancy and non-stoichiometry also improve the free carrier concentration but it limits the free carrier mobility. Mobility of the free carriers is also possibly affected by defect level scattering including grain boundaries, grain size, dislocations, and phonon interaction [77]. Among the oxide based TCOs, ITO has the highest conductivity followed by donor elements doped SnO_2 host material. Apart from SnO_2, ZnO host is also a promising TCO material appropriately doped with Al/Ga which is currently explored intensely and is also commercialized recently.

1.4.3. Figure of Merit of TCO materials

Effective TCO materials should have excellent electrical conductivity combined with higher optical transmittance in the visible region. The combination of these two properties is defined as Figure of Merit (FoM) proposed in 1972 [78]. However, it is difficult to find the accurate value of FoM by this method. To overcome this issue, Haacke proposed a new FoM in 1976 which also used the relation between T_r and R_s, however, adding an exponent factor to yield a better FoM value expressed as follows [79],

$$FoM = \frac{T_r^{(x)}}{R_s} \qquad (1.4)$$

The exponential x value varies with various transmittance range. For example, if the transmittance is in the range 90 %, 95 % and 100 % have different x values, x = 10, 20, 100 respectively. The requirement of the FoM value depends on the necessity of a particular device.

As an example, flat panel display devices should have TCO's with higher transmittance and moderate sheet resistance (≅ 500 Ω/□) as also shown earlier in Fig. 1.1 [22].

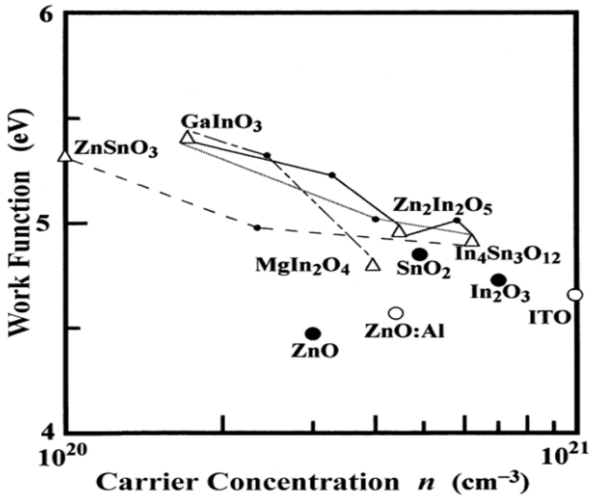

Fig. 1.14. Variation of work function and carrier concentration of various TCO materials. Adopted from Batzill and Diebold [72].

1.4.4. Work function of TCO materials

The applicability of TCO materials in various devices also depends on the electron affinity or work function of the materials. The surface work function of the metal oxide layer plays a vital role in the performance of optoelectronic devices [80]. The energy difference between the Fermi level to the vacuum level is generally known as work function. The work function (ϕ) of a semiconductor is dependent on the Fermi level position with respect to the vacuum level ($\phi = E_{vac} - E_F$) [55]. However, in a non-degenerate n-type semiconductor the Fermi level lies below the conduction band minimum, but in the case of the doped degenerate n-type semiconductor, the Fermi level possibly lies above the conduction band. The work function (ϕ) of a material is generally estimated by Kelvin probe (KP) or Ultraviolet photoelectron spectroscopy (UPS) methods [81]. The KP method is a unique non-contact method to determine the contact potential difference between the film's surface and the reference electrode tip working similar to the principle of a vibrating capacitor. Generally, in n-type metal oxides, carrier concentration is also a reason for high work function as illustrated in Fig. 1.14.

1.5. Tin oxide

The AO_2 binary oxide system offers high flexibility to incorporate dopants at the 'A' site (Also significantly at the 'O' site), and this incorporation of donor/acceptor is very much useful for tuning the optical and electrical properties significantly [15]. Among the AO_2 compounds, SnO_2 is one of the best host materials with the 'Sn' cation from group-IV elements of the periodic table for TCO applications. Tin oxide is found in two major crystalline phases such as stannic oxide (SnO_2) and stannous oxide (SnO). The key factor to distinguish these two phases is through their valence states. In SnO system, Sn is in 2+ valence state but in SnO_2 system, Sn exists in 4+ valence state [82]. Density-functional theory (DFT) provides the electronic band structure of a system by employing various approximation methods [83]. For example, the ground-state energy of SnO_2 system is computationally calculated by a linear combination of atomic orbitals (LCAO) approximation [84]. Tight binding approximation (TBA) was used to evaluate the position of conduction and valence band energy of the system. The structural, optical and electrical properties of undoped and donor doped SnO_2 system are briefly discussed in the following sub-sections.

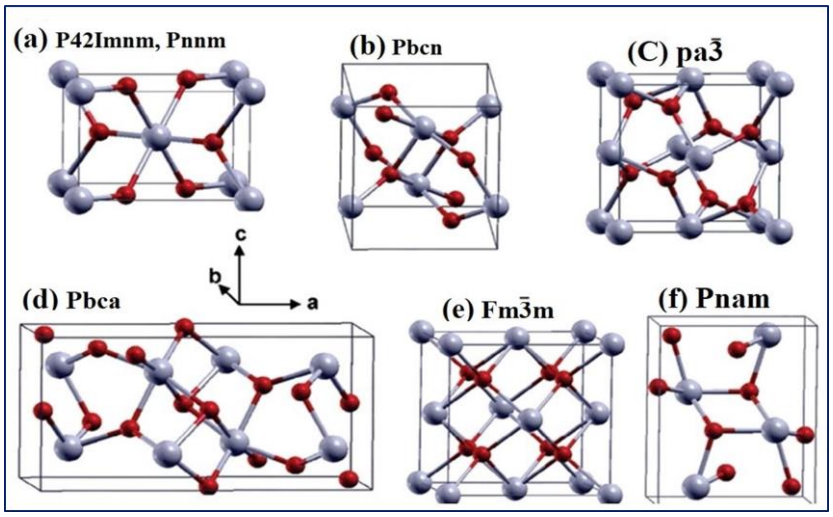

Fig. 1.15. Polymorphs of SnO_2 (a) Rutile, (b) PbO_2-type, (c) pyrite-type, (d) ZrO_2-type, (e) fluorite-type, and (f) cotunnite-type. Adopted from Das and Jayaraman [85].

1.5.1. Structural properties of SnO_2 system

The SnO_2 system possesses several polymorph crystalline phases as shown in Fig. 1.15. These phases possess different chemical and physical behavior as investigated by Das and Jayaraman [85]. Among these phases, the rutile phase is naturally occurring in the form of

cassiterite, and this phase is more stable than all other phases. The rutile SnO_2 system possesses a tetragonal crystal structure with P42/mnm space group. The tetragonal unit cell with lattice constants a = b= 4.7374(1) Å and c = 3.1864(1) Å contains two tin and four oxygen atoms with covalent bonding [82]. Each Sn atom is six-fold coordinated while the oxygen atoms are threefold coordinated. Edge-sharing octahedral coordinated tin atoms form chains along the [001] direction.

1.5.2. The vibrational modes of SnO_2 system

From the X-Ray diffraction analysis, it is difficult to distinguish the SnO_2 phase and SnO phase since some of the peak position of both the phases have the same 2θ values [82]. For example, the (201) plane of SnO_2 and (101) plane of SnO are centered at the same 2θ value of 42°. To overcome this issue. Raman analysis will help to identify the actual existing phase, because for a SnO_2 system the active Raman modes are present in the higher wavenumber region around 628 cm^{-1}, but in the case of SnO system., it appears in the lower wavenumber region around 234 cm^{-1} [85]. According to group theory, SnO phase exhibits the following vibrational modes expressed as follows and also shown in Fig. 1.16 [72],

$$\Gamma = A_{1g} + B_{1g} + 2E_g + A2_u + E_u + 3 \text{ acoustic modes} \qquad (1.5)$$

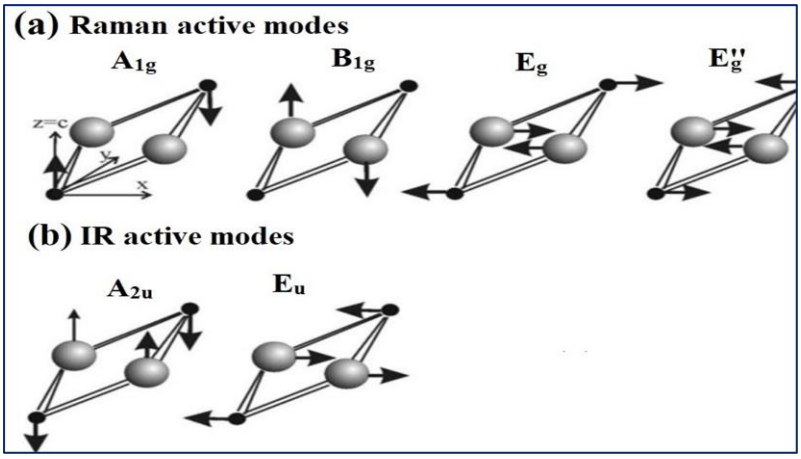

Fig. 1.16. Raman-active (a) and IR-active (b) modes of SnO system. Adopted from Batzill and Diebold [72].

In the case of SnO_2 system, there are 18 vibrational modes which are observed and denoted as follows,

$$\Gamma = A_{1g} + A_{2g} + B_{1g} + B_{2g} + E_g + 2A_{2u} + 2B_{1u} + 4E_u \qquad (1.6)$$

where "A_{1g}, B_{1g}, $B_{2g,}$ and E_g" are Raman active modes, "A_{2u} and $4E_u$" are IR active, and two modes "A_{2g} and B_{1u}" are IR inactive. The non-degenerate Raman active modes, "A_{1g}, B_{1g}, and B_{2g}" vibrate in a plane perpendicular to the c-axis, whereas the doubly degenerate "E_g" mode vibrates along the direction of the c-axis [86]. The infrared active mode "A_{2u}" of Sn and oxygen atoms vibrate along the c-axis direction, and the "E_u" modes vibrate on the plane perpendicular to the c-axis [82]. The "B_{1u} and A_{2g}" silent modes of the Sn and O atoms vibrate in the direction of the c-axis and in a plane perpendicular to the direction of c-axis respectively as illustrated in Figs. 1. 16 and 1.17. Importantly, the Raman peak shift can be used to map the surface, to identify the degree of homogeneity of atoms/molecules distribution on the sample's surface [87].

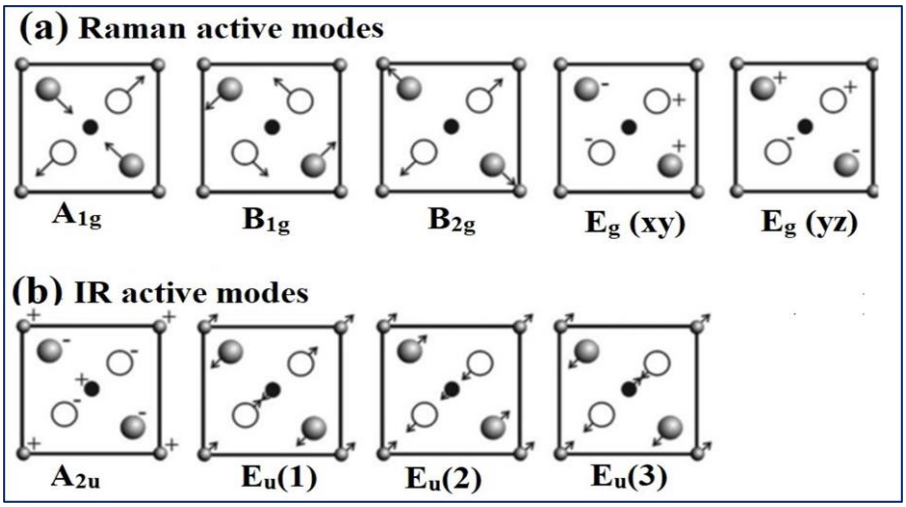

Fig. 1.17. Raman-active (a) and IR-active (b) modes of SnO_2 system. Adopted from Batzill and Diebold [72].

1.5.3. Electrical transport properties of SnO_2 system

If the SnO_2 system is completely stoichiometric, it shows insulating behavior. However, practically metal oxide systems are not completely stoichiometric in reality. This is due to the formation of oxygen vacancies in the crystal system [88] which are responsible for the electrical conduction process. Another important property of SnO_2 material is that it possesses high reflectance in the IR region [87]. Application of undoped SnO_2 system is limited due to the low electrical and optical properties compared to conventional ITO material. Undoped SnO_2 exhibit poor electrical resistivity of ~10^{-2} Ω cm, carrier concentration of ~6.42×10^{19} cm^{-3}, mobility of ~7.5 cm^2/Vs as reported by Shanthi et al [89].

Lin et al. reported that the undoped SnO_2 film deposited by RF magnetron sputtering possesses electrical resistivity of 6.78×10^{-2} Ω cm, mobility of 54.3 cm^2/Vs, and carrier concentration of 1.70×10^{18} cm^{-3} [90]. The applicability of undoped SnO_2 system is that it could be used as a buffer layer in photovoltaic devices [85].

1.5.4. Doped SnO_2 as a TCO system

The SnO_2 system serves as an effective TCO electrode in various optoelectronic devices when the donor/acceptor element is doped into its crystal structure. The donor/acceptor can occupy the interstitial sites of SnO_2 crystal lattice [91]. This donor/acceptor can easily shift the Fermi level of the sample, which is pictorially represented for both the undoped and doped SnO_2 system in Fig. 1.18. The reason for the coexistence of electrical conductivity and optical transparency of the metal oxide system is still not completely explored [10]. To understand the phenomenon of coexisting transparency and conductivity in doped SnO_2 system, the first-principles calculations were carried out to estimate the formation energy and energy levels (donor & acceptor) for various intrinsic defects, such as oxygen vacancy, metallic vacancy, and oxygen interstitial and metallic interstitials under different chemical potential conditions in SnO_2 system [92]. The potential to introduce desirable TCO behavior in SnO_2 for various dopants such as F, I, P, Sb, Nb, and Ta using standard density functional theory (DFT) was reported by Maziar Behtash etal., [10].

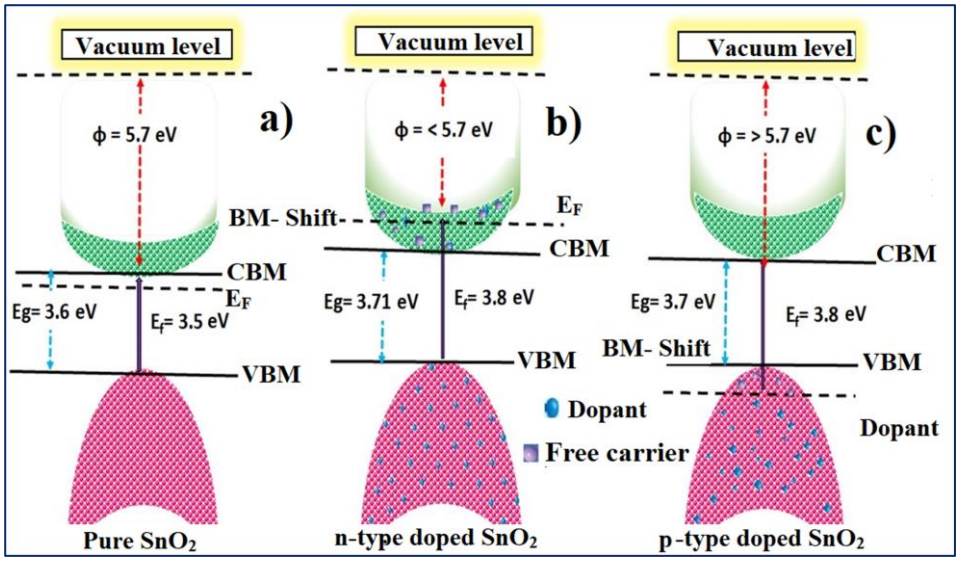

Fig. 1.18. Pictorial representation of electronic structure of undoped and doped SnO_2 system.

In computational approach, band gaps of Ga, Mg, Nd and Al doped SnO_2 decreased, and Nb, Ta, W, and Mn doped SnO_2 increased compared to undoped SnO_2 [93–96]. These theoretical findings contradict with the experimental results as reported by various authors. For example, Turgut et al. reported the optical band gap of Nb-doped SnO_2 to gradually reduce from 3.98 to 3.73 eV with doping concentration of Nb at 1 to 4 wt% [96].

Table 1.2. The SnO_2 based TCO system with various dopants and deposition methods.

TCO Material	Method*	Tr* (%)	Resistivity (Ω cm)	Rs* (Ω/□)	Ref No.
SnO_2: Sb	Spray	85	8.6×10^{-4}	20	[97]
SnO_2: F, Sb	RF-MS	79.7	9.1×10^{-4}	12.5	[98]
SnO_2: F	Spray	86	4×10^{-4}	28	[99]
SnO_2: F	Spray	80	9×10^{-4}	28	[100]
SnO_2: F	Spray	85	3.9×10^{-4}	7.8	[101]
SnO_2: F	Spray	85	4.1×10^{-4}	8.1	[102]
SnO_2: Nb	RF-MS	80	7×10^{-3}	500	[103]
SnO_2: Sb	Spray	85	3.85×10^{-4}	1.75	[104]
SnO_2	Spray	86	1.15×10^{-3}	16.03	[105]
SnO_2: Sb	Spray	70	8.9×10^{-4}	8.84	[106]
SnO_2: Sb/Ag	RF-MS	81.7	2.4×10^{-5}	3.9	[107]
SnO_2: Nb	Spray	68	6.6×10^{-3}	6.84	[108]
SnO_2: Ta	Spray	95	2.35×10^{-3}	26.97	[109]
SnO_2: Ga	DC-MS	80	6.3×10^{-2}	15.7	[110]
SnO_2: Sb	Spray	93.8	7.35×10^{-4}	15	[111]
SnO_2: Mn	Spray	55	2.98×10^{-3}	22.8	[112]
SnO_2: Sb	Spin coating	85	4.57×10^{-3}	47	[113]
SnO_2: Sb	CVD	85	6.48×10^{-4}	331	[114]
SnO_2: F: Nb	Spray	92	3.62×10^{-4}	3.9	[115]

*Tr- Transmittance, Rs- Sheet Resistance, DC-MS: DC-Magnetron sputtering, RF- MS; Radio frequency Magnetron Sputtering, CVD- Chemical Vapor Deposition.

The n-type donor doped SnO_2 materials are interesting TCOs than the p-type SnO_2 system. The SnO_2 based TCOs have been deposited by several methods. There are several reports on doped SnO_2 thin films with various dopants and their methods are given in Table 1.2. The electrical and optical properties of donor doped SnO_2 system can be enhanced by tuning various parameters such as deposition method, choice of precursor, film thickness, substrate temperature, post-annealing temperature, and rate of deposition. Each method has its own advantages and limitations. For example, the electrical and optical properties can be easily tuned by spray pyrolysis method but the surface quality of the film is not smooth as that of sputtered thin films [108]. Sputtering methods require ultra-high vacuum to deposit smooth film, but for chemical vapor deposition methods generally there is no need for such vacuum condition. The solution concentration and substrate temperature play a vital role in the chemical vapor deposition method [116]. In the case of physical vapor deposition, thickness and post-annealing temperature play an important role to achieve a good adhesive film. Sibel Gürakar et al. reported enhanced optical and electrical properties of Sb-doped SnO_2 films as a function of precursor solution concentration [117]. Recently, Fauzia et al reported Sb-doped SnO_2 system to exhibit transmittance of 88 %, and the low resistivity of 5.8×10^{-5} Ω cm [118].

1.6. Scope of the research work

In the present-day technology, in designing various gadgets based on touch screen display devices, the role of a TCE material is inevitable. The ITO is a commercially available and dominantly used TCE material in optoelectronic devices. However, the enormous usage of ITO is dependent on scarce of the indium source element. Among several TCE host materials, the SnO_2 system is a well-known wide-bandgap semiconductor which is easy to tune the physical and chemical properties by donor doping methods. The desirable optoelectronic properties of the host SnO_2 system is explored by doping with suitable donor elements. The donor doped SnO_2 thin films are deposited by cost-effective chemical spray pyrolysis technique on to glass substrates.

The main objective of this dissertation is to focus on optimization of indium free SnO_2 based TCO materials, namely Sb-doped SnO_2 (ATO), Ba and Sb co-doped SnO_2 (BATO), Nb-doped SnO_2 (NTO) and Ta-doped SnO_2 (TTO) systems. After optimization of these TCO materials, large area film deposition (10×10 cm^2) was performed and finally tested as an electrode in dye sensitized solar cell.

The objectives of this dissertation are as follows:

- To identify the optimal substrate temperature for the ATO thin films is deposited on a glass substrate at different substrate temperature by cost-effective spray pyrolysis method.

- To deposit a large area (10×10 cm^2) coating of ATO film all the deposition parameters are fine-tuned to overcome the issues like a grey tinge and milky white colour, etc.

- To enhance the electrical conductivity of the ATO film is co-doped with barium (Ba). Further, to achieve low sheet resistance value structural, surface, optical, and electrical properties are fine-tuned at different Ba concentration for large area (10×10 cm^2) coating of BATO film.

- To identify the optimal doping concentration of NTO thin films spray deposited at different Nb doping concentration on a glass substrate. Further, a large area (10 ×10 cm^2) coating of NTO film to achieve by fine-tuning the deposition conditions.

- To achieve high-quality large area (10×10 cm^2) TTO film achieved by controlling the structural, optical, and temperature-dependent electrical properties of TTO thin films with different Ta concentration.

- To know the suitability of the large area deposited ATO, BATO, NTO, and TTO thin films, the DSSC device has been fabricated using these electrodes as an alternative to the standard FTO electrode.

- To understand the variation of sheet resistance across the large area (10×10 cm^2) spray deposited ATO, BATO, NTO and TTO films, the sheet resistance is investigated at every 1×1 cm^2 area of the entire region using four-probe method.

- To study the resistance stability of the large area (10×10 cm^2) deposited ATO, BATO, NTO and TTO films, part of these films was post annealed at different temperature for various duration and measured for variation in sheet resistance.

- In addition to these studies, the surface work function of the optimal large area deposited ATO, BATO, NTO and TTO thin films are also performed using Kelvin probe method to identify its suitability for application in optoelectronic devices.

CHAPTER: 2

Thin Film Deposition Methods and Characterization Techniques

In this chapter a brief overview of the basics of thin film technology, thin film formation and thin film deposition methods are discussed. This chapter also covers the instrumentation details of various characterization techniques used for the studies.

2.1. Thin film technology

Fast growing technological developments in the modern society demands newer, compact, cost-effective advanced materials and technology for the various applications [119]. Thin film technology has tremendous advantages over the bulk properties, due to its better electrical, optical, surface, and luminescence properties [120]. Thin film is defined as a low dimensional material created by condensing one-by-one, atomic/molecular/ionic species of matter. An ideal thin film can be mathematically defined as a homogeneous solid material contained between two parallel planes and extended infinitely in two directions (x, y) but restricted along the third direction (z), perpendicular to the x-y plane [120]. The thickness of thin film is generally less than one micron, however depending on the species/methodology/requirement it can vary up to even few nanometers. The bulk material does not possess the better optical transmittance because of absorption, but the thin film of materials possesses good transmittance due to low absorption. The thin film also has advantages over bulk materials such as compactness, better performance, more reliability, low-cost production, and low packaging weight. Thin film of materials were probably first proposed in a synthetic manner by Michael Faraday in 18^{th} century by electrochemical method [121]. There are several review articles reported for thin film technology for various applications in advanced technologies [122].

2.2. Thin film formation mechanism

The thin film formation mechanism has several steps such as; creation of the appropriate atom/ion/molecule/species, transport towards the substrate, and formation of film on the substrate via physicochemical reaction. Based on several theoretical, computational, and experimental studies thin film growth processes are illustrated in Fig. 2.1.

i. Arrival of single atom/ion/molecule

The created single atom/ion/molecular species arrive onto the substrate and lose their kinetic energy. The homogeneous, and uniform adsorption of unit species depend on deposition parameter including substrate temperature, rate of arrival, target to substrate distance, nature of the source materials, etc. Each deposition parameter has its role to result in thin, dense, and uniformly distributed atom/ion/molecule species for the initial monolayer formation.

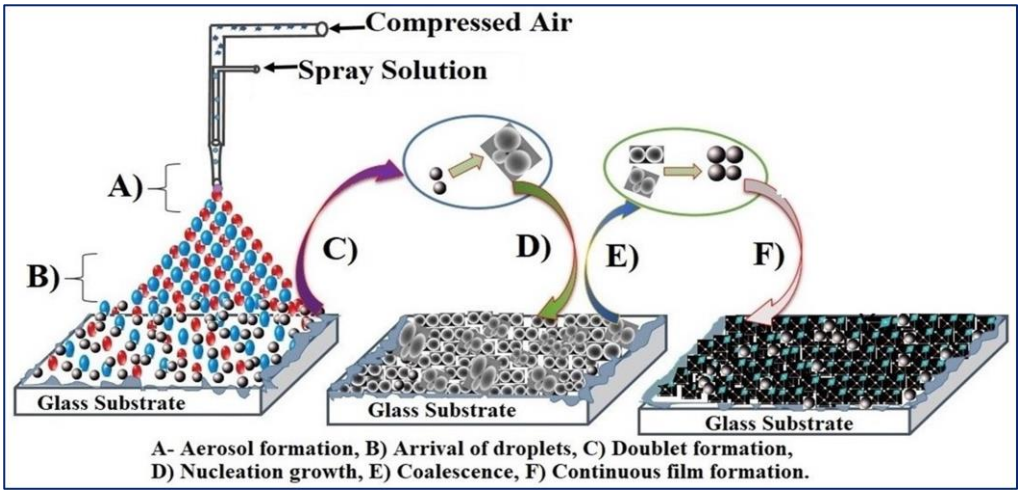

Fig. 2.1. The process of formation of thin film by spray pyrolysis technique.

ii. Doublet formation

The adsorbed atom/ion/molecule species are not in thermal and chemical equilibrium with the substrate due to the temperature gradient, so they can move around the substrate, and interact themselves to form a doublet. Furthermore, deposition causes chemical bonding of clusters, but these clusters are not in thermal equilibrium and adhering to the substrate [123]. The clusters are thermodynamically unstable and may possibly affect by quality of film. It is possible to collide with each other to form a bigger sized cluster.

iii. Nucleation and growth

When the deposition parameters are favorable for film growth, the clusters can attain a critical size, then the cluster becomes thermodynamically stable onto the substrate. This chemisorbed critical size of the cluster is called as nucleation. The nucleated critical sized cluster will grow when the saturation nucleation density is achieved. The nucleation density and the average nucleation size depend on various parameters such as rate of deposition, substrate temperature,

activation energy of adsorbent, and velocity of unit species [123]. The nucleation growth occurs in three dimensions, but the rate of lateral growth at this stage is much higher than the perpendicular growth (island growth). The island growth depends on the nucleation rate. The number of stable nuclei formed in an unit area per unit volume per unit time is called as a nucleation rate [124].

iv. Coalescence

The coalescence happens at a relatively higher substrate temperature. The small islands start to coalesce with each other, and also try to attempt to enhance the substrate coverage area via the growing bigger sized islands which is also called as an agglomeration of nucleates or coalescence [123]. In some cases, the formation of new nuclei may occur on the freshly exposed area. A consequence of larger island growth, some of the uncovered area are also filled with these newer nuclei. The surface structure of the film formation at this stage appear like a discontinuous island type to a porous network.

v. Continuous film formation

The final stage of the thin film formation is filling up of the uncovered area of the substrate by new nucleates, resulting in the formation of continuous film. Thus, the numerical process of nucleation and controlled growth lead to form a network structure and subsequently form a continuous film [125].

2.3. Thin films growth modes

Thin film formation occurs by three major growth modes depending on the choice of the deposition methods such as (i) island growth or Volmer–Weber mode (VW), (ii) layer-by-layer growth or Frank–Van der Merwe mode (FV), and (iii) mixed type growth or Stranski–Krastanov (SK) mode [126]. The island or Volmer–Weber growth mode is shown in Fig. 2.2(a): A small nuclei formed in random three-dimensional directions is generally called as an island growth [126]. The force of attraction (adherence) is very low between the substrate and adsorbed species is the reason for the island growth. The deposition parameter such as low vacuum, low substrate temperature, and dilute solution concentration are also reason for this type of growth mode. In general, the metal oxide semiconductor system deposited in low vacuum follows the island growth. The layer-by-layer growth or Frank–Van der Merwe growth has the opposite behavior of the island growth as shown in Fig. 2.2(b). The smallest nucleation growth occurs in two dimensions by addition of one by one atom/ion/molecule resulting in the

formation of layer by layer growth mode. The force of attraction between the substrate and film is very strong compared to all other growth modes. The epitaxial thin film growth is generally formed by layer by layer growth mode. This growth mode requires high vacuum conditions, and low rate of deposition. The mixed growth mode or Stranski–Krastanov mode is a combination of a layer by layer and island growth modes (Fig. 2.2c). In this growth mode, after forming one or two monolayers via layer-by-layer mode, this growth mode becomes unfavorable and island mode begins to dominate. This type of growth mode is formed in metal-metal and metal–semiconductor materials thin film deposition [126].

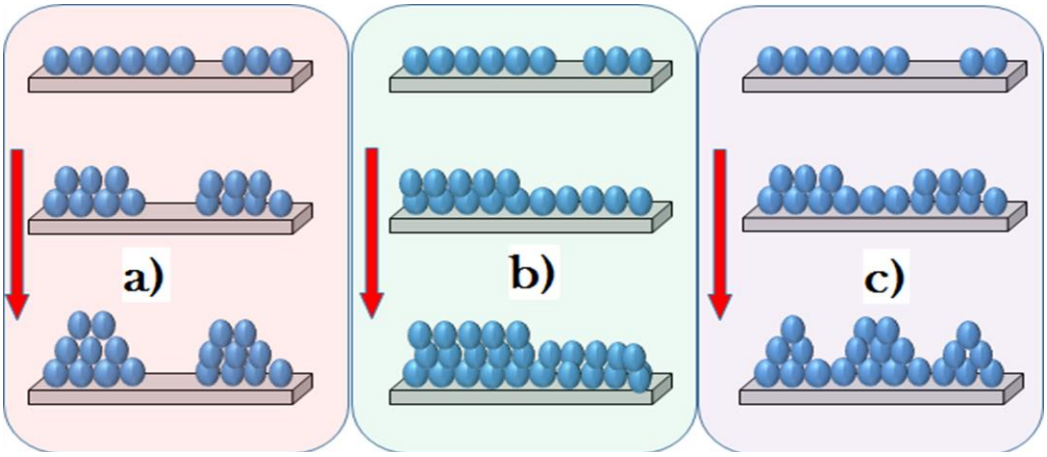

Fig. 2.2. Thin film growth modes; (a) island growth (Volmer–Weber), b) layer by layer growth (Frank–Van der Merwe), and c) mixed growth mode (Stranski–Krastanov).

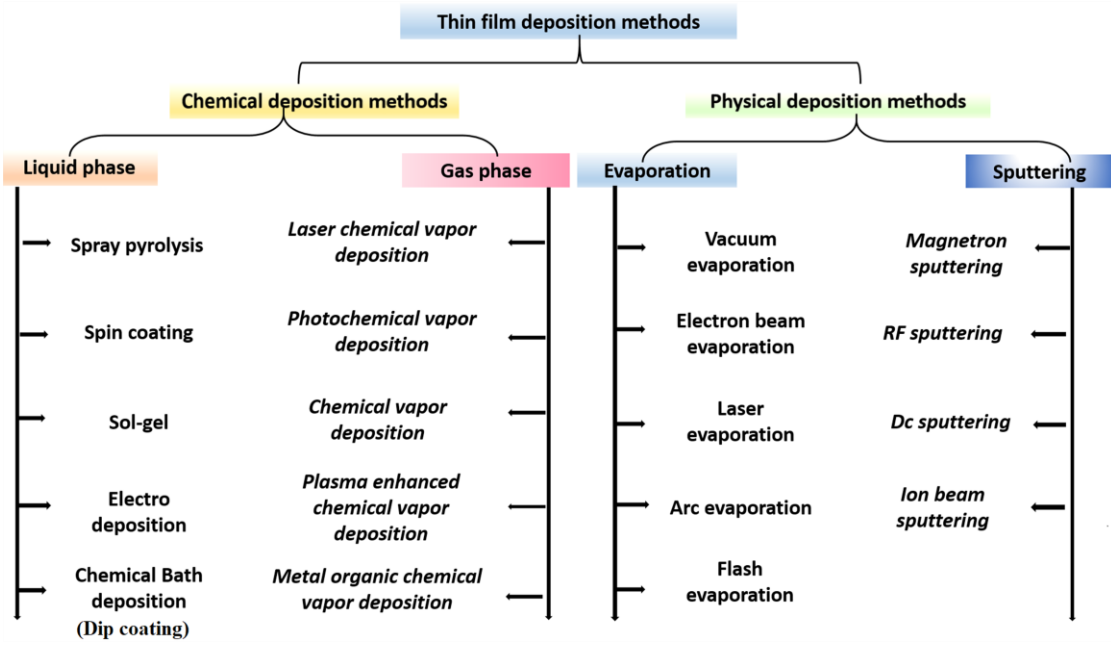

Fig. 2.3. Classification of chemical and physical thin film deposition methods.

2.4. Thin film deposition methods

The thin film deposition methods are classified based on the working principle into two major categories such as physical and chemical deposition methods. Fig. 2.3 shows the various chemical and physical deposition methods, and these two methods are further sub-classified into the liquid phase, gas phase, evaporation, and sputtering [127]. In the chemical deposition method (CDM) the oxidation and reduction process will play a crucial role in film formation. In the case of physical deposition method (PDM), physical phenomenon such as evaporation, ejection, condensation, and sputtering play a crucial role. However, both the methods have their own advantages and disadvantages. The quality of the film and cost make it difficult to choose the best method for particular material deposition [120]. The high vacuum deposition methods are much useful to fabricate films for commercial devices, but it is more expensive than a low vacuum deposition method. For large scale production, we require a cost-effective deposition method, but the problem is, it is difficult to obtain high-quality thin films by these methods. In the present research work, the cost-effective chemical spray pyrolysis method was used for the deposition of various element doped SnO_2 based TCO materials.

2.4.1. Chemical spray pyrolysis method

Spray pyrolysis is a cost-effective chemical vapor deposition method to deposit metal oxide semiconducting thin films. Cadmium oxide thin film was first deposited using spray pyrolysis in 1907 by Karl Baedeker [24]. The spray deposition parameters are more responsible for obtaining unique structural, surface, optical and electrical transport properties of thin films. Simplicity and easy to tune the deposition parameters are major advantages of the spray method to make large scale production of several oxide-based materials. Spray dynamics play a very crucial role to achieve good quality and uniform thin film. It depends on various parameters such as the size of the atomized droplet, spray flow rate, velocity, substrate temperature, and solution concentration. The size distribution of the particles formed is estimated by the inter-particle spacing in the films and the higher spacing values make more inhomogeneity and ununiform particle size in the films [128]. The solution concentration also plays a significant role in film formation, since the droplets reaching the heated substrate are expected to contain sufficient amount of solvent to form a relatively uniform surface. The probability of atomized droplet formation and droplet size depend on spray dynamics [128]. The substrate temperature gradient affects the film formation, and this thermal gradient can be minimized by adjusting the

substrate to gun nozzle distance. Higher the substrate to gun nozzle distance larger the coverage area, but higher distance causes more time of flight of the precursor solution, which will reduce the rate of deposition, leading to non-continuous film formation. There are several research reports, and review articles on spray coated thin film for application in various devices [120].

Mechanism of spray pyrolysis

The several steps involved in spray pyrolysis mechanism and all process together are classified into three major steps as follows: i) atomization of the precursor solution, ii) transportation of the resultant aerosol, and iii) decomposition and thin film formation. These three steps are more important for good quality thin film formation [123].

i. Atomization of the precursor solution

In atomization of the precursor solution, the solution and compressed air/gas combine together to form an aerosol in the spray nozzle gun [129]. There are many theoretical, computational and experimental study reported for the formation of the aerosol. Spray nozzle size, solution concentration, and compressed air or gas pressure are the factors influencing more on aerosol formation.

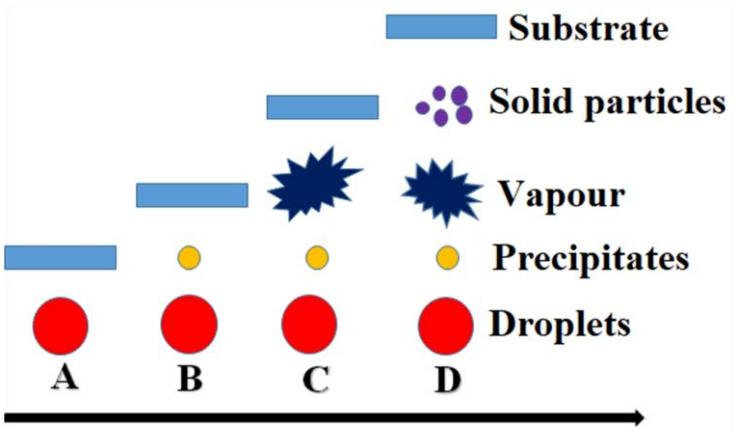

Fig. 2.4. Viguie and spitz mechanism of spray deposition and film formation.

ii. Aerosol transport

The aerosol transportation plays an important role in the determination of film's surface microstructure, optical and electrical properties. The optimum spray flow rate, velocity and substrate positioning are the essential parameters to control the aerosol transport. To form a

more homogeneous and uniform thin film, all the droplet should reach the preheated substrate without particulate formation. The aerosol transportation depends more on the solution velocity, nozzle diameter, and substrate temperature. The droplet velocity is affected by various forces such as gravitational, thermophoretic and stokes forces. The thermophoretic force arises because of more temperature and pressure gradient during film formation [128].

iii. Decomposition of the precursor solution

The decomposition of aerosol on to the preheated substrate is an important process for thin film formation. There are several processes that occur simultaneously during the aerosols impinging on the substrate: solvent evaporation, spreading of the droplet, and decomposition of the aerosol. There are several theoretical and computational models proposed for decomposing of the droplet, and among them, viguie and spitz proposed a model that is easy to understand the thin film growth mechanism [130]. Fig. 2.4 shows various stages of viguie and spitz model, and this model gives complete information on aerosol dynamics. It is also reported that spray deposited thin film forms via island growth mode. Viguie and Spitz suggested the following processes which occur with increasing substrate temperature. Stage A: The lowest substrate temperature condition droplet splashes onto the substrate without proper decomposition.

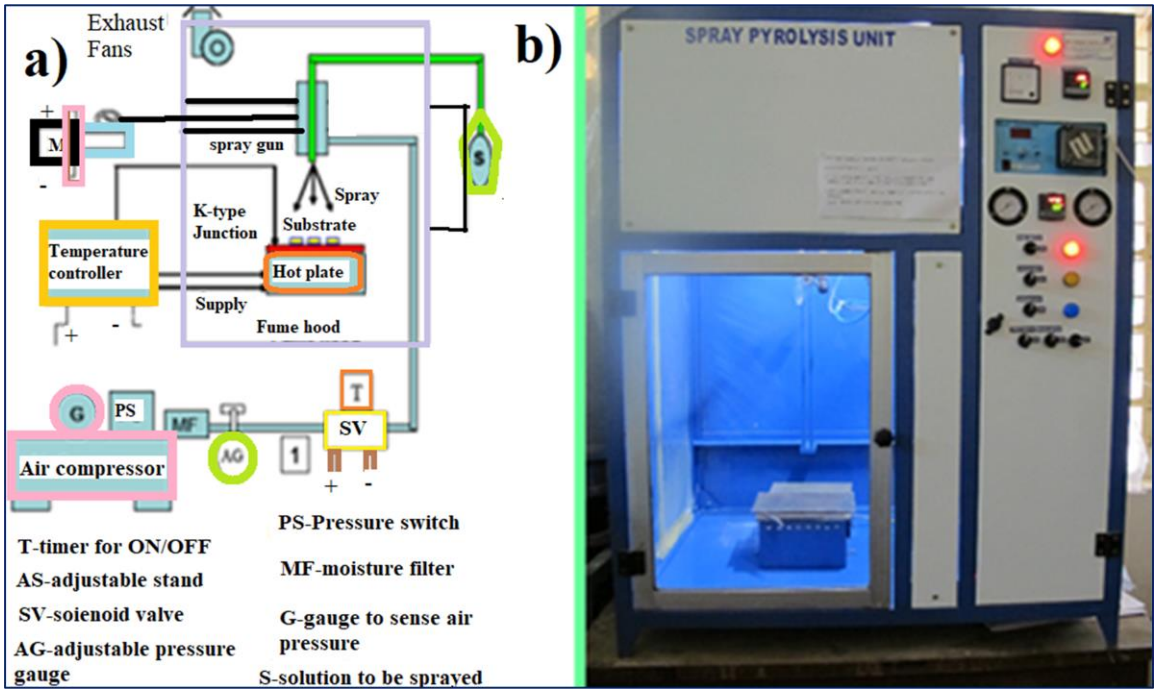

Fig. 2.5. The schematic diagram (a) and photograph of spray pyrolysis system (b).

Stage B: At moderate substrate temperatures, the solvent evaporates completely during the flight of the droplet and dry precipitate hits the substrate, where decomposition occurs. Stage C: At higher substrate temperatures, solvent also evaporates before the droplet reaches the substrate. It is identified that most of the thin film formation by chemical deposition method occur in stage C. Stage D: At the highest temperature precursor vaporizes before it reaches the substrate, and consequently the solid particles are formed after the chemical reaction in the vapor phase. In this research work a single static nozzle spray instrument was used for deposition of various TCO films, which is shown in Fig 2.5.

Advantages

- *Cost effective deposition method and easy to control the deposition parameters.*
- *Easy way to dope the donor/acceptor into host materials in required proportion*
- *It does not require vacuum, and high-quality targets and/or substrates*
- *It requires only a relatively small quantity of source materials.*

Drawbacks

- *It's difficult to achieve high surface quality thin film and it is a time-consuming process*
- *Film thickness and roughness are relatively difficult to control unlike PVD methods.*
- *Spray dynamics, temperature and pressure gradient affect the film growth easily.*

2.4.2. Solution preparation method

The precursor solution concentration (molarity) was different for various donor (Sb, Ba, Nb, Ta) doped SnO_2 thin films. Tin chloride di-hydrate ($SnCl_2\ 2H_2O$) salt was chosen for the host material for all the four different donors doped TCO systems. We followed the same solution preparation method, but we used different solvent for dissolving different donor elements. The precursor solutions are prepared using magnetic stirring at room temperature. First host and donor element precursor were dissolved separately in 10 ml of distilled water and 2 propanol (IPA) for 30 minutes by magnetic stirring method respectively. After these, both solutions were mixed together and then stirred for 30 minutes, the mixed solution are not transparent in nature. Further 2 drops of HCl was added to make the solution transparent [131]. Finally, the desired quantity of ethylene glycol was added to make the final precursor solution for spray pyrolysis.

2.4.3. Substrate cleaning

Glass slides with high softening temperature (~730 °C) purchased form Zhuhai Kaivo, Optoelectronic Co. Ltd were used as substrates. For substrate cleaning purpose, acetone, IPA, soap solution, and distilled water were used. We followed standard substrate cleaning procedure to clean the substrates using ultrasonic cleaner. Solvents are used to remove the oil and grease contaminated on the glass substrate during the manufacturing process [131]. Further, the ultrasonically cleaned substrates ware placed in a high energy plasma cleaner (model: PDC-002 Harrick plasma) to remove the ionic contamination present on the substrate. Finally, the plasma cleaned substrate was loaded onto a substrate holder in the spray pyrolysis chamber.

2.5. Thin film characterization techniques

2.5.1. X-ray diffraction

The crystalline structure, phase purity, lattice parameter, degree of crystallinity, and composition of the sample are analyzed by non-destructive X-ray Diffraction (XRD) technique**.** It is also useful to estimate quantitative parameters of the samples such as grain size (crystallite size), texture coefficient, and stress analysis/lattice strain of the sample. For X-ray to be diffracted, the spacing in the lattice grating should be of the same order as that of the wavelength. In crystals, the typical interatomic distance is ~ 2-3 Å which is suitable for X-rays to be diffracted.

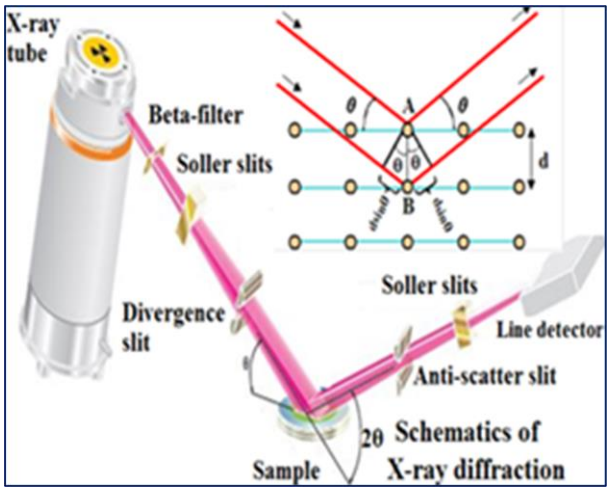

Fig. 2.6. The schematics of X-ray diffractometer and the inset is Bragg's law representation.

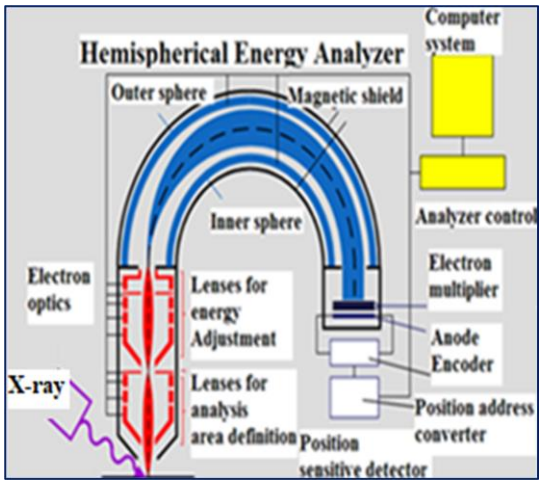

Fig. 2.7. The schematics of X-ray photoelectron spectroscopy.

X-ray diffraction is based on interference of diffracted X-rays by crystalline sample [132]. The X-ray diffraction condition is also known as Bragg's condition at $2d_{hkl} \sin\theta = n\lambda$, d_{hkl} is the inter-planar spacing of the respective hkl plane, θ is the Bragg's angle, n is the order of diffraction, and λ is the wavelength of the incident X-ray radiation. The diffracted peak pattern has non-zero width due to several factors including instrumental effect, grain size, lattice stain, etc. [133]. The Bragg's equation indicates the inter-planar distance in a given material which can be estimated from the diffracted angle and the known wavelength. Figure 2.6 shows the schematic representation of X-ray diffraction process, and also the extended view of Bragg's plane in the inset of Fig. 2.6.

Instrument Specifications

Model***:*** *XPERT-PRO* equipped with Cu-K*α* radiation (wavelength 1.5406 Å), Goniometer configuration: *Horizontal goniometer (θ-θ)*; Detector: Scan range: *3° to 136°.* Scanning angle rate of 0.01° and a 1s/step count time.

2.5.2. X-ray photoelectron spectroscopy

The X-ray photoelectron spectroscopy (XPS) is an sophisticated technique to analyze the binding energy and surface oxidation of the elemental constituents of samples [134]. When the X-ray is focused on the sample, electrons absorb the X-ray energy and escape from the orbital with maximum kinetic energy of $E_k = h\nu - E_B - e\Phi$, where E_B is electron binding energy, ν is the photon frequency, and Φ is work function, which is the minimum energy essential to remove an electron from the surface of the material [135]. The X-ray radiation is continuously incident on the sample's surface, and the photoelectrons are ejected from the sample surface. The ejected photoelectron is a function of its binding energy and is characteristic of the element from which it is emitted. The energy of this conversion is adjusted by the emission of an Auger electron or a characteristic x-ray spectrum. Investigation of Auger electrons can be used in XPS measurement. The XPS is a surface sensitive technique because only those electrons generated near the surface escape and are detected. The photoelectrons of interest have relatively low kinetic energy. Due to inelastic collisions within the sample's atomic structure, photoelectrons originating more than 20 to 50 Å below the surface cannot escape with sufficient energy to be detected. The XPS instrument consists of three major parts such as photoelectron production unit, a detector unit and analyzer unit as shown in Fig. 2.7.

Instrument Specifications

Model: *Theta probe angle-resolved X-ray photoelectron spectrometer (ARXPS) system*; Analyzer Type: *180° double focusing hemispherical analyzer with PARXPS detector*; X-Ray

Source Type: *monochromatic, micro-focused Al K-Alpha, X-Ray*; Spot Size: *15–400 µm*; Sampling area: *maximum 70×70 mm.*

2.5.3. Scanning Electron Microscopy

The scanning electron microscope (SEM) is the most extensively used technique to study the surface morphology of samples with high resolution and depth of focus [136]. The highly accelerated electron beam interacts with sample surface in two way; elastic and inelastic interaction. Elastic interaction results from the deflection of the incident electron beam by the sample by outer shell electrons of similar energy. Incident electrons that are elastically scattered through an angle of more than 90˚ are called backscattered electrons (BSE). Inelastic scattering take place over an interaction between the incident electrons and the sample, which results in the primary beam electron transferring substantial energy to that atom. As a result, the excitation of the specimen electrons during the ionization of specimen atoms leads to the generation of secondary electrons (SE). These two types of the electrons are used to image the surface morphology of the samples. Figure 2.8 shows the schematics of the SEM instrument. The electron beam is produced by an electron gun by field emission. The produced electron is accelerated around 300 V- 30 kV using anode grid towards the sample surface. The accelerated electron beam is focused on the sample surface using various electromagnetic lenses and apertures. When the electron beam is scanned over the sample surface, different types of signals are obtained from the sample's surface. The emitted signal can be collected by several detectors for a particular application. The X-ray Energy Dispersive Spectroscopy (EDS) method is useful to identify the quantitative information of chemical composition of the samples, from the energy of the emitted X-ray radiation. For the present research work, surface morphology and chemical composition of the films was analyzed by using a TESCAN SEM instrument with specifications given below.

Instrument Specifications

Model: *TESCAN-VEGA 3LMV attached with Oxford Scanning Electron Microscope*; Electron Source: *pre-centered tungsten hairpin type*; Accelerating voltage: *300 V to 30 kV*; Resolution: *3.0 nm*; Magnification: *5X to 300,000X*; Secondary electron detector*: Everhart-Thornley;* Backscattered electron detector: *Thin five-segment solid-state detector*.

2.5.4. Atomic force microscopy

The atomic force microscopy (AFM) is a very high-resolution surface scanning microscopy with established resolution of the order of nanometer. The force of attraction or repulsion between the tip and sample's surface make the cantilever to bend or deflect from the sample surface. The cantilever deflection arises due to the electrostatic force between the tip and sample and also the Vander Waals force of attraction between the inter-atomic species [137]. A detector measures the cantilever movement as a function of tip scanning on the sample surface. The deflection of the cantilever monitors the surface topography. Based on the interaction between tip and sample surface, the AFM instrument work in three different modes: contact mode, non- contact mode, and tapping mode. The schematics of working principle of the AFM instrument is shown in Fig. 2.9, and it consists of three parts; laser source, cantilever part, and a detector part. When the tip is brought close to the sample surface, forces between the tip and the sample lead to a deflection of the cantilever according to Hooke's law [138]. The reflected laser light is detected by a photodiode with the respective motion of cantilever. Further, the detected light signal and the reference signal are sent to the feedback amplifier to analyze and record the surface variations on the sample. For the present research work, surface topology of the films was analyzed by Park Scientific Instrument.

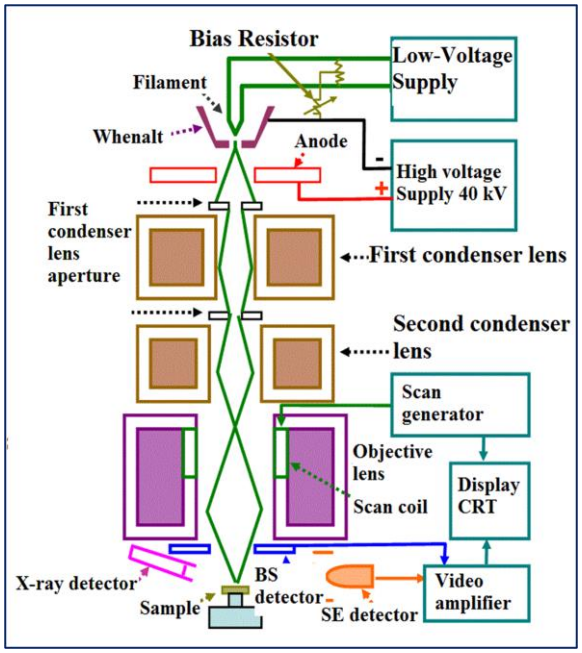

Fig. 2.8. Schematics of working principle the SEM instrument.

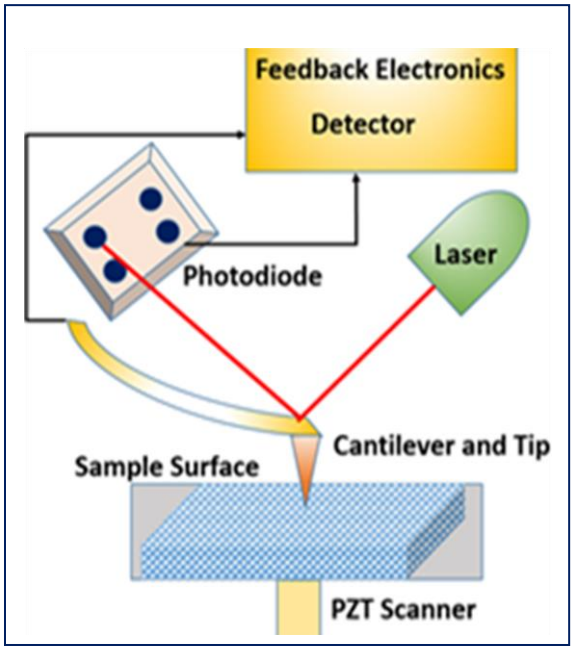

Fig. 2.9. Schematics of working principle of AFM instrument.

Instrument Specifications

Model: *Park NX10*; Type: *XY Scanner Single module flexure XY-scanner with closed-loop control 50 µm×50 µm*; Resolution: *0.05 nm*; XY stage travel range: *20×20 mm*; Sample size: *Open space up to 100×100 mm^2, thickness up to 20 mm^2 in contact mode*.

2.5.5. Stylus profilometer

It is essential to measure the film thickness to estimate various physical parameters of the thin film such as optical band gap and sheet resistivity [139]. Several optical methods are available to measure film thickness including ellipsometry, multiple beam interferometry, spectrophotometry, and stylus profilometry. Among them, stylus profilometer measurement is an accurate and more reliable method. Formation of sharp-step edge in the thin film during deposition is more important to measure the thickness by stylus profiler. The stylus profiler measures a small variation in vertical displacement as a function of the stylus position, which scribed across the step edge over the uncoated and coated area [140]. The stylus measures the thickness in contact mode. The present research work has been carried out using KLA Tencor stylus profiler as shown in Fig. 2.10.

Instrument Specification

Model: *Alpha-Step D-120 brings high resolution 2D & 3D profiling;* Force sensor range: *0.03mg –10 mg;* Stage: *motorized 150×178 mm X-Y stage.*

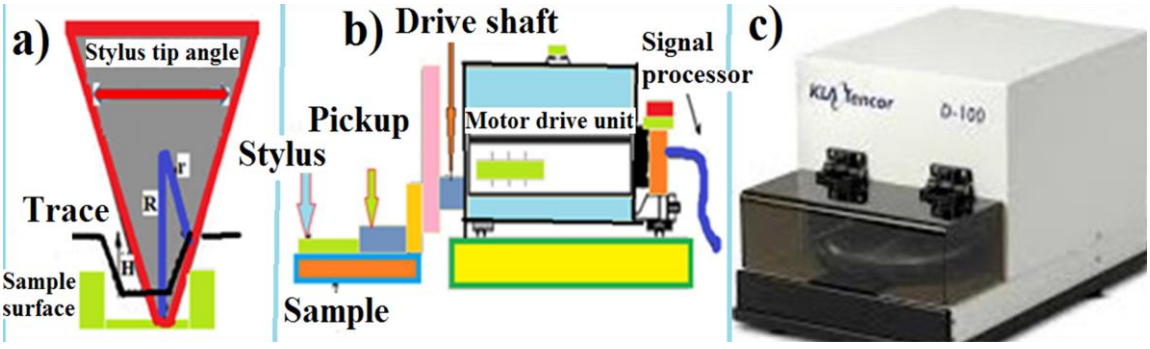

Fig. 2.10. Stylus profilometer tip on sample surface (a) working principle (b), Stylus profiler instrument (c).

2.5.6. UV-Visible Spectrometer

The UV-visible spectroscopy is a powerful tool to measure the optical properties (transmittance, absorption, reflectance, etc.) of samples [141]. If a material possesses higher

transmittance in the visible region it clearly indicates lower absorption and reflectance. If the sample does not absorb the incident light for a given wavelength range and the incident light intensity (I) and transmitted light intensity (I_o) are equal ($I = I_o$). However, in practice all the materials do not possess complete transmittance, Io is always lower than I ($I_o < I$). The relation between absorption (A), and transmittance (T) is given according to Beer-Lambert's law, and the absorption of the material is expressed as follows, ($A = -\log(T) = -\log I_o/I$) [142]. The absorption of the material also depends on the film thickness and absorption coefficient of the material (α). The absorption coefficient is intrinsic property of a material. The optical band gap is estimated using the transmittance and thickness of the sample. In the semiconducting system, electrons can be excited from the valence band to conduction band during the absorption of incident light energy. In the semiconducting system, there are two types of optical transitions that can occur; direct and indirect transitions. Both transitions arise because of the interaction of the electromagnetic radiation with the crystal lattice. The direct and indirect transitions are calculated from the momentum vector of the photon with respect to the position vector. The estimation of direct and indirect band gap of the samples by Tauc relation [143]. The schematic diagram of the UV-Vis-NIR spectrophotometer is shown in Fig. 2.11. In present research work, the optical properties were analyzed as a function of incident wavelength using Agilent Technologies UV-Vis spectrometer.

Instrument Specifications

Model: *Cary 5000 UV-Vis-NIR spectrometer*; Lamp: *deuterium*; Detectors: *photomultiplier tube for UV−Vis, InGaAs for (NIR)*; Wavelength range: *175–3300 nm for transmission*.

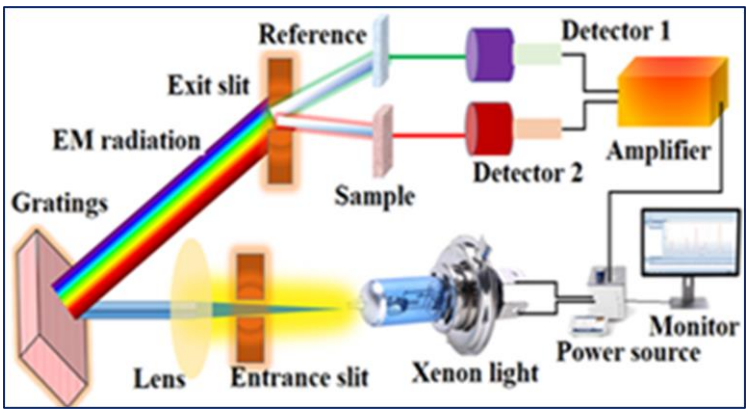

Fig. 2.11. Schematics of UV-visible spectrometer.

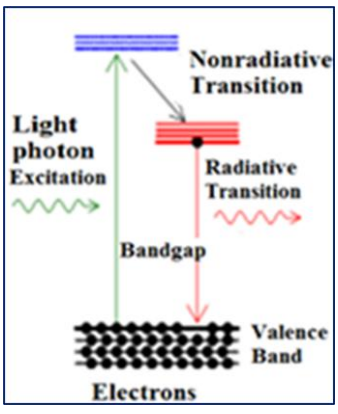

Fig. 2.12. Schematics of photoluminescence emission process.

2.5.7. Photoluminescence spectroscopy

The photoluminescence (PL) spectroscopy is an effective technique to understand various electronic transitions in materials. The luminescence study is useful to identify the excitation and emission process, band gap, and impurity defect levels of materials, based on the emission spectra [144]. The PL is emission of light when the incident photon energy is equal or higher than the band gap energy. The electrons will be excited from valence band to conduction band during the absorption of light energy. The excited state is not a stable state; hence the electrons return to ground state by radiating energy as illustrated in Fig. 2.12. It is also possible for non-radioactive transition from excited state to ground state. The photoluminescence property spectra emitted in a material because of core shall electron, valence electron, free electron, localized impurity states or defect state of the system. The electronic transitions of materials are classified into two types, i) radiative transition and ii) non-radiative transition. The radiative transition happens due to the intrinsic states formed by the impurities. There are different types of radiative transitions arise in materials such as band-to-band transition, free exciton transition, and free-to-bound transition. Non-radiative transition happens before or after the radiative transition and during the non-radiative process, no emission will be delivered [145]. The present research work the Horiba scientific PL instrument is used for studies.

Instrument Specifications

Model: *Fluorolog 3-2; Light source: 450 W CW Ozone-free xenon arc lamp (250 to 2500 nm); Monochromators: Czerny-Turner design with plane gratings for optimized focus at all wavelengths and minimum stray light; Sample detector: Photomultiplier R928P, spectral coverage 200 to 870 nm; Reference detector: UV enhanced silicon photodiode.*

2.5.8. Hall-Effect

The estimation of electrical transport properties of TCE thin film is more important from applications point of view. Investigations of the electrical transport properties of thin film indicate that it depends on thickness, structural and surface properties of the thin films. The electrical transport properties were estimated by Hall-Effect method using standard Van der Pauw geometry. Hall-Effect method is a widely used techniques to distinguish the type of conduction (n-type or p-type), and to estimate the carrier concentration, mobility, conductivity of semiconducting sample accurately. The basic principle of hall effect is, when a current (I_H)

carrying conductor is placed in a uniform perpendicular magnetic field (B), a voltage is developed in opposite to these two plane direction which is called as Hall voltage (VH) [146] as schematically represented in Fig. 2. 13(a). In present research work the Hall Effect studies were performed by using Ecopia instrument.

Instrument Specifications

Model: *HMS 3000*; Sample holder: *Spring clipboard is for use with the 0.51 Tesla magnet kit (20×20 mm^2)*; Resistivity range: *10^{-4} to 10^{7} Ω cm*; Magnet: Permanent magnet; Magnet flux density: *0.51 Tesla nominal +/-1% of market value*; Hall voltage range: *1μV to 2 V*

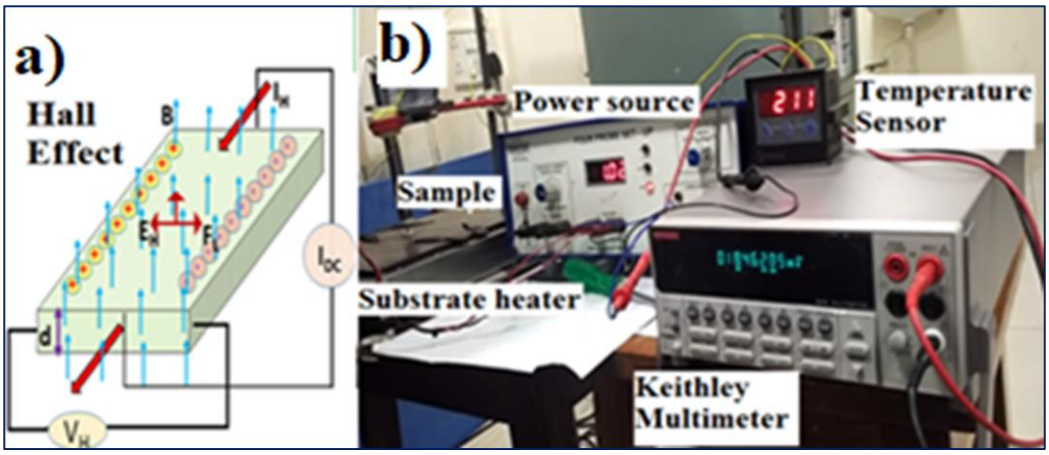

Fig. 2.13. The schematics of Hall-Effect (a) and the photograph of four probe resistivity measurement setup (b).

2.5.9. Four-probe measurement setup

The four-probe setup is the commonly used technique to determine the sheet resistance and resistivity of the thin film as a function of temperature or at room temperature. In four-probe method, the probes are connected in equal distance, and placed over the surface of the sample. The sheet resistance is estimated by using equation $R_S = F\ (V/I)\ \Omega/\square$, where F = 4.532 is the correction factor, t is the thickness of the sample, V is the voltage drop across any two probes and I is the current applied between the any two probes. The temperature dependent resistivity and the sheet resistance of the films were calculated by home-made four-probe instrument equipped with power source (range 0.1 mA to 2 mA), Keithly multimeter, and controlled heater whose temperature is maintained accurately within ±1 K with the use of an NC2438 precision temperature controller. A chromel–alumel thermocouple served as a temperature sensor.

Temperature of the film was also externally measured by a K-type thermocouple and a DC1010 digital voltmeter. Photograph of home-made four probe unit is shown in Fig. 2.13(b).

2.5.10. Raman spectroscopy

Raman spectroscopy first proposed by C. V. Raman in 1928, it is a non-destructive analytical method to identify functional groups present in a variety of samples [147]. Raman effect arises due to inelastic scattering of incident light by the atoms/molecules. When atoms/molecules are absorbing the light energy, it is possible to radiate or re-emit the energy through vibration or rotational motion. The energy transition by rotational/vibrational mode depends on the excited energy level. The rotational energy is lesser than the vibrational energy. The atoms/molecules re-emit the same energy as that of incident light energy, indicating no Raman active mode to be present in the system ($\nu o = \nu$), and this type of transition is called as Rayleigh's elastic scattering. The re-emitted photon energy lower than the incident energy indicate active Raman mode, this mode is generally called as stokes mode ($\nu o > \nu$). When reemitted photon energy is higher than the incident photon energy, this also indicates the active Raman mode, this mode is called as anti-stokes mode ($\nu o < \nu$) [148]. The pictorial representation of Raman modes is shown in Fig. 2.14(a). The Raman spectroscopic instrument consists of four major components, a laser source, sample illuminator, filter, and detector as shown in Fig. 2.14(b). The monochromatic laser light source converged with a focal lens is sent via interference filter to obtain the Raman spectrum. Nowadays, Raman spectrometer has more advancement in its instrumentation, in optics, laser, and other features.

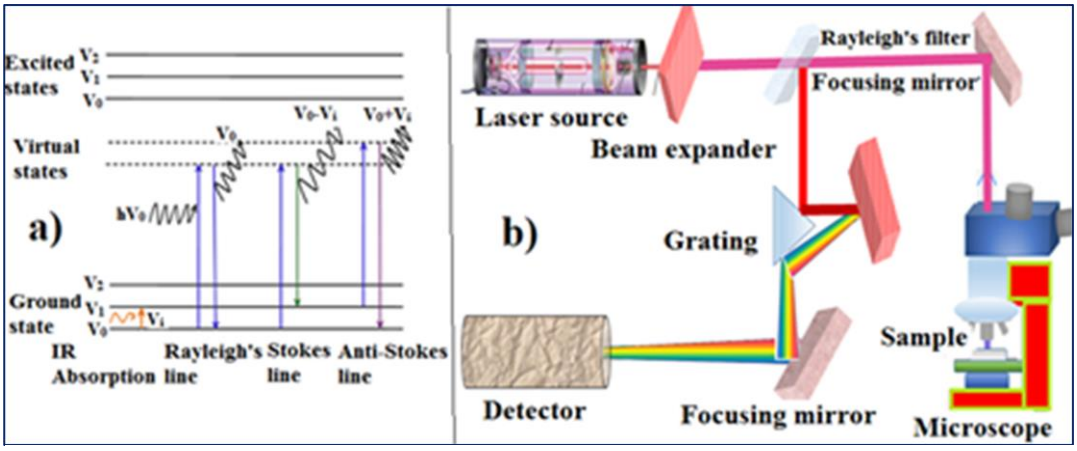

Fig. 2.14. The schematics of Raman scattering effect (a) and the instrumentation of Raman spectroscopy (b).

Raman confocal microscopy is used to investigate the surface homogeneity and uniformity of the sample. In the present research work, Raman analysis was carried out using a Horiba Raman instrument.

Instrument Specifications

Model: *XploRA ONE*; Laser options: *Integrated internally – 532 nm CLS high brightness lasers*; Spectral range: *100 cm^{-1} to 3500 cm^{-1} minimum*; Detector: *1024×256 TE air-cooled scientific CCD, USB control, 16 bit and up to 1.48 MHz readout speed*; Confocal sampling: *Rugged confocal spatial filtering, offering maximum 1×1 µm lateral resolution for micron-scale Raman analysis and imaging*; Computer software: Lab Spec 6 spectral software.

2.5.11. Surface work function by Kelvin probe technique

It is important to measure the surface work function of a material for assessing their potential in optoelectronic device applications. The energy level difference between the Fermi level and the vacuum level of the material is called as work function. The work function of a material is strongly influenced by surface behavior. The work function of a material can be estimated by ultraviolet photoelectron spectroscopy (UPS) and Kelvin probe (KP) method. The UPS method measures the absolute work function, whereas the KP method gives the contact potential difference (CPD) between the actual probe and sample's surface [149]. The KP method is a unique non-contact method to determine the contact potential difference between the sample and the reference electrode tip. The working principle is similar to that of a vibrating capacitor.

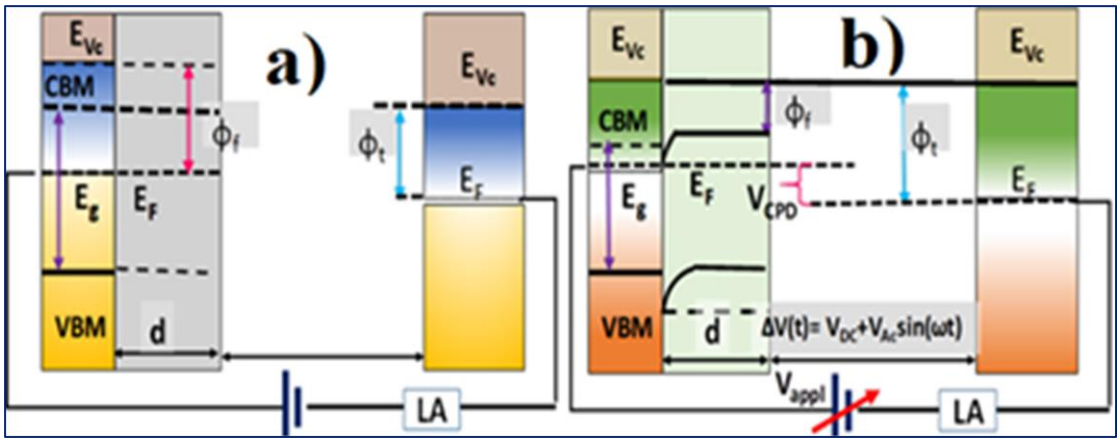

Fig. 2.15. The schematics of KP method for two different cases: a) Non-electrical contact mode, b) Electrical contact mode.

The scanning procedure is similar to a non-contact AFM measurement. Figure 2.15(a and b) depicts the work function for two different cases. The energy level of the electrode and sample are aligned but the Fermi level is not aligned in an ideal case (non-contact mode) as shown in Fig. 2.15(a). Electron tunneling can take place when the surface of these two electrodes are brought very close to each other at a distance 'd'. Figure 2.15(b) clearly indicates the Fermi level to align due to the external current flowing through the circuit (contact mode) and the produced apparent electrostatic potential between the reference electrode and sample surface is called the contact potential difference (CPD). This CPD will generate an oscillating electrical force ($V_{DC}+V_{AC}$ sin (ωt)), which can be nullified with an externally applied voltage (V_{appl}). When the external voltage is applied in the opposite direction with the same magnitude as the CPD, it can eliminate the surface charges present in the sample [150]. Hence, the work function of the sample can be estimated when the reference electrode's work function is known. In the present research work the surface work function was carried out using an home-made Kelvin Probe instrument (Indigenous Design, Department of Physics, Indian Institute of Technology, Madras) [151].

CHAPTER: 3

Spray Deposition and Characterization of Antimony-Doped SnO_2 Thin Films

This chapter is mainly focus on antimony (Sb) doped tin oxide (ATO) thin film deposited by cost-effective spray pyrolysis technique. The ATO thin film is a well-known n-type TCO material explored by several research groups but not yet commercialized due to unfavorable optical and electrical properties. This chapter looks into fine turning of the deposition parameters to achieve better TCO properties of ATO film. The optimized conditions are used for the deposition of large area (10×10 cm^2) ATO thin film. More importantly, for the first time, the resistance stability and surface variation in electrical properties of ATO films are studied in order to elucidate the TCO properties for optoelectronic applications.

3.1. Introduction

The binary metal oxide SnO_2 is a well-known wide band gap semiconductor which has various applications in renewable energy sector, and display devices [152]. The valence band electrons play an essential role in tuning the physical and chemical properties of metal oxide systems. The hybridization between O2p state and the 'Sn' metal valence state is an important aspect to understand the electronic properties of system [15]. The electronic band structure of the metal oxide systems are influenced by the dopant and other defects present in the system [10]. The ATO thin film possesses properties similar to commercial ITO and FTO, and is an n-type semiconducting material with a large band gap >3.6 eV and high electron mobility (33.11 $cm^2\ V^{-1}\ s^{-1}$) and, making it suitable for several device applications [153]. The optimization of ATO has been reported by using various methods such as DC and RF magnetron sputtering [107], thermal evaporation [154], Pulsed laser deposition [155], spin coating [156], and spray pyrolysis methods [109]. ATO is a promising candidate for TCO application since it shows significant electrical and optical properties with thermal and chemical stability [157]. There are several research reports available on the structural, surface, optical, and electrical properties of ATO films investigated by controlling various parameters. K. Y. Rajpure et al reported that the ATO film's physical properties are influenced by film thickness [158] and E. Shanthi et al reported the influence of physical properties on the annealing temperature of spray deposited SnO_2 film [159].

Limited literature is available on substrate temperature effect on the electrical and optical properties of ATO thin films. There are no much literature reports available for temperature dependent electrical properties of ATO films.

The influence of Sb-dopant on the physicochemical properties like crystallinity, transparency, and conductivity of the SnO_2 films are investigated and the optimum conditions are employed to deposit large area (10×10 cm^2) ATO film. The suitability of the large area coated ATO thin film is also verified with various analytical studies. The systematic temperature dependent sheet resistance (resistance stability) study of ATO film has not yet been reported in literature, which has been performed and discussed in this chapter. The surface work function of the optimized spray deposited ATO film has been estimated by Kelvin probe measurement for the first time. These results are presented and discussed elaborately in the forthcoming sections.

3.2. Experimental Procedure

The ATO thin films are deposited by cost-effective chemical spray pyrolysis technique on to glass substrates. The spray precursor solution was prepared by dissolving 95 wt% of tin (IV) chloride dihydrate ($SnCl_2.2H_2O$) (8.036 g) in 10 ml of distilled water and 5 wt% of antimony trichlorides ($SbCl_3.5H_2O$) (0.42 g) in 10 ml of distilled water individually and stirred for 30 minutes. These two solutions were then mixed together and added with 130 ml of ethylene glycol and stirred for two hours under ambient condition. Further, 2 ml of concentrated HCl was added dropwise into the mixture to reduce the turbidity of the precursor solution. The glass substrates (7.5×2.5 cm^2) were cleaned ultrasonically by the standard procedure prior to deposition after treating in a high energy plasma cleaner (Harrick plasma, Model PDC-002) to remove the ionic charge contamination on the surface of the substrates. The plasma treated glass substrates were loaded onto the substrate holder. When the aerosol solution was sprayed onto the substrate, the temperature reduced significantly and therefore a small interval is given to regain the original substrate temperature. All the deposition parameters are given in Table 3.1.

The ATO thin films which were deposited at 360 °C, 380 °C, 400 °C, 420 °C, 450 °C, 460 °C, 480 °C and 490 °C, are hereafter designated as ATO1, ATO2, ATO3, ATO4, ATO5, ATO6, ATO7, and ATO8 respectively.

Table 3.1. Optimized spray deposition parameters of ATO thin films.

Parameters	Optimization details of ATO thin films
Source materials	Host: $SnCl_2$ $2H_2O$, Donor: $SbCl_3$. $5H_2O$, Solvent: ethylene glycol, distilled water, and 2 ml of HCl
Host: Donor (concentration)	95 wt% of Sn: 5 wt% of Sb (0.5 M concentration)
Spray solution quantity	150 ml
Substrate	Glass substrate (7.5×2.5 cm^2)
Substrate temperature	360 °C to 490 °C
Substrate to nozzle distance	35 cm
Spray duration ON: OFF	0.5 s: 30 s
Air pressure	46 kg/cm^2
Total number of sprays	420

3.3. Results and discussion

3.3.1. X-ray diffraction analysis

Figure 3.1 shows the X-ray diffraction (XRD) patterns of ATO thin films deposited at different substrate temperatures consistent with the standard pattern of JCPDS card No (41–1445), indicating the polycrystalline tetragonal crystal structure of SnO_2 [109]. No other secondary peak was found in the XRD spectra, indicating that the ATO thin films having only SnO_2 phase formation [117]. There was no Sb_2O_3 phase observed in the XRD pattern, which implies that the substitution of Sb into the Sn lattice site. The XRD peak intensities increase as a function of substrate temperature up to ATO5 film deposited at 450 °C. With further increase the peak intensity was found to decrease. It has been reported that the increasing substrate temperature higher than the critical substrate temperature may lead to higher peak broadening, and these variations of peak intensity may be reflected in the crystallite size of the films. The average crystallite size of films are estimated by using Scherer equation expressed below [109],

$$L = \frac{0.9\lambda}{\beta\cos\theta} \qquad (3.1)$$

Where θ is diffraction angle, λ is wavelength and β is the full width at half maximum (FWHM). The calculated values of average crystallite size are presented in Table 3.2. The estimated values clearly indicate the decrease in crystallite size up to 450 °C. Beyond 450 °C of substrate temperature, higher crystallite size resulted.

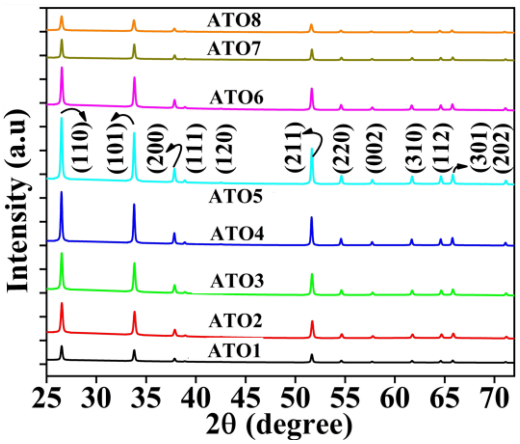

Fig. 3.1. The XRD patterns of ATO films as a function of substrate temperature.

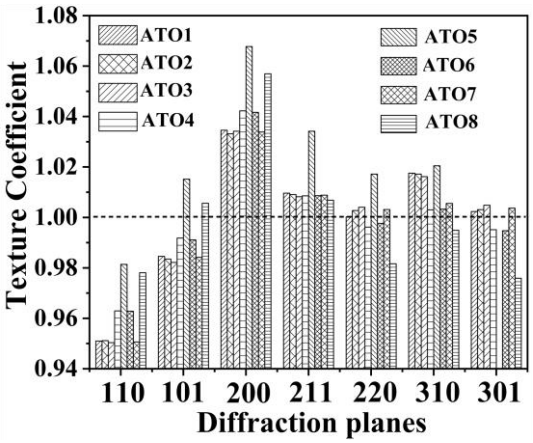

Fig. 3.2. Texture coefficient of various diffraction planes of ATO films.

Texture coefficient (TC_{hkl}) is an important factor which influences the physical properties of ATO thin films [156]. TC_{hkl} indicates the preferred orientation of each peak to a particular crystallographic hkl plane direction. The texture coefficient of the ATO film was estimated using the Harris method as follows [160],

$$TC_{hkl} = \frac{I_{hkl}/I_{0hkl}}{\frac{1}{N}\sum_{N=1}^{N} I_{hkl}/I_{0hkl}} \qquad (3.2)$$

Where I_{hkl} is the observed peak intensity, I_{0hkl} is standard peak intensity and N is the number of diffraction peaks. The TC_{hkl} values of crystallographic planes (110), (101), (200), (211), (220) (310), and (301) are presented in Fig 3.2. It can be understood that the relative intensity of all the crystallographic planes are strongly dependent on the substrate temperature. Among all the peaks, the (200) plane of ATO thin films are highly textured and the lowest peak value of TC_{hkl} is observed for the (110) plane. The estimated texture coefficient values as a function of substrate temperature are presented in Table 3.2. The highest TC_{hkl} value is observed for ATO5 thin film, indicating enhanced film growth. The lowest TC_{hkl} value observed for ATO8 film indicates polycrystallinity. The obtained results of TC_{hkl} values are in good agreement with the values reported by Chang-Yeoul Kim et al., [161].

3.3.2. X-ray photoelectron spectroscopic study

The XPS measurement was performed to study the oxidation states of the elements present in ATO thin films to understand the basic charge transport mechanism. Figure 3.3 (a) indicates the survey scan spectra of Sn, O, Sb and C elements and it has been identified that the Sb peak was relatively of low intensity due to low dopant concentration (5 wt%) of the films [106]. The C1s peaks at 285 eV corresponds to the surface contamination due to exposure of the film to ambient atmosphere [106]. The peak centered at 976 eV for SnMN1 is the auger electron peak of Sn ion [162]. Figure 3.3(b) presents the narrow scan spectra of Sn $3p_{3/2}$ peak and $Sn3p_{5/2}$ for ATO4 and ATO5 thin films respectively. The higher binding energy peak of $Sn3p_{3/2}$ peak observed at 482 eV is attributed to the presence of Sn in 4+ charge state [162]. A small peak shifting is observed with increased substrate temperature from ATO4 film to ATO5 film.

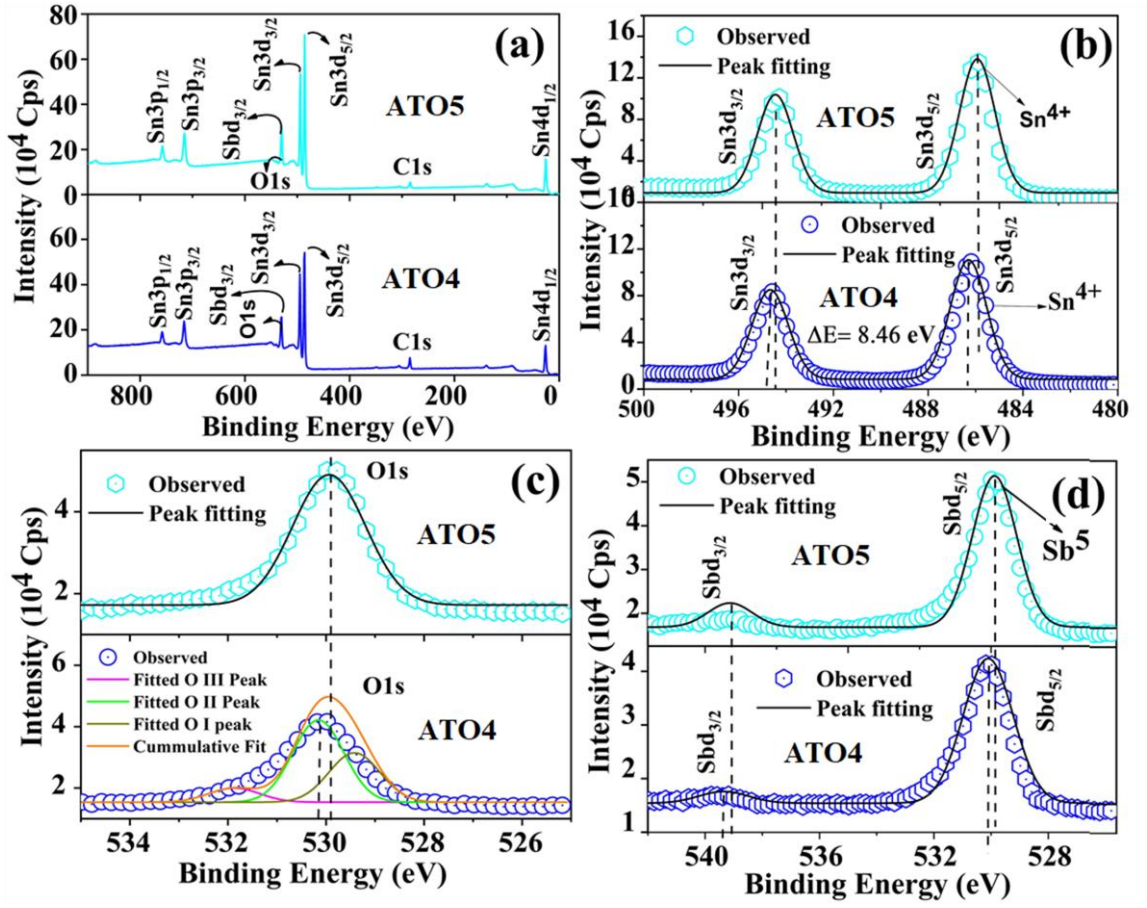

Fig. 3.3. The XPS full survey scan spectrum (a), Sn3d narrow scan spectrum (b), O1s narrow scan spectrum (c), and Sb3d narrow scan spectra (d) of ATO4 and ATO5 films.

The bonding states of O1s spectra centered at 530.1 eV (O I), 531.2 eV (O II) and 532.3 eV (O III) for ATO4 and ATO5 films are shown in Fig. 3.3(c). The O I peak is due to formation of oxygen with metal Sn (SnO_2 bond), OII peak is due to oxygen deficiency in SnO_2 film while the O III peak is generally attributed to the dissociated oxygen or hydroxyl groups on the film's surface [106]. Figure 3.3(d) shows the narrow scan spectra of $Sb3p_{3/2}$ and $Sb3p_{5/2}$ oxidization states with binding energy at 539.1 eV and 529.8 eV respectively [106]. The Sb binding energy reveals that the Sb exists in Sb^{5+} charge state. Higher substrate temperatures around 450 °C enhances the effectiveness of Sb doping which may lead to improved electrical and optical properties of ATO5 film. It has been reported that the doping of Sb in the Sn lattice site may increase the free carrier concentration and higher mobility [106,153] .

3.3.3. AFM analysis

The surface topography of ATO films were investigated by atomic force microscopy (AFM). Figure 3.4 (ATO1 to ATO8) shows the 3D topographic images of ATO thin films deposited as a function of substrate temperature. It is apparent from the images that surface topography is influenced by substrate temperature. It is also noticed that the surface topography of the films gradually changed from particulate to needle-like shape as substrate temperature increases. The particulate surface topography of the films possesses relatively higher surface roughness than the needle-like topography. The root mean square (RMS) roughness of the films estimated from the AFM images were more or less similar to values estimated from stylus profiler measurement (Table. 3.2). The lowest RMS roughness was about 7 nm for the ATO5 film deposited at 450 °C, and the highest surface roughness was about 21.5 nm for the ATO1 film. The variation in surface roughness of the ATO film is attributed to varying kinetics of the grain growth during the film formation. Generally, grain growth happens in two ways; one is mass transport from smaller to bigger grain growth, which can reduce the surface to volume ratio, while the other occurs at high temperature, where two bigger grains combine to form a bigger particle (coalescence) [163]. The agglomeration of grains increases the surface roughness. The higher surface roughness of the films also affects the electrical and optical properties.

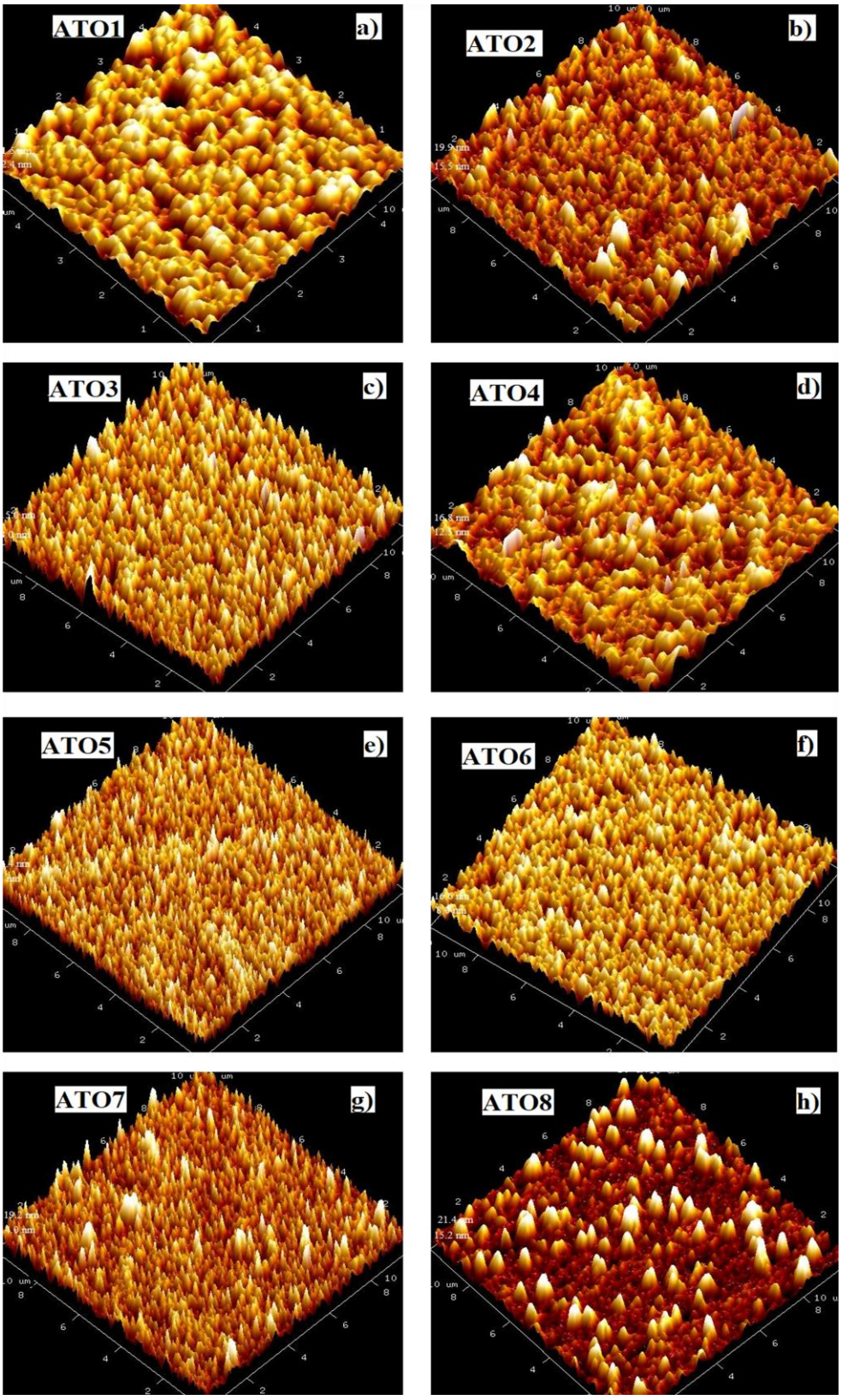

Fig. 3.4. The AFM images of ATO thin films deposited as a function of substrate temperature.

Table 3.2. Structural, surface and optical properties of ATO films deposited as a function of substrate temperature.

Sample	ATO1	ATO2	ATO3	ATO4	ATO5	ATO6	ATO7	ATO8
L (nm)	55.3 ± 1.10	49.2 ± 0.98	47.2 ± 0.94	46.2 ± 0.92	40.5 ± 0.81	42.8 ± 0.85	51.0 ± 1.02	53.6 ± 1.07
a (Å)	4.746	4.743	4.745	4.748	4.744	4.752	4.747	4.753
c (Å)	3.191	3.187	3.188	3.190	3.188	3.192	3.191	3.196
TC_{hkl}	1.034	1.033	1.034	1.042	1.052	1.041	1.033	1.056
Thickness (nm)	1245 ± 62.2	820 ± 41.0	512 ± 25.6	648 ± 32.4	317 ± 15.8	850 ± 42.5	947 ± 47.3	1560 ± 78.0
Roughness (nm)	27	19	17.3	18.6	5.8	14	24.2	30.4
Transmittance (%)	62	68	82	77	89	73	62	52
Direct E_g (eV)	3.80	3.79	3.80	3.81	3.81	3.81	3.77	3.73
E_u (meV)	1.00	1.09	1.23	1.27	1.56	1.25	1.47	1.48

3.3.4. SEM and EDS analysis

A significant change in surface morphology is observed in SEM images of the films with substrate temperature. The surface morphology of ATO thin films analyzed using SEM are shown in Fig 3.5. The surface morphology gradually changed from particle to polyhedron shape as substrate temperature increases [109,157]. The well-oriented grains are observed and their size is homogenous, and they are uniformly distributed over the entire region of the films as shown in Fig. 3.5. The film deposited at 450 °C consists of relatively uniform, homogeneous and crack free surface formed by island grain growth combined with nucleation effect to form continuous film. The ATO films surface morphology is also influenced by film thickness and roughness. The film that has higher thickness possesses relatively low homogeneity, but it shows higher dense film formation. The higher film thickness is also one of the reasons for large surface roughness present in the films. The thickness and roughness of the films were estimated using stylus profiler measurement, and values are given in Table 3.2. The stoichiometry and chemical composition of selected ATO thin films (ATO1, ATO3, ATO5, and ATO7) confirmed by Energy dispersive X-ray spectroscopy (EDS) are depicted in Fig. 3.6. The EDS analysis confirms the presence of Sn, Sb and O elements in the films deposited at different substrate temperatures. A nominal change in the stoichiometry of the ATO films is observed with the substrate temperature (Insets of Fig. 3.6).

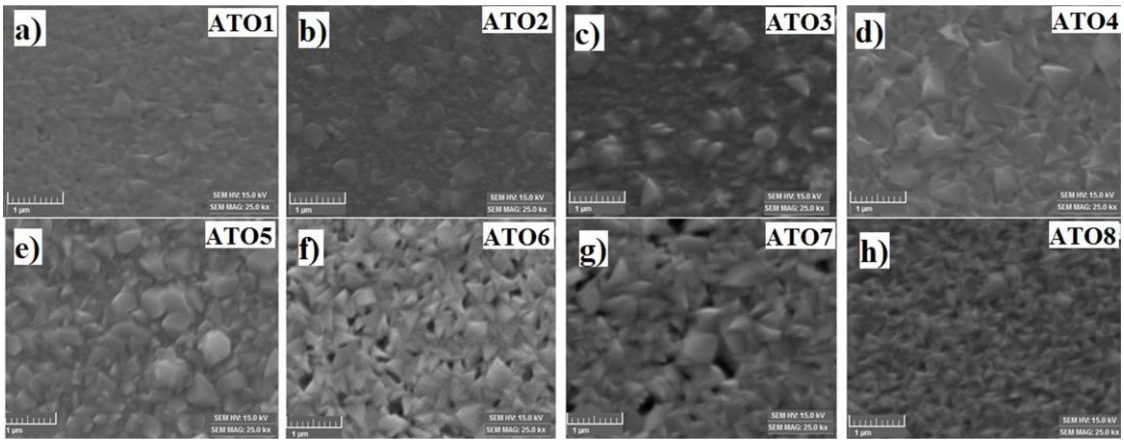

Fig. 3.5. The SEM images of ATO thin films deposited as a function of substrate temperature.

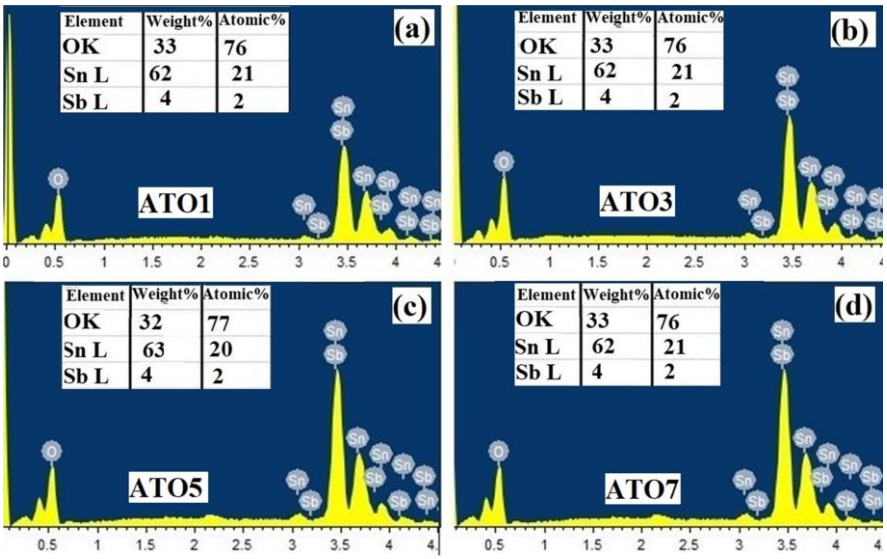

Fig. 3.6. The EDS image of selected ATO thin films deposited as a function of substrate temperature.

3.3.5. Optical properties

Figure 3.7 illustrates the optical transmittance spectra of ATO thin films deposited as a function of substrate temperature. It is clear that ATO5 film exhibit the high average transmittance of 89% at 550 nm due to low surface roughness and good crystalline properties. The transmittance value decreased beyond 450 °C indicating increase of oxygen formation energy which leads to enhanced grain boundary scattering. In addition, it is also noted that the near IR region transmittance values exceed more than 90% for ATO5 film. These results reveal that the ATO5 thin film may be suitable as an alternative transparent conducting electrode. All

the films exhibited strong absorption at the lower wavelength in UV- visible region, which are in good agreement with earlier reports [109]. The optical band gap energy (E_g) can be estimated by Tauc plot [164], which is an extrapolation method from the photon energy Vs absorption coefficient relation as follows;

$$(\alpha h\nu) = A\,(h\nu - E_g)^n \qquad (3.3)$$

Here A is constant, α is the absorption coefficient, h is Planck's constant, ν is the frequency of the incident photon, and n is a variable (n = 1/2 is the direct allowed transition and n = 2 is the indirect allowed transition) [165]. The direct band gap values of ATO films deposited as a function of substrate temperature are given in the table 3.2 and shown in Fig 3.8. The estimated direct band gap (E_g) values did not show any particular trend, but the transmittance was found to be improved with a higher value of 3.81 eV for ATO5 film. The E_g also varies due to change in carrier concentration in the bottom of conduction band [72]. This enhanced carrier concentration shifts the Fermi level toward the conduction band. This Fermi level shifting in semiconductors is called the Burstein–Moss effect [152]. This shift in Fermi level modify the optical properties of the materials. Hence, the estimation of total optical band gap (E^{opt}_g) is expressed as follows [152],

$$E_g^{opt} = E_g + \Delta E_g \qquad (3.4)$$

The Burstein–Moss shift ΔE_g is given by

$$\Delta E_g = \frac{h^2}{2m^*}\left(3\pi^2 n_e\right)^{2/3} \qquad (3.5)$$

Here h is Planck constant, E_g is the fundamental optical band gap, ΔE_g is the band gap shifting of the degenerate energy level due to B-M effect in an n-type semiconductor, n_e is the free carrier concentration and m* is the reduced mass $m^* = (m_e m_h / m_e + m_h)$, where m_e and m_h are effective mass of electron and hole, respectively. Table 3.2. is evidencing the variation in band gap as a function of substrate temperature and indicates that band gap is not only influenced by carrier concentration but also by other scattering defects. In general the films possessing higher surface roughness exhibit more light scattering, which generally decreases transmittance of light [77]. Transmission spectra clearly indicate the absorption tail is near the band edge and it influences the band gap of films due to various defects present in the system [152].

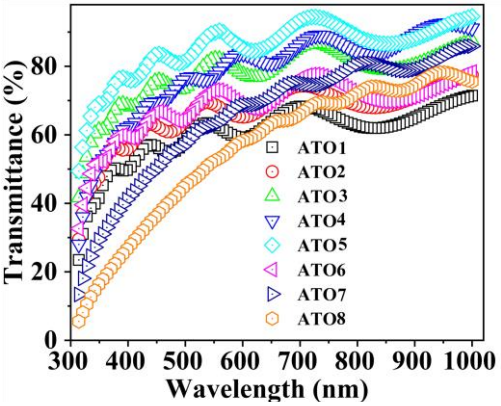

Fig. 3.7. The transmittance spectra of ATO films deposited as a function of substrate temperature.

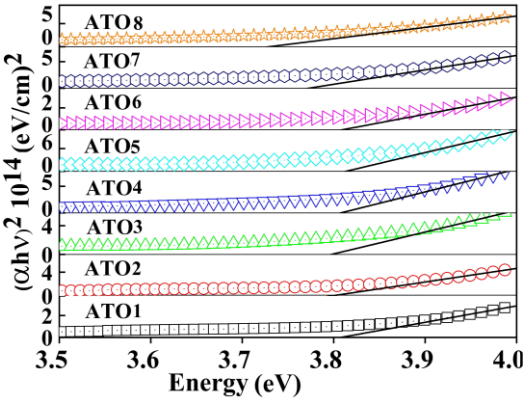

Fig. 3.8. The estimation of direct band gap of ATO films deposited as a function of substrate temperature.

This absorption tail width near band edge spectra is useful to calculate the Urbach energy (E_u) of the films. The E_u value is estimated by the following relation [166],

$$\alpha = \alpha_0 e^{\left[\frac{h\nu - E_g}{E_u}\right]} \qquad (3.6)$$

where a_0 is a characteristic material parameter, E_g is band gap, and E_u is the Urbach energy. Equation (3.6) implies that the logarithm of a plotted as a function of the photon energy can be approximated by a straight line in energies below the absorption edge. The E_u values of the ATO films are extracted from the slope of ln(α) Vs. photon energy (hν) plot as shown in Fig 3.9. The estimated E_u values are presented in Table 3.2.

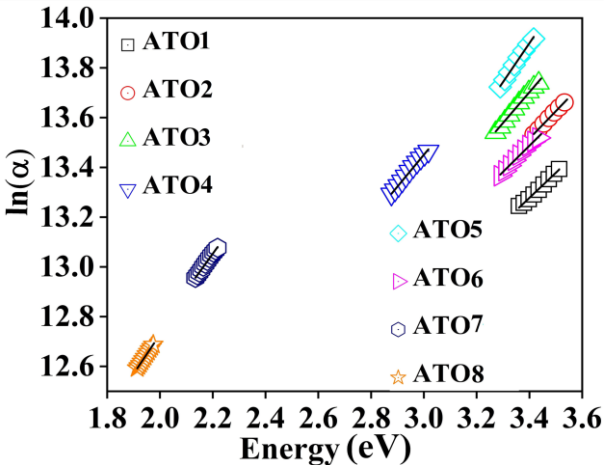

Fig 3.9. Urbach energy plot of the ATO films deposited at different substrate temperatures.

It can be understood from the graph that Eu is higher for ATO5 film, indicating more oxygen vacancy defects to be present in the film. In general, oxygen vacancy defects play a crucial role in controlling the optical and electrical properties of the system. The creation of oxygen vacancies induces free carriers near the bottom of the conduction band. Further, increasing free carrier may form a new defect energy levels near conduction band. These defect energy levels may possibly affect the energy band structure of the system.

3.3.6. Electrical property

3.3.6.1. Charge transport mechanism

The charge transport mechanism is influenced by the structural and surface properties of TCO thin films and it is very essential from application point of view. The doped binary metal oxides charge transfer can occur not only between the O2p state of oxygen-metallic charge transfer (O-Sn-O), but also with the intermetallic charge transfer (metal to metal charge transport Sn-Sb). The binary SnO_2 has a tetragonal cassiterite crystal structure with P42/mnm space group, and Sn atoms are six-fold coordinated to threefold coordinated oxygen atoms [72].

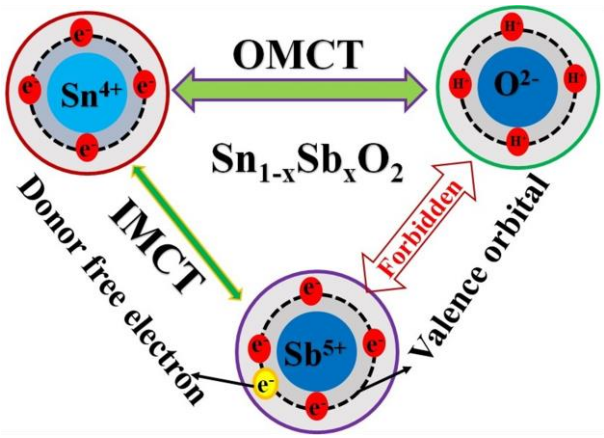

Fig. 3.10. The illustration of **c**harge carrier transport mechanism of Sb-doped SnO_2 system.

The oxygen anions form a distorted tetrahedral structure; each cation octahedron shares one tetrahedral face with the anions of the other type in an adjacent layer whereas the face opposite is shared with an empty octahedral position [72]. The total charge of the oxygen anion is -4 and that of Sn cation is +4, so that the SnO_2 system possesses a neutral charge state. When pentavalent antimony is doped into the Sn lattice site, four valence electrons are shared with Sn lattice covalently and induce one free electron to the Sn lattice. The charge transfer between

Sn^{4+} and Sb^{5+} states is well known and has been investigated computationally [10]. The conductivity of the SnO_2 film is due to compensation effect of donor electrons that charge transfer between cations and also due to native oxygen vacancies [10]. The charge transport mechanism is classified into two types: (i) oxide-metal charge transport (OMCT) and (ii) intermetallic charge transport (IMCT). The metal-oxide charge transport exercises more influence on the optical properties while the intermetallic charge transport influences the electrical properties. Figure 3.10 shows the possible charge transport mechanism of Sb-doped SnO_2 thin film. The optical properties of SnO_2 depend on charge transport between Sn5p to –O2p state and the electrical properties depend on the charge transport between Sn5p2–Sb5p3 states [167]. If the tin oxide shows good optical properties, then OMCT charge transfer is stronger (green arrow) than IMCT charge transport state (narrow grey arrow); similarly, in the case of highly conducting metal oxide system IMCT charge transport dominates the OMCT. The energy of the shaded area is similar to the charge-transfer energy between OMCT and IMCT states. The Sn cation when replaced with Sb creates donor electron and adjacent oxygen causes high electronegativity to form the SnO_2 phase. As the interaction between Sb and O is forbidden, there is no strong OMCT between them. The IMCT between Sn5p2–Sb5p3 states provide one free electron and is the reason for the increased conductivity of ATO films.

3.3.6.2. Room temperature electrical transport properties

Hall effect measurement was carried out to study the electrical transport properties of the ATO thin films. The room temperature Hall mobility, carrier concentration, and resistivity estimated for ATO films deposited at different substrate temperatures are shown in Fig. 3.11 and Fig. 3.12. The electrical properties of the films are related to the following equation [109],

$$\rho = \frac{1}{ne\mu}\ (\Omega cm) \qquad (3.7)$$

Here ρ is the resistivity, n is the number of charge carriers, e is the charge of the electron, and μ is the mobility. The carrier concentration of ATO films increase with substrate temperature (Table 3.3). The carrier concentration of the film improving from 0.28×10^{20} cm^{-3} for ATO1 film to from 3.64×10^{20} cm^{-3} for ATO8 film. The film deposited at 450 °C (ATO5) film exhibits maximum mobility of 25.1 cm^2/Vs, whereas the film deposited at 490 °C (ATO8) film exhibits lowest mobility of 19 cm^2/Vs (Table. 3.3). Figure. 3.11 shown the mobility of the film increased up to ATO5 film , and further decreased due to large number of free carrier collisions, surface

defect also plays crucial role in mobility of the films [10]. Similar trends also observed that the resistivity of the ATO films decreased from 125.5×10^{-4} Ω (ATO1) to 7.89×10^{-4} Ω (ATO5) film, and then increased with increasing substrate temperature up to maximum of 187.8×10^{-4} Ω (ATO8) (Table. 3.3). The increase of resistivity indicates the decrease of mobility by free carrier collision and scattering effects [152]. The electrical properties of ATO films depend on the charge transport between Sn5p2–Sb5p3 states. A metal oxide system possesses excellent electrical properties when IMCT is stronger than the OMCT. The estimated electrical resistivity of the ATO films are given in Table. 3.3. The sheet R_S of the ATO thin films is estimated using the following relation [168],

$$R_S = 4.532 \left(\frac{V}{I}\right) \quad (\Omega/\square) \qquad (3.8)$$

Here 4.532 is the correction factor (1×1 cm^2) for equally spaced (≈ 1 mm) probes, I is applied current, and V measured potential difference. Since the film thickness is much lower than the spacing between the probes. The sheet resistance of ATO films is presented in Fig 3.12 and values are given in Table 3.3. The ATO5 film was found to have the lowest value of sheet resistance of 24.9 Ω/□ due to lowest resistivity of the film, whereas ATO8 film was found to have the lowest value of sheet resistance of 120 Ω/□ and other films also have considerably higher sheet resistance values (Table. 3.3).

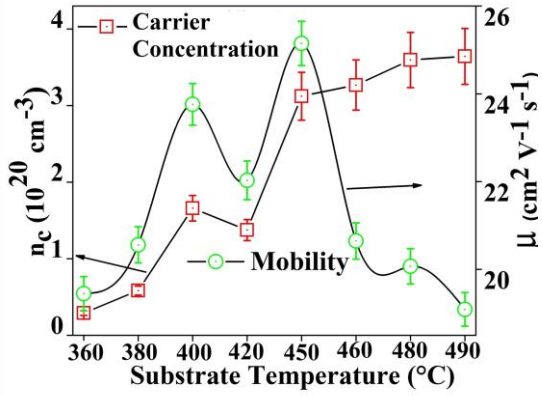

Fig. 3.11. The variation of carrier concentration and mobility of ATO films measured at room temperature.

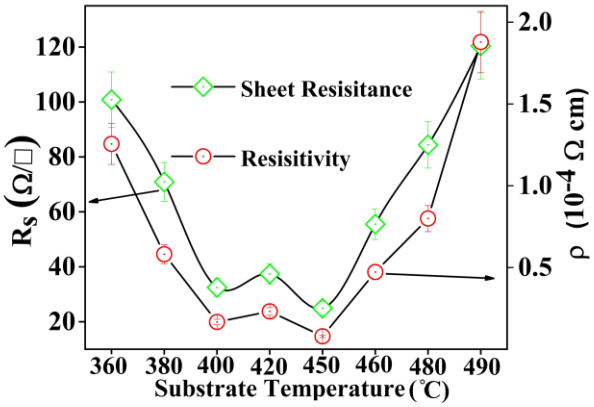

Fig. 3.12. The variation of sheet resistance and resistivity of ATO films measured at room temperature.

3.3.6.3. Temperature dependent electrical properties

The temperature dependent electrical properties of the ATO films were measured in the range 30 °C to 300 °C by linear four probe method. Figure 3.13 represents the temperature

dependent sheet resistance of the ATO films deposited at different substrate temperatures. The ATO films possess two different electrical conducting behaviors at two distinct regions of temperature. The electrical conductivity of the ATO films increased up to 210 °C indicating the semiconducting nature of the films. Beyond 210 °C conductivity of the ATO films abruptly decreased. This decreasing conductivity was due to decreasing mobility by free carrier collision effect. It is also reported that the ITO material exhibits a resistance stability up to 300 °C, beyond these temperatures the resistance stability decreases due to structural and surface defect may felicitate more fee carrier collision [169]. The free carrier mobility is influenced more by the scattering processes such as ionized impurity scattering, phonon scattering, and grain boundary scattering [170]. The metal oxide film is influenced more by the ionized impurities and grain boundaries scattering. Hence, the electrical resistivity of the film are expressed in terms of different scattering process by Matthiessen's rule as follows [159],

$$\frac{1}{\rho} = \left(\frac{1}{\mu_g} + \frac{1}{\mu_i} + \frac{1}{\mu_l} \right) \qquad (3.9)$$

Here, μ_g, μ_i, and μ_l are mobility values of the grain boundary, ionized, and phonon scattering respectively. The mobility of the free carriers are affected more by grain boundary scattering and through trapping of free carriers at the interface [170]. The trapping state induced by lattice defect is compensated by an ionized free carrier concentration and increasing oxygen formation energy. The increasing oxygen formation energy captures the free electrons at interface [171]. This process creates a potential barrier across the junction, which will affect the free carrier mobility in the crystal lattice. It is necessary to estimate potential barrier when the depletion layer width is equal to the crystallite size. The relation between the mobility affected by grain boundary and potential barrier is given by Petritz model as follows [159],

$$\mu_g = A\, T^{-1/2} \exp^{-\left(\frac{e\Phi}{kT}\right)} \qquad (3.10)$$

Where constant (A) is calculated by the following relation

$$A = \frac{el}{(2\Pi m^* k)^{1/2}} \qquad (3.11)$$

Here T is the absolute temperature, Φ is the potential barrier and K is the Boltzmann constant. Figure 3.13 presents the plot of ln ($\mu T^{1/2}$) against 1/T, and the slope of the straight line indicates the potential barrier. From the graph, the low resistive ATO5 film exhibits a potential barrier of 95 meV and the high resistive ATO8 film shows a potential barrier of 238 meV (Table. 3.3).

It is identified that the potential barrier is increased at higher temperature. This increasing potential barrier will affect the free carrier mobility. The ATO thin films show varying conducting behavior as a function of substrate temperature, which can be identified by estimating the activation energy by Arrhenius approach, as follows [168],

$$\sigma_{Tot} = \sigma \exp\left(\frac{-E_a}{K_B T}\right) \quad (3.12)$$

Here, σ_{Tot} is the d.c. conductivity, σ is the pre-exponential factor, E_a is the activation energy, K_B is Boltzmann constant and T is the absolute temperature. The activation energy of ATO films were estimated from the slope of the linear fit given to the plot of log (σT) against 1000/T. The estimated values of activation energies are presented in Table 3.3. The estimated activation energies from the Arrhenius plot show that the ATO films possess two different conduction behavior. The conduction range 30 °C to 210 °C indicate negative slope due to the semiconducting nature of the ATO thin films [168]. In the temperature range 210 °C to 300 °C, the ATO films possess positive slope indicating metallic like behavior. The activation energy of films varied with temperature indicating the variation of electrical properties (Table 3.3).

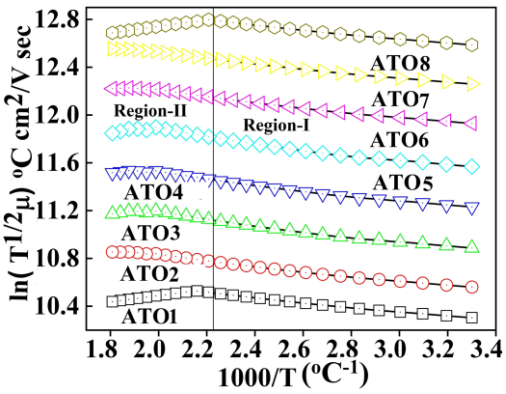

Fig. 3.13. The temperature dependent mobility plot of ATO films.

3.3.7. Figure of merit

The figure of merit (FoM) is an important property to consider TCO materials for optoelectronic device applications. For an ideal TCO, both the electrical conductivity and optical transmittance should be as large as possible. The FoM values is defined by the ratio of transmittance to sheet resistance. Generally the accepted figure of merit equation is expressed by Haacke relation [79],

$$FoM = \frac{T_r^{10}}{R_S} (\Omega)^{-1} \quad (3.13)$$

Here T_r is the transmittance at λ = 550 nm (the average value of visible wavelength) and R_S is the sheet resistance. It can be identified that the estimated FoM value varied due to different electrical and optical properties as a function of substrate temperature. The ATO5 film was found to have the highest FoM value of 1.25× 10^{-2} Ω^{-1} (Table. 3.3) indicating better optical transmittance and lowest sheet resistance of the film. Whereas ATO8 film was found to have the lowest FoM value of 1.20× 10^{-5} Ω^{-1} indicating more variation in optical transmittance and sheet resistance of the film due to more structural and surface defect in the films.

Table 3.3. The electrical transport parameters and FoM values of ATO thin films.

Sample	n_c (cm^{-3}) 10^{20}	μ_e (cm^2/Vs)	ρ (Ω cm) 10^{-4}	Rs ($\Omega/\square$)	E_{a1} (meV)	E_{a2} (meV)	FoM (Ω^{-1})
ATO1	0.28	19.4	125.5	100	54.5	754	8.32×10^{-5}
ATO2	0.58	20.5	58.13	70.9	85.8	762	2.98×10^{-4}
ATO3	1.65	23.7	16.65	32.5	51.0	819	4.22×10^{-3}
ATO4	1.37	22.0	23.13	37.4	66.3	809	1.95×10^{-3}
ATO5	3.12	25.1	7.895	24.9	105	883	1.25×10^{-2}
ATO6	3.26	20.6	47.22	55.5	80.2	771	7.73×10^{-4}
ATO7	3.59	20.0	79.92	84.3	80.9	763	9.94×10^{-5}
ATO8	3.64	19.0	187.8	120	48.4	744	1.20×10^{-5}

3.4. Large area (10×10 cm^2) coating of optimized ATO5 thin film

3.4.1. Optical and electrical properties of large area deposited ATO5 thin film

The best optimized ATO5 film deposition parameters were chosen for large area (10×10 cm^2) ATO5 thin film deposition by spray pyrolysis technique. The spray deposition parameters of large area coated ATO5 film are given in Table 3.4. The UV-Vis transmittance spectra of large-area deposited ATO5 film showed average transmittance of 77.5 % at 550 nm. The large area ATO5 thin film was found to exhibit n-type electrical conductivity. The undoped SnO_2 was reported to exhibit the electrical resistivity of 6.78×10^{-2} Ω cm and carrier concentration of 1.70×10^{18} cm^{-3} [172]. The large area deposited ATO5 film exhibits a lower resistivity value of 6.71×10^{-4} Ω cm with higher mobility value of 28.45 cm^2/Vs. The film was also having a higher

carrier concentration of 7.89×10^{20} cm^3. The large area coated ATO5 film showed slightly lower optical and electrical properties compared to small area (7.5×2.5 cm^2) coated ATO5 film due to higher film thickness and roughness resulted due to a large number of spray and also due to slight deviation of spray dynamics due to large area coating. The obtained results of large area deposited ATO5 film are in good agreement with previously reported spray deposited ATO5 thin film values in comparison with literature values as shown in Table 3.5.

Table 3.4. Spray deposition parameters of large area (10×10 cm^2) deposited ATO5 thin film.

Parameters	Deposition details of large area ATO5 thin film
Source materials	Host: $SnCl_2$ $2H_2O$, Donor: $SbCl_3$•$5H_2O$, Solvent: ethylene glycol, distilled water, and 2 ml of HCl
Host: Donor (concentration)	95 wt% of Sn: 5 wt% of Sb (0.5 M concentration)
Spray solution quantity	200 ml solution
Substrate	Glass substrate (10×10 cm^2)
Substrate temperature	450 °C
Substrate to nozzle distance	35 cm
Spray duration ON: OFF	0.5 s: 30 s
Air pressure	46 kg/cm^2
Total number of sprays	560

3.4.2. Sheet resistance variation across the surface of large area ATO5 film

Since the area of deposition is large, it is preferred to have an estimate of variation of sheet resistance across the entire area of the deposited 10×10 cm^2 ATO5 film. For this purpose, every 1×1 cm^2 area was measured by linear four probe method. Sheet resistance of the ATO5 film was calculated using the equation 3.8 [173], The photograph of the large area deposited ATO5 thin film is shown in Fig 3.14(a). The 2D contour plot shows the variation of sheet resistance across the surface of the large area ATO5 film (Fig. 3.14b). The colour representation in the 2D contour indicate the regions of nearly same R_S. In spite of the substrate holder positioned below the spray nozzle to maintain better uniformity in coating of the film, it is evident that the value of R_S is not uniform over the entire deposited area. The R_S was lower in the middle region and it increased eventually outwards at the edges. This is due to variation in spray dynamics that is inherent to spray method. The variation in flux of the created cone of aerosol reaching the hot substrate is modified with respect to lateral distance leading to pressure

gradient. This pressure gradient is also dependent on the nozzle type, spray height, heater surface condition, working fluid and droplet dynamics. It is also known that spraying of the precursor solution leads to cooling effect and also the droplets hitting the heated surface to splashing and rebounding [129]. Due to these inherent phenomena of spray deposition, a significant temperature gradient is present across the surface of the hot substrate. These effects are reported to lead to various reactions pertinent to spray deposition such as, vapor-solid, liquid-solid, and solid-solid to occur simultaneously [128]. These phenomena collectively influence the mass transport and hence the surface homogeneity leading to variations in thickness, electrical and optical properties of the thin film. These variations are more at the edges of the substrate leading to higher roughness and R_S compared to the center of the substrate. In spray method, it is difficult to achieve large-area uniform coating using a single static nozzle. The variation of the surface properties influences the electrical properties to a greater extent. For instance, Zheng et al reported in Sb-doped SnO_2 film, the surface grain boundary scattering to influence the free carrier mobility [174]. Batzill et al., investigated the scattering mechanisms for degenerate metal oxide films in terms of inter-grain potential barriers and defect disorder structure [20].

Table 3.5. Comparison of optical and electrical properties of spray deposited ATO5 film with literature reports.

Year	Tr (%)	ρ (Ω cm)	Rs (Ω/□)	Author (et al.)	Reference
1982	85	8.6×10^{-4}	20	H. Kaneko	[97]
2005	85	3.85×10^{-4}	1.75	E. Elangovan	[104]
2008	90	1.29×10^{-3}	20.2	K. Ravichandran	[175]
2011	70	8.9×10^{-4}	8.84	A. R. Babar	[176]
2014	80	2.1×10^{-3}	31	A. Rahal	[177]
2015	75	4.2×10^{-4}	3.12	A. R. Babar	[178]
2016	93.8	7.35×10^{-4}	15	M. Esro	[111]
2017	88	5.8×10^{-5}	0.61	V. Fauzia	[118]
2017	85	6.48×10^{-4}	331	A. Heiras-Trevizo	[114]
2020	89	7.89×10^{-4}	25.1	(7.5×2.5 cm^2)	Present
	77.5	6.71×10^{-4}	28.4	(10×10 cm^2)	work

Literature reports indicate that grain boundary scattering does not influence the film resistivity to a greater extent, instead it will be dominating the mobility of the carriers [20]. The 2D image

shown in Fig 3.14(b) clearly indicates the center of the film having low sheet resistance (≅ 31.91 Ω/□) and the corners of the substrate to possess higher variation in R_S ranging from 42 to 48 Ω/□. It is also reported that higher density of grain boundaries and agglomeration of grains generally affect the mobility of the carriers in the film, especially in spray method [179].

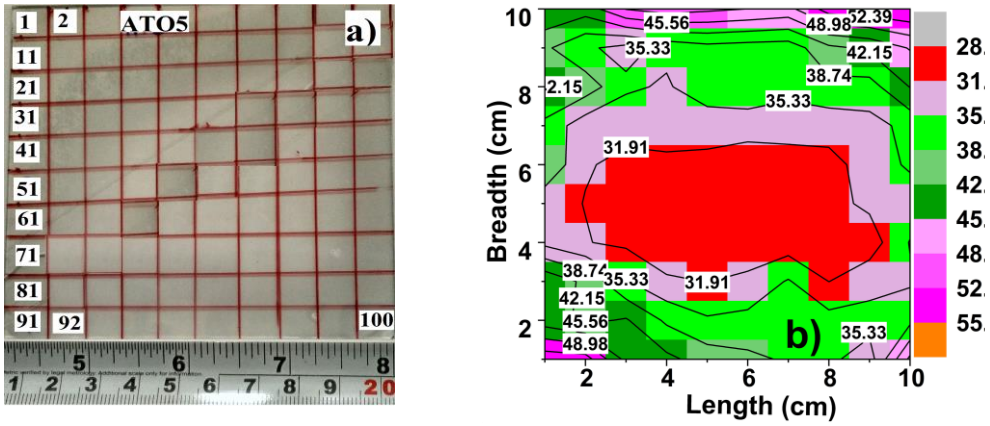

Fig. 3.14. Photograph of 10×10 cm^2 deposited ATO5 film (a), and the 2D contour plots of variation of sheet resistance (b).

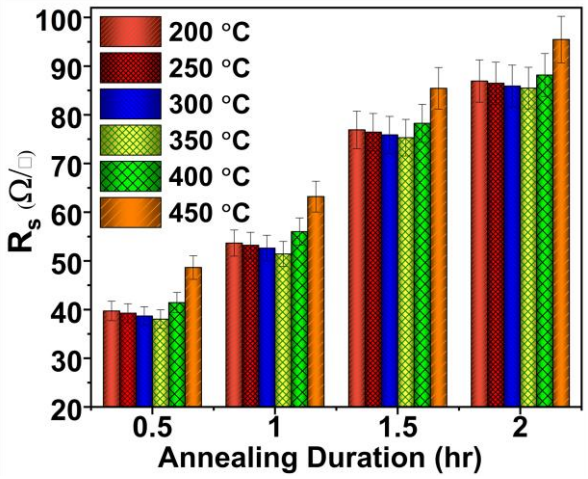

Fig. 3.15. The variation of sheet resistance of large area ATO5 film with annealing duration and annealing temperature.

3.4.3. Stability of sheet resistance analysis

In order to employ the ATO5 film for various device fabrication, the R_S should be nearly invariable when fabrication is performed at higher temperatures and for longer duration. The stability of R_S of the large area deposited ATO5 film at various temperature was evaluated to estimate the change in R_S with post annealing temperature (200 °C to 450 °C in steps of 50 °C) and duration (30 min to 2 hr in steps of 0.5 hr) as shown in Fig. 3.15. It has been identified from

the graphs that the optimum stability of R_s is around 350 °C with lowest sheet resistance achieved to be 39.7 Ω/□ for 30 min annealing duration. A gradual decline in R_S is observed with annealing temperature up to 350 °C and for the further increasing of the annealing temperature, it increased to higher values.

Moreover, when annealing temperature is kept constant and the duration is varied, the R_S increased to higher values (Fig 3.15). This variation of R_S is influenced by factors like, (i) thermal activation of free carriers leading to reduction of R_S up to 350 °C and (ii) thermally induced free carriers leading to scattering thereby decreasing the mobility beyond 350 °C [77,179]. In short, the value of R_S is better for post annealing the film within 350 °C and for a duration of 30 minutes.

3.4.4. Raman Analysis

The modes of vibration of the ATO5 thin film has been investigated by Raman spectroscopic technique with a 532 nm laser as an excitation source. Figure 3.16 is the Raman spectra of the optimized ATO5 thin film. It can be clearly seen that the peaks of ATO5 film at 479, 634, and 778 cm^{-1}, are due to the Raman active vibration modes of "E_g, A_{1g}, and B_{2g}" respectively, which are the characteristic peaks of SnO_2 system [85]. The "A1g and B_{2g}" modes vibrate in the plane perpendicular to the c-axis while the "Eg" mode vibrates in the direction of the c-axis. The "B_{1g}" mode consists of a rotation of the oxygen atoms around the c-axis, with all six oxygen atoms of the octahedral participating in the vibration [88].

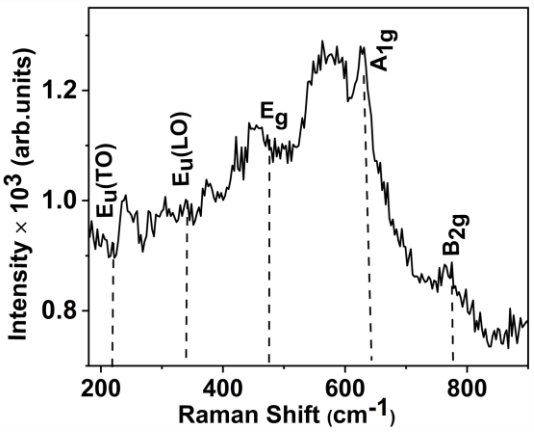

Fig. 3.16. Raman spectra of the large area deposited ATO5 thin film showing various modes of vibration from its surface.

The doubly degenerate Eu modes "Eu (TO) and Eu (LO)" of Sn and O atoms vibrate on the plane perpendicular to the c-axis. The broad Raman peaks clearly indicate that the as-deposited film to possess more defect structure in the film. The native oxygen vacancies and grain size and their distributions may be a reason for the appearance of broadened peaks in the Raman spectra.

3.4.5. Surface work function by Kelvin Probe

The surface work function of transparent conducting electrodes is an essential feature for employing the electrodes for various device applications. In semiconductors, the band gap can be engineered with respect to the vacuum level by altering the donor and/or defect level concentration yielding variation in the work function [180]. The work function (ϕ) of a semiconductor is dependent on the Fermi level position with respect to vacuum level ($\phi = E_{vac} - E_F$) [181]. The work function of the large area deposited ATO5 film is estimated from the Contact Potential Difference (CPD) between surface of the film and a reference stainless steel electrode tip. The work function of the sample was estimated using the following equation [81],

$$\Phi_{film} = \Phi_{tip} - qV_{CPD} \qquad (3.14)$$

Where ϕ_{film} is the work function of the film, ϕ_{tip} is the work function of the stainless-steel tip (4.83 eV), q is the electric charge and V_{CPD} is the averaged-out contact potential difference value. The work function of undoped SnO_2 sample was reported to have values in the range of 4.4 eV to 5.7 eV [182].

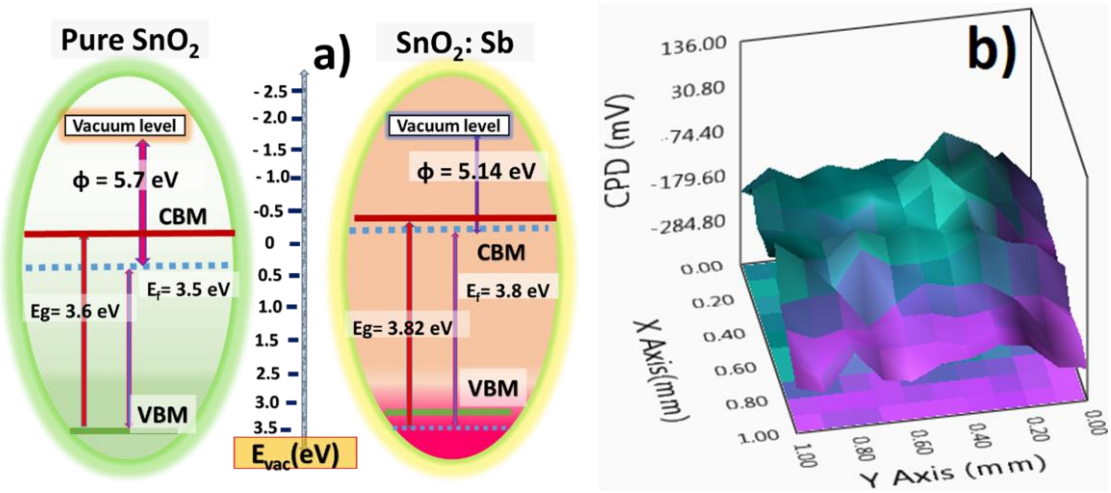

Fig. 3.17. The schematics of energy level diagram of undoped SnO_2 and ATO5 thin film (a). The variation of CPD of ATO5 film scanned over an area of 1×1 mm^2 (b).

The work function of SnO_2 could be tuned with effective dopants such as Sb, F etc. In the case of Sb doped SnO_2, the values were reported to be in the range 4.1 eV to 5.6 eV [182]. Upon doping with appropriate donor element, SnO_2 becomes a degenerate semiconductor thereby reducing the work function and enhancing electrical conductivity. The surface work function of ATO5 in comparison with undoped SnO_2 is illustrated with appropriate energy level diagram in Fig 3.17(a). The ATO film is found to have a surface work function value of 5.14 eV [167]. This value is within the range of values reported for doped degenerate SnO_2 thin films. The surface work function of ATO being less than undoped SnO_2 implies that Sb doping has lifted the degeneracy, leading to enhanced conductivity. Figure 3.17(b) displays the contact potential difference of the ATO5 film's surface scanned over an area of 1x1 mm^2. It is observed that the CPD measured over the region is not very uniform. The surface work function of a degenerate semiconductor is also sensitive to factors like surface roughness, preferred orientation, and oxygen stoichiometry of the thin film samples [77]. The variation of surface work function of SnO_2 based TCO is also reported to be dependent on oxygen stoichiometry [72]. The variations in spray dynamics has influenced the electrical properties as observed in the sheet resistance measurements. These variations lead to surface heterogeneity which eventually affect the surface work function of the large area spray deposited ATO5 thin film also. Hence, this variation of CPD is attributed to the rough granular surface of the film resultant from the inherent limitation of the spray methodology due to variations in spray dynamics of the aerosol.

3.5. Conclusion

In summary, antimony (Sb) doped SnO_2 thin films have been deposited at different substrate temperatures by a cost-effective spray pyrolysis method. The structural and surface properties of the film are influenced by substrate temperature. The XRD analysis revealed that the ATO films are textured along the (200) plane. It is also noticed that the surface topography (AFM) of the films gradually changed from particulate to needle-like shape as deposition temperature increases. The film deposited at 450 °C (ATO5) possesses relatively maximum optical transmittance of 89 % with a wide band gap of 3.81 eV than all other films. Furthermore, it shows good electrical properties such as higher carrier concentration of 3.12×10^{20} cm^{-3} with high mobility of 25.1 cm^2/Vs, low sheet resistance of 24.9 Ω/□ with low resistivity value of 7.89×10^{-4} Ω cm, and figure of merit value of 1.25×10^{-2} (Ω^{-1}). Finally, the optimized ATO5 thin film deposition parameters were chosen for large area (10×10 cm^2) depsotion. The variation of the sheet resistance of a large area deposited film is estimated across every 1×1 cm^2 surface

area. The obtianed results show that the center of the film possessess uniform, low sheet resistance than the edges of the film. The stability study of sheet resistance at different tempearture indicated maximum stability achieved at 350 °C for about 30 minutes. The estimated surface work function of ATO5 film (5.14 eV) clearly indicates the suitability of ATO5 as an TCE.

It is also identified that the ATO has issues like grey tinge which is also a reason for lower optical transmittance. The ATO film's grey tinge could be overcome by co-doping with suitable element along with Sb into the SnO_2 lattice. Hence, the obtained results of ATO film indicate the suitability to be used as an indium-free alternative TCE for optoelectronic applications.

CHAPTER: 4

Enhanced Electrical and Optical Properties of Barium and Antimony co-Doped SnO_2 Thin Films

In this chapter, the deposition of Ba and Sb co-doped SnO_2 (BATO) thin film by cost-effective spray pyrolysis method on to glass substrates are presented. This chapter mainly focus on the structural, surface, optical, and electrical properties of the BATO thin films studied as a function of Ba concentration. The antimony doped SnO_2 (ATO) thin film has been widely explored as an alternative TCO material for ITO/FTO, but the problem of this material is it exhibits low electrical and optical properties. Also, higher Sb doping concentration leads to problem of toxicity. This research work is intended to enhance the electrical and optical properties of ATO thin film by co-doping with alkaline earth metal like Ba, thereby reducing the Sb doping concentration. Finally, the optimized best deposition parameters have been selected for a large area (10×10 cm^2) coating of BATO and its suitability is tested in DSSC device as an alternative to FTO electrode.

4.1. Introduction

The antimony (Sb) doped tin oxide (ATO) thin film has been identified as a promising alternative TCO material due to its good electrical and optical properties, and is also abundant in nature [89,183]. Recently, lowest resistivity values of 4.0×10^{-3} Ω cm and 3.4×10^{-3} Ω cm were reported by Hyeon Seob So et al., and Min-Ying Tsai et al., respectively for ATO thin films [184,185]. ATO film has not yet been commercialized due to its stability issue and low optical and electrical properties than ITO/FTO. However, further enhancement in the electrical and optical properties were reported by few researchers using co-deposition method [186,187]. The simultaneous doping effects of Ba and Sb into the SnO_2 system is investigated in this chapter. The 'Sb' doping in SnO_2 yields a grey tinge to the film but improves the electrical conductivity. In order to overcome this issue without sacrificing the electrical property, the ATO films are explored by co-doping with varying 'Ba' concentration. The alkaline earth metals (Be, Mg, Ca, Sr, Ba, Ra) effectively reduce the oxygen formation energy of SnO_2 system as reported by Dong et al [188]. It was found that oxygen concentration in SnO_2 system to decrease with (Ba) doping compared to other alkaline metals. The doping of alkaline earth metal ion into SnO_2 system is found to enhance the resistance stability [189], in addition to better ionic conductivity due to the two 'S' orbital electrons in the system [190].

Finally, the optimal 5 wt% Sb and 2 wt% Ba concentration were used for a large area (10×10 cm^2) coating for TCO applications. The suitability of the large area Ba and Sb co-doped SnO_2 (BATO) film was investigated with several analytical techniques. Temperature dependent sheet resistance (resistance stability) study of BATO thin film was also performed. The surface work function of BATO film analyzed using Kelvin probe measurement. Finally, BATO thin film electrode suitability was tested in a DSSC device. These results are discussed in detail in the following sections.

Table 4.1. Spray deposition parameters of Ba and Sb co-doped SnO_2 thin films

Parameters	Optimization details of BATO thin films
Source materials	Host: $SnCl_2$ $2H_2O$, Donor: $SbCl_3$•$5H_2O$ and $BaCl_2.2H_2O$, Solvent: ethylene glycol, distilled water, and 2 ml of HCl
Host: Donor (concentration)	94 wt% of Sn: 5 wt% of Sb: 0, 2, 4,6 wt% of Ba co-doped in 'Sn' site (0.2 M concentration)
Spray solution quantity	150 ml
Substrate	Glass substrate (7.5×2.5 cm^2)
Substrate temperature	400 °C
Substrate to nozzle distance	40 cm
Spray duration ON: OFF	0.5 s: 30 s
Air pressure	46 kg/cm^2
Total number of sprays	420

4.2. Experimental Section

4.2.1. Deposition of BATO thin films

The undoped SnO_2, 'Sb' 5 wt% doped SnO_2 and 'Ba' 2, 4, and 6 wt% with a fixed 5 wt% of 'Sb' co-doped SnO_2 thin films were deposited by spray pyrolysis method onto ultrasonically cleaned and high energy plasma treated glass substrates (7.5×2.5 cm^2) maintained at 400 ˚C. The precursor solution was prepared using a mixture of ethylene glycol (130 ml), distilled water (20 ml), HCl stabilizer (2 ml) for 0.2 M with the metal salts, $SnCl_2.2H_2O$, $SbCl_3.5H_2O$, and $BaCl_2.2H_2O$. When the aerosol was sprayed, the substrate temperature is reduced significantly and therefore, intermittent spray for a duration of 0.5 s was performed with a time interval of 30 s to regain the actual substrate temperature of 400 °C in order to decompose the solutes completely. The other crucial deposition parameters are given in table

4.1. The undoped SnO_2 film, 'Sb' 5 wt% doped SnO_2 film and 'Ba' 2, 4, and 6 wt% with fixed 5 wt% of 'Sb' co-doped SnO_2 thin films are hereafter denoted as TO, ATO, BATO2, BATO4, and BATO6 respectively.

4.3. Results and Discussion

4.3.1. Structural properties

The XRD pattern in Fig. 4.1(a) shows the polycrystalline nature of the undoped SnO_2, 'Sb' (5wt %) and 'Ba' (2, 4, and 6 wt%) co-doped SnO_2 thin films. The diffraction peaks were indexed to the tetragonal crystal structure with space group P42/mnm [191] and are matched with the standard JCPDS # 41-1445 [111]. It is also identified that some of the peak position of SnO_2 and SnO system has the same 2θ values. For example, the (210) plane of SnO_2 and (101) plane of SnO are centered at the same 2θ value of 42°, indicating that a fraction of SnO phase may also be present in the system [191]. More importantly, maximum intensity peak position dominantly matched with SnO_2 phase than any other possible secondary phases. The crystal lattice parameters 'a' and 'c' of the tetragonal phase were determined using the following relation [192],

$$\frac{1}{d^2} = \left(\frac{h^2}{a^2} + \frac{k^2}{a^2}\right) + \left(\frac{l^2}{c^2}\right) \qquad (4.1)$$

Where d is the inter-planar distance and (hkl) are the miller indices. The estimated lattice constants 'a' and 'c' are given in Table 4.2. The estimated lattice constants matched well with the reported values [191]. A small variation of c/a ratio upon doping may be due to co-doping effect. The ionic size of Sb, 0.64 Å is lower than 'Sn' of 0.69 Å, and it can be easily substituted into the 'Sn' lattice site. However, in the case of 'Ba', the ionic size (1.35 Å) is much higher than 'Sn', hence it has to occupy the interstitial site of the SnO_2 lattice. At higher 'Ba' concentration, it may lead to more defect formation in the films [21]. The increasing defect level may affect the structural properties of the film. This is also reflected as a slight peak shift in the (110) plane position as seen in the XRD pattern (Fig. 4.1b). In order to estimate the variation of average crystallite size with respect to Ba concentration it has been calculated using Scherrer formula [193–195]. The estimated values of average crystallite size are given in Table 4.2. It is also reported that the Sb-doped SnO_2 has a lower grain size due to low ionic radii of Sb (0.64 Å) substituted into Sn (0.69 Å) site [188].

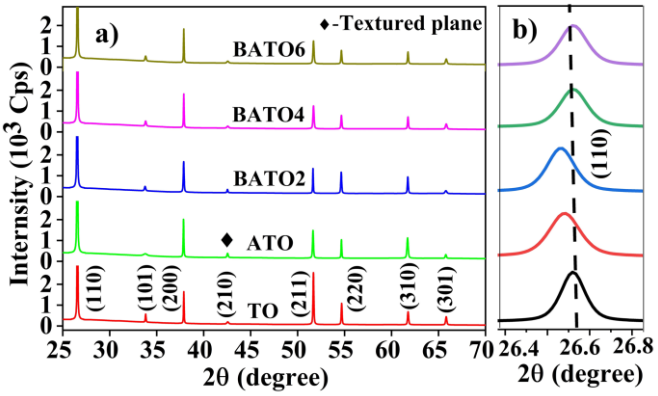

Fig. 4.1. The XRD patterns BATO films, and the expanded view of (110) plane indicates the peak shift as a function of Ba doping.

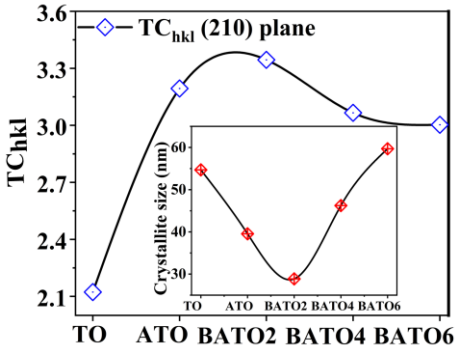

Fig. 4.2. Texture coefficient along (210) plane, and inset is the average crystallite size of the films.

Simultaneous co-doping of Ba into Sb-doped SnO_2 system may create more defects. The 2 wt% Ba doping concentration was found to have the lowest average crystallite size of 28.8 nm implying that Ba doping contributes to low grain growth. When the doping concentration is greater than 2 wt%, the grain size increased due to defect induced formation of stress, enhancing the grain growth shifting the peak position to higher values (Inset of Fig. 4.2). This shift towards the higher angle may be due to the stress induced by the 'Ba' occupying the interstitial position. The TC_{hkl} was estimated using equation 3.2. All the deposited films have preferred orientation along the (210) plane direction as illustrated in Fig. 4.2. It is identified that the texture coefficient value increases up to 2 wt% Ba dopant indicating increase in preferred orientation. For higher Ba dopant concentration, the texture co-efficient value slightly decreased.

Table 4.2. Structural properties of undoped SnO_2, Sb doped and Ba-Sb co-doped SnO_2 films.

Parameters	TO	ATO	BATO2	BATO4	BATO6
L (nm)	54.6 ± 1.09	39.5 ± 0.79	28.8 ± 0.57	46.2 ± 0.92	59.6 ± 9.19
a (Å)	4.742	4.745	4.745	4.747	4.748
c (Å)	3.186	3.186	3.186	3.188	3.188
c/a	0.6719	0.6710	0.6714	0.6715	0.6714
TC_{hkl}	2.122	3.153	3.344	3.066	3.003
t (nm)	342 ± 17.1	334 ± 16.7	258 ± 12.9	166 ± 8.30	286 ± 14.3
R_{gh} (nm)	18	11	8	13	16

The thickness of the BATO thin films was estimated using stylus profilometer. The large variation of the thickness (t) and roughness (R_{gh}) occurred during the film formation due to inherent deviation in the spray dynamics. The structural, surface, optical, and electrical properties of the films are influenced by the film thickness and surface roughness as given in Table 4.2. It could be expected that roughness or disorder in the film is high especially in spray pyrolysis method leading to more effective scattering mechanism in it [196].

4.3.2. X- ray photoelectron spectroscopy

The BATO thin films binding energy and oxidation states are investigated by XPS analysis. The XPS survey spectrum of TO, BATO2, and BATO4 thin films are scanned over a wide energy range (0-1200 eV) as shown in Fig. 4.3(a), indicate presence of Sn, Sb, Ba, O, and traces of C elements [197]. The presence of the C1s peak at 285.5 eV correspond to traces of contamination upon exposure to air before the XPS measurements. In addition, the SnMN1 peak around 976.08 eV is due to X-ray induced Auger emission with Sn3p, Sn3d, and Sn 4d core level electronic transitions indicated in Fig. 4.3(a) [197]. The XPS spectra of $Sn3d_{5/2}$ oxidization state binding energy corresponding to TO, BATO2, BATO4 films are centered around 486.7, 486.8, 486.5 eV respectively (Fig. 4.3b). The $Sn3d_{3/2}$ oxidation state binding energy was observed around 495.2, 495.3, 495.1 eV for TO, BATO2, BATO4 films respectively as shown in Fig. 4.3(b). The observed binding energies indicate that Sn to exist only in 4+ charge state with difference between these two binding energy states to be 8.46 eV which is in good agreement with literature report [198]. A small chemical shift observed in the $Sn3d_{5/2}$ and $Sn3d_{3/2}$ energy states with respect to Ba doping concentration is in the range of 0.07–0.24 and 0.04 –0.14 eV, respectively. This may be due to slight structural distortion in lattice due to introduction of 'Ba' at the interstitial sites. Figure 4.3(c) shows the binding energy of O1s state for TO, BATO2 and BATO4 thin films. The peaks centered at 531.0 eV, 530.7 eV and 531.9 eV indicate the oxygen to be in various oxidation states [198]. The binding energy at 530.7 eV generally indicate bonding of the oxygen with Sn atom (O-Sn-O). The higher oxygen binding energies at 531.0 and 531.9 eV is assigned to chemisorbed or adsorbed oxygen associated with hydroxyls groups. This hydroxyl group (O-H) may exist as neutral impurities in the film and may thus reduce the mobility by scattering process. The binding energy of $Sb3d_{5/2}$ and $Sb3d_{3/2}$ at 530.9, 540.7 in BATO2 film and at 531.9, 540.9 eV in BATO4 film respectively are shown in Fig. 4.3(d).

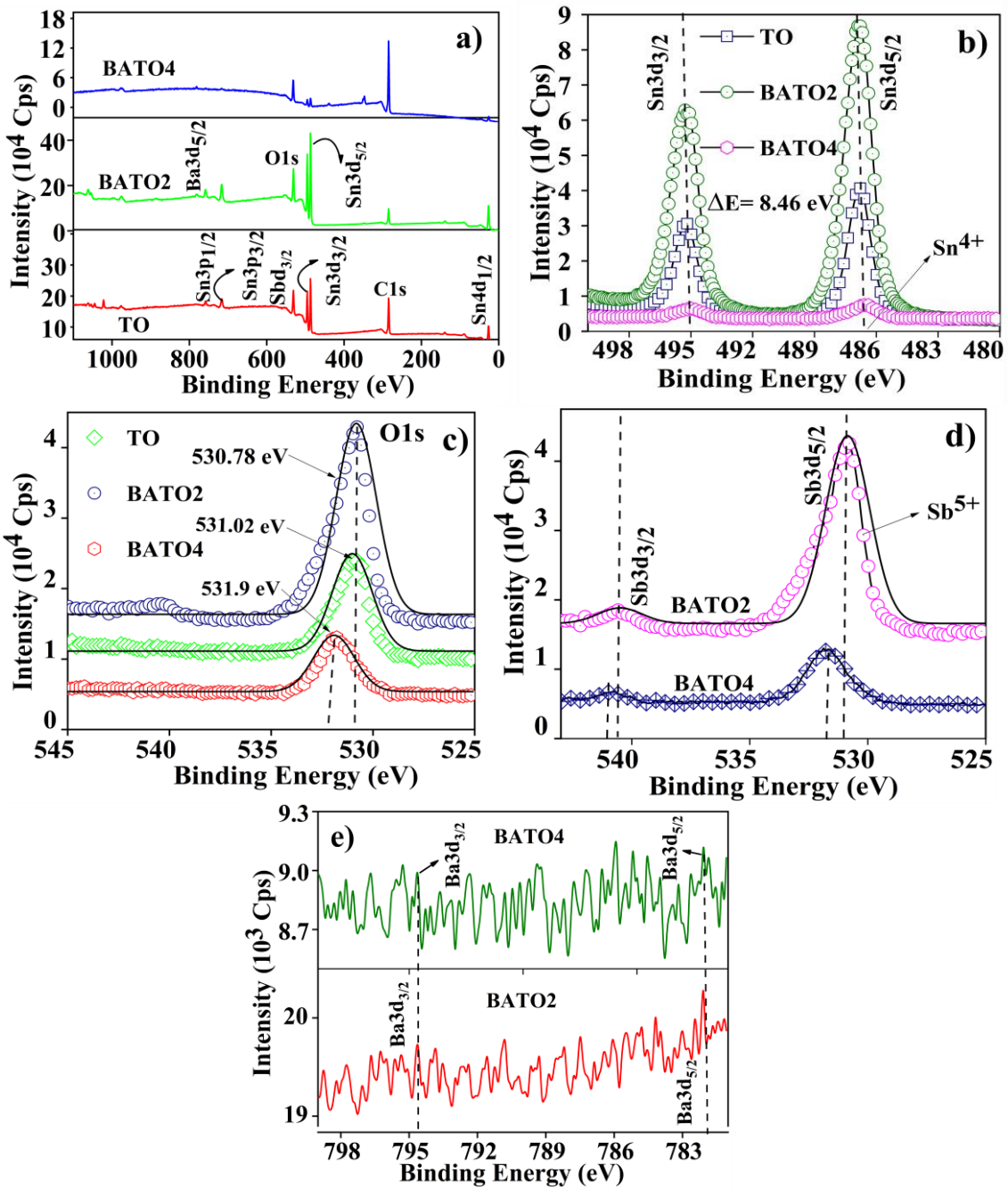

Fig. 4.3. The XPS survey spectra of undoped SnO_2, BATO2 and BATO4 films (a), Sn3d spectra (b), O1s spectra (c), Sb3d spectra (d), and Ba3d spectra of BATO2 and BATO4 films (e).

The $Sb3d_{5/2}$ peak and O1s peak overlap each other, due to similar binding energy [196]. The peak observed at 531.98 eV is the binding energy of the $Sb3d_{3/2}$ oxidation state clearly indicating 'Sb' to be in 5+ charge state. It is identified from Fig. 4.3(d) that the peak shift in the BATO4 film is due to slight variation of dopant concentration and oxygen vacancies.

The presence of oxygen vacancy can improve the electrical conductivity [199]. The Ba binding energies centered around 782.08 and 794.68 eV are assigned to $Ba3d_{5/2}$ and $Ba3d_{3/2}$ states respectively (Fig. 4.3e) [200]. These binding energies indicate that Ba^{2+} ions are incorporated into the Sn^{4+} ion lattice sites with induced lattice defects in the film playing crucial role on the structural, surface, optical, and electrical properties of the film.

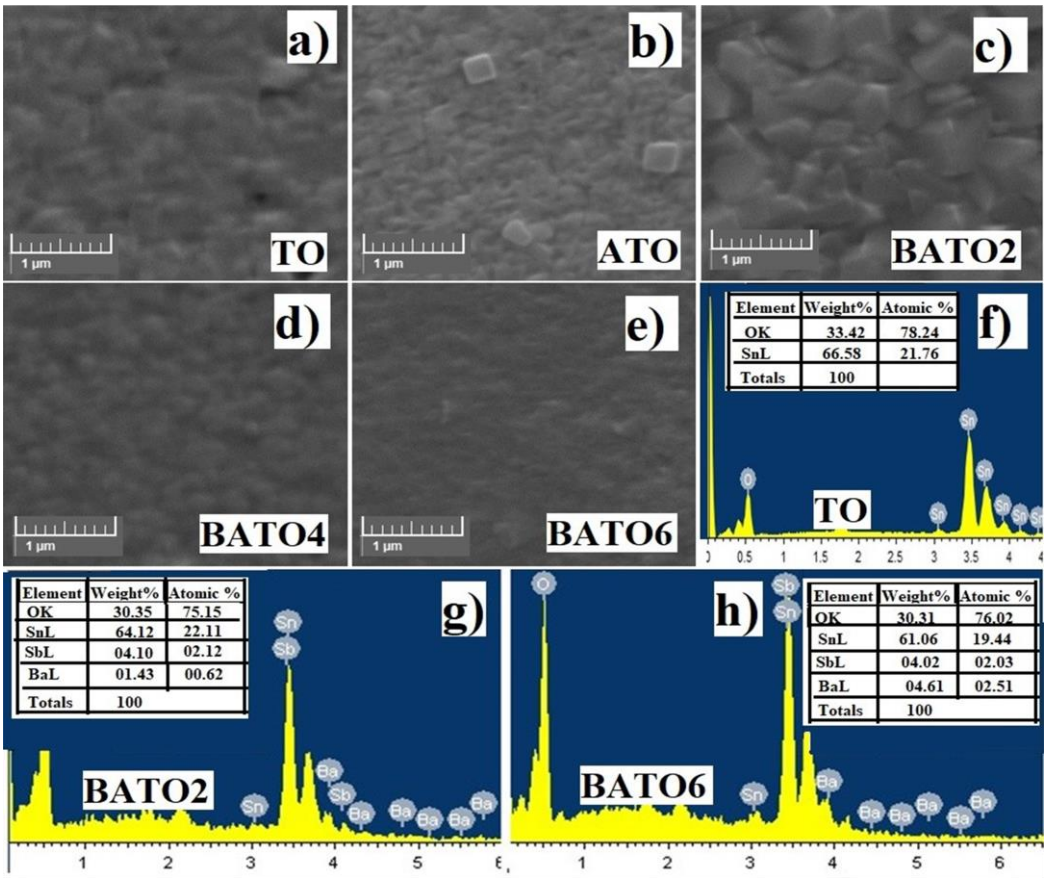

Fig. 4.4. The SEM images as a function of Ba concentration (a - e) and EDS images (f - h) of TO, ATO, and BATO thin films.

4.3.3. Surface morphology and composition analysis

The surface morphology and elemental analysis of BATO thin films were performed by SEM-EDS measurement. Figure 4.4(a - e) show the SEM images of all the BATO thin films are possesses different size polyhedron like shape partials. These particles size increased upon doping with Ba as clearly seen in SEM image of BATO2 thin film. Similar surface morphology was also observed by several authors for donor doped SnO_2 film [36,187,196]. The progressive variation in morphology may be attributed to the variation in precursor solution concentration resulting in the change of surface feature towards polyhedron shape. From the Fig. 4. 4, it is

clearly understood that the surface morphology of BATO2 film is uniform and densely packed. However, with increasing Ba concentration, the morphology changed significantly. The SEM images showing variation with concentration may be due to cracking of varying size aerosol bubble just on the substrate and forming the oxide layer. The stoichiometric ratio of chemical constituents for selected samples corresponding to Sb, Ba, Sn and oxygen estimated from EDS are shown in Figs. 4.4(f - h). However, it should be noted that a significant change in the stoichiometric ratio as a function of Ba concentration is also observed.

4.3.4. Optical properties

The optical transmittance of thin films investigated by UV-Visible spectrometry in the wavelength range 285 nm to 800 nm is shown in Fig. 4.5. The as-deposited undoped SnO_2 thin film has a lower percentage of transmittance in the UV-vis region compared to the doped samples. The average percentage of transmittance at 550 nm are shown in the inset of Fig. 4.5. The average transmittance (T_{av}) can be calculated by the following relation [199],

$$T_{av} = \int \frac{v(\lambda)\ T(\lambda)\, d\lambda}{\int v(\lambda)\ d\lambda} \qquad (4.2)$$

Where T_{av} is the average transmittance and ν (λ) is the frequency in the standard observer for photometry [201]. The simultaneous doping of Sb and Ba could improve the transparency of the SnO_2 film for up to 2 wt% Ba dopants due to improved crystalline properties with low surface roughness of the film. The transmittance decreased for more than 2 wt% Ba dopant concentration. The increasing defect formation may absorb more visible light and also enhance the scattering process. The BATO2 film was having higher transmittance of 85 % for 550 nm, which may be due to the dense morphology as seen in Fig. 4.4 (e) leading to lesser scattering effects. The absorption coefficient can be calculated from the Lambert's relation [168],

$$\alpha = \left(\frac{1}{t}\right) \ln\left[\frac{1}{T_r}\right] \qquad (4.3)$$

Here α is the absorption coefficient, T_r is transmittance, and t is the thickness of the film. The 2p level of occupied and unoccupied states between the band edges of each spectrum provides the band gap. The band gap can be estimated by using Tauc relation (Eqn. 3.9) [165], The estimated direct band gap values (Table 4.3.) varying between 3.52 eV to 3.71 eV (Fig. 4.6 and inset) matched with the reported values [202,203] In the simultaneous doping of Ba and Sb into SnO_2 lattice site, Sb occupies the substitutional sites and enhances the free carrier concentration.

The Ba dopant occupies the interstitial sites, reducing the oxygen formation energy of SnO_2 system resulting in more oxygen vacancy induced in the samples. These enhanced free carrier concentration and oxygen vacancy shifting the Fermi level towards the conduction band implies small variation in band gap. Further increasing Ba concentration creates more defects, which may possibly affect the mobility by collision and free carrier absorption, implying the declination of the band gap due to shift in Fermi level towards valence band. The decreasing band gap at higher Ba concentration indicates Burstein-Moss effect [184]. The obtained results suggest that Ba is a very effective co-dopant along with Sb for tuning the optical band gap of SnO_2 system.

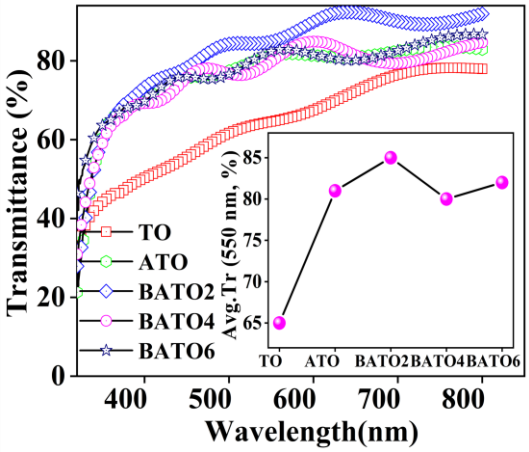

Fig. 4.5. Optical transmittance spectra of TO, ATO, and BATO films. Inset is the average transmittance spectra.

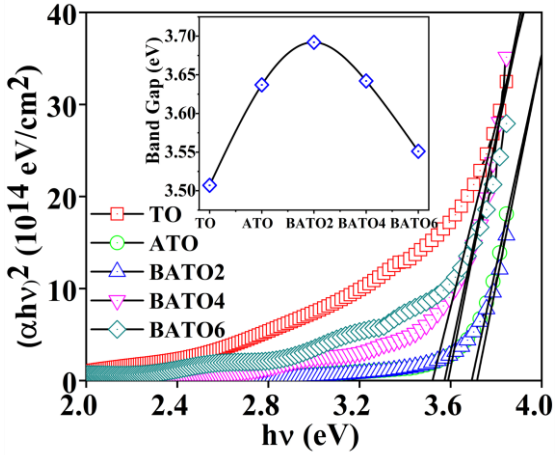

Fig. 4.6. Direct band gap estimation of TO, ATO, and BATO thin films. Inset is the variation of band gap.

4.3.5. Photoluminescence study

Figure 4.7 depicts the room temperature photoluminescence (PL) emission spectra of the thin films as a function of Ba concentration. In all the films, we observe broad ultraviolet (UV) emission located around 392 nm indicating strong electron transition from the bottom of the conduction band to the top of the valence band (Near band edge emission, NBE). The narrow emission peak centered at 541 nm is due to oxygen vacancy defects present in the samples [204]. The peak at 392 nm is composed of two additional sub-bands, one around 364 nm and the other at 448 nm. The most common defect is oxygen vacancy due to Ba dopant that occupy the interstitial site of SnO_2 lattice forming defect energy level near the conduction band play important role in the luminescence properties. These defects usually act as luminescence centers giving rise to defect level emission [204,205]. During excitation, more excitons after

absorbing the energy move to the top of the conduction band, this will lead to the shift from 392 nm to 364 nm of the UV emission after the radiative recombination. Upon increasing Ba concentration up to 2 wt%, intensity of the emission spectrum increases, beyond which it decreases due to absorption by charge carriers. The increase in defect level concentration in the SnO_2 system is due to dopants and dopant induced oxygen vacancies. The defects density N can be estimated by using the Smakula's formula [154],

$$N = 1.29\times10^{17}\frac{n}{f\left(n^2+2\right)^2}\alpha W_{1/2} \qquad (4.4)$$

Where the value of refractive index (n) is 2, the oscillator strength of optical transmission (f) is 1, and the αW1/2 is the Gaussian peak area of the PL emission peak [154]. The defect density plotted as a function of Ba concentration is shown in Fig. 4.8. It is observed that the defect density increased with Ba concentration up to BATO2 film. Further it decreases with increasing concentration of Ba dopant which may be due to the concentration quenching effect [154]. Moreover, increasing free carrier absorption, and reduced defect concentration leads to decrease of the luminescence properties. These results are in good agreement with the previous literature report [154].

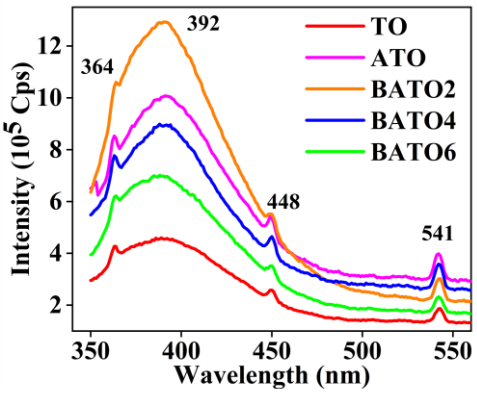

Fig. 4.7. PL emission spectra of TO, ATO, and BATO thin films.

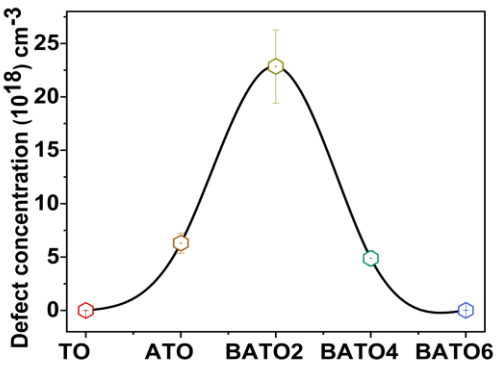

Fig. 4.8. Estimated defect density of TO, ATO, and BATO thin films.

4.3.6. Electrical transport properties

In order to understand the electrical transport properties of the spray deposited undoped SnO_2, ATO, and BATO thin films, Hall Effect measurements at 300 K were performed. The as-deposited films were found to have n-type conductivity. The estimated electrical transport parameters are given in Table 4.3. The sheet resistance (Rs), and resistivity (ρ) with Ba concentration at 300 K are shown in Fig. 4.9. The sheet resistance and resistivity are calculated

from equation 3.14 [168]. The sample BATO2 was found to have lower resistivity and lower sheet resistance about 4.41×10^{-4} Ω cm and 23.14 ohm/□ respectively. The sheet resistance of Ba and Sb co-doped films decreases due to free carriers donated by Sb^{5+} dopant and due to the Ba^{2+} ions incorporated into the interstitial sites of SnO_2 lattice creating oxygen vacancies leading to enhanced electrical properties [206]. The conductivity of Sb doped SnO_2 film was higher for the 2 wt% of Ba doping concentration due to higher concentration of oxygen vacancy defects. Further increasing Ba doping level caused free carrier collision in the system, leading to decrease in free carrier mobility. The incorporation of Sb and Ba into the Sn lattice interstitial sites improves the free carrier concentration by creating oxygen vacancies. These enhanced free charge carrier concentration and oxygen vacancy lead to better electrical properties [59,90]. Figure 4.10 shows variation of carrier concentration and mobility of Ba and Sb co-doped SnO_2 films. The sample BATO2 was found to have higher carrier concentration and higher mobility of 47.30×10^{20} cm^{-3} and 22.2 cm^2/Vs respectively. However, the resistivity of the optimized BATO films were comparably higher than the previous reports [185,207].

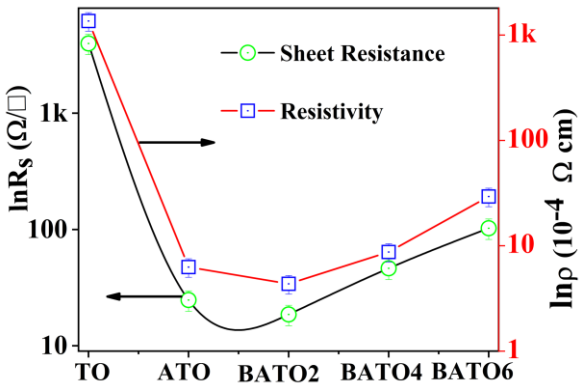

Fig 4.9. Variation of sheet resistance and resistivity of TO, ATO, and BATO films.

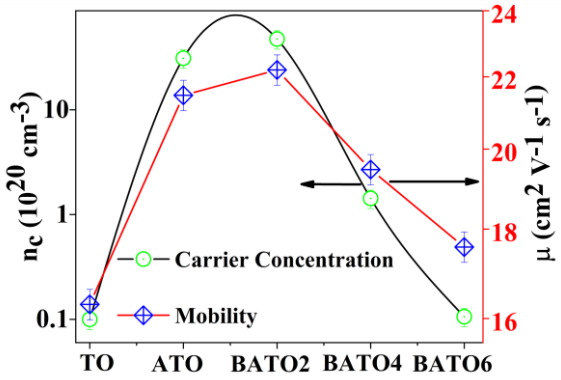

Fig 4.10. The carrier concentration and mobility of TO, ATO, and BATO films.

4.3.7. Figure of merit

Figure of merit (FoM) is an essential parameter to discuss the suitability of any TCO thin film for various optoelectronic device applications. In order to compare the performance of various transparent conductors the most widely used FoM is the Haacke relation as given in equation 3.18 [208]. For an ideal TCO, the FoM should be as high as possible, but depending on the type of application and requirement, either of these two parameters defining FoM has to be compromised [201]. Though maximum transparency and low sheet resistance are desired

for a TCO in general, achievement of both of these contradicting properties in a single host material is very difficult. The calculated value of the FoM as a function of Ba concentration is given in Table 4.3. This indicates that the BATO2 sample to have the highest figure of merit of 1.05×10^{-2} Ω^{-1}. Hence, further systematic exploration of 2 wt% of Ba and 5 wt% of Sb co-doped SnO_2 could make it a suitable alternative TCO material.

Table 4.3. Optical band gap, electrical transport parameters and figure of merit of TO, ATO, and BATO films.

Parameters	TO	ATO	BATO2	BATO4	BATO6
E_g (eV)	3.52	3.69	3.71	3.58	3.57
n_c (cm^{-3})	1.01×10^{19}	31.1×10^{20}	47.1×10^{20}	1.42×10^{20}	1.06×10^{19}
μ (cm^2/Vs)	16.30	21.47	22.20	19.47	17.58
ρ (Ω cm)	4.11×10^{-2}	6.28×10^{-4}	4.41×10^{-4}	8.72×10^{-4}	2.93×10^{-3}
R_s ($\Omega/\square$)	4151	26.99	23.14	46.41	102.6
FoM (Ω^{-1})	3.42×10^{-6}	4.92×10^{-3}	1.05×10^{-2}	2.31×10^{-3}	1.33×10^{-3}

4.4. Large area (10×10 cm^2) coating of optimized BATO2 thin film

4.4.1. Optical and electrical properties of large area deposited BATO2 film

The BATO2 thin film deposition conditions are chosen for large-area (10×10 cm^2) coating for use as a TCO electrode in dye-sensitized solar cell (DSSC) application. The spray deposition parameters of large area coated BATO2 film is given in Table 4.4 The large-area deposited BATO2 thin film is characterized for potential application. Importantly, the UV-Vis transmittance spectra of the film showed average transmittance of 86 % at 550 nm. The BATO2 film was found to exhibit n-type electrical conductivity with a resistivity value of 4.61×10^{-4} Ω cm, mobility value of 33.2 $cm^2/V\cdot s$, and carrier concentration of 4.117×10^{21} cm^{-3}. The obtained values were better than undoped SnO_2 film which was reported to have resistivity value of 6.78×10^{-2} Ω cm and carrier concentration of 1.70×10^{18} cm^{-3} [172]. The large-area (10×10 cm^2) BATO2 film showed slightly lower optical and electrical properties compared to small area (7.5×2.5 cm^2) BATO2 film due to increases in film thickness with increasing number of sprays.

Table 4.4. Spray deposition parameters of large area deposited BATO2 thin film.

Parameters	Deposition details of large area BATO2 thin film
Source materials	Host: $SnCl_2$ $2H_2O$, Donor: $SbCl_3$•$5H_2O$ and $BaCl_2.2H_2O$, Solvent: ethylene glycol, distilled water, and 2 ml of HCl
Host: Donor (concentration)	93 wt% of Sn: 5 wt% of Sb: 2 wt% of Ba co-doped in 'Sn' site (0.2 M concentration)
Spray solution quantity	200 ml
Substrate	Glass substrate (10×10 cm^2)
Substrate temperature	400 °C
Substrate to nozzle distance	40 cm
Spray duration ON: OFF	0.5 s: 30 s
Air pressure	46 kg/cm^2
Total number of sprays	500

4.4.2. Surface topology of large area deposited BATO2 thin film

Figure 4.11(a) and (b) are the 2D, and 3D AFM images of large-area (10×10 cm^2) deposited BATO2 film. The 2D AFM image clearly indicates an aggregate of particles indicating dense film formation. The 3D AFM image shows needle like shape implying significant surface roughness. The surface roughness (Fig. 4.11b) of the film is higher than that of ATO film [157] which may be due to the Ba co-dopant induced surface defects during film formation. However, large area deposited BATO2 film exhibits dense film formation.

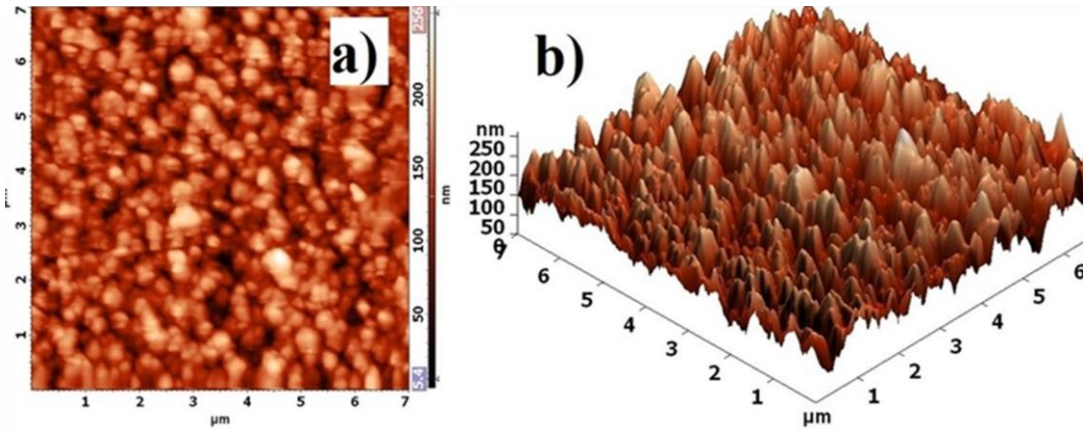

Fig. 4.11. The 2D (a) and 3D surface topology of the large area deposited BATO2 film (b).

The uniform, dense surface area provides better performance of optical and electrical properties due to the low defect scattering process. The dense film formation of the optimized BATO2 thin film may lead to a better performance when employed in device.

4.4.3. Sheet resistance – Variation across the surface

In order to investigate the variation of sheet resistance in large area (10×10 cm^2) spray deposited BATO2 thin film, sheet resistance was measured at every 1×1 cm^2 area by linear four probe method. The sheet resistance of BATO2 film was estimated using equation 3.14 [100]. The photograph of the large area deposited BATO2 film is shown in Fig. 4.12(a). The measured variation of sheet resistance across the surface area of the film is depicted in Fig. 4.12(b) as an 2D contour plot. Color representation for range of sheet resistance is given in the contour map. It could be clearly identified that the sheet resistance does not prevail uniform over the entire area of the film. The R_S was minimum at the center of the substrate and increased gradually outward with higher values at the periphery. This is mainly due to the inherent variation in spray dynamics. The variation in the flux of the created cone of aerosol reaching the hot surface of the substrate gets modified with respect to lateral distance leading to a pressure gradient. It is difficult to achieve a highly uniform large-area coating using a single nozzle by chemical spray pyrolysis method. This variation of Rs across the surface influences the mobility of the free carriers to a greater extent. For example, Haoran Zheng et al reported the surface grain boundary scattering influencing the free carrier mobility of Sb-doped SnO_2 film [209].

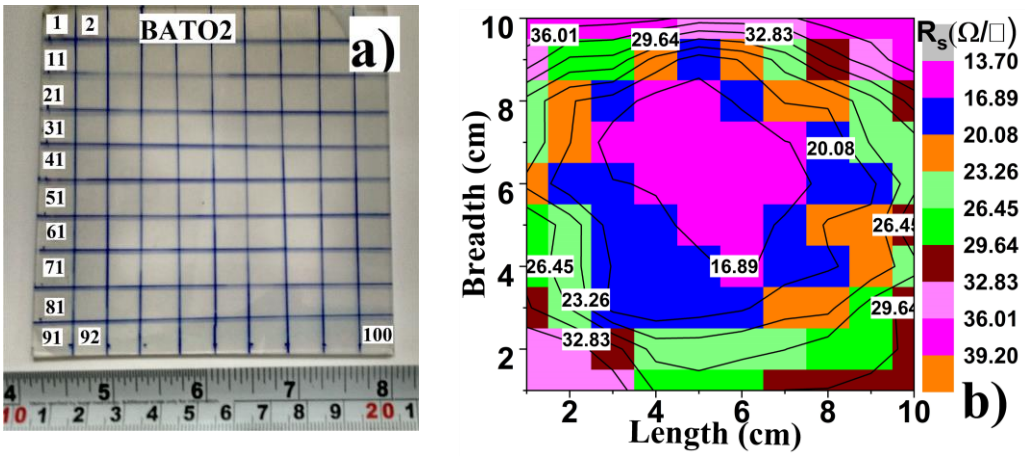

Fig. 4.12. Photograph of large area deposited BATO2 thin film (a), 2D image of surface variable sheet resistance contour map (b).

The grain boundary scattering does influence the mobility of film than the resistivity of the film [77]. Figure 4.12(b) clearly indicates the center of the film having low sheet resistance (≅ 16 Ω/□). However, the film at the corners of the substrate possesses more variation in sheet resistance ranging from 26 to 36 Ω/□. The deposited BATO2 film has significant variation in sheet resistance across the surface [179]. Hence, it is to choose the low resistance part of the film for device fabrication.

4.4.4. Temperature dependent sheet resistance study

In order to use the BATO2 film for device application, the R_S should be nearly invariable when various fabrication processes are performed at higher temperatures. Hence, temperature-dependent sheet resistance was carried out to understand the variation of the sheet resistance. Annealing temperature was varied from 200 °C to 450 °C in steps of 50 °C and annealing duration was varied from 0.5 to 2 hr. in steps of 0.5 hr. It is observed that the sheet resistance decreased up-to 350 °C, and the lowest sheet resistance achieved 29.3 Ω/□ for 0.5 hr is due to the dopant effect indicating the semiconducting behavior generally ascribed to the thermally induced free carrier concentration and improved mobility as presented in Fig. 4.13. However, with increasing annealing temperature higher than 350 °C, the Rs value increased consistently [72]. In general, ionized impurity scattering is dominant at low temperature range and phonon scattering occurs significantly in the high-temperature range. The sheet resistance increasing linearly upon annealing duration, indicate more defect level contribution in the film. Overall, the value of R_S is better for annealing the film around 350 °C and for a duration between 0.5 hr. to 1 hr.

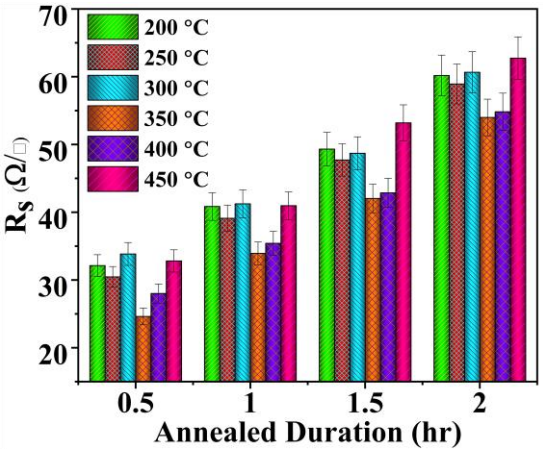

Fig. 4.13. Annealing temperature and duration dependent sheet resistance of the large area deposited BATO2 thin film.

4.4.5 Surface work function measurement by Kelvin Probe

The surface work function (ϕ) of BATO2 film was estimated by Kelvin probe (KP) measurement. The relative contact potential difference (CPD) between the sample and reference electrode tip will provide the work function of the sample [210]. A stainless-steel electrode was used as the reference electrode due to its electrical stability. The relative work function of the sample is given using equation 3.19 [180]. Figure 4.14(a) illustrates the contact potential difference of the BATO2 film scanned over an area of 1×1 mm^2. The estimated CPD values show slight variation in the scanned region. This variation in CPD may be attributed to the variation in surface features such as homogeneity, uniformity, roughness, and texture of the film [211]. The variation in ϕ value is also influenced by crystallographic plane direction, since the grains grow with some preferential orientation along a particular plane direction. The surface morphology might change the orientation of the plane which may affect the work function of the film [212]. The ϕ value strongly depends on the Fermi level position. The Fermi level position is strongly influenced by donor and defect level contribution. The undoped and Sb and Ba co-doped SnO_2 thin films Fermi level energy diagram with their respective work function is shown in Fig 4.14(b). The Fermi level of BATO film shifted towards the conduction band causing the decrease in work function compared to undoped SnO_2 film. The BATO2 thin film with lower work function can improve the free charge carrier mobility, and this can lead rise to enhanced electrical properties of the film. Undoped SnO_2 have ϕ value ranging between 4.4 eV to 5.7 eV [155]. In the case of BATO2 film, the estimated ϕ_{film} was 5.09 eV.

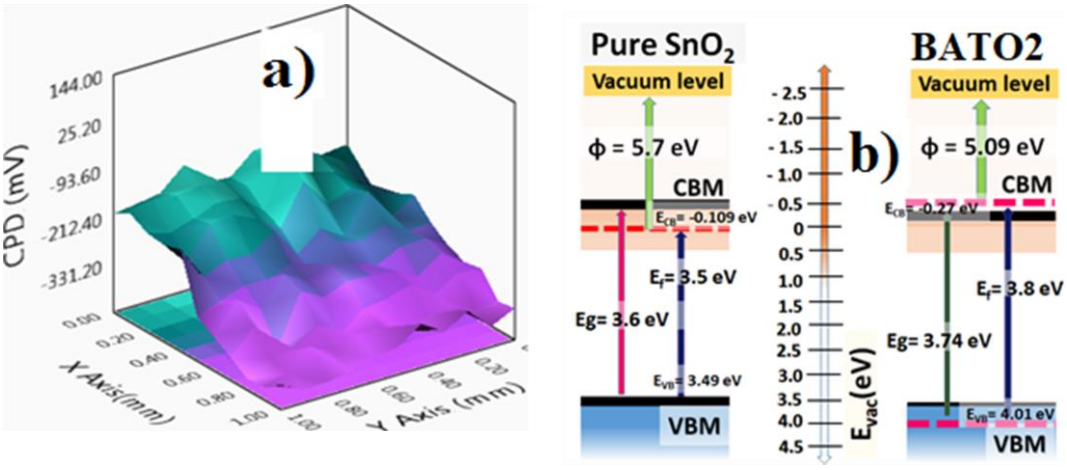

Fig. 4.14. Contact potential difference of BATO2 film scanned over an area of 1×1 mm^2 (a) and energy band diagram of pure SnO_2 and BATO2 films (b).

4.5. Solar cell fabrication and testing

A dye-sensitized solar cell (DSSC) was fabricated using BATO2 transparent conducting electrode. The efficiency of BATO2 based DSSC device was compared with commercial FTO electrode based DSSC device. The similar device structure was followed for both case (BATO2/ TiO2/N719 dye + electrolyte/ Pt/ BATO2) and (FTO/ TiO2/ N719 dye + electrolyte/ Pt/ FTO) except transparent conducting electrode layer. Also, similar coating method and optimization condition are followed except post annealing temperature of the electrode layer. For TiO_2 coated BATO2 photoanode was post annealed at 400 °C for 30 min, in case of FTO with TiO_2 coated photoanode was post annealed at 500 °C for 30 min and the same procedure followed to prepare the counter electrode. The fabricated devices were tested under AM1.5 conditions using a Newport 91160A solar simulator. The light source comprised a 150 W Xe lamp and the light intensity corresponded to AM1.5 (100 mW cm^2) calibrated with a standard Si cell (Oriel SRC1000 TC). The pictorial representation of mechanism of DSSC device with the various layers is shown in Fig. 4.15.

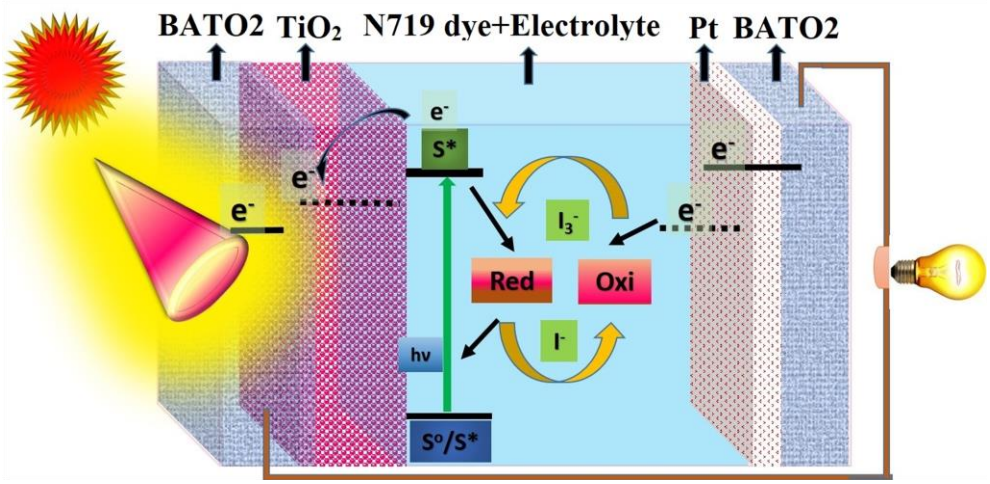

Fig. 4.15. Pictorial representation of mechanism of BATO2 electrode used in a DSSC device structure with various layers.

Though there are mechanisms that have been proposed for DSSC device working principle [213,214] but still there are several unraveled issues need to be explored to improve the device performance. The performance of DSSC device also depends on the TCO material's properties. The BATO2 thin film exhibits low sheet resistance of 17 Ω/□, resistivity of 5.05×10^{-4} Ω cm, and optical transparency around 86 % at 550 nm in the visible region. It also exhibits a maximum resistance stability up to 350 °C, indicating the applicability in solar cell devices.

The device performance can be investigated based on incident light to electric power conversion efficiency (η) is estimated by the following equation [215],

$$\eta = \frac{V_{oc} \times J_{sc} \times FF}{P_{in}} \times 100\% \quad (4.5)$$

Here V_{oc} is an open-circuit voltage (V), J_{sc} is short-circuit current density (mA cm^{-2}), FF is the fill factor, and P_{in} the incident light power [216]. The DSSC device fabricated using BATO2 electrode shows an output efficiency of 0.76 % whereas commercial FTO based DSSC showed 3.4 %. Figure 4.16(a), illustrates the J-V characteristics of BATO2 based device in comparison with FTO electrode-based device. The maximum efficiency achieved for DSSC using BATO2 was 0.76 %, yielding a J_{sc} of 2.8 mA cm^{-2}, V_{OC} of 0.77 V, and FF of 24 %. Whereas FTO electrode-based device shows maximum efficiency of 3.05 %, yielding a J_{sc} of 5.1 mA cm^{-2}, V_{OC} of 0.85 V, and FF of 68.6 %. The DSSC devices fabricated using BATO2 and commercially available FTO electrodes are shown in inset of Fig. 4.16(a). A reasonable J_{sc} value was obtained from the incident photon-to-electron conversion efficiency. However, the BATO2 electrode based DSSC device exhibited quite lower fill factor due to the charge transfer resistance between the counter electrode and electrolyte interface (R1). The sheet resistance (Rs) was also high compared to FTO electrode device. These higher resistances may be due to the higher surface roughness and thickness of BATO2 electrode compared to commercial FTO electrode. To further explore the stability and performance of BATO2 based DSSC device, the electrochemical impedance spectroscopy (EIS) measurement was performed.

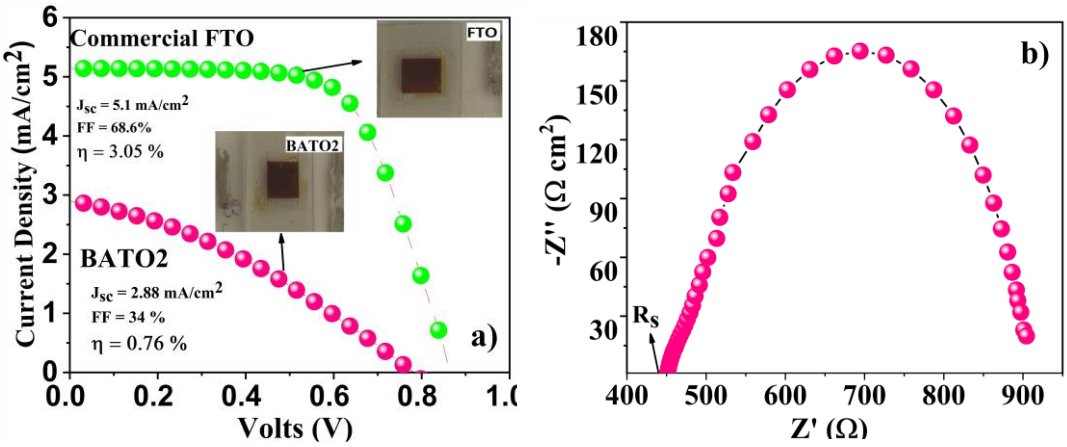

Fig. 4.16. The J-V characteristics of DSSCs fabricated using BATO2 and FTO electrodes, inset are the images of the fabricated devices (a). Nyquist plot of the DSSC device fabricated using BATO2 electrode (b).

Table 4.5. The photocurrent density-voltage (J-V) parameters of DSSCs fabricated using commercially available FTO and optimized BATO2 electrodes.

DSSC electrode	V_{oc} (mV)	J_{sc} (mAcm^{-2})	Fill factor (%)	η (%)
Reference FTO	0.85	5.1	86.6	3.05
BATO2	0.77	2.08	24	0.76

Figure 4.16(b) illustrates the Nyquist plot of DSSC device fabricated using BATO2 electrode. From the Nyquist plot the obtained semicircle in higher frequency region indicates the charge transfer resistance at the counter electrode and redox (I^--I^{3-}) interface. The low-frequency region indicate the Nernst diffusion process of the dye electrolyte and photoanode interface [217,218].

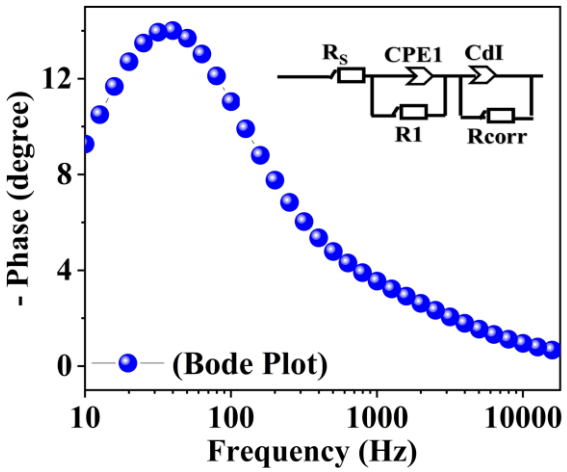

Fig. 4.17. Bode plot of DSSC device fabricated using BATO2 electrode and inset is the equivalent circuit.

The saturation value of the open circuit voltage and short circuit current depends more on free carrier regeneration and charge transport in the redox chemical reaction. The photoanode indicates the high charge transfer resistance of 422.7 Ω, and also a very high series resistance of the electrode of 452.5 Ω. This may be a reason for the lower fill factor. The bode plot provides information related to the electron lifetime and stability of the solar cell device. The Bode plot is frequency vs phase graph. The electron lifetime was estimated using the maximum cut of frequency (maximum phase angle) of the bode plot. Figure 4.17 clearly indicate the maximum cut off frequency at 39.9 Hz, from which the estimated electron lifetime was around 3.99 ms, indicating the lower probability of the exciton recombination in BATO2 electrode based DSSC device [219]. The lower charge transfer resistance indicates the electron injection time from

dye molecule to TiO_2 interface is higher than that of the free carrier generation at the dye and electrolyte interface. The interfacial layer equivalent circuit is illustrated in inset of Fig. 4.17. To conclude, the performance of BATO2 electrode based DSSC device seem to be promising, and is worth exploring further in this direction.

4.6. Conclusion

In this chapter, the Ba and Sb co-doped SnO_2 thin films have been deposited by a cost-effective spray pyrolysis method. The structural, optical and temperature dependent electrical properties of the BATO thin films were studied as a function of varying Ba concentration. The XRD analysis of as-deposited thin films showed textured growth. The XPS analysis confirmed the charge states of constituent elements of BATO films with appropriate binding energy. The highest average transmittance and lowest electrical resistivity was observed in the BATO2 thin film with value around 85 % and 4.41×10^{-4} Ω cm respectively. The figure of merit value indicated that the best-combined properties of transparency and conductivity to be exhibited in the BATO2 thin film. Finally, a large area (10×10 cm^2) BATO2 thin film was also deposited and characterized by various analytical techniques. The resistance stability study clearly showed significant variation in sheet resistance values from 26 to 36 Ω/□, and a resistance stability up to 350 °C. The surface work function value of BATO2 film was estimated to be 5.09 eV from the Kelvin probe measurement. The BATO2 film electrode has also been successfully used in DSSC device. It showed a current density of 2.28 mA/cm^2 due to higher charge transfer resistance (R2) of 31.8 Ω in between the photoanode and electrolyte interface. The efficiency achieved was 0.76 %. Interestingly, the optimized results indicate that the Ba and Sb co-doped SnO_2 (BATO2) thin film is a promising alternative TCE material, which can be further explored by fine tuning various parameters.

CHAPTER: 5

Optimization of Spray Deposited Transparent Conducting Niobium-doped SnO_2 Thin Films

This chapter describes the optimization and characterization of highly transparent and conductive niobium (Nb)-doped SnO_2 (NTO) thin films deposited on glass substrate by chemical spray pyrolysis method. The first part of this chapter discusses the optimization of NTO films, and characterization of structural, surface, optical, and temperature dependent electrical properties as a function of Nb concentration. The second part describes the deposition of large area (10×10 cm^2) NTO film and its characterization. The sheet resistance stability is investigated to understand the quality of the film. The Kelvin probe measurement was also carried out to estimate the surface work function of the stabilized NTO film. The obtained results are discussed in detail in this chapter.

5.1. Introduction

The invention of newer type of transparent conducting oxide (TCO) thin films are very important for optoelectronic applications, due to the unique combinational (electrical and optical) properties without which many of the advantages in display technology and renewable energy sector would not be possible [9]. Indium Tin Oxide (ITO) is the commercially available TCO material [220]. However, it cannot be considered to be economically viable because of the concerns about the scarcity of its supply. In recent days, the developments in the display industry requires cost-effective and better performance TCO materials. The donor doped SnO_2 thin films have been widely investigated from alternative TCO point of view by various groups with different dopants for application in devices including solar cells, OLEDs, display devices, sensors and batteries [18,111,221–223]. The niobium doped tin oxide (NTO) thin film has been recently identified as one of the potential alternative TCO material due to its non-toxicity, chemical stability and resistance stability in an oxidizing environment [108]. The NTO film shows improved n-type conductivity compared to undoped SnO_2 and Nb can exist in three different charge states Nb^{3+}(0.72 Å), Nb^{4+} (0.79 Å) and Nb^{5+} (0.64 Å). The ionic radius of Nb^{5+} (0.78 Å) is nearly equal to Sn^{4+} (0.69 Å) ionic radius value and it can be easily substituted in the Sn lattice site [10,11]. The NTO films have been optimized using various methods, such as chemical spray pyrolysis, pulsed laser deposition (PLD), DC & RF sputtering methods [224,225].

In this chapter, the NTO thin films are optimized by spray pyrolysis technique and their structural, optical, and temperature dependent electrical properties are studied as a function of Nb concentration. The electrical properties of NTO thin films investigated in the temperature range 30 ˚C to 300 ˚C are reported for the first time. The optimal concentration of 1.5 wt% Nb doped SnO_2 was identified to deposit on a large area (10×10 cm^2) substrate. The properties of the large area coated thin film is also verified by various analytical studies.

5.2. Experimental Section

5.2.1. Optimization of Nb doped SnO_2 thin films

The precursor spray solution was prepared with a stoichiometric amount of 0.5 M of tin (II) chloride dehydrate ($SnCl_2.2H_2O$), and niobium (V) chloride ($NbCl_5$) salts by dissolving in a mixture 130 ml of ethylene glycol and 20 ml of propanol [IPA]. Finally, 2 ml HCl was added to make the solution transparent. All the precursor solutions were prepared according to the stoichiometric ratio as a function of Nb concentration. The glass slides (7.5×2.5 cm^2) were cleaned ultrasonically in acetone, IPA, and de-ionized water to remove traces of grease or oil adhered to the surface. Finally, the ionic charge contamination on the substrates is cleaned by ex-situ high energy plasma cleaner (model: PDC-002 Harrick plasma). All the essential deposition parameters are given in the Table. 5.1.

Table 5.1. Optimized spray deposition parameters of Nb doped SnO_2 thin films.

Parameters	Optimization details of NTO films
Source materials	Host: $SnCl_2$ $2H_2O$, Donor: $NbCl_5$, Solvent: ethylene glycol, 2 propanol, distilled water, and 2 ml of HCl
Host: Donor (concentration)	98 wt% of Sn: (0, 5, 1, 1.5, 2, and 2.5 wt%) of Nb (0.5 M concentration)
Spray solution quantity	150 ml
Substrate	Glass substrate (7.5×2.5 cm^2)
Substrate temperature	400 ℃
Substrate to nozzle distance	35 cm
Spray duration ON: OFF	0.5 s: 30 s
Air pressure	46 kg/cm^2
Total number of sprays	420

The undoped SnO_2 and Nb doped SnO_2 thin films with 0.5, 1, 1.5, 2 and 2.5 wt% Nb doping are hereafter designated as TO, NTO1, NTO2, NTO3, NTO4, and NTO5 respectively. The deposited NTO films are investigated by several analytical techniques for their structural, surface, optical, and electrical properties.

5.3. Results and Discussion

5.3.1. Structural analysis

Figure 5.1(a) is the XRD patterns of undoped and Nb-doped SnO_2 (NTO) thin films with varying Nb dopant concentration (0 to 2.5 wt%). The diffraction peaks of NTO films matched with the tetragonal crystal structure with space group P42/mnm (JCPDS No. 41–1445) [108,224]. A small shift of the (110) position value is observed as a function of Nb concentration as shown in Fig. 5.1(b). Inset of Fig. 5.2 shows the variation in the crystallite size with respect to Nb concentration. It can be identified that the average crystallite size changes from 52.4 to 65.4 nm with variation in Nb dopant concentration. The Nb ions are easily substituted at the Sn lattice site, since the ionic radius of Nb^{5+} is 0.64 Å, which is nearly matching with that 0.69 Å of Sn^{4+} ionic radius. The crystallite size decreased with increasing concentration up to 1.5 wt% (NTO3) and for further increasing of Nb concentration it slightly decreased due to structural defects (lattice mismatch, impurity defect). For higher the content of Nb doping, it induces an impurity defect or lattice defect leading to change in crystallite size. The increasing lattice defects by Nb doping affect the grain growth in lateral direction leading to peak broadening effect. The crystallite size values obtained are in good agreement with the previous report by Güven Turgut et al [225].

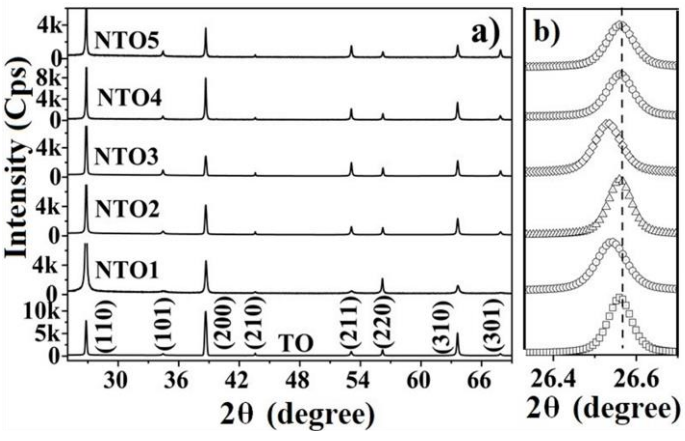

Fig. 5.1. The XRD patterns of the TO and NTO thin films (a), (110) peak shift with Nb doping concentration (b).

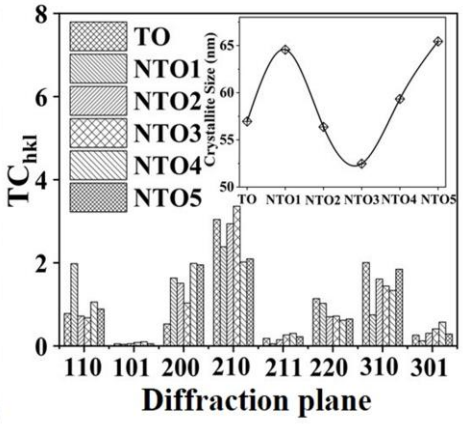

Fig. 5.2. The texture coefficient of TO and NTO films for various diffraction planes. Inset is the variation of average crystallite size.

Figure 5.2 shows the quantitative analysis of the texture coefficient (preferred orientation) estimated from the XRD patterns of the NTO films. Several of the physical properties of the film vary due to textured growth. The texture coefficient (TC_{hkl}) for each (h k l) crystallographic direction of the NTO films is estimated by using Harris method [160]. We chose eight intense diffraction peaks (110), (101), (200), (210), (211), (220) (310), and (301) for estimation of TC_{hkl} values as shown in Fig. 5.2. For a textured sample, few of the TC_{hkl} were more than value 1 while the others were equal to or less than 1 [226]. The TC_{hkl} values are listed in Table 5.2. The higher values of the TC_{hkl} indicate preferred grain growth normal to the substrate. It is identified that the higher TC_{hkl} values are along (200), (210), and (310) directions.

5.3.2. X- ray photoelectron spectroscopic study

The XPS survey spectrum of TO, NTO3 and NTO4 thin films are shown in Fig. 5.3(a) and it can be clearly seen from the survey spectra that the NTO films contain Sn, Nb, O, and traces of C peak (285.5 eV) that corresponds to surface contamination upon exposure to air before XPS measurements. The narrow scan spectra of $Sn3d_{5/2}$ and $Sn3d_{3/2}$ peaks are shown in Fig. 5.3(b), where the binding energy difference of 8.5 eV between these two binding energy states is in agreement with previous report [72]. The binding energies (485.9, 486.1, 486.0 eV) of $Sn3d_{5/2}$ state and that of $Sn3d_{3/2}$ state (494.4, 494.4, 494.4 eV) of the films show tin to exist only in the 4+ charge state [17]. The narrow scan XPS spectra of O1s peak with varying Nb concentration are shown in Fig. 5.3(c). It is clear that the spectra of O1s have the binding energy of 529.1 eV, 530.1 eV and 532.3 eV for O (I), O (II) and O (III) oxidation states respectively [223,227]. The binding energy centered around 530. 3 eV O (II) indicate metal-oxygen binding energy (O-Sn-O) [72]. The binding energy at 529.0 eV O (I) is assigned to chemisorbed oxygen associated with hydroxyl states, while 532.3 eV O (III) occurred due to the defect oxygen formation [17]. Figure 5.3(d) shows the Nb binding energies in NTO3 film located at 207.6 and 210.2 eV for Nb $3d_{5/2}$ and Nb $3d_{3/2}$ charge states, respectively. Whereas NTO4 film binding energies are located at 207.8 and 210.6 eV for Nb $3d_{5/2}$ and Nb $3d_{3/2}$ charge states, respectively [228]. The Nb^{5+} substitution into the Sn^{4+} lattice site acts as donors and creates more free electrons. However, Nb^{3+} and Nb^{4+} substitutions at the Sn^{4+} site act as acceptors which would compensate the donor levels to make the electrical conductivity poor. Therefore, the substitution of Sn^{4+} by Nb^{5+} leads to better electrical conductivity of the NTO films.

Moreover, the electrical properties are not only determined by the defect concentration influencing the mobility but optimal concentration of free carriers also plays an important role in NTO films.

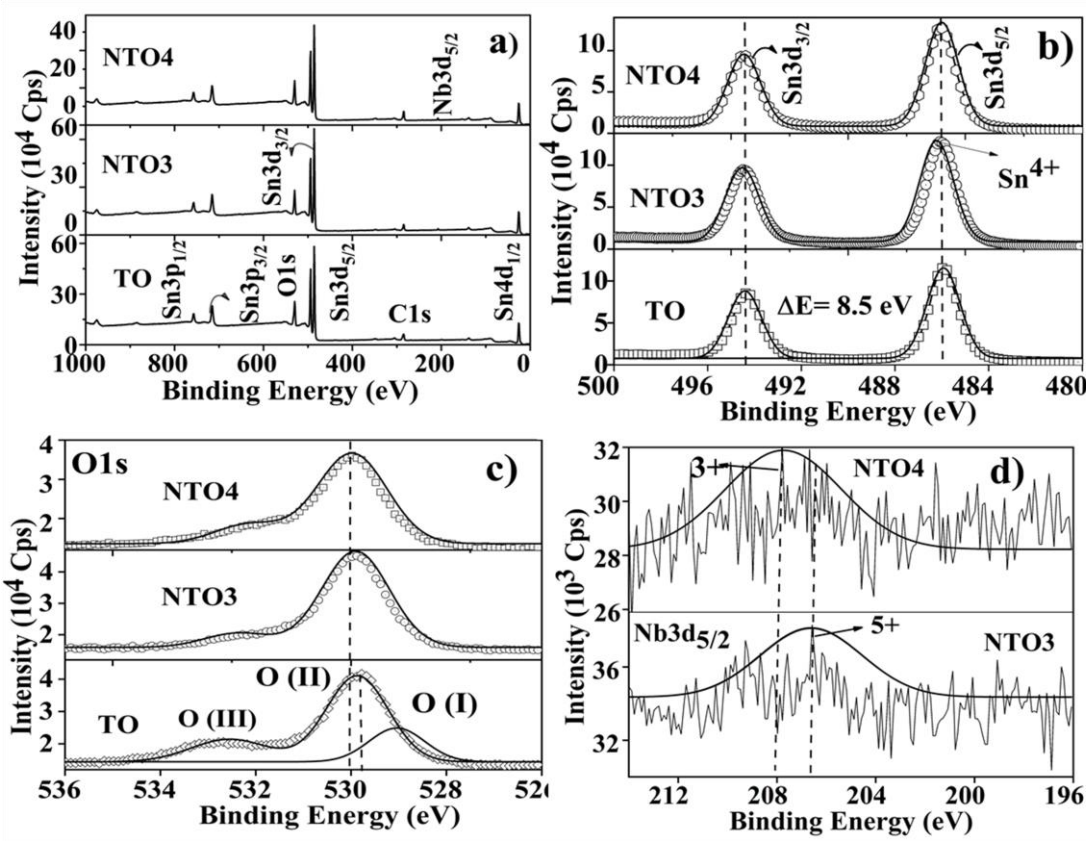

Fig. 5.3. The XPS spectra of TO, NTO3 and NTO4 films; survey spectra (a), Sn3d spectra (b), O1s spectra (c), and Nb3d spectra (d).

5.3.3. Surface morphology analysis by SEM

The surface morphology of the deposited films has been investigated by scanning electron microscopy (SEM). The surface properties of the thin films significantly changed as a function of Nb concentration. All the films exhibit uniform, homogeneous and crack free surface morphology. Figure 5.4 shows the SEM images of deposited NTO thin films. It is a clear evidence that the as-deposited thin film has a relatively uniform surface morphology in the entire region. The particle shape varied from nanoparticle (TO) to polyhedron like structure (NTO3) as a function of Nb concentration. The results are in good agreement with previous reports [18,108]. The NTO film with a Nb concentration of 1.5 wt% was found to have distinct, bigger and continuous polyhedron particulate surface morphology.

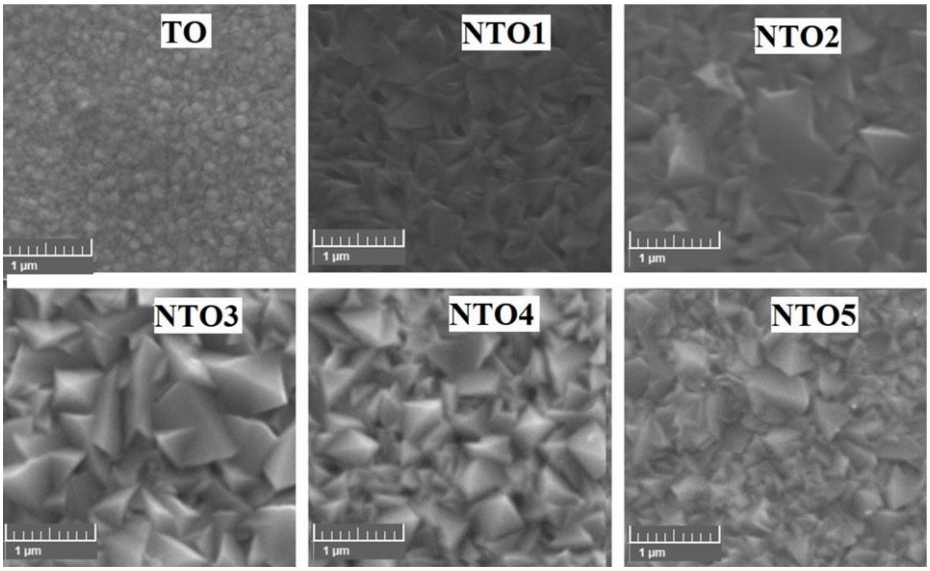

Fig. 5.4. SEM morphology of the TO and NTO thin films with varying Nb dopant concentration.

The chemical composition of the as-deposited TO and NTO thin films are investigated by energy dispersive X-ray spectroscopy (EDS) and the results are depicted in Fig. 5.5. The EDS analysis confirms the presence of Sn, Nb and O elements in the film deposited with different Nb weight percentage.

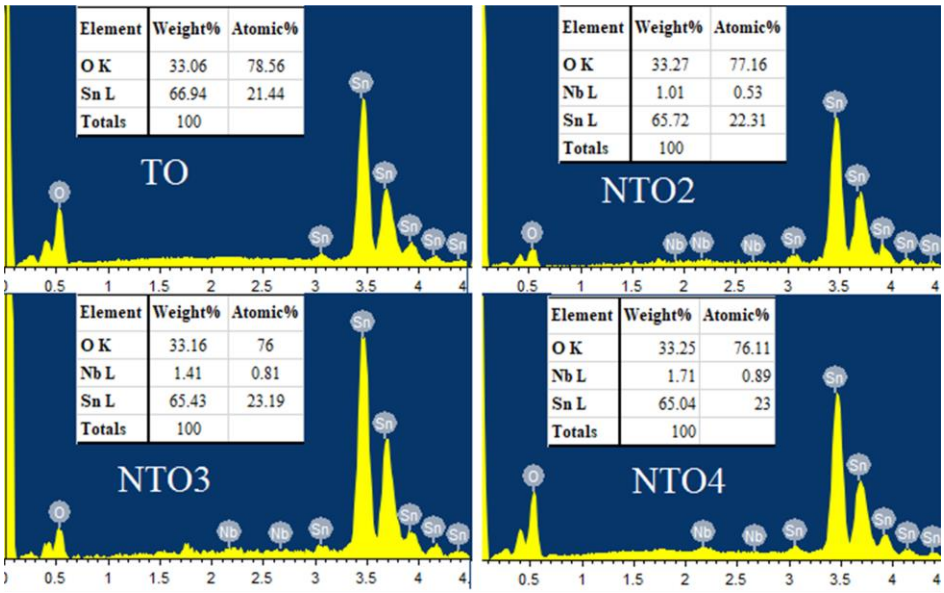

Fig. 5.5. The EDS spectra of selected TO, NTO2, NTO3 and NTO4 films.

The stoichiometry of NTO films can be changed based on dopant concentration of the films. The metal oxide based TCO films generally show a significant change in optical and electrical properties with a change in chemical composition. Thickness and roughness of the films were

measured by a profilometer and the values obtained are given in Table 5.2. More importantly, spray dynamics and spray deposition parameters such as substrate temperature, substrate to nozzle distance, solution concentration, and droplet size play crucial role during the film formation. The uniform density, smoothness and adherence of the film to the substrate generally increase with increasing film thickness and decrease with higher roughness [97].

Table 5.2. Structural, surface, and optical properties of deposited TO and NTO thin films.

Parameters	TO	NTO1	NTO2	NTO3	NTO4	NTO5
L (nm)	56.9 ± 1.13	64.5 ± 1.29	56.3 ± 1.12	52.4 ± 1.0	59.3 ± 1.18	65.4 ± 1.30
a (Å)	4.742	4.745	4.745	4.747	4.748	4.742
c (Å)	3.186	3.186	3.186	3.188	3.188	3.186
TC_{hkl}	3.09	1.92	2.94	3.36	2.02	1.51
R_{gh} (nm)	17	15	13	11	12	19
t (nm)	597 ± 29.8	521 ± 26.1	506 ± 25.3	347 ± 13.1	352 ± 18.6	584 ± 29.2
E_g (eV)	3.67	3.78	3.79	3.82	3.70	3.65
Eu (meV)	790	699	1275	1321	728	1137

5.3.4. Optical transmittance studies

Figure 5.6 illustrates the UV- visible transmittance spectra of the TO and NTO thin films. The average transmittance value increased as a function of Nb dopant concentration up to NTO3 film due to enhanced grain growth and it decreased for further increasing dopant concentration. The maximum average transmittance observed in NTO3 film is 76 % at 550 nm in the visible region. The average transmittance as a function of dopant concentration is shown in the inset of Fig. 5.6. It is also clearly identified that the enhanced transmittance in the NIR region indicates the absence of Moss-Burstein effect caused by low free carrier absorption [184]. In the near IR region, an obvious increase in transmittance is explained by Drude's model [229]. This model is generally used to study the change in transmittance and reflectance in the IR region. In brief, this model explains that the plasma frequency is proportional to the square root of the carrier concentration. The absorption of NTO2, NTO3, and NTO4 thin films was lower in the visible region, so it shows higher transmittance. However, in the case of undoped TO, NTO1 and NTO5 films show relatively increased absorption in the visible region. The change in absorption coefficient of NTO films can be calculated from Lambert's equation 4.3 [166]. The absorption coefficient is intrinsic property of a system, which is influenced by dopant effect. The band gap of the material depends on the variation of absorption coefficient. The

band gap (E_g) values of NTO thin films are estimated by using Tauc relation given in equation 3.3 [165]. Figure. 5.7 shows the direct band gap values as a function of Nb concentration and the estimated values are given in Table 5.2. The direct band gap value was varying between 3.65 to 3.81 eV. The band gap increases with increase in Nb concentration up to NTO3 film. Further increase in Nb concentration decreased the band gap value due to higher film thickness causing more absorption of light. It is reported that the increasing dopant concentration may shift the Fermi level position, which generally occurs in degenerate semiconductors [184,229].

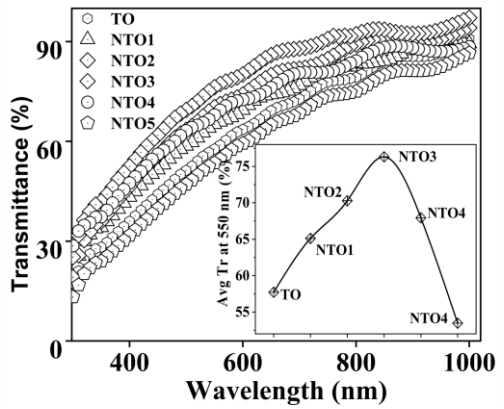

Fig. 5.6. The optical transmittance spectra of TO and NTO thin films. Inset is the average transmittance of the thin films.

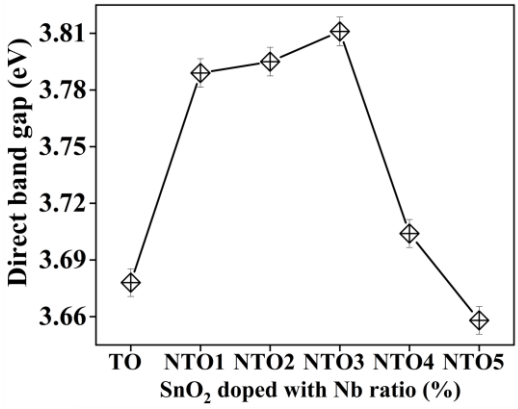

Fig. 5.7. Variation of band gap values of TO and NTO thin films with Nb concentration.

Figure 5.8 shows energy level diagram of degenerate SnO_2 semiconductor, indicating possible changes in optical and electrical properties modified by the degeneracy energy levels of samples due to Fermi level shifting [72]. The surface defect also plays crucial role for Fermi level shift, affecting the band-to-band absorption, Urbach tail absorption, mid-gap defect state absorption and free carrier absorption are due to dopant effect. The Urbach tail absorption influences the band gap properties. It is often referred to as the tail width of localized states near the band edge of the spectrum, since their influence cannot be neglected in the estimation of the band gap [230]. A significant change in Urbach energy has been observed as a function of Nb concentration as illustrated in Fig. 5.8. The change in Urbach energy of NTO films was calculated using equation 3.6 [231]. The Urbach energy (E_u) values of NTO films are identified from the slope of ln (α) vs. photon energy (Fig. 5.9). It is clearly evident that the E_u is related to the dopant and structural defects in the films [232]. The estimated E_u are given in Table 5.2. The lowest E_u values of 699 meV was obtained for NTO1 film. The NTO3 thin film has the highest E_u value of 1321 meV which may be caused by increased oxygen vacancy defects.

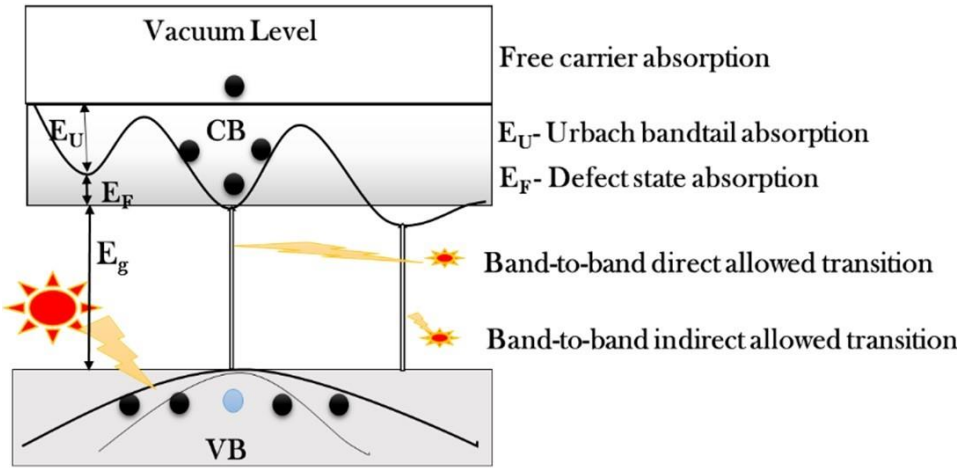

Fig. 5.8. The energy level diagram of degenerate SnO_2 semiconductor indicating various transition levels.

5.3.5. Photoluminescence properties of NTO thin films

Figure 5.10 shows the photoluminescence (PL) emission spectra of the TO and NTO films as a function of Nb concentration. The luminescence intensity increases with increasing dopant concentration up to NTO3 film (Fig. 5.10) and for further increasing of Nb concentration, it led to decrease in luminescence intensity. Generally, there are two types of emission in the n-type metal oxide system, one caused by the strong electron transition from the bottom of the conduction band to the top of the valence band also called as near band edge emission (NBE emission). In these samples, the intense emission was observed at 392 nm for all the films [112]. The other emission is due to the defective energy levels or transition between the defect levels to the conduction band, which is called as defect-related emission due to native oxygen vacancy. In this case, the defect level emission peak was observed around 551 nm for all the films. The NBE emission energy is generally equal or lower than the band gap energy, but defect-related emission energy is always less than the band gap energy. In order to estimate the emission intensity accurately, the NTO thin film emission spectra are fitted with Gaussian function as shown in Fig. 5.10. The intense emission spectra are actually composed of three emission peaks such as the strong emission located at 372 nm, 392 nm and 459 nm [154]. The sub-emission level indicates the defects present in the films. The defect density N can be estimated using the equation 4.4 [154]. The Sn interstitial defect density is plotted as a function of Nb concentration in inset of Fig 5.10. It is observed that Sn interstitial defect density was the highest for NTO3 film, which decreased at higher concentrations of Nb.

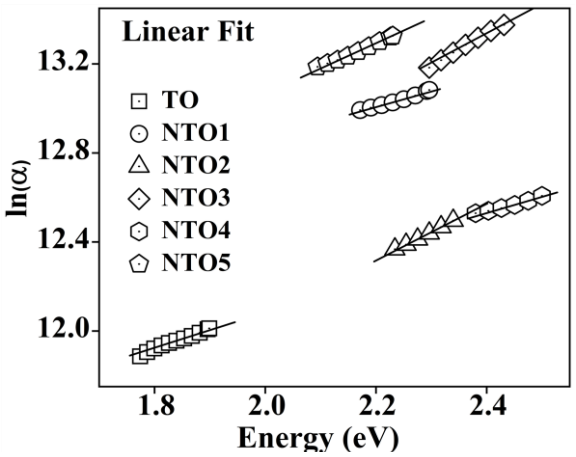

Fig. 5.9. Urbach energy of the TO and NTO films as a function Nb concentration.

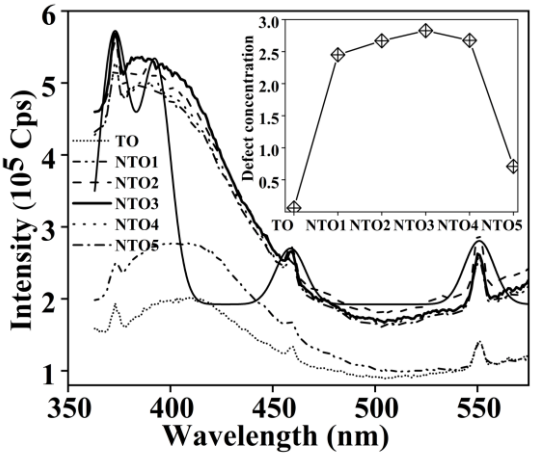

Fig. 5.10. PL spectrum of as-deposited TO and NTO films. Inset is defect density plot.

5.3.6. Electrical transport properties of NTO thin films

5.3.6.1. Hall Effect measurement

From the electrical transport study by Hall effect, it is confirmed that the as-deposited TO and NTO films were having n-type conductivity. The variation in sheet resistance (R_s) and electrical resistivity (ρ) of films at different Nb dopant concentration is presented in Fig. 5.11 and the values are given in Table 5.3. The sheet resistance (R_s) was estimated from equation 3.8 [168]. The sheet resistance of NTO films was found to decrease with increasing Nb concentration up to 1.5 wt% (NTO3) due to enhanced free carrier concentration. However, the Rs value increased beyond 1.5 wt% dopant concentration due to defect level scattering [224,233]. Figure 5.12 shows the variation in mobility and carrier concentration with Nb dopant concentration. The mobility of films increased proportional to Nb concentration until NTO3 film, and beyond this concentration, mobility decreased sharply (Fig. 5.12). The change in mobility can be attributed to defect scattering process like oxygen vacancies in the films [233]. At lower Nb concentration, the substitution makes a positive contribution so that the mobility and carrier concentration of NTO films become maximum reaching to 37.86 cm^2/Vs and $4.636\times10^{20}cm^{-3}$, respectively. Therefore, the enhanced electrical transport properties are due to the dopant effect and oxygen vacancies in the sample. In fact, a strong defect structure could be expected in a spray deposited thin film. The surface roughness and thickness also influence the electrical properties of the film [108].

Table 5.3. Electrical transport properties of TO and NTO thin films.

Parameter	TO	NTO1	NTO2	NTO3	NTO4	NTO5
n_c (cm^{-3})	0.2×10^{19}	1.8×10^{19}	4.4×10^{19}	4.63×10^{20}	1.19×10^{20}	0.8×10^{19}
μ_e (cm^2/Vs)	15.04	27.3	32.68	37.86	21.61	17.46
ρ (Ω cm)	5.35×10^{-2}	9.96×10^{-3}	7.56×10^{-3}	6.45×10^{-4}	4.65×10^{-3}	3.72×10^{-2}
Rs ($\Omega/\square$)	4176	190.1	122.9	25.94	73.73	283.5
FoM $(\Omega)^{-1}$	3.22×10^{-6}	1.71×10^{-4}	4.57×10^{-4}	5.29×10^{-3}	5.82×10^{-4}	2.13×10^{-5}
E_{a1} (meV)	78.3	78.2	78.5	78.4	78.3	78.1
E_{a2} (meV)	110	2723	2721	2128	2312	2578

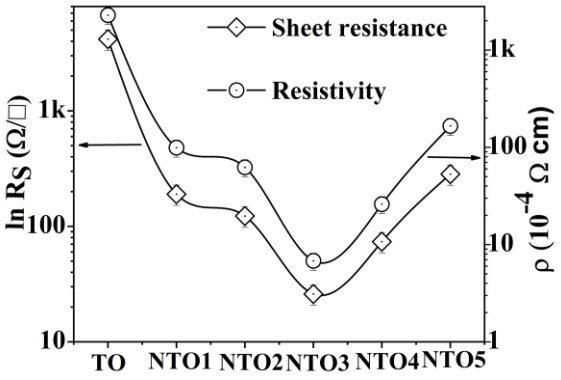

Fig. 5.11. Sheet resistance and resistivity of the TO and NTO films at room temperature.

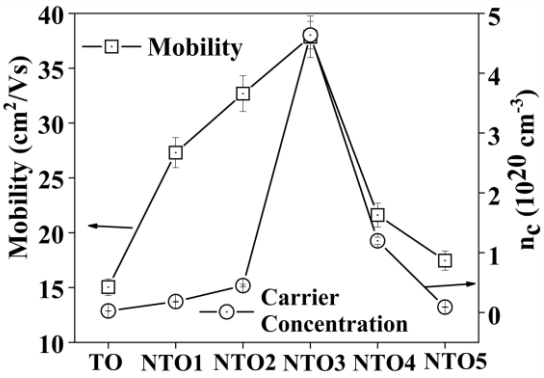

Fig. 5.12. Mobility and carrier concentration of the TO and NTO films at room temperature.

5.3.6.2. Temperature dependent electrical conductivity

To further explore the properties of the films, the temperature dependent electrical studies were performed by four linear probe method in the temperature range from 30 °C to 300 °C. The purpose of this section is to discuss the effect of temperature on the conduction process and to explore the conduction mechanisms involved in the NTO films. The increase in conductivity with increasing temperature represent the semiconducting nature of the films. At higher temperature, ionic conduction dominates the electronic conduction in NTO films [234]. The electrical properties of deposited NTO films exhibit both electronic and ionic contribution to the observed conductivity. The different conduction mechanism prevailing as a function of temperature has been clearly identified from the activation energies obtained from the

Arrhenius plot. The estimation of activation energies of NTO films are shown in Fig. 5.13, which were calculated from the slope of the linear fit given to the plot of log (σT) against 1000/T. The values of the estimated activation energies are given in Table 5.3. The activation energies of the NTO thin films were found to obey the Arrhenius relation given in equation 3.4 [235]. It is clear from the plot that the linear behavior observed with respect to temperature, deviated into another region around 230 ˚C indicating presence of two different conduction mechanism. The conduction in the temperature range from 30 ˚C to 230 ˚C for undoped and NTO films was having semiconducting behavior (Region-I). In the temperature range from 230 ˚C to 300 °C, the deposited films indicate metal-like behavior (Region-II). In region II, the Arrhenius plot shows a positive slope indicating negative slope also called as diffusion activation energy [6], which decreases the concentration of ionic conduction in the sample. In general, at high-temperatures, activation energy is equal to band gap energy and diffusion energy. The estimated values which are higher than the values for region-I indicate higher energy required to promote ionic conduction and this may arise due to presence of more defects in the films [236].

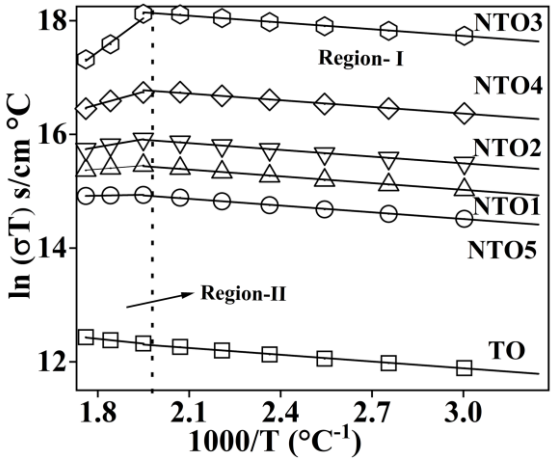

Fig. 5.13. The Arrhenius plots of the TO and NTO thin films.

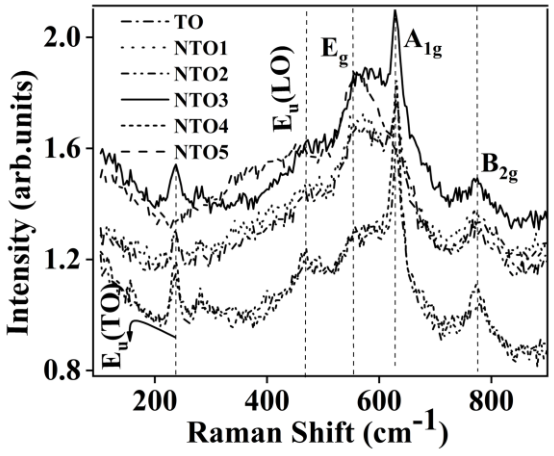

Fig. 5.14. The Raman spectra of the as deposited TO and NTO thin films.

5.3.7. Figure of Merit of NTO thin films

The estimation of the figure of merit (FoM) is an important aspect of transparent conducting films for optoelectronic device applications since most of the devices require good electrical and high transmittance in the visible region. The FOM is estimated using Haacke relation given in equation 3.13 [79]. Table 5.3 shows the FOM value of the TO and NTO thin

films for varying Nb dopant concentration. It is clear that FoM value increases with increase in dopant concentration up to 1.5 wt % (NTO3) and then for higher concentration this value decreases. The NTO3 film shows a maximum FoM value of $5.29\times10^{-3}\ \Omega^{-1}$ when compared to other films, due to its excellent electrical and optical properties. The estimated ϕ values are in good agreement with previously reported values [201]. Hence, the 1.5 wt% of Nb-doped SnO_2 film may be more suitable for optoelectronic applications.

5.3.8. Raman analysis of NTO thin films

Figure 5.14 shows the Raman spectra of the TO and NTO thin films with various Nb concentration. The NTO films have a tetragonal crystal structure with space group symmetry of P42/mnm with unit cell of lattice parameters a = b = 4.737 Å and c = 3.186 Å [72]. The tin (Sn) cations are located at the corner of the unit cell, and the oxygen anions are located at the face center of the unit cell. There are 18 vibrational modes predicted for SnO_2 rutile crystal structure by using group theory, among which there are four set of Raman active modes, within which "A_{1g}, B_{1g}, and B_{2g}" are non-degenerate modes, while "E_g" is a doubly degenerate mode. Two set of IR active modes denoted by "A_{2u}" are non-degenerate and "E_u" is triply degenerated mode. Two are silent mode ("A_{2g} and B_{1u}") and then three are acoustic modes within one "A_{2u}" and two "E_u" modes. The non-degenerate modes "A_{1g}, B_{1g}, and B_{2g}" represent transverse optical (TO) modes and the degenerate "E_g" modes represent the longitudinal optical (LO) modes respectively. The IR active mode denoted by "A_{2u}" is comprised of low and high-frequency modes. Low frequency phonon ("E_u") mode may be associated with oxygen atom whereas the high frequency phonon mode ("A_{2g} and B_{1u}") may correspond to Sn sublattice [72,237]. To understand the effect of Nb dopant on vibrational modes of SnO_2, the thin films were studied at room temperature. The Raman spectrum of NTO films clearly indicate a peak at 631 cm^{-1} which is characteristic Raman active mode of vibration attributed to non-degenerate A_{1g} optical mode. A band appearing as a shoulder at about 559 cm^{-1} is ascribed to the "E_g" mode. The peaks at 276 and 466 cm^{-1} are attributed to the SnO_2 E_u (LO) and the "E_u" (TO) modes, respectively, where this low energy mode is associated with oxygen deficiency [238]. The higher-order Raman peaks observed at 774 cm^{-1} ("B_{2g}") indicate the presence of surface and structural defects in the film.

5.4. Large area (10×10 cm^2) coating of optimized NTO3 thin film

5.4.1. Optical and electrical properties of large area NTO3 film

The optimized deposition condition of 1.5 wt% of Nb doped SnO_2 (NTO3) was chosen for deposition of large-area (10×10 cm^2) NTO3 thin film. The spray deposition parameters of large area coated NTO3 film are given in Table 5.4. The large-area deposited NTO3 film optical and electrical properties were analyzed using various characterizations techniques. The UV-Vis transmittance spectra of the large area coated film showed average transmittance of 75 % at 550 nm. In this case, the film exhibits a lower resistivity value of 1.6985×10^{-3} Ω cm with higher mobility value of 39.4 $cm^2/V\cdot s$. The film was also having a higher carrier concentration of 9.3345×10^{19} cm^3. The large area coated NTO3 film shows relatively lower optical and electrical properties compared to small area (7.5×2.5 cm^2) coated NTO3 film, which may be due to increase of film thickness by way of large number of spraying and inherent deviation in spray dynamics.

Table 5.4. The spray deposition parameters of large area (10×10 cm^2) NTO thin film.

Parameters	Deposition details of large area NTO thin film
Precursors	Host: $SnCl_2$ $2H_2O$, Donor: $NbCl_5$, Solvent: ethylene glycol, 2 propanol, distilled water, and 2 ml of HCl
Host: Donor (concentration)	98.5 wt% of Sn: 1.5 wt% of Nb (0.5 M concentration)
Spray solution quantity	200 ml
Substrate	Glass substrate (10×10 cm^2)
Substrate temperature	400 °C
Substrate to nozzle distance	35 cm
Spray duration ON: OFF	0.5 s: 30 s
Air pressure	46 kg/cm^2
Total number of sprays	520

5.4.2. Surface topology of large area coated NTO3 thin film

The surface topology of the large area NTO3 film was investigated by atomic force microscopy (AFM). Figures 5.15(a) and 5.15 (b) show the surface features of the NTO3 thin film in 2D and 3D view. The 2D image of the film indicates the surface to be granular in nature. The 3D AFM image shows needle-like particulates, which may be the reason for the observed high surface roughness of the film (144 nm) as estimated using a stylus profiler.

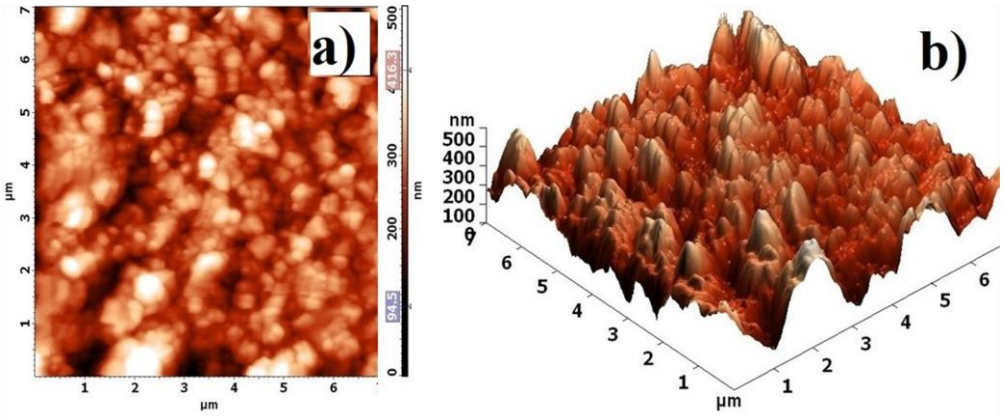

Fig. 5.15. The 2D (a) and 3D (b) AFM images of surface topology of the large area coated NTO3 film.

5.4.3. Variation of sheet resistance across the surface of large area coated NTO3 film

In general, the sheet resistance (R_S) of large area spray deposited thin films varies significantly due to deviation in spray dynamics. Hence, in order to have an estimate on how the sheet resistance varies across the entire region of the large area coated NTO3 thin film, every 1×1 cm^2 area was measured by linear four probe method. Sheet resistance of the large area coated NTO3 film was calculated using equation 3.8 [168]. The photograph of the large area deposited NTO3 thin film marked for every 1×1 cm^2 area is shown in Fig. 5.16(a). The 2D contour image of the estimated variation of R_S across the surface of the deposited film is illustrated in Fig. 5.16(b). The colour representation of the contours in 2D image indicates regions of nearly same sheet resistance. It is observed that the sheet resistance does not prevail uniform over the entire deposited area. The R_S was minimum at the center of the substrate and it increased gradually outwards with higher values at the periphery. This is mainly due to inherent variation in spray dynamics. The variation in intensity of the created cone of aerosol reaching the hot surface of the substrate is modified laterally leading to a pressure gradient. This effect eventually leads to variation of mass transport affecting the film thickness and

properties. This variation is more at the corners of the substrate with higher roughness and sheet resistance compared to center of the substrate. In the spray method, it is difficult to achieve large-area uniform coating using a single nozzle. The variation of the surface properties influences the electrical mobility of the free carriers to a larger extent. For example, Shanthi et al [159] reported in F and Sb co-doped SnO_2 film, the surface grain boundary scattering to influence the free carrier mobility. Muraoka et al [171] investigated the scattering mechanism for degenerate metal oxide films in terms of defect disorder structure. Literature reports indicate that the grain boundary scattering does not influence the film resistivity to a greater extent, instead it will be dominating the mobility of the carriers [170]. In particular, ionized impurity scattering is dominant at high temperature range [179]. The 2D image clearly indicate the center of the film to have low sheet resistance (≅ 26 Ω/□). However, the corners of the substrate possess more variation in sheet resistance ranging from 54 to 67 Ω/□. It is also reported that higher density of grain boundaries and agglomeration of grains generally affect the mobility of the carriers in the film [72,77]. Due to these reasons, the deposited large area NTO3 film is possessing significant variation in sheet resistance across the surface. This variation in sheet resistance could be minimized by adapting multiple spray nozzle system and/or by using ultrasonic spray pyrolysis technique.

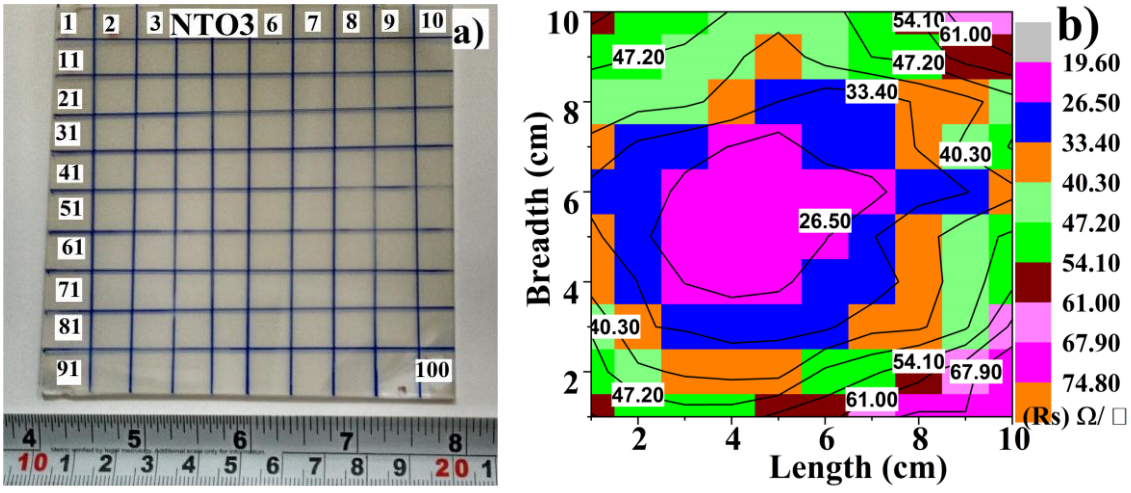

Fig. 5.16. The photograph of the large area coated NTO3 thin film (a) and the 2D contour plot showing variation of sheet resistance over the entire measured area (b).

5.4.4. Sheet resistance stability of large area coated NTO3 film

In order to use the large area NTO3 films for device fabrication, the R_S should be nearly invariable when various fabrication steps are performed at higher temperatures. The resistance stability of R_S of the large area NTO thin film sample was evaluated to study the change in R_S with post annealing temperature (200 °C to 450 °C in steps of 50 °C) and annealing duration (0.5 to 2 h in steps of 0.5 h) as shown in Fig. 5.17. It is identified from the plots; the optimum resistance stability is around 300 °C with lowest sheet resistance achieved to be 37.2 Ω/□ for 0.5 h annealing duration. A slight dip in R_S is observed with annealing temperature up to 300 °C, and with further increasing the temperature it increased to higher values. Also, in the same temperature range, R_S increased linearly with increasing annealing duration (Fig. 5.17). This variation of R_S is caused by factors like, (i) thermally activated free carriers leading to reduction of R_S up to 300 °C, (ii) thermally activated free carriers leading to collision thereby decreasing the mobility beyond 300 °C and (iii) free carriers being localized at oxygen vacancy and getting scattered by defects and grain boundaries [72,77]. Overall, the value of R_S is better for annealing the film at 300 °C for about 0.5 h to 1 h as shown in Fig. 5.17.

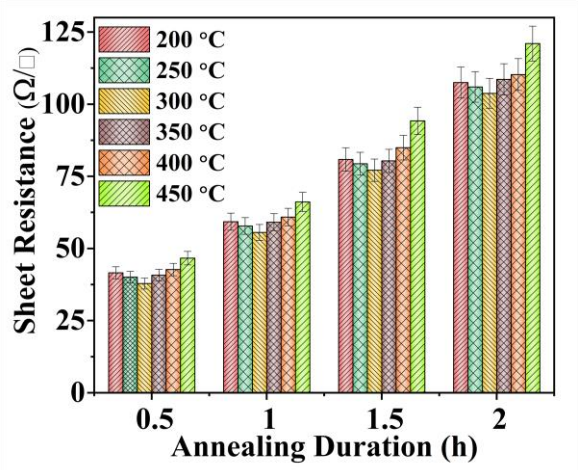

Fig. 5.17. Effect of annealing temperature and duration on the sheet resistance of the large area coated NTO3 film.

5.4.5. Surface work function study by Kelvin Probe

The surface work function of transparent conducting oxide electrodes is an essential parameter for employing them in various device applications. In semiconductors, the band gap can be tuned with respect to the vacuum level by altering the donor and/or defect level concentration [72] leading to change in the work function of the sample. The work function (ϕ)

of a semiconductor sample is dependent on the Fermi level position with respect to vacuum level ($\phi = E_{vac} - E_F$) [81]. The work function of the sample is estimated from the Contact Potential Difference (CPD) between the surface of the film and the standard stainless-steel electrode tip. The work function of the sample was estimated using equation 3.14 [210,239]. The work function of undoped SnO_2 was reported to be in the range from 4.4 eV to 5.7 eV [81]. The work function of SnO_2 gets tuned with effective dopants such as Sb, F etc. In the case of Sb doped SnO_2, the values were reported to be in the range from 4.1 eV to 5.6 eV. Upon doping with appropriate donor element, SnO_2 becomes a degenerate semiconductor thereby decreasing the work function and enhancing the electrical conductivity. The surface work function of NTO3 film in comparison with undoped SnO_2 is illustrated with appropriate energy levels in Fig. 5.18(a). Figure 5.18(b) displays the contact potential difference of the NTO sample scanned over an area of 1×1 mm^2. The NTO3 film is found to have a surface work function value of 5.13 eV. This value is within the range of values reported for doped degenerate SnO_2 system. The lower surface work function of NTO3 film compared to undoped SnO_2 implies that Nb doping has lifted the degeneracy leading to improved conductivity. However, the surface work function of NTO3 is higher than that of the standard ITO films which is around 4.3 eV. Though the surface work function is higher, it has an advantage of being employed in some specific optoelectronic device requirements wherever it is necessary [239,240]. The CPD over the measured region was not very much uniform. This variation of CPD may be attributed to the rough granular surface morphology of the sample. Moreover, the surface work function of a degenerate semiconductor is also sensitive to factors like preferred orientation and oxygen vacancy defects of the film.

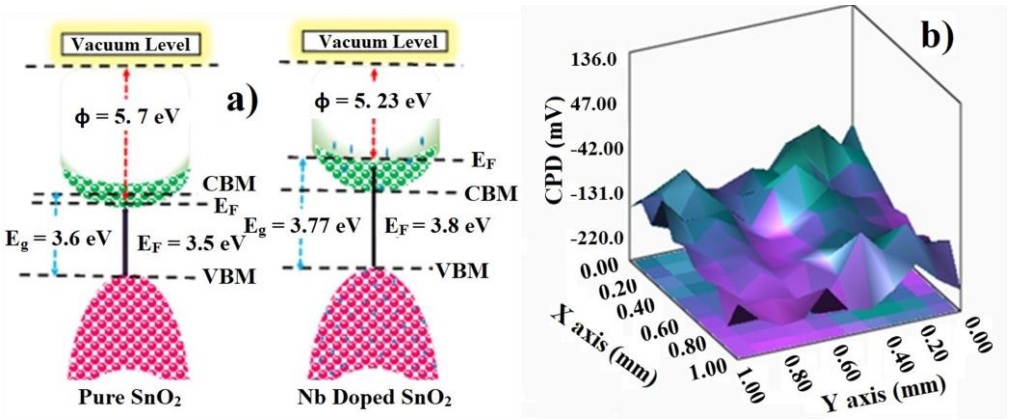

Fig. 5.18. Energy band diagram of undoped and Nb doped SnO_2 thin film (a). Contact potential difference of NTO3 thin film scanned over an area of 1×1 mm^2 (b).

5.5. Conclusion

In this study, Nb doped SnO_2 thin films deposited by spray pyrolysis technique onto the glass substrate at 400 °C were investigated. The XRD studies confirmed that all the NTO films were polycrystalline in nature with tetragonal crystal structure. The highest average optical transmittance of 76 % was observed for 1.5 wt% of Nb doped SnO_2 (NTO3) film in the visible region and found to decrease up to 65 % with increasing dopant concentration above 1.5 wt%. The band gap values are found to be in the range from 3.65 to 3.82 eV for direct band gap for TO and NTO films. From the luminescence spectrum, the UV strong emission is located at 392 nm and the narrow emission peak is centered at 545 nm. The room temperature sheet resistance and resistivity were found to decrease from 4176 to 25.94 Ω/□ and 5.35×10^{-2} Ω cm to 6.45×10^{-4} Ω cm respectively with increasing Nb dopant concentration. The large area (10×10 cm^2) spray deposited NTO3 thin film showing significant enhancement of the optical and electrical properties with appreciable resistance stability seems to be a promising alternative TCO electrode. However, further detailed exploration by fine tuning several parameters for effective usage in various optoelectronic devices are to be performed.

CHAPTER: 6

Spray Deposited Highly Transparent Conducting Tantalum-Doped SnO_2 Thin Films

This chapter first discusses the optimization of Ta-doped SnO_2 (TTO) thin films by cost-effective facile spray pyrolysis method. Main intention is to fine tune the deposition parameters to enhance the TCO properties of the TTO thin films. Further, the optimized deposition parameters have been selected for a large area (10×10 cm^2) coating of the TTO film. Finally, the optimized TTO thin film was tested in a DSSC device as an alternative TCO electrode and the results are discussed in detail.

6.1. Introduction

Newer energy related materials innovations are the heart of modern technology that are enabled by the unique properties of certain materials. Transparent conducting oxide (TCO) thin films have been widely studied for their potential applications in various optoelectronic gadgets [15,152]. The TCOs are a unique class of materials that exhibit contradicting properties like excellent electrical conductivity and optical transmittance. These materials have wide range of applications in flat panel displays, light-emitting diodes, gas sensors, potential storage devices, and solar cells [179,185]. The indium tin oxide (ITO) thin film has been widely used in this field as a TCO material. The scarcity of indium in the earth's crust ranging from 0.05 to 0.072 parts per million (ppm) as reported by Schwarz-Schampera and Herzig [40], and also by the European commission reported the global production of refined indium to be 1,345 tons per annum [42]. However, indium's rarity and an increasing demand for high-performance TCOs have motivated researchers to develop new alternative TCO materials. The doped tin oxide (SnO_2) film has shown great attention in this research field because of properties similar to ITO due to its excellent electrical conductivity, optical transmittance, non-toxicity, low cost and abundance in nature [10]. In general, undoped SnO_2 exhibits poor electrical and optical properties, and to improve it, SnO_2 system is doped with various dopants. The Sb/F doped SnO_2 films were found to be better TCO electrode for optoelectronic device applications. Tantalum (Ta) doped SnO_2 (TTO) film was recently identified as one of the potential materials for TCO application due to its non-toxicity and chemical stability. The TTO attracts more attention due to its excellent electrical conductivity and optical transmittance when compared to other dopants, since the ionic radius of Ta^{+5} (0. 64 Å) is similar to that of Sn^{+4} ionic radius (0. 69 Å); therefore, Ta dopant is properly substituted at the Sn site of SnO_2 lattice [109]. Very few groups

have studied the basic properties of TTO films, and the lowest resistivity value (7.5×10^{-3} Ω cm) of the film was reported by Y. Muto et al [241].

In this chapter, the structural, optical, and temperature dependent electrical properties of TTO thin films are explored by varying Ta concentration. The electrical properties of TTO thin films have been investigated in the temperature range from 30 °C to 450 °C. More importantly, the optimized Ta dopant concentration was chosen for large area coating. The TCO properties of the large area (10×10 cm^2) deposited TTO film is investigated by several analytical techniques. Finally, the suitability of TTO thin film electrode is tested in DSSC device. These results are discussed in detail in the following sections.

Table 6.1. Spray deposition parameters of Ta-doped SnO_2 thin films.

Parameters	Optimization details of TTO thin films
Source materials	Host: $SnCl_2$ $2H_2O$, Donor: $TaCl_5$, Solvent: 2 propanol, ethylene glycol, distilled water, and 2 ml of HCl
Host: Donor (concentration)	95 wt% of Sn:1 to 5 wt% of Ta in 'Sn' site (0.7 M concentration)
Spray solution quantity	150 ml
Substrate	Glass substrate (7.5×2.5 cm^2)
Substrate temperature	400 °C
Substrate to nozzle distance	30 cm
Spray duration ON: OFF	0.5 s: 30 s
Air pressure	50 kg/cm^2
Total number of sprays	420

6.2. Experimental Section

6.2.1. Optimization of TTO thin films

The undoped SnO_2 film and 1, 2, 3, 4 and 5 wt% of Ta-doped SnO_2 thin films were deposited onto glass substrates (7.5×2.5 cm^2) using spray pyrolysis method. The stoichiometric amount of metal salts $SnCl_2.2H_2O$ and $TaCl_5$ are dissolved in a mixture of ethylene glycol (130 ml), distilled water (10 ml), 2 propanol (10 ml), HCl stabilizer (2 ml) resulted in 0.7 M of precursor solution. All the deposition conditions such as substrate to nozzle distance, air

pressure, number of spray and spray duration were kept constant for all the films. The other deposition parameters are given in Table 6.1. The as-deposited TTO film's structural, surface, optical, electrical, and temperature dependent electrical conductivity were characterized by several analytical methods. The as-deposited undoped SnO_2 film and 1, 2, 3, 4 and 5 wt% of Ta-doped SnO_2 thin films hereafter will be denoted as TO, TTO1, TTO2, TTO3, TTO4, and TTO5 respectively with respect to Ta concentration.

6.3. Results and Discussion

6.3.1. X-ray diffraction studies

The X-ray diffraction (XRD) patterns of the TTO thin films deposited with different Ta donor concentration are shown in Fig. 6.1. The as-deposited films show polycrystalline nature with tetragonal SnO_2 structure matching well with the standard joint committee on powder diffraction standards (JCPDS) card No: 41–1445 [109]. No other secondary peaks related to SnO and Sn_2O_3 were found in the XRD pattern confirming the tetragonal SnO_2 phase [117]. There was no Ta_2O_5, Ta_2O_3, TaO_6 phases observed in the XRD pattern, indicating proper incorporation of Ta^{+5} ions into the Sn site of SnO_2 lattice. In general, Ta has multi-valance state of Ta^{3+} (0.76 Å), Ta^{4+} (0.74 Å) and Ta^{5+} (0.64 Å), and among them Ta^{+5} charge state has nearly the same ionic radii of Sn^{+4} state (0.69 Å), and it can be substituted at the Sn site of SnO_2 lattice without affecting the crystal structure. It is also reported that at lower doping level, Sb is perfectly substituted at the Sn site of SnO_2 lattice due to similar ionic radius.

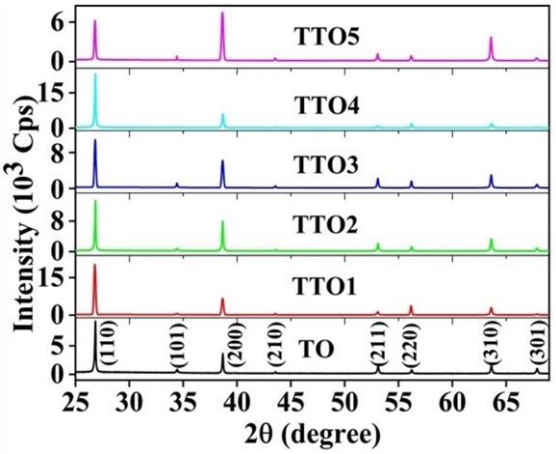

Fig. 6.1. The XRD patterns of spray deposited TO and TTO thin films.

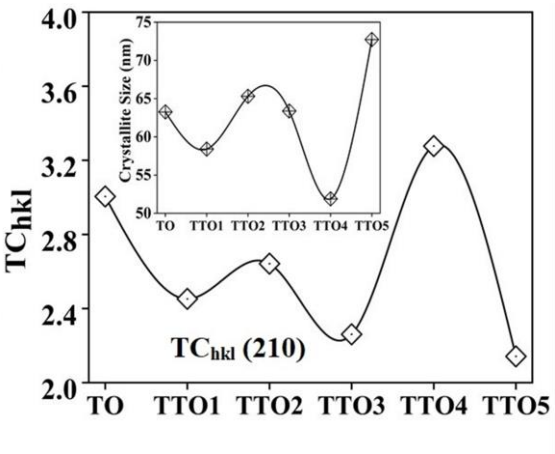

Fig. 6.2. Texture coefficient of (210) plane, and average crystallite size of TO and TTO films (inset).

Higher amount of Sb doping leads to interstitial site occupancy in SnO_2 lattice due to higher ionic radius of Sb^{+3} ionic state (0.76 Å) [114]. In this case, at lower Ta doping concentration, it may occupy the substitutional site of Sn in the SnO_2 lattice, whereas at higher doping concentration, Ta may occupy the interstitial site rather than substitutional site due to higher ionic radius of Ta^{+3}. It is also reported that the doping of higher amount donor element may shift the peak position significantly [114,242]. The variation of average crystallite size with Ta concentration is calculated using scherrer equation 3.1 [243]. It should be noted that a significant change in the crystallite size is observed as a function of Ta concentration. The estimated average crystallite size was lowest for 4 wt% of Ta dopant concentration. Beyond 4 wt%, the average crystallite size increases [243]. The estimated values are listed in Table 6.2 and shown in inset of Fig. 6.2. The estimation of texture (TC_{hkl}) coefficient (preferred orientation) was carried out from the XRD pattern of TTO films using equation 3.2, and it is one of the important structural properties of a thin film. Texture may be developed at various stages of film formation depending upon the growth conditions. The physical properties of the film can vary with texture [158]. The systematic variation of crystallite orientation in different regions of the films can be understood by estimating TC_{hkl} of the films. The texture coefficient of each (h k l) plane of the TTO films was estimated using Harris method (3.2) [160]. The estimated TC_{hkl} value of TTO thin film are shown in Table 6.2 and illustrated in Fig. 6.2. Among all the planes of TTO film, (210) plane possess the highest TC_{hkl} value. The TC_{hkl} value of (210) plane was the highest for 4 wt % doping.

6.3.2. X-ray photoelectron spectroscopic analysis

The XPS analysis on selected films was carried out to identify the oxidation states of elements in order to elucidate the charge transport mechanism of the TTO thin films. Figure. 6.3(a) illustrates the XPS survey scan spectra of Sn3d, O1s, and Ta4f of the TTO thin films deposited with different Ta concentration. Evidence for Ta substitution can be obtained by looking at the binding energies of Ta doped SnO_2 films compared with the undoped SnO_2 film. The peak at 285 eV correspond to C1s peak indicating surface contamination by atmospheric carbon [173]. The peak at 976.8 eV is the auger electron peak (SnMn1) of Sn ion. Figure. 6.3(b) illustrates the Gaussian fitted XPS narrow scan spectra of Sn $3d_{3/2}$, and Sn $3d_{5/2}$ oxidation states of their binding energy centered at 494.6 eV and 485.8 eV respectively [158]. The binding energy of Sn in TTO films is shifted by 0.25 eV as compared to the undoped SnO_2 film. Distinguishing between Sn^{2+} and Sn^{4+} is somewhat difficult due to small variation between their

binding energies. The difference between Sn $3d_{3/2}$ and Sn $3d_{5/2}$ oxidation states is 8.5 eV, indicates Sn to exist in 4+ charge state. Figure 6.3(c) illustrate the binding energy states of O1s spectra deconvoluted into three peaks appearing at 529.1 eV (OI) which is attributed to Sn-O bonds, 530.3 eV (OII) is associated with O^{2-} ions in non-stoichiometry state, and 531.4 eV (OIII) which is usually attributed to chemisorbed or dissociated oxygen or OH species on the surface of the films [244]. The increase in oxygen vacancy defects indicate increasing of free carrier concentration [245]. These free carriers may possibly be captured by chemisorbed oxygen or OH species. Figure 6.3(d) indicates binding energies centered at 26.8 eV and 27.3 eV that are related to the Ta in 5+ charge state. The binding energy appearing at 26.8 eV for the TTO3 and TTO4 films indicate the Ta in 5+ charge state. The Ta $4f_{7/2}$ peak of TTO3 shifted slightly to lower binding energy, compared to TTO4 film. This shift indicates the variation in charge state of Ta ions in Sn site of SnO_2 lattice. These obtained results are well matched with the literature report [246].

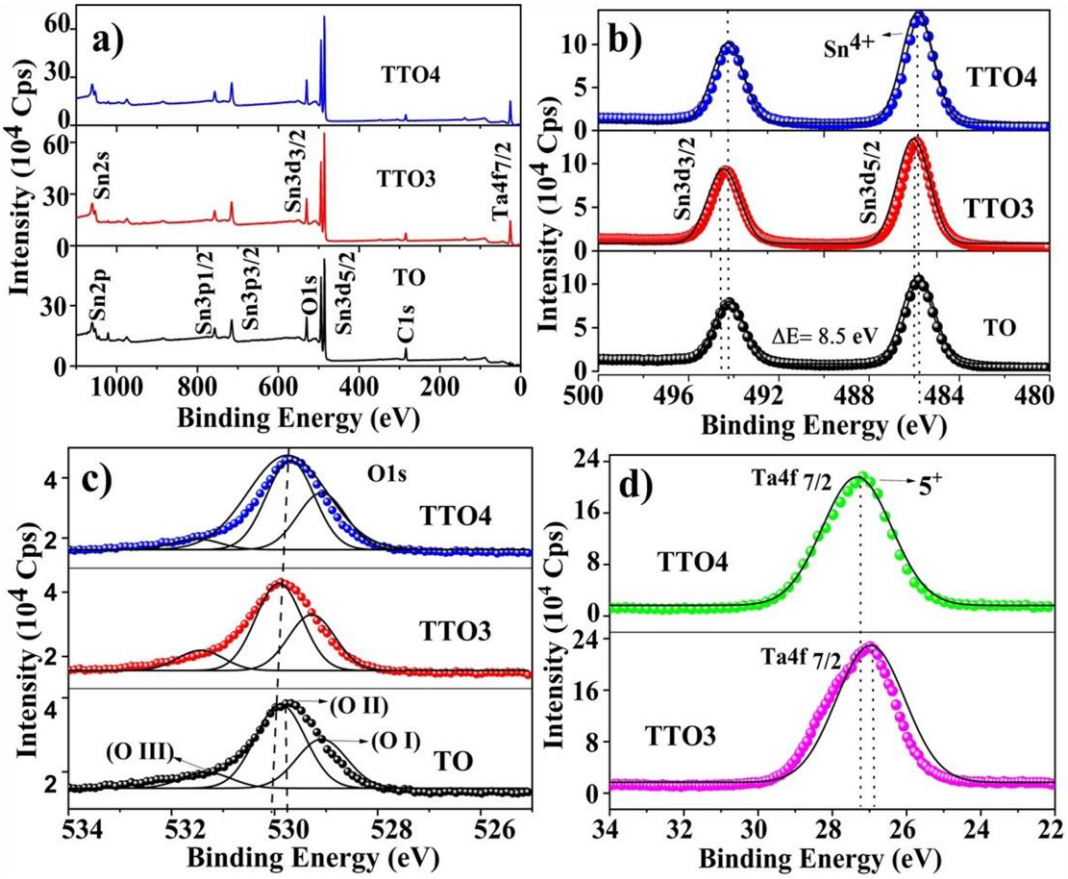

Fig. 6.3. The XPS survey scan spectra (a), Sn3d narrow scan spectra (b), O 1s narrow scan spectra (c), and Ta 4f narrow scan spectra of TO, TTO3 and TTO4 films.

6.3.3. Morphology study

Figure 6.4 shows the SEM images of TTO thin films at 2 μm magnification, and the surface morphology significantly changes with Ta concentration. The TTO films possess different size and shape of the particles and are distributed throughout the surface of the films. The films TO, TTO1, and TTO2 show fine particulates, but for higher dopant concentration, the films TTO3, TTO4, and TTO5 show polyhedron structure [205]. The particle size increased with increasing dopant concentration up to TTO4 film, after which it decreased. The inhomogeneity of the particles on the surface of the film causes more surface roughness, thereby affecting the electrical and optical properties of the deposited films. The surface roughness of the films is also influenced by film thickness. The as-deposited TTO thin film thickness and roughness are estimated by stylus profiler (Table 6.2). The higher surface roughness of the film may lead to more surface scattering effects.

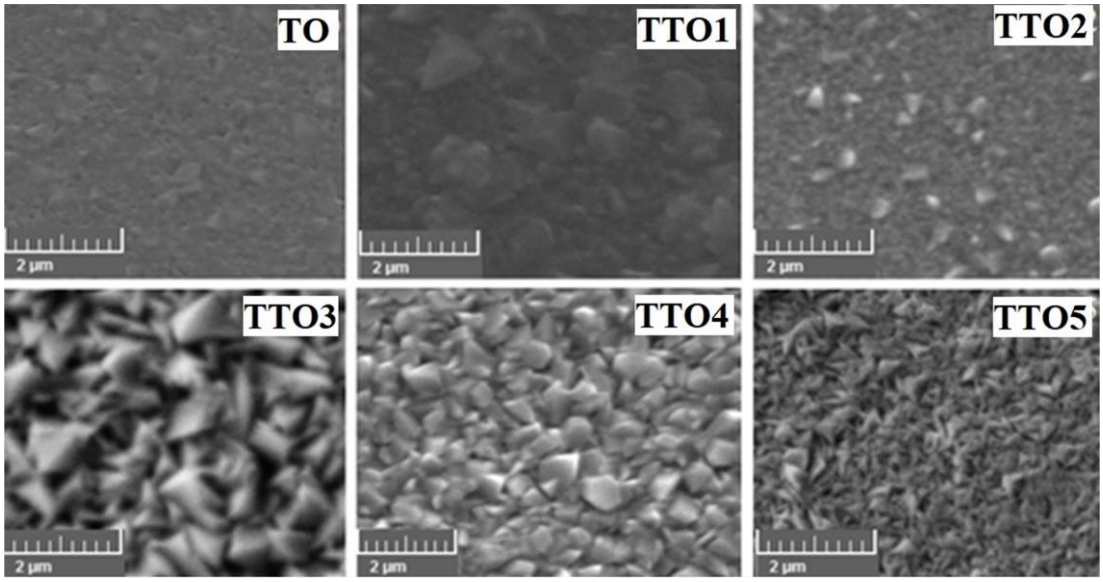

Fig. 6.4. The SEM morphology of spray deposited TO and TTO thin films.

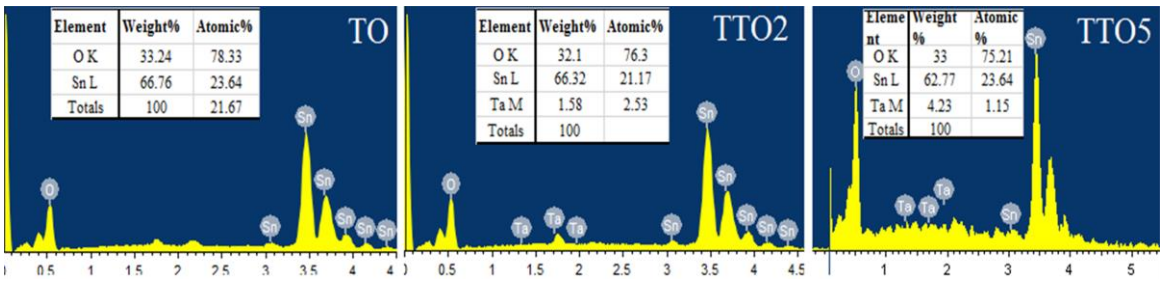

Fig. 6.5. The EDS images of TO, TTO2 and TTO5 thin films.

This higher surface scattering affects the transmittance and conductivity of the films. Figure 6.5 shows the energy dispersive spectroscopic (EDS) images of the selected TO, TTO2 and TTO5 films. It is identified that a nominal deviation in the stoichiometric ratio is observed with Ta concentration.

Table 6.2. Structural, surface, and optical properties of TO and TTO thin films

Parameter	TO	TTO1	TTO2	TTO3	TTO4	TTO5
L (nm)	63.2 ± 1.26	58.3 ± 1.16	65.3 ± 1.30	63.3 ± 1.26	51.8 ± 1.03	72.7 ± 1.45
a (Å)	4.742	4.745	4.745	4.747	4.748	4.742
c (Å)	3.186	3.186	3.186	3.188	3.188	3.186
TC_{hkl} (210 plane)	3.00	2.45	2.64	3.26	3.27	2.14
Roughness (nm)	17	15	13	11	9	19
Thickness (t) (nm)	250 ± 7.50	350 ± 10.5	289 ± 8.67	193 ± 5.79	303 ± 9.09	274 ± 8.22
E_g (eV)	3.95	3.97	3.99	3.98	4.01	3.97
E_u (meV)	622	857	705	771	661	913

6.3.4. Optical Study

Figure 6.6 shows the transmittance spectra of TTO thin films analyzed by UV- visible spectrometer in the wavelength range 300 to 1000 nm and insets are the photographs of the as-deposited films. The TTO thin films have lower transmittance in the ultraviolet region compared to infrared region. The TTO4 film was having transmittance of ~ 75-86 %, but the TO film showed lower transmittance values of around ~ 70 -75% due to high absorption in the visible region. The higher roughness of the films will reduce the transmittance [201]. The TTO films show relatively higher transmittance in the near infrared region (NIR). The absorption coefficient is calculated from Lambert's relation (Eqn. 4.3) [247]. The higher absorption coefficient value indicates lower transmittance of light. The optical transmittance spectra of the film depend on band gap properties of the system. The optical band gap of the film is estimated by Tauc relation (Eqn. 3.3) [143]. The estimated direct band gap values of the films are illustrated in Fig. 6.7 and given in Table 6.2. The direct band gap values varied between 3.95 eV to 4.00 eV and match well with previous reports [184,248]. The band gap of the film

increases upon increasing the Ta concentration up to TTO4 thin film, and further, band gap decreased with increasing Ta concentration. The estimated wide band gap values are indicating the suitability in optoelectronic applications.

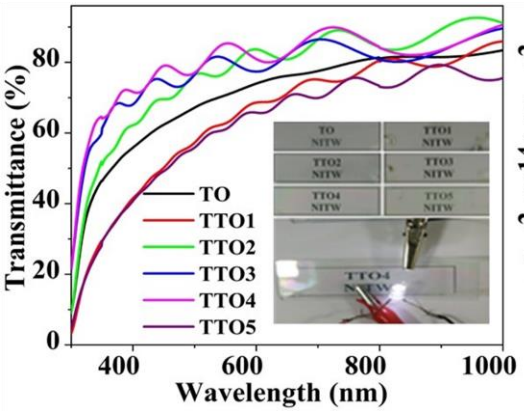

Fig. 6.6. Transmittance spectra of TO and TTO films as a function of Ta concentration, Inset are the photographs of the same.

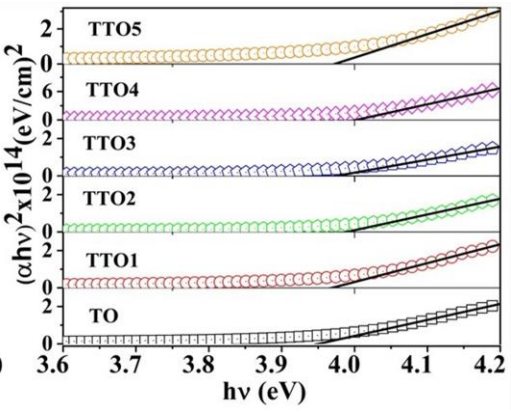

Fig. 6.7. Direct band gap values of TO and TTO films as a function of Ta concentration.

The degenerate metal oxide systems exhibit band tail in the transmittance spectrum, because the fundamental absorption edge is also dependent on the photon energy. The fundamental absorption edge (E_g) less than the fermi energy (E_F) ($E_g < E_F$) is generally called as Urbach tail [109]. The band tail of the spectrum arises by various factors such as dopant, impurity, and defect structure [249]. The Urbach energy (E_u) of the TTO films were estimated by equation 3.6 [250]. The Eu is equal to the slope of the linear fit, and the estimated values are shown in Fig. 6.8. The Eu does not show any linear trend with Ta concentration (Table 6.2). The lowest Eu value was observed for TO film (622 meV) and the highest value was obtained for TTO5 film (913 meV). Higher Ta doping concentration yields higher Eu value. The film deposited at lower Ta content shows structural and surface defects due to oxygen vacancy defects of the films [251]. It is also noticed that the Ta doped films that possess higher surface roughness show higher Eu value indicating more absorption/reflection of light.

6.3.5. Photoluminescence study

Figure. 6.9 shows the photoluminescence (PL) emission spectra of as-deposited TO and TTO films. All the samples are excited with wavelength of 325 nm. The PL emission spectra clearly show the broad emission at 393 nm and the narrow emission at 546 nm [106]. The broad emission around 393 nm is emitted due to strong electron transition from the bottom of the

conduction band to the top of valence band, and it is also called as near band edge emission (NBE emission) [88]. The broad emission of 393 nm also exhibits two sub-bands at 369 nm and 454 nm, indicating contribution of defect emission to be present in the films. The narrow emission peak of 546 nm is appeared due to the oxygen vacancy defect formation in the films. The most common defects in SnO_2 films are oxygen vacancies and impurities due to dopant that plays essential role in the photoluminescence properties [106]. The intensity of the emission peaks increased up to TTO4 film, and with further increasing Ta concentration, the intensity of the emission peak decreased which is due to the concentration quenching effect. The defect density N is estimated by using the Smakula's relation (Eqn. 4.4) [154]. The defect density was estimated from the PL emission spectrum in which, we have replaced the term $\alpha W_{1/2}$ by the Gaussian peak area. The SnO_2 oxygen vacancy defect density is plotted as a function of Ta doping concentration (inset of Fig. 6.9). It is observed that in the SnO_2 system oxygen vacancy defect density increased with Ta concentration up to TTO4 concentration. Beyond this concentration, the decrease of oxygen vacancy defect density in SnO_2 lattice correlates with the increasing more surface and structural defects, and these defects can also lead to change in the photoluminescence properties.

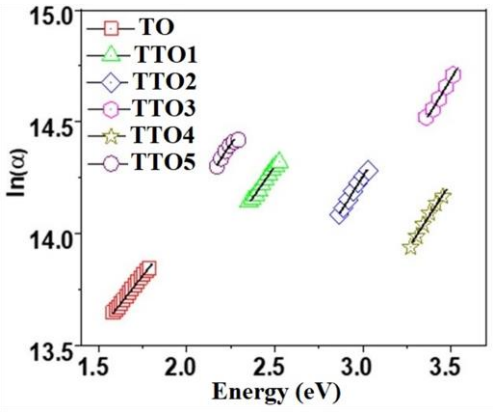

Fig. 6.8. Urbach tail energy of TO and TTO films as a function of Ta concentration.

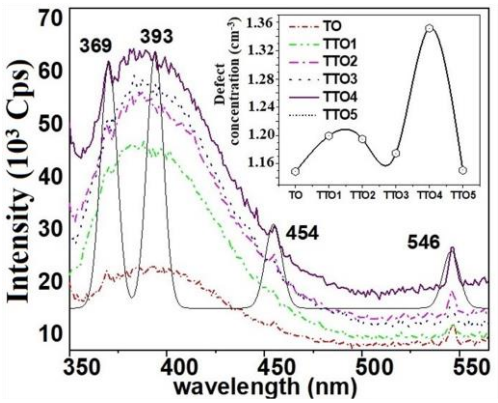

Fig. 6.9. The PL emission spectra of TO and TTO thin films as a function of Ta concentration. Inset is the defect density plot.

6.3.6. Electrical properties

6.3.6.1. Hall Effect measurement

The electrical transport properties of TTO thin films are estimated by Hall effect measurement, and it exhibited n-type electrical behavior. The estimated electrical transport parameters are presented in Table 6.3. The TTO thin film's resistivity (ρ) and sheet resistance

(Rs) as a function of Ta concentration are illustrated in Fig. 6.10. The sheet resistance was calculated using equation 3.8 [160,251]. The resistivity of the TTO films decreases with increasing Ta concentration because of the substitution of Ta^{5+} donor at the Sn lattice sites. This will lead to free carriers in the Sn lattice site, as a result, the conductivity increased up to 4wt % of Ta doping, and then decreases with further increase in Ta concentration, because of free carrier collision. The variation of electrical transport properties of the TTO films are influenced by several factors such as grain size, surface roughness, thickness, oxygen vacancies, dopant concentration and defect concentration, etc. [253]. Here, the electrical transport properties of the films are discussed in terms of dopant concentration and oxygen vacancies. The incorporation of Ta into Sn site of SnO_2 lattice creates free carriers leading to improvement of the conductivity of the films [212].

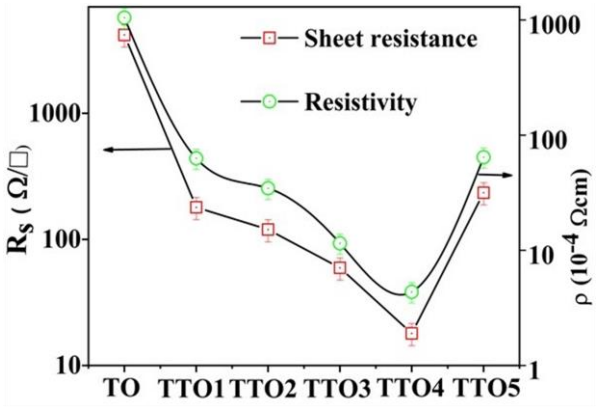

Fig. 6.10. The room temperature sheet resistance and resistivity of TO and TTO films.

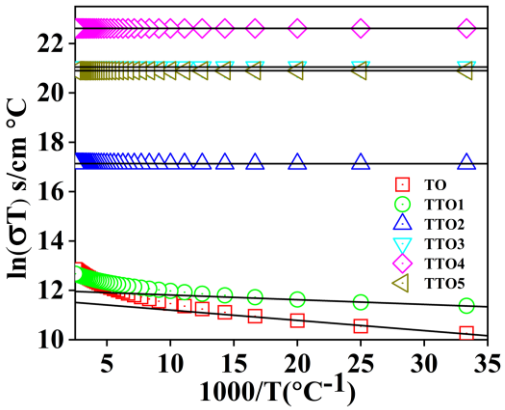

Fig. 6.11. Arrhenius plot of TO and TTO thin films.

Also, the free carriers may be captured by the localized acceptor and oxygen vacancy states, which also affect the electrical mobility and free carrier concentration of the films. The TO film shows poor conductivity due to low free carrier concentration and low mobility. Table 6.3 shows the carrier concentration and mobility to increase with increasing Ta doping level up to 4wt %, and then decrease with further increase in Ta doping content. The Ta substitution decreases the resistivity from 1.04×10^{-2} Ω cm to 4.36×10^{-4} Ω cm. However, the resistivity values of the optimized TTO thin films are comparably better than previous report [254].

6.3.6.2. Temperature dependent electrical conductivity

The temperature dependent electrical properties of the undoped and Ta-doped SnO_2 thin films were carried out using four probe method in the temperature range 30 °C to 450 °C. Very

few research groups have studied the temperature dependent electrical properties to understand the conduction mechanism of SnO_2 film at different temperatures [255]. Generally, temperature dependent electrical conductivity of semiconducting material is due to electronic and ionic contribution. The temperature dependent electrical conductivity of the TTO films exhibited different conduction mechanism with distinct regions of temperature. The conductivity of the films increased as a function of temperature up to 380 °C due to thermally created free carriers, and further gradually increased up to 400 °C indicating ionic contribution. Beyond 400 °C electrical conductivity of the films decreases drastically implying the metallic like conducting behavior due to several defect contribution at higher temperature. This varying conduction mechanism is understood by estimating activation energy from the Arrhenius plot. The activation energies of TTO films are calculated for varying Ta dopant concentration as shown in Fig. 6.11. The experimental data can be well described by the activation energy values as estimated from the slope of the linear region (Table 6.3). The TO and TTO5 films show lower activation energy than other films. The thermally activated conduction process is controlled by free carrier concentration and oxygen vacancy. As the free carrier concentration increases, electrical conductivity will increase up to some dopant level and at higher dopant concentration these free carriers may possibly lead to reduced mean free path, influencing the mobility of the carriers.

Table 6.3. The electrical transport properties of TO and TTO thin films.

Parameters	TO	TTO1	TTO2	TTO3	TTO4	TTO5
n_c (cm^{-3})	1.21×10^{19}	1.89×10^{20}	1.92×10^{20}	5.19×10^{20}	53.1×10^{20}	1.9×10^{19}
μ_e ($cm^2/V\cdot s$)	14.2	21.6	25.3	31.9	45.5	20.6
ρ (Ω cm)	1.04×10^{-2}	6.29×10^{-3}	3.46×10^{-3}	1.14×10^{-3}	4.36×10^{-4}	6.42×10^{-3}
R_s ($\Omega/\square$)	4188	179.7	119.7	59.54	17.96	234.6
E_{a1} (meV)	73	86	95	118	153	82
E_{a2} (meV)	105	135	155	282	527	124
FoM (Ω^{-1})	1.43×10^{-4}	3.50×10^{-3}	6.43×10^{-3}	1.36×10^{-2}	4.73×10^{-2}	2.60×10^{-3}

6.3.7. Figure of Merit

The Figure of Merit (FoM) values of the films are estimated by Haacke relation using equation 3.13 [79]. For an ideal TCO, the FoM should be high. However, depending on the application and requirement, either of the transmittance or sheet resistance may be

compromised. The estimated values of the FoM as a function of Ta concentration are listed in Table 6.3. The TTO4 film has the highest FoM value than other films. This implies that Ta dopant into the Sn site of SnO_2 lattice improves the transparency and conductivity of the films. However, the effect of carrier concentration, mobility and the variations in deposition parameters can also influence the FoM. Hence, the optimized 4wt % Ta-doped SnO_2 film may be suitable for large area deposition.

Table 6.4. Spray deposition parameters of large area (10×10 cm^2) coated TTO4 thin film.

Parameters	Deposition details of large area TTO4 thin film
Source materials	Host: $SnCl_2$ $2H_2O$, Donor: $TaCl_5$, Solvent: 2 propanol, ethylene glycol, distilled water, and 2 ml of HCl
Host: Donor (concentration)	96 wt% of Sn: 4 wt% of Ta in Sn site (0.7 M concentration)
Spray solution quantity	200 ml
Substrate	Glass substrate (10×10 cm^2)
Substrate temperature	400 °C
Substrate to nozzle distance	30 cm
Spray duration ON: OFF	0.5 s: 30 s
Air pressure	50 kg/cm^2
Total number of sprays	520

6.4. Large area (10×10 cm^2) coating of optimized TTO4 thin film

6.4.1. Optical and electrical properties of large area deposited TTO4 film

The optimal TTO4 thin film deposition parameters were chosen for large-area (10×10 cm^2) coating. The spray deposition parameters of large area coated TTO4 film are given in Table 6.4. The UV-Vis transmittance spectra of the film show average transmittance of 86 % in the visible region. The large area coated TTO4 thin film was found to exhibit lower resistivity of 4.36×10^{-4} Ω cm and higher mobility of 45.5 $cm^2/V\cdot s$. The film was also having a higher carrier concentration of 5.31×10^{21} cm^{-3} due to substitution of Ta into the Sn site of SnO_2 lattice leading to more free carriers. The increased number of sprays of large area coated film may lead to higher thickness, and this higher thickness possibly affects the electrical properties significantly. Due to higher thickness of large area coated film, it shows relatively low electrical properties compared to smaller area coated (7.5×2.5 cm^2) TTO4 thin film.

6.4.2. Surface topology of large area coated TTO4 thin film

In order to understand the effect of Ta doping concentration on the surface topography of the deposited TTO4 film was analyzed by using atomic force microscopy (AFM). Figures 6.12(a) and 6.12(b) clearly indicate the 2D and 3D AFM images of large area TTO4 film. The 2D AFM image reveal that the surface is nearly homogeneous, crack free, dense, with a granular microstructure. Figure. 6.12(b) is the 3D image showing the particles similar to needle like shape distributed on the surface of the film. This needle like particles are reason for the higher surface roughness of the film. The surface quality of the film was measured using the root-mean-square of the surface roughness (RMS), which was acquired through statistical investigation of the AFM image (Fig. 6.12(b)). The average RMS roughness value of the TTO4 film was 124 nm indicating higher surface roughness of the film, which may influence the optical and electrical properties [256].

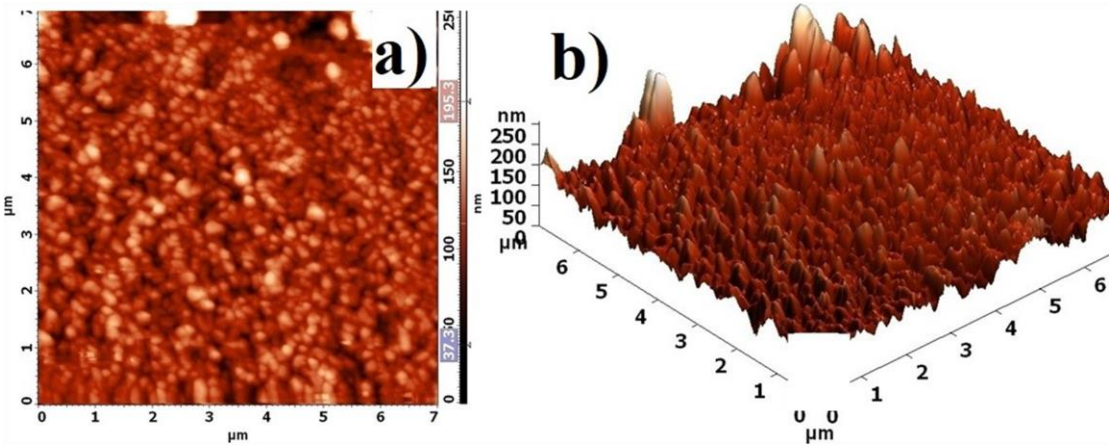

Fig. 6.12. The 2D surface topology (a) and the 3D surface topology (b) of the TTO4 film from AFM measurement.

6.4.3. Sheet resistance – Variation across the surface

The variation of sheet resistance across the large area deposited TTO4 film was investigated at every 1×1 cm^2 area of the entire region by using four-probe method. Figure 6.13(a) is the photograph of the large area spray deposited TTO4 film (10×10 cm^2). The sheet resistance of the TTO4 film was estimated using equation 3.8 [257]. The 2D contour map (Fig. 6.13b) indicates considerable variation in sheet resistance. The center region of the film possesses lowest sheet resistance than corner region of the film. This variation in sheet resistance depends on spray dynamics. During spraying there is a pressure gradient with respect

to the distance between substrate and center of the spray nozzle. The substrate below the spray nozzle has a uniform film formation than other regions of the film. The 2D image indicates the center region of the film to show the lowest sheet resistance of 26 Ω/□ (Fig. 6.13b). However, the film at the corners of the substrate possesses more variation in sheet resistance ranging from 54 to 67 Ω/□. The sheet resistance of the film is influenced more by the surface properties of the film [258]. The variation in surface roughness would cause a decline in mobility of the free carrier because of collision between the free carriers. Y. Muraoka et al studied and reported the mobility of the free carriers to be affected by grain boundary scattering [171]. Furthermore, higher RMS roughness may enhance the grain boundary scattering.

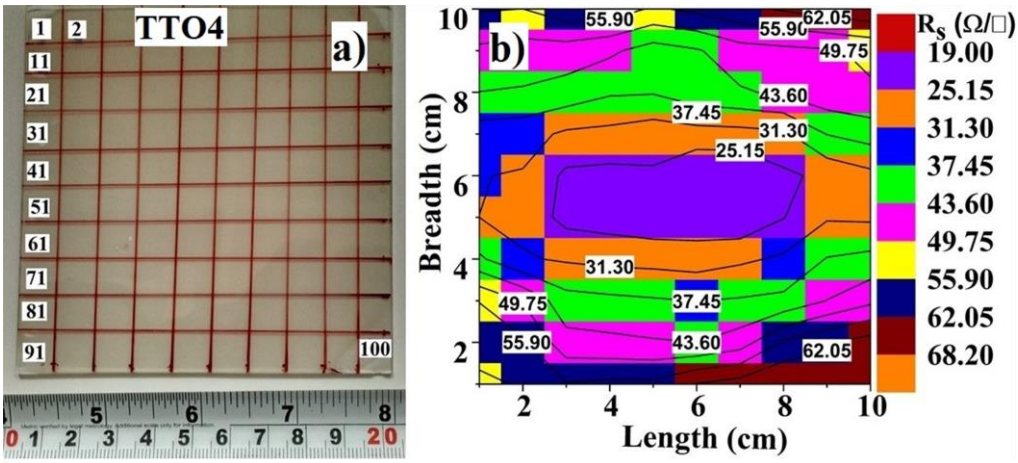

Fig. 6.13. Photograph of large area deposited TTO4 film (a) and the surface variation of sheet resistance as 2D contour map (b).

6.4.4. Resistance Stability of TTO4 film analysis

Figure 6.14 shows the variation of sheet resistance of large area deposited TTO4 film post annealed in air in the range 200 to 450 °C for duration ranging from 30 min. to 2 hours with a time interval of 30 min. The sheet resistance of the TTO4 film increased with post annealing duration from 30 min. to 2 h. However, the sheet resistance decreased up to 400 °C, which indicates clear evidence of semiconducting behavior in the film. The increase of conductivity of the film is due to thermally created free carrier concentration. In the metal oxide system at higher temperature the oxygen formation energy is decreased due to dopant effect. Further, with increase of post annealing temperature, the sheet resistance of the film increased indicating metallic-like behavior (Indicated by arrows in Fig. 6.14) due to free carrier collision and free carrier absorption. This behavior of electrical property is due to various scattering processes. The thermally generated free carrier mobility is affected by grain boundary scattering

and ionized impurity scattering [259]. In such a situation, electronic conductivity of the film dominates ionic conductivity. However, the observed results reveal that the TTO4 film has good stability up to 400 °C.

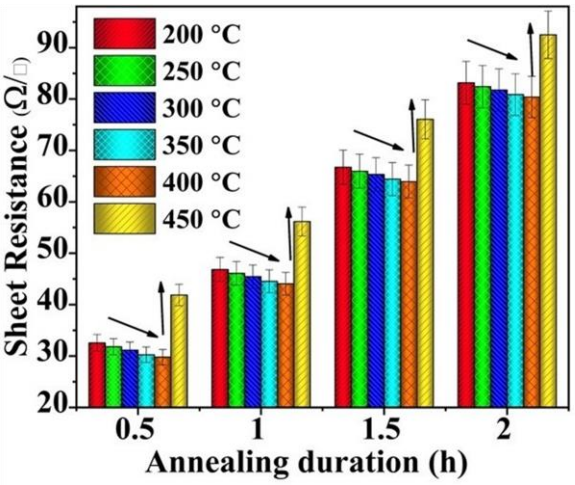

Fig. 6.14. Variation of sheet resistance of large area TTO4 film as a function of annealing temperature and duration.

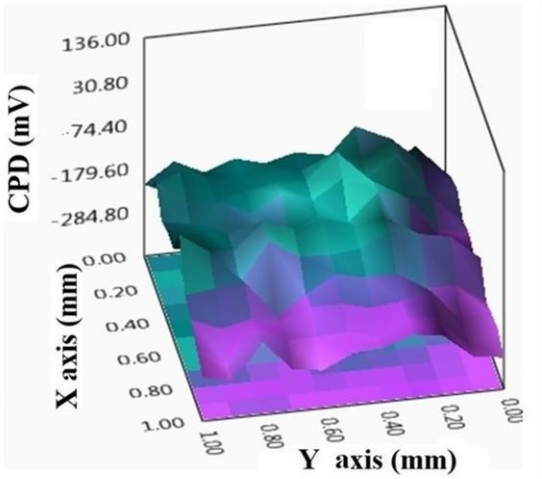

Fig. 6.15. The contact potential difference of large area TTO4 film scanned over an area of 1×1 mm^2.

6.4.5. Surface work function by Kelvin Probe method

The surface work function of the metal oxide layer plays a vital role in the performance of several optoelectronic devices. The energy level difference between the Fermi level and the vacuum level of the TTO4 film is termed as the surface work function. However, in a non-degenerate n-type semiconductor the Fermi level lies below the conduction band minimum, but in the case of n-type degenerate semiconductor, the Fermi level may lie above the conduction band [181]. Therefore, it is necessary to find the location of the Fermi level through the work function measurement by Kelvin probe (KP) technique. The KP method is a unique non-contact technique to determine the contact potential difference between the film and reference electrode tip. The work function (φ_{film}) of the film can be estimated when the reference electrode work function is known. Hence, the work function of TTO4 film is estimated using Schottky–Mott (S–M) relation (Eqn. 3.14) [260]. When the stainless steel tip is brought close to the film, an electrostatic force generated between the surface indicate the alignment of the Fermi level with respect to the vacuum level. Generally, n-type semiconducting materials while tuning the band gap, the Fermi level bend towards the vacuum level thereby decreasing the surface work function. But in the case of a p-type system, the Fermi level shift outward to the vacuum level,

thereby increasing the work function [261]. Figure 6.15 indicates the variation of the contact potential difference scanned over the range of 1×1 mm^2. It is identified that large variation in a contact potential difference value indicates inhomogeneous surface of the film. The work function of TTO4 thin film of 5.08 eV is estimated from the average contact potential difference. This estimated φ_{film} value is lower than the undoped SnO_2 sample value of 5.74 eV. The undoped SnO_2 sample has poor electrical conductivity since the Fermi level lies below the conduction band, but in case of TTO4 film, the Fermi level lies above the conduction band, indicating lower work function, thereby improvement in electrical conductivity.

6.4.6. Raman mapping analysis

It is difficult to distinguish SnO_2 phase and SnO phase from XRD data because some of the peak position of both the phases occupy the same 2θ values. For example, the (201) plane of SnO_2 and (101) planes of SnO peak centered at same 2θ value of 42°. To overcome this problem, Raman analysis will help to identify the actual existing phase, because for a SnO_2 system the active Raman mode is present in the higher wavenumber region (628 cm^{-1}), but in the case of SnO system active Raman modes appear in lower wavenumber (234 cm^{-1}) region [72]. Moreover, this analysis will provide the information regarding the possible secondary phases if any such as Sn_2O_3, Sn_3O_4, and Ta_2SnO_4 present in the TTO4 film. Nilesh Mazumder et al clearly identified 18 vibrational modes in SnO_2 system [88]. In this case there are four peaks present in the TTO4 film, among them 3 peaks are Raman active mode ("A_{1g}, B_{2g}, and E_g") and "A_{2g}" is silent mode as illustrated in Fig. 6.16(a). The active Raman modes 628 cm^{-1} ("A1g"), 456 cm^{-1} ("B2g") and 476 cm^{-1} ("Eg") arise by oxygen atoms vibrating perpendicular to the c axis, whereas doubly degenerate "E_g" mode vibrates along the direction of the c-axis [72]. In silent mode, oxygen and Sn vibrate perpendicular to c axis. This variation in the Raman mode is also used to map the surface to identify the homogeneity of distribution of the entire region of the film as illustrated in Fig. 6.16(b). The surface properties such as uniform coating, homogeneous distribution, and phase purity of TTO4 film are verified with the Raman mapping image analysis, and the nature of the surface can be understood from the intensity of vibrational modes [72].

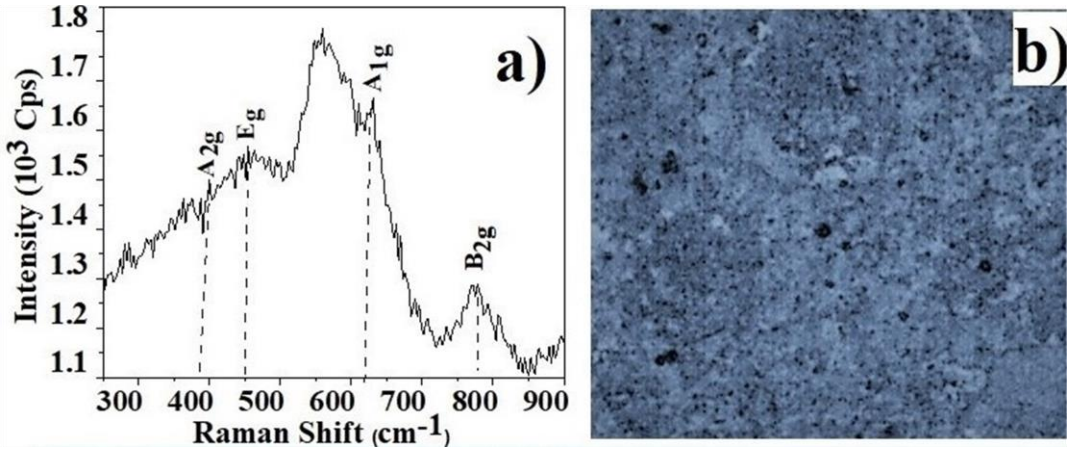

Fig. 6.16. The vibrational modes of Raman spectra (a) and micro Raman mapping image of TTO4 film scanned over an area of 1×1 mm^2 (b).

6.5. Dye-sensitized Solar cell fabrication and testing using TTO4 film

6.5.1. Dye-sensitized solar cell fabrication

Dye-sensitized solar cell (DSSC) was fabricated using optimized TTO4 transparent conducting electrode. The device fabrication procedure was followed as reported by G. Veerappan et al [262]. The photovoltaic performance of the TTO4 electrode based DSSC device is compared with commercial FTO electrode based DSSC device. Similar device structure was followed for TTO4 and FTO electrodes (TTO4 or FTO/ TiO_2/N719 dye + electrolyte/Pt/TTO4 or FTO for DSSC devices except for post-annealing temperature. The TTO4 photoanode was post-annealed at 450 °C for 30 min whereas FTO coated with TiO_2 was post-annealed at 500 °C for 30 min. Same annealing conditions were adopted for preparing the counter electrode also (Pt/TTO4). To prepare photoanode and counter electrode, the porous TiO_2 and Pt paste were coated respectively on-to the TTO4/FTO electrode by doctor blade method. The fabricated DSSC device's current density-voltage (J–V) measurements was tested under AM1.5 condition using a Newport 91160A solar simulator. The light source was 150 W Xe lamp and the light intensity correspond to AM1.5 (100 mW cm^2) calibrated with a standard Si cell (Oriel SRC1000 TC). The electrochemical impedance spectroscopy (EIS) measurement was performed using IVIUMSTAT electrochemical workstation at an amplitude of 10 mV, in the frequency range of 0.1 Hz to 1 MHz. Figure 6.17 shows the schematics of the working principle of the DSSC device. The basic mechanism of the DSSC is similar to the photosynthesis for starch creation by plants [263].

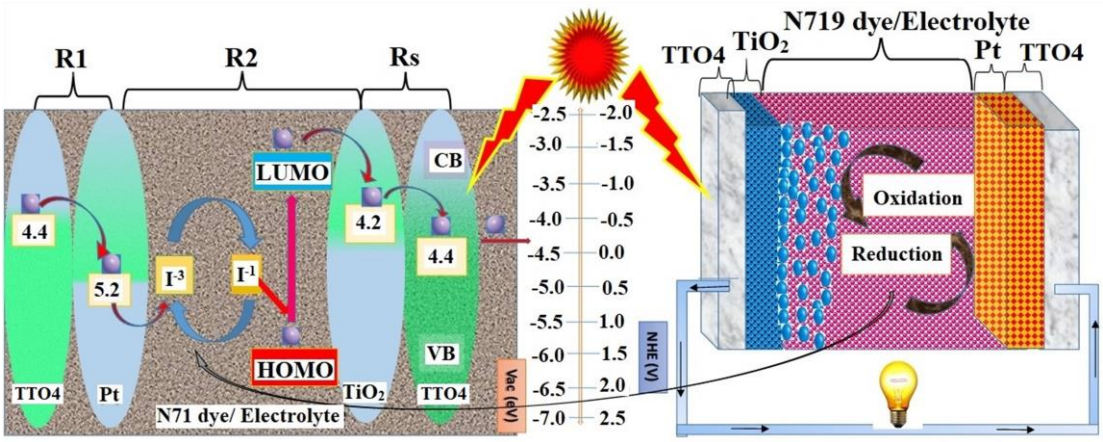

Fig. 6.17. Pictorial representation of working mechanism of TTO4 electrode in a DSSC device structure.

In DSSC device, electrical current is generated from solar light illumination by the artificial photo-electrochemical reaction. The energy band diagram indicates the dye sensitizing mechanism and charge transport mechanism of the DSSC device as shown in Fig. 6.17. The light illuminated on the photo-sensitized dye (N719 dye) molecule/electrolyte (iodide/tri-iodide couple) interface excite the charge carriers from the HOMO to LUMO level, and these photo-excited charge carriers are separated in a fraction of a second. Further, the separated charge carriers are collected by the respective electrodes. The original state of the N719 dye molecule is restored, and the electrons are accepted from the electrolyte couple. Generally, the redox electrolyte couple is made with an organic solvent (ethanol). The regeneration of the charge carriers in the electrolyte (iodide/tri-iodide couple) is compensated by the injection of the electrons from the counter electrode. The solar energy to electrical energy conversion is an instantaneous process [264]. In general, the power conversion efficiency of the DSSC device depends on charge transfer resistance between photoanode to dye electrolyte interface and the counter electrode to the electrolyte interface. Most importantly, the faster electron injection from the dye molecule to the TiO_2 layer decreases the recombination rate [265,266]. To achieve good efficiency, the forward reduction reaction (iodide/tri-iodide couple) rate of donor electron must be higher than the oxidation reaction of the injected electrons from the counter electrode [267]. Finally, the counter electrode should have lower sheet resistance to collect the generated charge carriers. The work function of layers in the DSSC should also match with other layers to achieve maximum efficiency of the device.

6.5.2. Photocurrent density–voltage (J–V) characteristics

Photocurrent density–voltage (J-V) characteristics of DSSCs based on reference FTO electrode and TTO4 electrode with same N719 dye contents are tested under AM 1.5 G illumination (100 mW cm^{-2}). Figure 6.18 shows the J–V plot for reference FTO electrode and TTO4 electrode based DSSCs and the corresponding photovoltaic parameters of the fabricated devices. The obtained J-V curve indicates that the performance of TTO4 electrode plays a significant role in the photovoltaic performance of fabricated DSSC. For DSSC based on TTO4 electrode, the open-circuit voltage is 0.71 V and short circuit photocurrent density is 7.27 mA cm^{-2}. The power conversion efficiency measured is 3.26 % (Table 6.5). Whereas DSSCs based on FTO electrode, V_{oc} depicts an obvious increase to 0.74 V, while J_{sc} shows a significant increase to 10.08 mA cm^{-2} with conversion efficiency of 5.58 % (Table 6.5). The efficiency of TTO4 based DSSC is low due to the low photocurrent density and low fill factor. The higher sheet resistance offered by TTO4 electrode compared to FTO electrode may be the reason for low photocurrent density. The low resistance stability of TTO4 electrode (400 °C) compared to standard FTO (500 °C) may also be the reason for the observed low power conversion efficiency. The commercial FTO electrode-based DSSC device possess better efficiency than the TTO4 electrode due to its good electrical, and optical properties. However, it is still needed to improve the electrical, optical, and surface properties to achieve a better power conversion efficiency using TTO4 electrode.

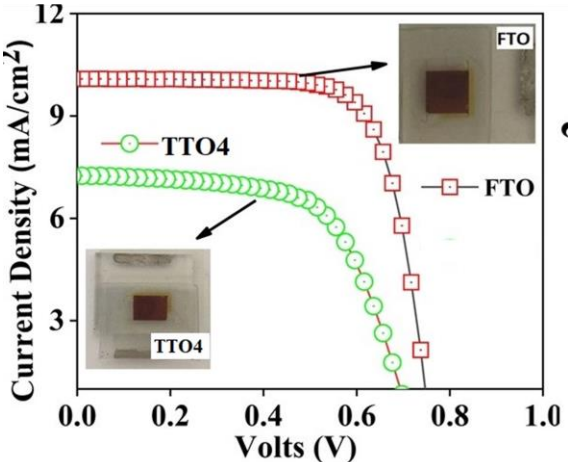

Fig. 6.18. J-V characteristics of the TTO4 and FTO based DSSC devices and inset are the photographs of the fabricated devices.

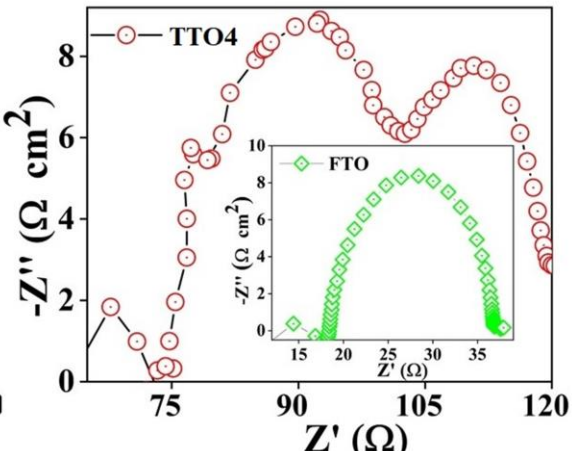

Fig. 6.19. Nyquist impedance spectra of TTO4 and FTO electrodes (inset).

Table 6.5. The photocurrent density-voltage (J-V) parameters of DSSCs fabricated using commercially available FTO and optimized TTO4 electrodes.

DSSC electrode	V_{oc} (mV)	J_{sc} ($mAcm^{-2}$)	Fill factor (%)	η (%)
Reference FTO	0.74	10.08	74.06	5.58
TTO4	0.71	7.27	63.1	3.26

6.5.3. Electrochemical impedance spectroscopic analysis

The charge transport properties of the DSSC fabricated using TTO4 electrode investigated by electrochemical impedance spectroscopy (EIS) provide the information of the photochemical and electrochemical mechanism of the device as a function of frequency [268]. The frequency dependence of the real (Z') and imaginary (Z") parts of the complex impedance spectra are presented in Fig. 6.19 in the form of Nyquist plots along with reference FTO electrode in the inset. The x-intercept of the Nyquist plots measures the series resistance of the respective electrodes. The IVIUMSOFT software was used to fit the equivalent circuit of the EIS spectra, in which the high-frequency intercept on the real axis representing the series resistance R_S is sheet resistance, R1 is the charge-transfer resistance at the photoanode and electrolyte interface, and R2 is the charge-transfer resistance at the counter electrode/electrolyte interface for I^{3-}/I^- redox reaction. The TTO4 electrode exhibits higher R_S of 71.69 Ω compared to reference FTO electrode of 17.69 Ω. This higher sheet resistance of TTO4 affect the collection of the charge carriers which may be the reason for the observed lower photocurrent density in the DSSC device. There are two nearly equal semicircles observed in the EIS data of DSSC based on TTO4 in the Nyquist plot. Whereas FTO electrode-based DSSC device shows smaller semicircle in the low frequency region (0.1 to 100 Hz) indicating low charge transport resistance in the photoanode and electrolyte interface (R1= 5.022 Ω). At higher frequency region (100 kHz to 1 MHz) it shows relatively higher semi-circle indicating the charge transport resistance (R2 = 13.8 Ω) at the electrolyte-counter electrode interface. For the TTO4 electrode-based DSSC device, the 1st semicircle in the lower frequency range correspond to higher recombination resistance (R1= 144.4 Ω) which may be the reason for better power conversion efficiency of the device. The 2nd larger semicircle in the higher frequency range indicates the charge transport resistance (R2= 16.21 Ω) between the counter electrode-electrolyte interface (counter electrode – redox I^-- I^{3-} couple) [263,268]. This higher charge transport resistance may influence the charge carrier collection of the counter electrode. The band matching of the TTO4

electrode with other layers is illustrated in Fig. 6.17. The photovoltaic performance of a DSSC device also depends on the work function of the interfacial layer [269]. The TTO4 thin film electrode possesses lower work function similar to the FTO electrode, and hence, it is suitable for solar cell applications [270]. The estimated efficiency of the TTO4 based DSSC device indicate that it has potential for being used as an alternative material for ITO/FTO.

6.6. Conclusion

In summary, the TTO films show polycrystalline nature with tetragonal structure. Preferred orientation was along the (210) plane direction. The estimated binding energies of the Sn, O, Ta elements confirm the oxidational states of Sn^{4+}, O^{2-} and Ta^{5+} charge states. The surface morphology of the films was strongly dependent upon the dopant concentration. The higher average transmittance (> 86 %) was observed in the visible region for TTO4 film. The PL emission spectra indicate strong near band edge emission centered at 393 nm and the oxygen vacancy defect emission centered at 546 nm. The TTO4 film possess the lowest electrical resistivity of 4.36×10^{-4} Ω cm and the lowest sheet resistance of 17.9 Ω/□ when compared to other films. Finally, the optimal TTO4 thin film was chosen for large area coating. The large area deposited TTO4 film electrode has been successfully tested in DSSC device. The TTO4 electrode based DSSC device showed open-circuit voltage of 0.71 V and short circuit photocurrent density of 7.27 mA cm^{-2} with a power conversion efficiency of 3.26 %. However, it is still needed to improve the electrical and surface properties of the TTO4 film for better power conversion efficiency when used as an electrode in DSSC. Hence, the TTO4 electrode could serve as a potential alternative transparent conducting electrode for supplementing the commercially available ITO/FTO electrodes.

CHAPTER: 7

Summary, Conclusions and Perspectives for Future Work

This chapter summarizes and concludes on all the results obtained on various elements doped alternative transparent conducting SnO_2 that are previously discussed in detail in the individual chapters. This chapter consists of two parts: firstly, comparison of the best optimum results of optical, electrical transport properties for four different transparent conduction oxide (TCO) materials. Secondly the future perspectives on the stabilized materials are briefly discussed.

7.1. Summary of the research work

This doctoral thesis work has been carried out for exploring alternative transparent conducting oxide materials. Optimization, characterization, and finally large area coating are performed with potential testing for DSSC application. The four different donors doped SnO_2 material; namely, Sb- doped SnO_2 (ATO), Ba and Sb co-doped SnO_2 (BATO), Nb-doped SnO_2 (NTO), and Ta-doped SnO_2 (TTO) thin films were successfully optimized by cost-effective chemical spray pyrolysis method. The structural, surface, optical, and electrical transport properties of all the deposited thin films are investigated by several analytical techniques. The ATO film deposited at 450 °C substrate temperature shows better transmittance and higher conductivity compared to undoped SnO_2 system. However, ATO film has a grey tinge during the film formation, this may affect the optical transmittance and conductivity of the films. To overcome this issue without sacrificing the TCO properties, the ATO film is co-doped with barium (Ba). The 5 wt% of Sb and 2 wt% of Ba co-doped SnO_2 system shows the enhanced electrical transparency and conductivity compared to ATO film. The 1.5 wt% of Nb doped SnO_2 (NTO3) thin film showing significant enhancement of the optical and electrical properties with appreciable resistance stability seems to be a promising alternative TCO electrode. The 4 wt% of Ta doped SnO_2 (TTO4) film exhibited significantly better optical transmittance and conductivity with Ta doping concentration. Also, TTO4 film has good resistance stability compared to other films explored in this thesis.

In addition to this, large area (10×10 cm^2) coating was also performed and surface variation and resistance stability of the TCO films are also studied. Finally, the suitability of selected TCO materials (BATO2, TTO4) were tested in dye sensitized solar cells (DSSC)

exhibiting appreciable efficiency. More importantly, the following conclusions have been optioned from this thesis work.

7.2. Conclusion

The comparison of the important properties such as deposition condition, optical transmittance, resistivity, mobility, carrier concentration, sheet resistance, resistance stability, work function and figure of merit of the best optimized films with their respective dopant element are shown in Table 7.1. and 7.2.

The important conclusion of this dissertation are as follows,

- ✓ The Ba and Sb co-doping strategy has significantly enhanced the electrical conductivity optimal transparency and effectively neutralized the grey tinge due to Sb doping in the SnO_2 system.

- ✓ The 1.5 wt% of Nb doping in SnO_2 (NTO3) film has yielded significant improvement in conductivity with low doping concentration and low substrate temperature compared to undoped SnO_2 system. There is scope for improving NTO film properties by fine tuning the deposition parameters and Nb doping concentration.

- ✓ Ta doped SnO_2 film was the best of the all the films explored in this work. A minimal 4 wt% of Ta could lead to high transparency with low sheet resistance and low resistivity (Table 7.1. and 7.2).

- ✓ The performance of the BATO2 and TTO4 electrode based DSSC device was also very significant.

Table 7.1. Comparison of optimized donor (Sb, Ba-Sb, Nb, Ta) doped SnO_2 films.

Films	Source (wt%)	Substrate temperature	Transmittance at 550 nm (%)	Band gap (eV)	Carrier density (cm^{-3})	Mobility ($cm^2/V{\cdot}s$)	Resistivity (Ω cm)	Sheet Resistance ($\Omega/\square$)	FoM (Ω^{-1})
ATO5	Sn: Sb = 95:5	450 °C	89	3.81	3.12×10^{20}	25.1	7.89×10^{-4}	24.9	1.25×10^{-2}
BATO2	Sn: Sb: Ba = 93:5:2	400 °C	85	3.71	4.73×10^{21}	22.2	4.41×10^{-4}	23.1	1.05×10^{-2}
NTO3	Sn: Nb = 98.5:1.5	400 °C	82	3.82	4.63×10^{20}	25.9	6.45×10^{-4}	25.9	5.29×10^{-3}
TTO4	***Sn: Ta = 96:4***	***400 °C***	***86***	***4.01***	***5.31×10^{21}***	***17.9***	***4.36×10^{-4}***	***17.96***	***4.73×10^{-2}***

Table 7.2. Comparison of large area (10×10 cm^2) deposited donor (Sb, Ba-Sb, Nb, Ta) doped SnO_2 films with ITO and FTO electrodes.

Films	Transmittance at 550 nm (%)	Resistivity (ρ, Ω cm)	Sheet Resistance (Rs, $\Omega/\square$)	FoM (Ω^{-1})	Resistance Stability	Work function (eV)	DSSC efficiency (η)
Large area coated ATO5	77.5	6.71×10^{-4}	31.9	2.29×10^{-3}	350 °C	5.14	-
Large area coated BATO2	86	4.60×10^{-4}	16	1.38×10^{-2}	350 °C	5.09	0.76
Large area coated NTO3	75	1.69×10^{-3}	26.5	2.47×10^{-3}	300 °C	5.13	-
Large area coated TTO4	***81***	***4.55×10^{-4}***	***25.1***	***6.15×10^{-2}***	***400 ℃***	***5.08***	***3.26***
Reference FTO	> 90	$> 10^{-5}$	15	0.19×10^{-2} [49]	550 °C	4.9 [178]	8.4 [271]
Reference ITO	> 89.1	$> 10^{-5}$	12.2	2.59×10^{-2}	350 °C	5.1 [209]	1.9 [272]

7.3. Perspectives for Future research work

Several avenues are wide open for further extending the research on these materials, some of which are suggested below:

- The optimized films are to be fine-tuned and replaced for use as an effective electrode in organic optoelectronic devices like OLEDs and solar cells.

- Other efficient co-doped SnO_2 materials may also be deposited and explored for better TCO properties.

- Other chemical/physical deposition methods can be adopted to deposit uniform and dense films so as to lead to better TCO properties.

- These films are to be explored intensively for resistance stability and surface work function properties so as to establish their suitability for several optoelectronic devices.

- Ternary metal oxide like Zn_2SnO_4 thin films may also be researched for OLED and solar cell applications.

References

[1] J. Conti, P. Holtberg, J. Diefenderfer, A. LaRose, J.T. Turnure, L. Westfall, International energy outlook 2016 with projections to 2040, USDOE Energy Information Administration (EIA), Washington, DC (United States), 2016. https://doi.org/DOE/EIA-0484(2016).

[2] J.D. Beach, B.E. McCandless, Materials Challenges, RSC Energy, The Royal Society of Chemistry, Thomas Graham House, Science Park, Milton Road, Cambridge CB4 0WF, UK, 2007. https://doi.org/10.1039/9781849733465.

[3] S. Chu, Y. Cui, N. Liu, The path towards sustainable energy, Nat. Mater. 16 (2016) 16–22. https://doi.org/10.1038/nmat4834.

[4] O. Ellabban, H. Abu-Rub, F. Blaabjerg, Renewable energy resources: Current status, future prospects and their enabling technology, Renew. Sustain. Energy Rev. 39 (2014) 748–764. https://doi.org/10.1016/j.rser.2014.07.113.

[5] X. Yu, T.J. Marks, A. Facchetti, Metal oxides for optoelectronic applications, Nat. Mater. 15 (2016) 383–396. https://doi.org/10.1038/nmat4599.

[6] K. Ellmer, Past achievements and future challenges in the development of optically transparent electrodes, Nat. Photonics. 6 (2012) 809–817. https://doi.org/10.1038/nphoton.2012.282.

[7] M. Grundmann, H. Frenzel, A. Lajn, M. Lorenz, F. Schein, H. Von Wenckstern, Transparent semiconducting oxides: Materials and devices, Phys. Status Solidi Appl. Mater. Sci. 207 (2010) 1437–1449. https://doi.org/10.1002/pssa.200983771.

[8] S.C. Dixon, D.O. Scanlon, C.J. Carmalt, I.P. Parkin, N-Type doped transparent conducting binary oxides: An overview, J. Mater. Chem. C. 4 (2016) 6946–6961. https://doi.org/10.1039/c6tc01881e.

[9] W. Guo, Z. Xu, F. Zhang, S. Xie, H. Xu, X.Y. Liu, Recent Development of Transparent Conducting Oxide-Free Flexible Thin-Film Solar Cells, Adv. Funct. Mater. 26 (2016) 8855–8884. https://doi.org/10.1002/adfm.201603378.

[10] M. Behtash, P.H. Joo, S. Nazir, K. Yang, Electronic structures and formation energies of pentavalent-ion-doped SnO_2 : First-principles hybrid functional calculations, J. Appl. Phys. 117 (2015) 175101. https://doi.org/10.1063/1.4919422.

[11] P. Erhart, A. Klein, K. Albe, First-principles study of the structure and stability of oxygen defects in zinc oxide, Phys. Rev. B - Condens. Matter Mater. Phys. 72 (2005) 1–7. https://doi.org/10.1103/PhysRevB.72.085213.

[12] S. Yun, Y. Qin, A.R. Uhl, N. Vlachopoulos, M. Yin, D. Li, X. Han, A. Hagfeldt, New-generation integrated devices based on dye-sensitized and perovskite solar cells, Energy

Environ. Sci. 11 (2018) 476–526. https://doi.org/10.1039/c7ee03165c.

[13] J. Werner, J. Geissbühler, A. Dabirian, S. Nicolay, M. Morales-Masis, S. De Wolf, B. Niesen, C. Ballif, Parasitic Absorption Reduction in Metal Oxide-Based Transparent Electrodes: Application in Perovskite Solar Cells, ACS Appl. Mater. Interfaces. 8 (2016) 17260–17267. https://doi.org/10.1021/acsami.6b04425.

[14] G.R.A. Kumara, S. Kaneko, A. Konno, M. Okuya, K. Murakami, B. Onwona-agyeman, K. Tennakone, Large area dye-sensitized solar cells: Material aspects of fabrication, Prog. PHOTOVOLTAICS Res. Appl. 14 (2006) 643–651. https://doi.org/10.1002/pip.695.

[15] Y. Zhang, L. Li, H. Su, W. Huang, X. Dong, Binary metal oxide: advanced energy storage materials in supercapacitors, J. Mater. Chem. A. 3 (2015) 43–59. https://doi.org/10.1039/C4TA04996A.

[16] D. Leister, K. Peters, H.N. Lokupitiya, J. Rathouský, M. Stefik, M. Labs, A. Kuhn, M. Pribil, D. Sarauli, D. Fattakhova-Rohlfing, Nanostructured Antimony-Doped Tin Oxide Layers with Tunable Pore Architectures as Versatile Transparent Current Collectors for Biophotovoltaics, Adv. Funct. Mater. 26 (2016) 6682–6692. https://doi.org/10.1002/adfm.201602148.

[17] M. Morales-Masis, F. Dauzou, Q. Jeangros, A. Dabirian, H. Lifka, R. Gierth, M. Ruske, D. Moet, A. Hessler-Wyser, C. Ballif, An Indium-Free Anode for Large-Area Flexible OLEDs: Defect-Free Transparent Conductive Zinc Tin Oxide, Adv. Funct. Mater. 26 (2016) 384–392. https://doi.org/10.1002/adfm.201503753.

[18] J.T. Wang, X.L. Shi, X.H. Zhong, J.N. Wang, L. Pyrah, K.D. Sanderson, P.M. Ramsey, M. Hirata, K. Tsuri, Morphology control of fluorine-doped tin oxide thin films for enhanced light trapping, Sol. Energy Mater. Sol. Cells. 132 (2015) 578–588. https://doi.org/10.1016/j.solmat.2014.09.043.

[19] Y. Sun, W.D. Chemelewski, S.P. Berglund, C. Li, H. He, G. Shi, C.B. Mullins, Antimony-doped tin oxide nanorods as a transparent conducting electrode for enhancing photoelectrochemical oxidation of water by hematite, ACS Appl. Mater. Interfaces. 6 (2014) 5494–5499. https://doi.org/10.1021/am405628r.

[20] M. Batzill, Surface science studies of gas sensing materials: SnO_2, Sensors. 6 (2006) 1345–1366. https://doi.org/10.3390/s6101345.

[21] H.J. Kim, S.H. Lee, J. Lee, E.S. Lee, J.H. Choi, J.H. Jung, J.Y. Jung, D.G. Choi, High-durable AgNi nanomesh film for a transparent conducting electrode, Small. 10 (2014) 3767–3774. https://doi.org/10.1002/smll.201400911.

[22] S. Bae, S.J. Kim, D. Shin, J.H. Ahn, B.H. Hong, Towards industrial applications of

graphene electrodes, Phys. Scr. 014024 (2012). https://doi.org/10.1088/0031-8949/2012/T146/014024.

[23] C.-L. Kim, C.-W. Jung, Y.-J. Oh, D.-E. Kim, A highly flexible transparent conductive electrode based on nanomaterials, NPG Asia Mater. 9 (2017) e438. https://doi.org/10.1038/am.2017.177.

[24] K. Badeker, fiber d&e elelctrische Leitf&hdgkedt und die themnoelektrische E'raft eimiger Sch wermetal Luerbindungew ; von E. BCideker., Ann. Phys. 22 (1907) 749–766.

[25] P.P. Edwards, A. Porch, M.O. Jones, D. V. Morgan, R.M. Perks, Basic materials physics of transparent conducting oxides, Dalt. Trans. (2004) 2995–3002. https://doi.org/10.1039/b408864f.

[26] K.L. Chopra, S. Major, D.K. Pandya, Transparent conductors-A status review, Thin Solid Films. 102 (1983) 1–46. https://doi.org/10.1016/0040-6090(83)90256-0.

[27] M. Descamps, H. Inion, L. Labaz, United States Patent Office V-O, (1970) 3–6.

[28] T.R. Society, Constitution and mechanism of the selenium rectifier photocell, Proc. R. Soc. London. Ser. A. Math. Phys. Sci. 202 (2006) 449–466. https://doi.org/10.1098/rspa.1950.0112.

[29] G. Bauer, Electrical and optical behavior of semiconductors. XIII measurements on Cd, Tl and Sn oxides, Ann. Phys. 422 (1937) 433–445.

[30] D.M. Mattox, V.H. Mattox, Review of transparent conductive oxides (TCO), in: Soc. Vac. Coaters, 2007.

[31] D.B. Fraser, H.D. Cook, Highly Conductive, Transparent Films of Sputtered $In_{2-x}Sn_xO_{3-y}$, J. Electrochem. Soc. 119 (2007) 1368. https://doi.org/10.1149/1.2403999.

[32] G. Rupprecht, Investigation of the electrical and photoelectric conductivity of thin indium oxide layers, magazine for physics Phys. 139 (1954) 504–517. https://doi.org/10.1007/BF01374559.

[33] L. Holland, G. Siddall, The properties of some reactively sputtered metal oxide films, Vacuum. 3 (1953) 375–391.

[34] G. Haacke, Transparent Conducting Coatings, Annu. Rev. Mater. Sci. 7 (1977) 73–93. https://doi.org/10.1146/annurev.ms.07.080177.000445.

[35] Z.M. Jarzebski, Preparation and physical properties of transparent conducting oxide films, Phys. Status Solidi. 71 (1982) 13–41. https://doi.org/10.1002/pssa.2210710102.

[36] V. Consonni, G. Rey, H. Roussel, D. Bellet, Thickness effects on the texture development of fluorine-doped SnO_2 thin films: The role of surface and strain energy, J. Appl. Phys. 111 (2012) 033523. https://doi.org/10.1063/1.3684543.

[37] R.G. Egdell, I. Mckenzie, C.F. Mcconville, S.F.J. Cox, T.D. Veal, Shallow donor state of hydrogen in In_2O_3 and SnO_2 : Implications for conductivity in transparent conducting oxides, (2009) 1–4. https://doi.org/10.1103/PhysRevB.80.081201.

[38] A. Alcayde, F.G. Montoya, J. Gómez, F. Manzano-Agugliaro, R. Baños, C. Gil, Optimization methods applied to renewable and sustainable energy: A review, Renew. Sustain. Energy Rev. 15 (2011) 1753–1766. https://doi.org/10.1016/j.rser.2010.12.008.

[39] L. Barraud, Z.C. Holman, N. Badel, P. Reiss, A. Descoeudres, C. Battaglia, S. De Wolf, C. Ballif, Hydrogen-doped indium oxide/indium tin oxide bilayers for high-efficiency silicon heterojunction solar cells, Sol. Energy Mater. Sol. Cells. 115 (2013) 151–156. https://doi.org/10.1016/j.solmat.2013.03.024.

[40] M. Lokanc, R. Eggert, M. Redlinger, M. Lokanc, R. Eggert, The Availability of Indium : The Present , Medium Term , and Long Term The Availability of Indium : The Present , Medium Term , and Long Term, 2015.

[41] U.S. Geological Survey, Mineral Commodity Summaries 2015 Mineral Commodity Summaries 2015, US Geol. Surv. (2015) 196. https://doi.org/10.3133/70140094.

[42] A. Chapman, J. Arendorf, T. Castella, P. Thompson, P. Willis, L. Espinoza, S. Klug, E. Wichmann, Study on Critical Raw Materials at EU level Final Report, (2014) 148–151.

[43] T.C. Films, Transparent Conductive Films (TCF) 2014- New market drivers Complex range of options, (2019) 1–6.

[44] J. Colegrove, Opportunities for metal mesh , silver nanowires , carbon nanotubes , graphene and other non-ITO transparent conductive films in the touch display industry and elsewhere, (2020) 2–5.

[45] N. Noor, I.P. Parkin, Enhanced transparent-conducting fluorine-doped tin oxide films formed by Aerosol-Assisted Chemical Vapour Deposition, J. Mater. Chem. C. 1 (2013) 984–996. https://doi.org/10.1039/c2tc00400c.

[46] G.U. Kulkarni, S. Kiruthika, R. Gupta, K.D.M. Rao, Towards low cost materials and methods for transparent electrodes, Curr. Opin. Chem. Eng. 8 (2015) 60–68. https://doi.org/10.1016/j.coche.2015.03.001.

[47] P.S. Huang, F. Qin, Z. Xiong, H.W. Shim, T. Gao, P. Leu, J.K. Lee, Novel Carrier Doping Mechanism for Transparent Conductor: Electron Donation from Embedded Ag Nanoparticles to the Oxide Matrix, ACS Appl. Mater. Interfaces. 9 (2017) 19973–19979. https://doi.org/10.1021/acsami.7b03871.

[48] J.T. Chen, C.S. Hsu, Conjugated polymer nanostructures for organic solar cell applications, Polym. Chem. 2 (2011) 2707–2722. https://doi.org/10.1039/c1py00275a.

[49] B.R. Koo, D.H. Oh, D.H. Riu, H.J. Ahn, Improvement of Transparent Conducting

Performance on Oxygen-Activated Fluorine-Doped Tin Oxide Electrodes Formed by Horizontal Ultrasonic Spray Pyrolysis Deposition, ACS Appl. Mater. Interfaces. 9 (2017) 44584–44592. https://doi.org/10.1021/acsami.7b12968.

[50] C.G. Granqvist, Transparent conductors as solar energy materials: A panoramic review, Sol. Energy Mater. Sol. Cells. 91 (2007) 1529–1598. https://doi.org/10.1016/j.solmat.2007.04.031.

[51] R.M. Pasquarelli, D.S. Ginley, R. O'Hayre, Solution processing of transparent conductors: From flask to film, Chem. Soc. Rev. 40 (2011) 5406–5441. https://doi.org/10.1039/c1cs15065k.

[52] K. Zilberberg, J. Meyer, T. Riedl, Solution processed metal-oxides for organic electronic devices, J. Mater. Chem. C. 1 (2013) 4796–4815. https://doi.org/10.1039/c3tc30930d.

[53] P. Lunca Popa, J. Crêpellière, P. Nukala, R. Leturcq, D. Lenoble, Invisible electronics: Metastable Cu-vacancies chain defects for highly conductive p-type transparent oxide, Appl. Mater. Today. 9 (2017) 184–191. https://doi.org/10.1016/j.apmt.2017.07.004.

[54] A. Stadler, Transparent Conducting Oxides—An Up-To-Date Overview, Materials (Basel). 5 (2012) 661–683. https://doi.org/10.3390/ma5040661.

[55] H.K. Yu, S. Kim, B. Koo, G.H. Jung, B. Lee, J. Ham, J.L. Lee, Nano-branched transparent conducting oxides: Beyond the brittleness limit for flexible electrode applications, Nanoscale. 4 (2012) 6831–6834. https://doi.org/10.1039/c2nr32228e.

[56] D.R. Lide, CRC Handbook of Chemistry and Physics, Internet Version 2005, CRC Press. Taylor Fr. Boca Rat. FL. (2005) 2660. https://doi.org/10.1016/0165-9936(91)85111-4.

[57] C.A. Hoel, T.O. Mason, J.F. Gaillard, K.R. Poeppelmeier, Transparent conducting oxides in the ZnO-In_2O_3-SnO_2 system, Chem. Mater. 22 (2010) 3569–3579. https://doi.org/10.1021/cm1004592.

[58] K.J. Saji, Y.P. Venkata Subbaiah, K. Tian, A. Tiwari, P-type SnO thin films and SnO/ZnO heterostructures for all-oxide electronic and optoelectronic device applications, Thin Solid Films. 605 (2016) 193–201. https://doi.org/10.1016/j.tsf.2015.09.026.

[59] G.B. González, Investigating the Defect Structures in Transparent Conducting Oxides Using X-ray and Neutron Scattering Techniques, Materials (Basel). 5 (2012) 818–850. https://doi.org/10.3390/ma5050818.

[60] S. Mathur, R. Ganesan, I. Grobelsek, H. Shen, T. Ruegamer, S. Barth, Plasma-assisted modulation of morphology and composition in tin oxide nanostructures for sensing applications, Adv. Eng. Mater. 9 (2007) 658–663. https://doi.org/10.1002/adem.200700086.

[61] R.E. Agbenyeke, S. Song, B.K. Park, G.H. Kim, J.H. Yun, T.M. Chung, C.G. Kim, J.H. Han, Band gap engineering of atomic layer deposited $Zn_xSn_{1-x}O$ buffer for efficient $Cu(In,Ga)Se_2$ solar cell, Prog. PHOTOVOLTAICS Res. Appl. 26 (2018) 745–751. https://doi.org/10.1002/pip.3012.

[62] D.B. Buchholz, J. Liu, T.J. Marks, M. Zhang, R.P.H. Chang, Control and characterization of the structural, electrical, and optical properties of amorphous zinc-indium-tin oxide thin films, ACS Appl. Mater. Interfaces. 1 (2009) 2147–2153. https://doi.org/10.1021/am900321f.

[63] A. Sitt, I. Hadar, U. Banin, Band-gap engineering, optoelectronic properties and applications of colloidal heterostructured semiconductor nanorods, Nano Today. 8 (2013) 494–513. https://doi.org/10.1016/j.nantod.2013.08.002.

[64] K.R. Poeppelmeier, V. Caignaert, K. Rickert, S. Malo, N. Sedefoglu, H. Kavak, Structural, Electrical, and Optical Properties of the Tetragonal, Fluorite-Related $Zn_{0.456}In_{1.084}Ge_{0.460}O_3$, Chem. Mater. 27 (2015) 5072–5079. https://doi.org/10.1021/acs.chemmater.5b01724.

[65] Y. Bitla, C. Chen, H.C. Lee, T.H. Do, C.H. Ma, L. Van Qui, C.W. Huang, W.W. Wu, L. Chang, P.W. Chiu, Y.H. Chu, Oxide Heteroepitaxy for Flexible Optoelectronics, ACS Appl. Mater. Interfaces. 8 (2016) 32401–32407. https://doi.org/10.1021/acsami.6b10631.

[66] J. Young Kim, J.W. Jang, D. Hyun Youn, J. Yul Kim, E. Sun Kim, J. Sung Lee, Graphene-carbon nanotube composite as an effective conducting scaffold to enhance the photoelectrochemical water oxidation activity of a hematite film, RSC Adv. 2 (2012) 9415–9422. https://doi.org/10.1039/c2ra21169f.

[67] T. Akter, W.S. Kim, Reversibly stretchable transparent conductive coatings of spray-deposited silver nanowires, ACS Appl. Mater. Interfaces. 4 (2012) 1855–1859. https://doi.org/10.1021/am300058j.

[68] C.F. Guo, Z. Ren, Flexible transparent conductors based on metal nanowire networks, Mater. Today. 18 (2015) 143–154. https://doi.org/10.1016/j.mattod.2014.08.018.

[69] D.S. Hecht, L. Hu, G. Irvin, Emerging transparent electrodes based on thin films of carbon nanotubes, graphene, and metallic nanostructures, Adv. Mater. 23 (2011) 1482–1513. https://doi.org/10.1002/adma.201003188.

[70] A.M. Nardes, M. Kemerink, M.M. de Kok, E. Vinken, K. Maturova, R.A.J. Janssen, Conductivity, work function, and environmental stability of PEDOT:PSS thin films treated with sorbitol, Org. Electron. Physics, Mater. Appl. 9 (2008) 727–734. https://doi.org/10.1016/j.orgel.2008.05.006.

[71] L. Peng-Fei, S. Yue, Y. Zhong-Yuan, Z. Long, L. Qiong-Yao, M. Shi-Jia, H. Li-Hong, L. Yu-Min, Electronic Structure and Optical Properties of Antimony-Doped SnO_2 from First-Principle Study, Commun. Theor. Phys. 57 (2012) 145–150. https://doi.org/10.1088/0253-6102/57/1/22.

[72] M. Batzill, U. Diebold, The surface and materials science of tin oxide, Prog. Surf. Sci. 79 (2005) 47–154. https://doi.org/10.1016/j.progsurf.2005.09.002.

[73] T. Minami, N ew n-Type TCOs, MRS Bull. (2000) 38–44.

[74] J. Cui, A. Wang, N.L. Edleman, J. Ni, P. Lee, N.R. Armstrong, T.J. Marks, Indium Tin Oxide Alternatives-High Work Function Transparent Conducting Oxides as Anodes for Organic Light-Emitting Diodes, Adv. Mater. 13 (2001) 1476–1480. https://doi.org/10.1002/1521-4095(200110).

[75] A.M.V.M. Agranovich, Modern Problems in Condensed Matter Sciences, 10th ed., North Holland, Amsterdam, 1985. https://doi.org/10.1016/b978-0-444-86945-6.50004-7.

[76] O.K. and T.K. Weiguo Hu*, Yukihiro Harada, Aiko Hasegawa, Tomoya Inoue, Intermediate band photovoltaics based on interband – intraband transitions using, Library (Lond). (2011) 308–317. https://doi.org/10.1002/pip.

[77] I.H. Kim, J.H. Ko, D. Kim, K.S. Lee, T.S. Lee, J. h. Jeong, B. Cheong, Y.J. Baik, W.M. Kim, Scattering mechanism of transparent conducting tin oxide films prepared by magnetron sputtering, Thin Solid Films. 515 (2006) 2475–2480. https://doi.org/10.1016/j.tsf.2006.07.020.

[78] T. Serin, A. Yildiz, N. Serin, N. Yildirim, F. Özyurt, M. Kasap, Electron–Electron Interactions in Sb-Doped SnO_2 Thin Films, J. Electron. Mater. 39 (2010) 1152–1158. https://doi.org/10.1007/s11664-010-1252-y.

[79] G. Haacke, New figure of merit for transparent conductors, J. Appl. Phys. 47 (1976) 4086–4089. https://doi.org/10.1063/1.323240.

[80] G. Haacke, Evaluation of cadmium stannate films for solar heat collectors, Appl. Phys. Lett. 30 (1977) 380–381. https://doi.org/10.1063/1.89439.

[81] A. Klein, C. Körber, A. Wachau, F. Säuberlich, Y. Gassenbauer, R. Schafranek, S.P. Harvey, T.O. Mason, Surface potentials of magnetron sputtered transparent conducting oxides, Thin Solid Films. 518 (2009) 1197–1203. https://doi.org/10.1016/j.tsf.2009.05.057.

[82] Z.Q. Li, Y.L. Yin, X.D. Liu, L.Y. Li, H. Liu, Q.G. Song, Electronic structure and optical properties of Sb-doped SnO2, J. Appl. Phys. 106 (2009) 1–6. https://doi.org/10.1063/1.3245333.

[83] M.P.S. Rana, F. Singh, S. Negi, S.K. Gautam, R.G. Singh, R.C. Ramola, Band gap

engineering and low temperature transport phenomenon in highly conducting antimony doped tin oxide thin films, Ceram. Int. 42 (2016) 5932–5941. https://doi.org/10.1016/j.ceramint.2015.12.141.

[84] J. Xu, S. Huang, Z. Wang, First principle study on the electronic structure of fluorine-doped SnO_2, Solid State Commun. 149 (2009) 527–531. https://doi.org/10.1016/j.ssc.2009.01.010.

[85] S. Das, V. Jayaraman, SnO2: A comprehensive review on structures and gas sensors, Prog. Mater. Sci. 66 (2014) 112–255. https://doi.org/10.1016/j.pmatsci.2014.06.003.

[86] N. Sarmadian, R. Saniz, B. Partoens, D. Lamoen, K. Volety, G. Huyberechts, J. Paul, High throughput first-principles calculations of bixbyite oxides for TCO applications, Phys. Chem. Chem. Phys. 16 (2014) 17724–17733. https://doi.org/10.1039/c4cp02788d.

[87] A. Ayeshamariam, S. Ramalingam, M. Bououdina, M. Jayachandran, Preparation and characterizations of SnO_2 nanopowder and spectroscopic (FT-IR, FT-Raman, UV-Visible and NMR) analysis using HF and DFT calculations, Spectrochim. Acta - Part A Mol. Biomol. Spectrosc. 118 (2014) 1135–1143. https://doi.org/10.1016/j.saa.2013.09.030.

[88] N. Mazumder, D. Sen, S. Saha, U.K. Ghorai, N.S. Das, K.K. Chattopadhyay, Enhanced Ultraviolet Emission from Mg Doped SnO 2 Nanocrystals at Room Temperature and Its Modulation upon H_2 Annealing, J. Phys. Chem. C. 117 (2013) 6454–6461. https://doi.org/10.1021/jp4000329.

[89] A.J.C. Lanfredi, R.R. Geraldes, O.M. Berengue, E.R. Leite, A.J. Chiquito, Electron transport properties of undoped SnO_2 monocrystals, J. Appl. Phys. 105 (2009). https://doi.org/10.1063/1.3068185.

[90] E. Shanthi, V. Dutta, A. Banerjee, K.L. Chopra, Electrical and optical properties of undoped and antimony-doped tin oxide films, J. Appl. Phys. 51 (1980) 6243–6251. https://doi.org/10.1063/1.327610.

[91] Y. Chen, Q. Meng, L. Zhang, C. Han, H. Gao, Y. Zhang, H. Yan, SnO_2-based electron transporting layer materials for perovskite solar cells: A review of recent progress, J. Energy Chem. 35 (2018) 144–167. https://doi.org/10.1016/j.jechem.2018.11.011.

[92] F.A. Akgul, C. Gumus, A.O. Er, A.H. Farha, G. Akgul, Y. Ufuktepe, Z. Liu, Structural and electronic properties of SnO_2, J. Alloys Compd. 579 (2013) 50–56. https://doi.org/10.1016/j.jallcom.2013.05.057.

[93] and W.Z. Baozeng Zhou, Ping Wu, Tunable bandgap and ferromagnetism in sputtered epitaxial $Sn_{1-x}Mg_xO_2$ thin films, Appl. Phys. Lett. 101,. 101 (2012). https://doi.org/View online: http://dx.doi.org/10.1063/1.4765346.

[94] M.S. Anwar, F. Ahmed, S.N. Heo, K.Y. Park, B.H. Koo, Indication of room temperature ferromagnetism in highly transparent and conductive Ga-doped SnO_2 thin films, Thin Solid Films. 547 (2013) 137–140. https://doi.org/10.1016/j.tsf.2013.04.053.

[95] M. Kumar, A. Kumar, A.C. Abhyankar, Influence of texture coefficient on surface morphology and sensing properties of W-doped nanocrystalline tin oxide thin films, ACS Appl. Mater. Interfaces. 7 (2015) 3571–3580. https://doi.org/10.1021/am507397z.

[96] K. Gopinadhan, S.C. Kashyap, D.K. Pandya, S. Chaudhary, High temperature ferromagnetism in Mn-doped SnO_2 nanocrystalline thin films, J. Appl. Phys. 102 (2007). https://doi.org/10.1063/1.2817825.

[97] H. Kaneko, K. Miyake, H. Kaneko, K. Miyake, Physical properties of antimonydoped tin oxide thick films n n n, 3629 (2014). https://doi.org/10.1063/1.331144.

[98] B. Stjerna, E. Olsson, C.G. Granqvist, Optical and electrical properties of radio frequency sputtered tin oxide films doped with oxygen vacancies, F, Sb, or Mo, J. Appl. Phys. 76 (1994) 3797–3817. https://doi.org/10.1063/1.357383.

[99] S.C. Ray, M.K. Karanjai, D. Dasgupta, Preparation and study of doped and undoped tin dioxide films by the open air chemical vapour deposition technique, 307 (1997) 221–227.

[100] S. Shanthi, C. Subramanian, P. Ramasamy, Growth and characterization of antimony doped tin oxide thin films, J. Cryst. Growth. 197 (1999) 858–864. https://doi.org/10.1016/S0022-0248(98)01066-5.

[101] K. Omura, P. Veluchamy, M. Tsuji, T. Nishio, M. Murozono, Pyrosol technique to deposit highly transparent, low-resistance SnO_2:F thin films from dimethyltin dichloride, J. Electrochem. Soc. 146 (1999) 2113–2116. https://doi.org/10.1149/1.1391900.

[102] P. Veluchamy, M. Tsuji, T. Nishio, T. Aramoto, H. Higuchi, S. Kumazawa, S. Shibutani, J. Nakajima, T. Arita, H. Ohyama, A. Hanafusa, T. Hibino, K. Omura, Pyrosol process to deposit large-area SnO_2:F thin films and its use as a transparent conducting substrate for CdTe solar cells, Sol. Energy Mater. Sol. Cells. 67 (2001) 179–185. https://doi.org/10.1016/S0927-0248(00)00279-8.

[103] N. Kikuchi, E. Kusano, E. Kishio, A. Kinbara, Electrical and mechanical properties of SnO2:Nb films for touch screens, Vacuum. 66 (2002) 365–371. https://doi.org/10.1016/S0042-207X(02)00156-2.

[104] E. Elangovan, S.A. Shivashankar, K. Ramamurthi, Studies on structural and electrical properties of sprayed SnO_2:Sb films, J. Cryst. Growth. 276 (2005) 215–221. https://doi.org/10.1016/j.jcrysgro.2004.11.387.

[105] R.R. Kasar, N.G. Deshpande, Y.G. Gudage, J.C. Vyas, R. Sharma, Studies and

correlation among the structural , optical and electrical parameters of spray-deposited tin oxide (SnO_2) thin films with different substrate temperatures, 403 (2008) 3724–3729. https://doi.org/10.1016/j.physb.2008.06.023.

[106] A.R. Babar, S.S. Shinde, A. V. Moholkar, C.H. Bhosale, J.H. Kim, K.Y. Rajpure, Sensing properties of sprayed antimony doped tin oxide thin films: Solution molarity, J. Alloys Compd. 509 (2011) 3108–3115. https://doi.org/10.1016/j.jallcom.2010.12.012.

[107] W. Yang, S. Yu, Y. Zhang, W. Zhang, Properties of Sb-doped SnO_2 transparent conductive thin films deposited by radio-frequency magnetron sputtering, Thin Solid Films. 542 (2013) 285–288. https://doi.org/10.1016/j.tsf.2013.06.077.

[108] G. Turgut, E.F. Keskenler, S. Aydin, E. Sönmez, S. Doğan, B. Düzgün, M. Ertuğrul, Effect of Nb doping on structural, electrical and optical properties of spray deposited SnO_2 thin films, Superlattices Microstruct. 56 (2013) 107–116. https://doi.org/10.1016/j.spmi.2013.01.004.

[109] G. Turgut, Effect of Ta doping on the characteristic features of spray-coated SnO_2, Thin Solid Films. 594 (2015) 56–66. https://doi.org/10.1016/j.tsf.2015.10.011.

[110] H.P. Dang, Q.H. Luc, V.H. Le, T. Le, The influence of deposition temperature and annealing temperature on Ga-doped SnO_2 films prepared by direct current magnetron sputtering, J. Alloys Compd. 687 (2016) 1012–1020. https://doi.org/10.1016/j.jallcom.2016.06.236.

[111] M. Esro, S. Georgakopoulos, H. Lu, G. Vourlias, A. Krier, W.I. Milne, W.P. Gillin, G. Adamopoulos, Solution processed SnO_2:Sb transparent conductive oxide as an alternative to indium tin oxide for applications in organic light emitting diodes, J. Mater. Chem. C. 4 (2016) 3563–3570. https://doi.org/10.1039/C5TC04117A.

[112] T.I. Gandhi, R.R. Babu, K. Ramamurthi, M. Arivanandhan, Effect of Mn doping on the electrical and optical properties of SnO_2 thin films deposited by chemical spray pyrolysis technique, Thin Solid Films. 598 (2016) 195–203. https://doi.org/10.1016/j.tsf.2015.12.008.

[113] B.R. Koo, J.W. Bae, H.J. Ahn, Low-temperature conducting performance of transparent indium tin oxide/antimony tin oxide electrodes, Ceram. Int. 43 (2017) 6124–6129. https://doi.org/10.1016/j.ceramint.2017.02.006.

[114] A. Heiras-Trevizo, P. Amézaga-Madrid, L. Corral-Bustamante, W. Antúnez-Flores, P. Pizá Ruiz, M. Miki-Yoshida, Structural, morphological, optical and electrical properties of Sb-doped SnO_2 thin films obtained by aerosol assisted chemical vapor deposition, Thin Solid Films. 638 (2017) 22–27. https://doi.org/10.1016/j.tsf.2017.07.017.

[115] L. Wang, J. Yu, X. Niu, L. Wang, C. Fu, R. Qiu, W. Yan, H. Zhao, J. Yang, Effect of F

and Nb co-doping on structural, electrical and optical properties of spray deposited tin oxide thin films, Thin Solid Films. 649 (2018) 147–153. https://doi.org/10.1016/j.tsf.2018.01.035.

[116] A.Y. Suzuki, K. Nose, A. Ueno, M. Kamiko, Y. Mitsuda, High transparency and electrical conductivity of SnO_2:Nb thin films formed through (001)-Oriented SnO:Nb on glass substrate, Appl. Phys. Express. 5 (2012) 5–8. https://doi.org/10.1143/APEX.5.011103.

[117] S. Gürakar, T. Serin, N. Serin, Studies on optical properties of antimony doped SnO_2 films, Appl. Surf. Sci. 352 (2015) 16–22. https://doi.org/10.1016/j.apsusc.2015.03.057.

[118] V. Fauzia, M.N. Yusnidar, L.H. Lalasari, A. Subhan, A.A. Umar, High figure of merit transparent conducting Sb-doped SnO_2 thin films prepared via ultrasonic spray pyrolysis, J. Alloys Compd. 720 (2017) 79–85. https://doi.org/10.1016/j.jallcom.2017.05.243.

[119] S. Chu, A. Majumdar, Opportunities and challenges for a sustainable energy future, Nature. 488 (2012) 294–303. https://doi.org/10.1038/nature11475.

[120] K. Chopra, Thin film device applications, Springer Science & Business Media, 2012.

[121] M. Faraday, LIX. Experimental relations of gold (and other metals) to light.—The bakerian lecture , London, Edinburgh, Dublin Philos. Mag. J. Sci. 14 (2018) 512–539. https://doi.org/10.1080/14786445708642424.

[122] E. Fortunato, D. Ginley, H. Hosono, D.C. Paine, Transparent conducting oxides for photovoltaics, MRS Bull. 32 (2007) 242–247. https://doi.org/10.1557/mrs2007.29.

[123] J.C. Vigui, J. Spitz, C h e m i c a l V a p o r Deposition a t Low T e m p e r a t u r e s Nozzte Furnace Qo Carrier gas Fogging system t ..... (, 268 (1971) 2–5.

[124] M.H. Grabow, G.H. Gilmer, Thin film growth modes, wetting and cluster nucleation, Surf. Sci. 194 (1988) 333–346. https://doi.org/10.1016/0039-6028(88)90858-8.

[125] G.H. Gilmer, M.H. Grabow, Models of Thin Film Growth Modes, Jom. 39 (1987) 19–23. https://doi.org/10.1007/BF03258055.

[126] R. Shriram, Thin Film Metal Oxides, Fundamentals and Applications in Electronics and Energy, 2010 Springer US, DOI10.1007/978-1-4419-0664-9.

[127] G.J. Exarhos, X.D. Zhou, Discovery-based design of transparent conducting oxide films, Thin Solid Films. 515 (2007) 7025–7052. https://doi.org/10.1016/j.tsf.2007.03.014.

[128] G. Korotcenkov, B.K. Cho, Spray pyrolysis deposition of undoped SnO_2 and In_2O_3 films and their structural properties, Prog. Cryst. Growth Charact. Mater. 63 (2017) 1–47. https://doi.org/10.1016/j.pcrysgrow.2016.12.001.

[129] S.S. Hsieh, S.Y. Luo, Droplet impact dynamics and transient heat transfer of a micro spray system for power electronics devices, Int. J. Heat Mass Transf. 92 (2016) 190–

205. https://doi.org/10.1016/j.ijheatmasstransfer.2015.08.099.

[130] P.S. Patil, Versatility of chemical spray pyrolysis technique, Mater. Chem. Phys. 59 (1999) 185–198. https://doi.org/10.1016/S0254-0584(99)00049-8.

[131] D. Paul Joseph, M. Saravanan, B. Muthuraaman, P. Renugambal, S. Sambasivam, S. Philip Raja, P. Maruthamuthu, C. Venkateswaran, Spray deposition and characterization of nanostructured Li doped NiO thin films for application in dye-sensitized solar cells, Nanotechnology. 19 (2008). https://doi.org/10.1088/0957-4484/19/48/485707.

[132] B.E. Warren, X-ray Diffraction, Courier Corporation, 1990.

[133] B.D. Cullity, Elements of X-ray Diffraction, (2001).

[134] N.S. McIntyre, Quantitative Surface Analysis of materials, ASTM Special Technical Publication, Ohio, 1977.

[135] C.J. Powell, SPECTROSCOPY, 1 (1978) 186–201.

[136] C.W. Oatley, D. McMullan, K.C.A. Smith, The development of the scanning electron microscope, Elsevier: Amsterdam, Netherlands, 1985.

[137] H.J. Butt, B. Cappella, M. Kappl, Force measurements with the atomic force microscope: Technique, interpretation and applications, Surf. Sci. Rep. 59 (2005) 1–152. https://doi.org/10.1016/j.surfrep.2005.08.003.

[138] G. Binnig, C.F. Quate, C. Gerber, Atomi Force Microscope, Phys. Rev. Lett. 56 (1986). https://doi.org/10.1103/PhysRevLett.56.930.

[139] D.H. Lee, 3-Dimensional profile distortion measured by stylus type surface profilometer, Meas. J. Int. Meas. Confed. 46 (2013) 803–814. https://doi.org/10.1016/j.measurement.2012.09.022.

[140] Z.J. Changsheng Li, Shuming Yang, Yiming Wang, Chenying Wang, Wei Ren, Measurement and characterization of a nano scale multipe step height sample using stylus profiler, Appl. Surf. Sci. 387 (2016) 732–735.

[141] Y. Leng, Related Titles Characterization of Surfaces and Nanostructures Basic Concepts of X-Ray Diffraction Characterization of Solid Materials and Heterogeneous Catalysts Advanced Characterization Techniques for Thin Film Solar Cells Characterization Techniques f, 2013.

[142] D.F. Swinehart, The Beer-Lambert Law, J. Chem. Educ. 39 (2009) 333. https://doi.org/10.1021/ed039p333.

[143] T. J., Tauc-1966.Pdf, Phys. Stat. Sol. 15 (1966) 627–637.

[144] G.D. Gilliland, Photoluminescence spectroscopy of crystalline semiconductors, Mater. Sci. Eng. R Reports. 18 (1997) 99–399.

[145] S. Perkowitz, Optical characterization of semiconductors: infrared, Raman, and

photoluminescence spectroscopy, Elsevier, 2012.

[146] L.J. van der Pauw, A method of measuring the resistivity and Hall coefficient on lamellae of arbitrary shape, Philips Tech. Rev. 20 (1958) 220–224. https://doi.org/537.723.1:53.081.7+538.632:083.9.

[147] G.F.S., A new radiation, J. Franklin Inst. 206 (2003) 276–277. https://doi.org/10.1016/s0016-0032(28)91546-x.

[148] M.A. Hazle, M. Mehicic, D.J. Gardiner, P.R. Graves, Practical Raman Spectroscopy: Springer Verlag, Berlin, 1989 (ISBN 3-540-50254-8). viii+ 157 pp. Price DM 78.00, (1990).

[149] D. Kohl, P. Mesquida, G. Schitter, Quantitative AC - Kelvin Probe Force Microscopy, Microelectron. Eng. 176 (2017) 28–32. https://doi.org/10.1016/j.mee.2017.01.005.

[150] W. Melitz, J. Shen, A.C. Kummel, S. Lee, Kelvin probe force microscopy and its application, Surf. Sci. Rep. 66 (2011) 1–27. https://doi.org/10.1016/j.surfrep.2010.10.001.

[151] D.K. Kaushik, M. Selvaraj, S. Ramu, A. Subrahmanyam, Thermal evaporated Copper Iodide (CuI) thin films: A note on the disorder evaluated through the temperature dependent electrical properties, Sol. Energy Mater. Sol. Cells. 165 (2017) 52–58. https://doi.org/10.1016/j.solmat.2017.02.030.

[152] S.C. Dixon, D.O. Scanlon, C.J. Carmalt, I.P. Parkin, n-Type doped transparent conducting binary oxides: an overview, J. Mater. Chem. C. 4 (2016) 6946–6961. https://doi.org/10.1039/C6TC01881E.

[153] M. Zheng, J. Ni, F. Liang, M.C. Wang, X. Zhao, Effect of annealing temperature on the crystalline structure, growth behaviour and properties of SnO_2:Sb thin films prepared by radio frequency (RF)-magnetron sputtering, J. Alloys Compd. 663 (2016) 371–378. https://doi.org/10.1016/j.jallcom.2015.12.037.

[154] H. Sefardjella, B. Boudjema, A. Kabir, G. Schmerber, Structural and photoluminescence properties of SnO_2 obtained by thermal oxidation of evaporated Sn thin films, Curr. Appl. Phys. 13 (2013) 1971–1974. https://doi.org/10.1016/j.cap.2013.08.017.

[155] H. Mun, H. Yang, J. Park, C. Ju, K. Char, High electron mobility in epitaxial SnO_{2-x} in semiconducting regime, APL Mater. 3 (2015) 076107. https://doi.org/10.1063/1.4927470.

[156] A.M. El Sayed, S. Taha, M. Shaban, G. Said, Tuning the structural, electrical and optical properties of tin oxide thin films via cobalt doping and annealing, Superlattices Microstruct. 95 (2016) 1–13. https://doi.org/10.1016/j.spmi.2016.04.017.

[157] S. Sharma, A.M. Volosin, D. Schmitt, D.-K. Seo, Preparation and electrochemical

properties of nanoporous transparent antimony-doped tin oxide (ATO) coatings, J. Mater. Chem. A. 1 (2013) 699–706. https://doi.org/10.1039/C2TA00002D.

[158] A.R. Babar, S.S. Shinde, A. V. Moholkar, C.H. Bhosale, J.H. Kim, K.Y. Rajpure, Physical properties of sprayed antimony doped tin oxide thin films: The role of thickness, J. Semicond. 32 (2011) 1–8. https://doi.org/10.1088/1674-4926/32/5/053001.

[159] E. Shanthi, A. Banerjee, V. Dutta, K.L. Chopra, Electrical and optical properties of tin oxide films doped with F and (Sb+F), J. Appl. Phys. 53 (1982) 1615–1621. https://doi.org/10.1063/1.330619.

[160] P. Taylor, G.B. Harris, Philosophical Magazine Series 7 X . Quantitative measurement of preferred orientation in rolled uranium bars, Communication. (2009) 37–41.

[161] C.Y. Kim, D.H. Riu, Texture control of fluorine-doped tin oxide thin film, Thin Solid Films. 519 (2011) 3081–3085. https://doi.org/10.1016/j.tsf.2010.12.096.

[162] Y. Li, Q. Xin, L. Du, Y. Qu, H. Li, X. Kong, Q. Wang, A. Song, Extremely Sensitive Dependence of SnOxFilm Properties on Sputtering Power, Sci. Rep. 6 (2016) 1–9. https://doi.org/10.1038/srep36183.

[163] I.J. Lee, J. Park, N.E. Sung, J. Kim, X-ray absorption fine structure investigation of the local structure of SnO_2-doped ZnO films, Mater. Chem. Phys. 206 (2018) 103–109. https://doi.org/10.1016/j.matchemphys.2017.12.004.

[164] J. Tauc, Amorphous and Liquid Semiconductors., Springer Science & Business Media, 1977. https://doi.org/10.1080/715120893.

[165] T. J., G. R., V. A., Optical Properties and Electronic Structure of Amorphous Germanium, Phys. Status Solidi. 15 (1966) 627–637. https://doi.org/10.1002/pssb.19660150224.

[166] J. Jiang, Y. Lu, B.K. Meyer, D.M. Hofmann, M. Eickhoff, Shift of optical absorption edge in SnO_2 films with high concentrations of nitrogen grown by chemical vapor deposition, J. Appl. Phys. 119 (2016) 245703. https://doi.org/10.1063/1.4954693.

[167] R. Ramarajan, M. Kovendhan, K. Thangaraju, D. Paul Joseph, Substrate Temperature Dependent Physical Properties of Spray Deposited Antimony-Doped SnO_2 Thin Films, Thin Solid Films. 704 (2020) 137988. https://doi.org/10.1016/j.tsf.2020.137988.

[168] D.P. Joseph, P. Renugambal, M. Saravanan, S.P. Raja, C. Venkateswaran, Effect of Li doping on the structural, optical and electrical properties of spray deposited SnO_2 thin films, Thin Solid Films. 517 (2009) 6129–6136. https://doi.org/10.1016/j.tsf.2009.04.047.

[169] Y. Wang, C. Zhang, J. Li, G. Ding, L. Duan, Fabrication and characterization of ITO thin film resistance temperature detector, Vacuum. 140 (2017) 121–125.

https://doi.org/10.1016/j.vacuum.2016.07.028.

[170] D.H. Zhang, H.L. Ma, Scattering mechanisms of charge carriers in transparent conducting oxide films, App. Phys. A Mater. Sci. Proc. 62 (1996) 487–492.

[171] Y. Muraoka, N. Takubo, Z. Hiroi, Photoinduced conductivity in tin dioxide thin films, J. Appl. Phys. 105 (2009). https://doi.org/10.1063/1.3126713.

[172] S.S. Lin, Y.S. Tsai, K.R. Bai, Structural and physical properties of tin oxide thin films for optoelectronic applications, Appl. Surf. Sci. 380 (2016) 203–209. https://doi.org/10.1016/j.apsusc.2016.01.188.

[173] M.M. Rahman, J. Ahmed, A.M. Asiri, Development of Creatine sensor based on antimony-doped tin oxide (ATO) nanoparticles, Sensors Actuators, B Chem. 242 (2017) 167–175. https://doi.org/10.1016/j.snb.2016.11.053.

[174] S. Yu, H. Zheng, L. Li, S. Chen, Highly conducting and transparent antimony doped tin oxide thin films: the role of sputtering power density, Ceram. Int. 43 (2017) 5654–5660. https://doi.org/10.1016/j.ceramint.2017.01.099.

[175] K. Ravichandran, P. Philominathan, Fabrication of antimony doped tin oxide (ATO) films by an inexpensive, simplified spray technique using perfume atomizer, Mater. Lett. 62 (2008) 2980–2983. https://doi.org/10.1016/j.matlet.2008.01.119.

[176] A.R. Babar, S.S. Shinde, A. V. Moholkar, C.H. Bhosale, J.H. Kim, K.Y. Rajpure, Sensing properties of sprayed antimony doped tin oxide thin films: Solution molarity, J. Alloys Compd. 509 (2011) 3108–3115. https://doi.org/10.1016/j.jallcom.2010.12.012.

[177] A. Rahal, A. Benhaoua, C. Bouzidi, B. Benhaoua, B. Gasmi, Effect of antimony doping on the structural, optical and electrical properties of SnO_2 thin films prepared by spray ultrasonic, Superlattices Microstruct. 76 (2014) 105–114. https://doi.org/10.1016/j.spmi.2014.09.024.

[178] A.R. Babar, K.Y. Rajpure, Effect of intermittent time on structural, optoelectronic, luminescence properties of sprayed antimony doped tin oxide thin films, J. Anal. Appl. Pyrolysis. 112 (2015) 214–220. https://doi.org/10.1016/j.jaap.2015.01.024.

[179] S. Calnan, A.N. Tiwari, High mobility transparent conducting oxides for thin film solar cells, Thin Solid Films. 518 (2010) 1839–1849. https://doi.org/10.1016/j.tsf.2009.09.044.

[180] T.C. Yeh, Q. Zhu, D.B. Buchholz, A.B. Martinson, R.P.H. Chang, T.O. Mason, Amorphous transparent conducting oxides in context: Work function survey, trends, and facile modification, Appl. Surf. Sci. 330 (2015) 405–410. https://doi.org/10.1016/j.apsusc.2015.01.026.

[181] K.J. Kumar, N.R.C. Raju, A. Subrahmanyam, Thickness dependent physical and

photocatalytic properties of ITO thin films prepared by reactive DC magnetron sputtering, Appl. Surf. Sci. 257 (2011) 3075–3080. https://doi.org/10.1016/j.apsusc.2010.10.119.

[182] P. Chetri, B. Saikia, A. Choudhury, Structural and optical properties of Cu doped SnO_2 nanoparticles: An experimental and density functional study, J. Appl. Phys. 113 (2013). https://doi.org/10.1063/1.4811374.

[183] A.K. Singh, A. Janotti, M. Scheffler, C.G. Van De Walle, Sources of electrical conductivity in SnO_2, Phys. Rev. Lett. 101 (2008) 1–4. https://doi.org/10.1103/PhysRevLett.101.055502.

[184] H.S. So, J.-W. Park, D.H. Jung, K.H. Ko, H. Lee, Optical properties of amorphous and crystalline Sb-doped SnO_2 thin films studied with spectroscopic ellipsometry: Optical gap energy and effective mass, J. Appl. Phys. 118 (2015) 085303. https://doi.org/10.1063/1.4929487.

[185] M.Y. Tsai, O. Bierwagen, J.S. Speck, Epitaxial Sb-doped SnO_2 and Sn-doped In_2O_3 transparent conducting oxide contacts on GaN-based light emitting diodes, Thin Solid Films. 605 (2016) 186–192. https://doi.org/10.1016/j.tsf.2015.09.022.

[186] L. Wang, J. Yu, X. Niu, L. Wang, C. Fu, R. Qiu, W. Yan, H. Zhao, J. Yang, Effect of F and Nb co-doping on structural, electrical and optical properties of spray deposited tin oxide thin films, Thin Solid Films. 649 (2018) 147–153. https://doi.org/10.1016/j.tsf.2018.01.035.

[187] G. Turgut, E. Sönmez, The effect of Mo and F double doping on structural, morphological, electrical and optical properties of spray deposited SnO_2 thin films, Ceram. Int. 40 (2014) 175–186. https://doi.org/10.1016/j.spmi.2014.02.009.

[188] Q. Dong, S. Yin, M. Yoshida, X. Wu, B. Liu, A. Miura, T. Takei, N. Kumada, T. Sato, Alkaline earth metal doped tin oxide as a novel oxygen storage material, Mater. Res. Bull. 69 (2015) 116–119. https://doi.org/10.1016/j.materresbull.2014.11.018.

[189] J.A. Aguilar-Martínez, E. Rodríguez, S. García-Villarreal, L. Falcon-Franco, M.B. Hernández, Effect of Ca, Sr and Ba on the structure, morphology and electrical properties of (Co,Sb)-doped SnO_2 varistors, Mater. Chem. Phys. 153 (2015) 180–186. https://doi.org/10.1016/j.matchemphys.2015.01.001.

[190] A. Actin, Cholinesterases—Advances in Research and Application: 2013 Edition, ScholarlyEditions, 2013. https://books.google.com/books?id=Z_ProivwaxgC&pgis=1.

[191] Z.W. Chen, Z. Jiao, M.H. Wu, C.H. Shek, C.M.L. Wu, J.K.L. Lai, Microstructural evolution of oxides and semiconductor thin films, Prog. Mater. Sci. 56 (2011) 901–1029. https://doi.org/10.1016/j.pmatsci.2011.02.001.

[192] F.P. Sabino, L. Nunes Oliveira, S.-H. Wei, J.L.F. Da Silva, Optical and fundamental band gaps disparity in transparent conducting oxides systems, J. Phys. Condens. Matter. 29 (2017) 085501. https://doi.org/10.1088/1361-648x/aa4e8c.

[193] B.D. Cullity, Elements of X-ray Diffraction, 3rd ed., London, United Kingdom, 2014. http://lib.hpu.edu.vn/handle/123456789/29008.

[194] F.H. Aragón, J.A.H. Coaquira, L. Villegas-Lelovsky, S.W. Da Silva, D.F. Cesar, L.C.C.M. Nagamine, R. Cohen, E. Menéndez-Proupin, P.C. Morais, Evolution of the doping regimes in the Al-doped SnO_2 nanoparticles prepared by a polymer precursor method, J. Phys. Condens. Matter. 27 (2015). https://doi.org/10.1088/0953-8984/27/9/095301.

[195] S.U. Lee, B. Hong, W.S. Choi, Structural, electrical, and optical properties of antimony-doped tin oxide films prepared at room temperature by radio frequency magnetron sputtering for transparent electrodes, J. Vac. Sci. Technol. A Vacuum, Surfaces, Film. 27 (2009) 996. https://doi.org/10.1116/1.3139891.

[196] M. Maleki, S.M. Rozati, Structural, electrical and optical properties of transparent conducting SnO_2 films: Effect of the oxygen flow rate, Phys. Scr. 86 (2012). https://doi.org/10.1088/0031-8949/86/01/015801.

[197] N. Lavanya, S. Radhakrishnan, N. Sudhan, C. Sekar, S.G. Leonardi, C. Cannilla, G. Neri, Fabrication of folic acid sensor based on the Cu doped SnO_2 nanoparticles modified glassy carbon electrode, Nanotechnology. 25 (2014). https://doi.org/10.1088/0957-4484/25/29/295501.

[198] V. Inderan, M.M. Arafat, S. Kumar, A.S.M.A. Haseeb, Z.T. Jiang, M. Altarawneh, H.L. Lee, Study of structural properties and defects of Ni-doped SnO_2 nanorods as ethanol gas sensors, Nanotechnology. 28 (2017). https://doi.org/10.1088/1361-6528/aa731c.

[199] D. Jousse, C. Constantino, I. Chambouleyron, Highly conductive and transparent amorphous tin oxide, J. Appl. Phys. 54 (1983) 431–434. https://doi.org/10.1063/1.331675.

[200] S. Sallis, D.O. Scanlon, S.C. Chae, N.F. Quackenbush, D.A. Fischer, J.C. Woicik, J.H. Guo, S.W. Cheong, L.F.J. Piper, La-doped $BaSnO_3$ - Degenerate perovskite transparent conducting oxide: Evidence from synchrotron x-ray spectroscopy, Appl. Phys. Lett. 103 (2013) 1–5. https://doi.org/10.1063/1.4816511.

[201] S. Yu, L. Li, X. Lyu, W. Zhang, Preparation and investigation of nano-thick FTO/Ag/FTO multilayer transparent electrodes with high figure of merit, Sci. Rep. 6 (2016) 1–8. https://doi.org/10.1038/srep20399.

[202] J. Li, J. Wang, L. Zhang, S. Zhang, Nanocrystalline SnO_2 thin films prepared by

anodization of sputtered Sn thin films, J. Vac. Sci. Technol. A. 33 (2015) 031508-1–7. https://doi.org/10.1116/1.4916944.

[203] Y.Y. Lin, H.Y. Lee, C.S. Ku, L.W. Chou, A.T. Wu, Bandgap narrowing in high dopant tin oxide degenerate thin film produced by atmosphere pressure chemical vapor deposition, Appl. Phys. Lett. 102 (2013). https://doi.org/10.1063/1.4798253.

[204] T. Rakshit, I. Manna, S.K. Ray, Effect of SnO_2 concentration on the tuning of optical and electrical properties of ZnO-SnO_2 composite thin films, J. Appl. Phys. 117 (2015) 25704. https://doi.org/10.1063/1.4905835.

[205] A.R. Babar, S.S. Shinde, A. V. Moholkar, C.H. Bhosale, J.H. Kim, K.Y. Rajpure, Structural and optoelectronic properties of antimony incorporated tin oxide thin films, J. Alloys Compd. 505 (2010) 416–422. https://doi.org/10.1016/j.jallcom.2010.06.091.

[206] A.D. Yoffe, Theory of Defects in Solids: Electronic Structure Defects in Insulators and Semiconductors, Oxford University Press, 1986. https://doi.org/10.1088/0031-9112/37/6/029.

[207] M.E. White, O. Bierwagen, M.Y. Tsai, J.S. Speck, Electron transport properties of antimony doped SnO2 single crystalline thin films grown by plasma-assisted molecular beam epitaxy, J. Appl. Phys. 106 (2009) 093704. https://doi.org/10.1063/1.3254241.

[208] G. Haacke, Transparent electrode properties of cadmium stannate, Appl. Phys. Lett. 28 (1976) 622–623. https://doi.org/10.1063/1.88589.

[209] H. Zheng, L. Li, Z. Sun, S. Yu, W. Luo, Preferential orientation, microstructure and functional properties of SnO_2:Sb thin film: The effects of post-growth annealing, Appl. Surf. Sci. 362 (2016) 230–236. https://doi.org/10.1016/j.apsusc.2015.11.230.

[210] W. Melitz, J. Shen, A.C. Kummel, S. Lee, Kelvin probe force microscopy and its application, Surf. Sci. Rep. 66 (2011) 1–27. https://doi.org/10.1016/j.surfrep.2010.10.001.

[211] M.G. Helander, M.T. Greiner, Z.B. Wang, W.M. Tang, Z.H. Lu, Work function of fluorine doped tin oxide, J. Vac. Sci. Technol. A Vacuum, Surfaces, Film. 29 (2011) 011019. https://doi.org/10.1116/1.3525641.

[212] M. Batzill, K. Katsiev, J.M. Burst, U. Diebold, A.M. Chaka, B. Delley, Gas-phase-dependent properties of SnO2 (110), (100), and (101) single-crystal surfaces: Structure, composition, and electronic properties, Phys. Rev. B - Condens. Matter Mater. Phys. 72 (2005) 1–20. https://doi.org/10.1103/PhysRevB.72.165414.

[213] J. Gong, K. Sumathy, Q. Qiao, Z. Zhou, Review on dye-sensitized solar cells (DSSCs): Advanced techniques and research trends, Renew. Sustain. Energy Rev. 68 (2017) 234–246. https://doi.org/10.1016/j.rser.2016.09.097.

[214] M.A. Green, S.P. Bremner, Energy conversion approaches and materials for high-efficiency photovoltaics, Nat. Mater. 16 (2016) 23–34. https://doi.org/10.1038/nmat4676.

[215] L.L. Li, Y.J. Chen, H.P. Wu, N.S. Wang, E.W.G. Diau, Detachment and transfer of ordered TiO 2 nanotube arrays for front-illuminated dye-sensitized solar cells, Energy Environ. Sci. 4 (2011) 3420–3425. https://doi.org/10.1039/c0ee00474j.

[216] S.Y. Kim, Y. Kim, K.M. Lee, W.S. Yoon, H.S. Lee, J.T. Lee, S.J. Kim, Y.H. Ahn, J.Y. Park, T.K. Lee, S. Lee, Fully solution-processed transparent conducting oxide-free counter electrodes for dye-sensitized solar cells: Spray-coated single-wall carbon nanotube thin films loaded with chemically-reduced platinum nanoparticles, ACS Appl. Mater. Interfaces. 6 (2014) 13430–13437. https://doi.org/10.1021/am5019447.

[217] K. Susmitha, M.M. Kumari, A.J. Berkmans, M.N. Kumar, L. Giribabu, S. V. Manorama, M. Raghavender, Carbon nanohorns based counter electrodes developed by spray method for dye sensitized solar cells, Sol. Energy. 133 (2016) 524–532. https://doi.org/10.1016/j.solener.2016.03.059.

[218] J. Qiu, F. Zhuge, K. Lou, X. Li, X. Gao, X. Gan, W. Yu, H.K. Kim, Y.H. Hwang, A facile route to aligned TiO_2 nanotube arrays on transparent conducting oxide substrates for dye-sensitized solar cells, J. Mater. Chem. 21 (2011) 5062–5068. https://doi.org/10.1039/c0jm03689g.

[219] F. Xie, Y. Li, T. Xiao, D. Shen, M. Wei, Efficiency improvement of dye-sensitized $BaSnO_3$ solar cell based surface treatments, Electrochim. Acta. 261 (2018) 23–28. https://doi.org/10.1016/j.electacta.2017.12.117.

[220] S. Bouden, A. Dahi, F. Hauquier, H. Randriamahazaka, J. Ghilane, Multifunctional Indium Tin Oxide Electrode Generated by Unusual Surface Modification, Sci. Rep. 6 (2016) 1–9. https://doi.org/10.1038/srep36708.

[221] S. Nakao, N. Yamada, T. Hitosugi, Y. Hirose, T. Shimada, T. Hasegawa, Fabrication of transparent conductive W-doped SnO_2 thin films on glass substrates using anatase TiO2 seed layers, Phys. Status Solidi. 8 (2011) 543–545. https://doi.org/10.1002/pssc.201000505.

[222] J. Montero, J. Herrero, C. Guillén, Preparation of reactively sputtered Sb-doped SnO_2 thin films: Structural, electrical and optical properties, Sol. Energy Mater. Sol. Cells. 94 (2010) 612–616. https://doi.org/10.1016/j.solmat.2009.12.008.

[223] S. Vallejos, S. Selina, F.E. Annanouch, I. Gràcia, E. Llobet, C. Blackman, Aerosol assisted chemical vapour deposition of gas sensitive SnO_2 and Au-functionalised SnO_2 nanorods via a non-catalysed vapour solid (VS) mechanism, Sci. Rep. 6 (2016) 1–12.

https://doi.org/10.1038/srep28464.

[224] K. Bouras, G. Schmerber, H. Rinnert, D. Aureau, H. Park, G. Ferblantier, S. Colis, T. Fix, C. Park, W.K. Kim, A. Dinia, A. Slaoui, Structural, optical and electrical properties of Nd-doped SnO_2 thin films fabricated by reactive magnetron sputtering for solar cell devices, Sol. Energy Mater. Sol. Cells. 145 (2016) 134–141. https://doi.org/10.1016/j.solmat.2015.07.038.

[225] G. Turgut, E. Sonmez, S. Duman, Evaluation of an Nd doping effect on characteristic properties of tin oxide, Mater. Sci. Semicond. Process. 30 (2015) 233–241. https://doi.org/10.1016/j.mssp.2014.10.008.

[226] R.Y. Korotkov, P. Ricou, A.J.E. Farran, Preferred orientations in polycrystalline SnO_2 films grown by atmospheric pressure chemical vapor deposition, Thin Solid Films. 502 (2006) 79–87. https://doi.org/10.1016/j.tsf.2005.07.248.

[227] S. Zhang, J. Zhang, G. Cao, Q. Wang, J. Hu, P. Zhang, G. Shao, Strong interplay between dopant and SnO_2 in amorphous transparent (Sn, Nb)O_2 anode with high conductivity in electrochemical cycling, J. Alloys Compd. 735 (2018) 2401–2409. https://doi.org/10.1016/j.jallcom.2017.12.021.

[228] S. Suresh, G.E. Unni, M. Satyanarayana, A.S. Nair, V.P.M. Pillai, Ag@Nb_2O_5 plasmonic blocking layer for higher efficiency dye-sensitized solar cells, Dalt. Trans. 47 (2018) 4685–4700. https://doi.org/10.1039/c7dt04825d.

[229] D.C. Tsai, Z.C. Chang, B.H. Kuo, Y.H. Wang, E.C. Chen, F.S. Shieu, Thickness dependence of the structural, electrical, and optical properties of amorphous indium zinc oxide thin films, J. Alloys Compd. 743 (2018) 603–609. https://doi.org/10.1016/j.jallcom.2017.12.062.

[230] A. Rahal, A. Benhaoua, M. Jlassi, B. Benhaoua, Structural, optical and electrical properties studies of ultrasonically deposited tin oxide (SnO_2) thin films with different substrate temperatures, Superlattices Microstruct. 86 (2015) 403–411. https://doi.org/10.1016/j.spmi.2015.08.003.

[231] F. Urbach, The Long-Wavelength Edge of Photographic Sensitivity and of the Electronic Absorption of Solids, Phys. Rev. 92 (1953) 1324. https://link.aps.org/doi/10.1103/PhysRev.92.1324.

[232] M.P.S. Rana, F. Singh, K. Joshi, S. Negi, R.C. Ramola, Influence of electronic excitations on structural, optical and electrical properties of undoped and antimony doped tin oxide thin films, Thin Solid Films. 616 (2016) 34–42. https://doi.org/10.1016/j.tsf.2016.07.070.

[233] S. Nakao, N. Yamada, Y. Hirose, T. Hasegawa, Enhanced carrier generation in Nb-

doped SnO_2 thin films grown on strain-inducing substrates, Appl. Phys. Express. 5 (2012) 3–6. https://doi.org/10.1143/APEX.5.061201.

[234] J. Haeberle, S. Machulik, C. Janowitz, R. Manzke, D. Gaspar, P. Barquinha, D. Schmeißer, Gap states in the electronic structure of SnO2 single crystals and amorphous SnOx thin films, J. Appl. Phys. 120 (2016) 105101. https://doi.org/10.1063/1.4962313.

[235] K.P. Khrishnakumar, C.S. Menon, Determination of the thermal activation energy and grain size of iron phthalocyanine thin films, Mater. Lett. 48 (2001) 64–73. https://doi.org/10.1016/S0167-577X(00)00281-0.

[236] I.M. Costa, E.P. Bernardo, B.S. Marangoni, E.R. Leite, A.J. Chiquito, Metal to insulator transition in Sb doped SnO_2 monocrystalline nanowires thin films, J. Appl. Phys. 120 (2016). https://doi.org/10.1063/1.4971870.

[237] K. Vijayarangamuthu, S. Rath, Nanoparticle size, oxidation state, and sensing response of tin oxide nanopowders using Raman spectroscopy, J. Alloys Compd. 610 (2014) 706–712. https://doi.org/10.1016/j.jallcom.2014.04.187.

[238] M. Marikkannan, V. Vishnukanthan, A. Vijayshankar, J. Mayandi, J.M. Pearce, A novel synthesis of tin oxide thin films by the sol-gel process for optoelectronic applications, AIP Adv. 5 (2015) 0–8. https://doi.org/10.1063/1.4909542.

[239] K. Muthu Karupp[1] K. Muthu Karuppasamy, A. Subrahmanyam, Sol. Energy Mater. Sol. Cells 2008, 92, 1322.asamy, A. Subrahmanyam, The electrochromic and photocatalytic properties of electron beam evaporated vanadium-doped tungsten oxide thin films, Sol. Energy Mater. Sol. Cells. 92 (2008) 1322–1326. https://doi.org/10.1016/j.solmat.2008.05.004.

[240] M. Balestrieri, D. Pysch, J.P. Becker, M. Hermle, W. Warta, S.W. Glunz, Characterization and optimization of indium tin oxide films for heterojunction solar cells, Sol. Energy Mater. Sol. Cells. 95 (2011) 2390–2399. https://doi.org/10.1016/j.solmat.2011.04.012.

[241] Y. Muto, S. Nakatomi, N. Oka, Y. Iwabuchi, H. Kotsubo, Y. Shigesato, High-rate deposition of Ta-doped SnO_2 films by reactive magnetron sputtering using a Sn-Ta metal-sintered target, Thin Solid Films. 520 (2012) 3746–3750. https://doi.org/10.1016/j.tsf.2011.10.061.

[242] M. Esro, S. Georgakopoulos, H. Lu, G. Vourlias, A. Krier, W.I. Milne, W.P. Gillin, G. Adamopoulos, Solution processed SnO_2:Sb transparent conductive oxide as an alternative to indium tin oxide for applications in organic light emitting diodes, J. Mater. Chem. C. 4 (2016) 3563–3570. https://doi.org/10.1039/c5tc04117a.

[243] A. Suryanarayana, M.G. Nortonpproach, X-Ray Diffraction A Practical Approach, 1st

ed., Springer Science+Business Media, LLC, New York, 1998.

[244] A.R. Babar, S.S. Shinde, A. V. Moholkar, C.H. Bhosale, J.H. Kim, K.Y. Rajpure, Physical properties of sprayed antimony doped tin oxide thin films: The role of thickness, J. Semicond. 32 (2011). https://doi.org/10.1088/1674-4926/32/5/053001.

[245] S.C. Dixon, D.O. Scanlon, C.J. Carmalt, I.P. Parkin, N-Type doped transparent conducting binary oxides: An overview, J. Mater. Chem. C. 4 (2016) 6946–6961. https://doi.org/10.1039/c6tc01881e.

[246] R. Simpson, R.G. White, J.F. Watts, M.A. Baker, XPS investigation of monatomic and cluster argon ion sputtering of tantalum pentoxide, Appl. Surf. Sci. 405 (2017) 79–87. https://doi.org/10.1016/j.apsusc.2017.02.006.

[247] S. Nakao, Y. Hirose, T. Fukumura, T. Hasegawa, Carrier generation mechanism and effect of tantalum-doping in transparent conductive amorphous SnO_2 thin films Carrier generation mechanism and effect of tantalum-doping in transparent conductive amorphous SnO2 thin fi lms, Jpn. J. Appl. Phys. 53 (2014) 1–5.

[248] H. Kim, A. Piqué, Transparent conducting Sb-doped SnO2 thin films grown by pulsed-laser deposition, Appl. Phys. Lett. 84 (2004) 218–220. https://doi.org/10.1063/1.1639515.

[249] M. Abdel-Baki, F.A. Abdel-Wahab, F. El-Diasty, One-photon band gap engineering of borate glass doped with ZnO for photonics applications, J. Appl. Phys. 111 (2012). https://doi.org/10.1063/1.3698623.

[250] R.C. Rai, Analysis of the Urbach tails in absorption spectra of undoped ZnO thin films, J. Appl. Phys. 113 (2013). https://doi.org/10.1063/1.4801900.

[251] S.S. Pan, G.H. Li, L.B. Wang, Y.D. Shen, Y. Wang, T. Mei, X. Hu, Atomic nitrogen doping and p-type conduction in SnO_2, Appl. Phys. Lett. 95 (2009) 10–13. https://doi.org/10.1063/1.3258354.

[252] G. Rey, C. Ternon, M. Modreanu, X. Mescot, V. Consonni, D. Bellet, Electron scattering mechanisms in fluorine-doped SnO_2 thin films, J. Appl. Phys. 114 (2013) 183713. https://doi.org/10.1063/1.4829672.

[253] A.A. Alsac, A. Yildiz, T. Serin, N. Serin, Improved conductivity of Sb-doped SnO_2 thin films, J. Appl. Phys. 113 (2013) 1–5. https://doi.org/10.1063/1.4790879.

[254] Y. Kim, S.W. Lee, H. Chen, Microstructural evolution and electrical property of Ta-doped SnO_2 films on Al_2O_3(0001) by metalorganic chemical vapor deposition, Thin Solid Film. 405 (2002) 256–262. https://doi.org/10.1016/S0040-6090(01)01635-2.

[255] Y. Muto, N. Oka, N. Tsukamoto, Y. Iwabuchi, H. Kotsubo, Y. Shigesato, High-rate deposition of Sb-doped SnO_2 films by reactive sputtering using the impedance control

method, Thin Solid Films. 520 (2011) 1178–1181. https://doi.org/10.1016/j.tsf.2011.04.151.

[256] M. Weidner, J. Brötz, A. Klein, Sputter-deposited polycrystalline tantalum-doped SnO_2 layers, Thin Solid Films. 555 (2014) 173–178. https://doi.org/10.1016/j.tsf.2013.05.147.

[257] D.P. Joseph, P. Renugambal, M. Saravanan, S.P. Raja, C. Venkateswaran, Effect of Li doping on the structural, optical and electrical properties of spray deposited SnO_2 thin films, Thin Solid Films. 517 (2009) 6129–6136. https://doi.org/10.1016/j.tsf.2009.04.047.

[258] Q. Wan, E.N. Dattoli, W. Lu, Transparent metallic Sb-doped SnO_2 nanowires, Appl. Phys. Lett. 90 (2007) 2005–2008. https://doi.org/10.1063/1.2743746.

[259] B. Bissig, T. Jäger, L. Ding, A.N. Tiwari, Y.E. Romanyuk, Limits of carrier mobility in Sb-doped SnO_2 conducting films deposited by reactive sputtering Limits of carrier mobility in Sb-doped SnO_2 conducting films deposited by reactive sputtering, 062802 (2015). https://doi.org/10.1063/1.4916586.

[260] Y. Harima, H. Okazaki, Y. Kunugi, K. Yamashita, H. Ishii, K. Seki, Formation of Schottky barriers at interfaces between metals and molecular semiconductors of p- and n-type conductances, Appl. Phys. Lett. 69 (1996) 1059–1061. https://doi.org/10.1063/1.116930.

[261] D.P. Puzzo, M.G. Helander, P.G. Obrien, Z. Wang, N. Soheilnia, N. Kherani, Z. Lu, G.A. Ozin, Organic light-emitting diode microcavities from transparent conducting metal oxide photonic crystals, Nano Lett. 11 (2011) 1457–1462. https://doi.org/10.1021/nl104036c.

[262] G. Veerappan, K. Bojan, S.W. Rhee, Sub-micrometer-sized graphite as a conducting and catalytic counter electrode for dye-sensitized solar cells, ACS Appl. Mater. Interfaces. 3 (2011) 857–862. https://doi.org/10.1021/am101204f.

[263] M. Gratzel, Dye-sensitized solar cells, J. Photochem. Photobiol. C Photochem. Rev. 4 (2003) 145–153. https://doi.org/10.1016/s1389-5567(03)00026-1.

[264] J. Wu, Z. Lan, J. Lin, M. Huang, Y. Huang, L. Fan, G. Luo, Y. Lin, Y. Xie, Y. Wei, Counter electrodes in dye-sensitized solar cells, Chem. Soc. Rev. 46 (2017) 5975–6023. https://doi.org/10.1039/c6cs00752j.

[265] M. Kevin, G.H. Lee, G.W. Ho, Non-planar geometries of solution processable transparent conducting oxide: From film characterization to architectured electrodes, Energy Environ. Sci. 5 (2012) 7196–7202. https://doi.org/10.1039/c2ee21296j.

[266] S. Hore, C. Vetter, R. Kern, H. Smit, A. Hinsch, Influence of scattering layers on efficiency of dye-sensitized solar cells, Sol. Energy Mater. Sol. Cells. 90 (2006) 1176–

1188. https://doi.org/10.1016/j.solmat.2005.07.002.

[267] M.S. Su'ait, M.Y.A. Rahman, A. Ahmad, Review on polymer electrolyte in dye-sensitized solar cells (DSSCs), Sol. Energy. 115 (2015) 452–470. https://doi.org/10.1016/j.solener.2015.02.043.

[268] R. Liu, W. Du, Q. Chen, F. Gao, C. Wei, J. Sun, Q. Lu, Fabrication of Zn_2SnO_4/SnO_2hollow spheres and their application in dye-sensitized solar cells, RSC Adv. 3 (2013) 2893–2896. https://doi.org/10.1039/c2ra22320a.

[269] B. Yoo, K. Kim, D.K. Lee, M.J. Ko, H. Lee, Y.H. Kim, W.M. Kim, N.G. Park, Enhanced charge collection efficiency by thin-TiO_2-film deposition on FTO-coated ITO conductive oxide in dye-sensitized solar cells, J. Mater. Chem. 20 (2010) 4392–4398. https://doi.org/10.1039/b926145a.

[270] A. Kar, A. Patra, Recent development of core-shell SnO_2 nanostructures and their potential applications, J. Mater. Chem. C. 2 (2014) 6706–6722. https://doi.org/10.1039/c4tc01030b.

[271] L. Kavan, P. Liska, S.M. Zakeeruddin, M. Grätzel, Optically transparent FTO-free cathode for dye-sensitized solar cells, ACS Appl. Mater. Interfaces. 6 (2014) 22343–22350. https://doi.org/10.1021/am506324d.

[272] C. Sima, C. Grigoriu, S. Antohe, Comparison of the dye-sensitized solar cells performances based on transparent conductive ITO and FTO, Thin Solid Films. 519 (2010) 595–597. https://doi.org/10.1016/j.tsf.2010.07.002.

List of Publications

1. R. Ramarajan, M. Kovendhan, K. Thangaraju D. Paul Joseph, R. Ramesh Babu, Viswanathan Elumalai, *Enhanced optical transparency and electrical conductivity of Ba and Sb co-doped SnO_2 thin films*. Journal of Alloys and Compounds 823 (2020) 1537092, https://doi.org/10.1016/j.jallcom.2020.153709.
2. R. Ramarajan, M. Kovendhan, K. Thangaraju D. Paul Joseph, *Indium-free large area Nb-doped SnO_2 thin film as an alternative transparent conducting electrode*. Ceramics International, Volume 46, Issue 8, Part B, 1 June 2020, Pages 12224-12231. https://doi.org/10.1016/j.ceramint.2020.01.270.
3. R. Ramarajan, M. Kovendhan, K. Thangaraju, D. Paul Joseph, R. Ramesh Babu, Facile deposition and characterization of large area highly conducting and transparent Sb-doped SnO_2 thin film, Applied Surface Science 487 (2019) 1385–1393, https://doi.org/10.1016/j.apsusc.2019.05.079.
4. R. Ramarajan, M. Kovendhan, Duy-Thach Phan, K. Thangaraju, R. Ramesh Babu, Ki-Joon Jeon, D. Paul Joseph, *Optimization of Zn_2SnO_4 thin film by post oxidation of thermally evaporated alternative Sn and Zn metallic multi-layers*, Applied Surface Science, 449 (2018) 68-76, https://doi.org/10.1016/j.apsusc.2018.01.029. *(Not included in thesis)*
5. R. Ramarajan, M. Kovendhan, K. Thangaraju D. Paul Joseph, *Substrate Temperature Dependent Physical Properties of Spray Deposited Antimony-Doped SnO_2 Thin Films*, Thin Solid Films. 704 (2020) 137988. https://doi.org/10.1016/j.tsf.2020.137988.

Book chapter

1. R. Ramarajan, D. Paul Joseph, K. Thangaraju, M. Kovendhan ***"Indium-Free Alternative Transparent Conducting Electrodes: An Overview and Recent developments"*** Metal and metal oxides for energy and electronics, Springer Nature *(Accepted)*.

Conference Proceedings

1. R. Ramarajan, M. Kovendhan, R. Ramesh Babu, K. Thangaraju and D. Paul Joseph, *Optimization and transport properties of 'Nb' doped SnO_2 thin film as an alternative TCO application*, AIP Conference Proceedings 2115, 030427 (2019); https://doi.org/10.1063/1.5113266.
2. Mahantesh Khetri, R. Ramarajan, N. Purusotham Reddy, M. Kovendhan, K. V. Ashish Srivatsav, Bonta Srinivasa Rao, K. Thangaraju and D. Paul Joseph, *Stabilization of 5 wt % 'Sb' doped SnO_2 thin film by post oxidation of thermally evaporated metallic layer*, AIP Conference Proceedings 2115, 030278 (2019); https://doi.org/10.1063/1.5113117.

3. Gnyaneshwar Dasi, R. Ramarajan, and Kuppusamy Thangaraju, *Improved electron injection in spin coated Alq_3 incorporated ZnO thin film in the device for solution processed OLEDs*, AIP Conference Proceedings 1942, 060015 (2019); https://doi.org/10.1063/1.5028785.
4. R. Ramarajan, K. Thangaraju, R. Ramesh Babu, and D. Paul Joseph, *Electrical transport Properties of spray deposited transparent conducting ortho Zn_2SnO_4 thin films*, AIP Conference Proceedings 1942, 110042 (2018); https://doi.org/10.1063/1.5029025.
5. Gnyaneshwar Dasi, R. Ramarajan, and Kuppusamy Thangaraju, *Improved performance in the aged electron-only devices based on tris-(8-hydroxyquinoline) aluminum thin film as electron transport layer for OLED applications*, AIP Conference Proceedings 1942, 060015 (2018); https://doi.org/10.1063/1.5113050.
6. Gnyaneshwar Dasi, R. Ramarajan, R. Thangappan, R. Jayavel, and K. Thangaraju, *Improved electroluminescence in organic light emitting diodes by thermal annealing of indium tin oxide anode*, AIP Conference Proceedings 1832, 060017 (2017), https:// doi.org /10.1063 /1. 4980422.